Universidad Autonóma de Madrid

Doctoral Thesis

Practical Control of Multipactor Threshold and Insertion Losses on RF Satellite Devices and Study of Secondary Electron Emission for Multipactor and Electron Cloud Mitigation

Author:

Luis. A González

Supervisor:

Dr. Luis Galán

A thesis submitted in fulfilment of the requirements for the degree of

PhD. in Advanced Materials and Nanotechnology

at

Departamento de Fisíca Aplicada - Facultad de Ciencias

June 5, 2015

Acknowledgements

En primer lugar, quiero agradecer a la Prof. Luis Galán Estella, director de esta tesis, por la ayuda y los conocimientos científicos que me ha trasmitido, por la valiosísima ayuda que he recibido por su parte y su dedicación profesional durante estos años para hacer posible la finalización de esta tesis así como su gran apoyo en la escritura de este manuscrito. Quiero expresar mis mas sinceros agradecimientos a Valentin Nistor por haber sido mi mentor durante mi incio en el doctorado y por su apoyo y paciencia y por haberme ensañado todo lo necesario sobre el manejo de los equipos. También me gustaría agradecer a la Dra. Isabel Montero por su ayuda y disponibilidad, siempre que la he necesitado.

Contents

List of Figures

List of Tables

Abbreviations

SEE	**S**econdary **E**lectron **E**mission
SE	**S**econdary **E**lectron
EDC	**E**nergy **D**istribution **C**urve
SEY	**S**econdary **E**lectron **Y**ield
LHC	**L**arge **H**adron **C**ollider
EM	**E**lectro**M**agnetic
DC	**D**irect **C**urrent
EC	**E**lectron **C**loud
CSDA	**C**onstant **S**lowing **D**own **A**pproximation
CSIC	**C**onsejo **S**uperior de **I**nvestigaciones **C**ientificas
ICMM	**I**nstituto de **C**iencia de **M**ateriales de **M**adrid
ONERA	**O**ffice **N**ational d'**E**tudes et de **R**echerches **A**erospatiales
VSC	**V**al **S**pace **C**onsortium
RF	**R**adio **F**requency
MEST	**M**ultipactor **E**lectron **S**imulation **T**ool
IL	**I**nsertion **L**oss
UHV	**U**ltra **H**igh **V**acuum
KRPM	**K**ilo **R**evolutions **P**er **M**inute
PVD	**P**hysical **V**apour **D**eposition
CVD	**C**ehmical **V**apour **D**eposition
FWHM	**F**ull **W**idth at **H**alf **M**aximum
UAM	**U**niversidad **A**utonoma de **M**adrid
INFN	**I**nstituto **N**azionale di **F**isica **N**ucleare
LNF	**L**aboratori **N**azionali di **F**rascati

CRR	**C**onstant **R**etardation **R**atio
CAE	**C**onstant **A**nalyzing **E**nergy
WF	**W**ork **F**unction
PES	**P**hotoemission **S**pectroscopies
XPS	**X**-Ray **P**hotoemission **S**pectroscopy
SEM	**S**canning **E**lectron **M**icroscopy
FE-SEM	**F**ield **E**mmision **S**canning **E**lectron **M**icroscopy
EDX	**E**nergy **D**ispersive **X**-Ray spectroscopy
AFM	**A**tomic **F**orce **M**icroscopy
ITI	**A**tomic **F**orce **M**icroscopy
TPP-2M	**T**anuma **P**owell and **P**enn
DUT	**D**evice **U**nder **S**tudy
MP	**M**ulti**P**actor
MPT	**M**ulti**P**actor *T*hreshold
VB	**V**alence *B*and

Symbols

E_0	Primary Energy	eV
SEY_{max}	Maximum value of SEY	
$E_{0,m}$	Primary Energy at which SEY_max occurs	eV
$E_{0,1}$	Primary Energy at which first SEY crossover occurs	eV
δ_{True}	True secondary electrons contribution to SEY	
$\delta_{Inelastic}$	Inelastically backscattered electrons contribution to SEY	
$\delta_{Elastic}$	Elastically backscattered electrons contribution to SEY	
ζ	Average energy loss per generated SE	eV
B	SE scape probability	
α	SE absorption coefficient	
A	Primary electron absorption coefficient	
d	Primary electron range	nm
n	Power law coefficient	eV
d_g	Gap distance	mm
v	Velocity	m/s
e	Electron charge	$1.60217657 \cdot 10^{-19}$ C
$\mathfrak{E}$	Electric Field	N/C
$\mathfrak{B}$	Magnetic Field	T
ω	Angular frequency	rads^{-1}
μ_o	Magnetic permeability	H/m
σ	Electric conductivity	S/m
γ	EM wave spatial dumping factor	nm^{-1}
ϵ	Electric permittivity	F/m
δ	Skin depth	nm

α_c	Power attenuation constant	dB/m
R_s	Surface resistance	Ω/m
η	Wave impedance	Ω
f_c	Cut-off frequancy	Hz
F	Scrubbing fluence or dose	C/mm^2
I	Intensity of electrical current	A
$\mathfrak{A}$	Area	mm^2
ϕ	Work function	eV
$\mathfrak{I}$	XPS intensity	$a.u.$
S	XPS sensitivity factor	
N	Atomic concentration	cm^{-3}
d_{Thick}	Thickness	nm
λ	Inelastic mean free path	nm
P	Power	W
V	$Voltage$	V
$\mathfrak{D}$	Domain	

Chapter 1

Introduction

The secondary electron emission (SEE) is the process through which, electrons bounded to a solid are released to the vacuum due to the exchange of energy with electrons impacting on that solid. SEE is an extremely surface sensitive phenomenon and is at the origin of numerous technological detrimental events regarding the exponential growth of electron population of vacuum systems under electromagnetic resonant conditions.

The avalanche growth of the electron population in vacuum by SEE under radio frequency (RF) resonance conditions is known as Multipactor effect. It was first observed and studied by Taylor Farnsworth in the early 1930's [1]. Multipactor effect has been an important object of study during the last three decades due to the adverse effects it can originate on vacuum operating RF systems. Not only it is a disturbing effect of the operation of high power RF devices in vacuum, but also represents a very important technical problem due to the detrimental effects that it can cause on those equipments leading to degradation and system failure [2–6]. In the realm of satellite waveguides, it can be the cause of numerous signal related issues such as reduction of signal to noise ratio and detune of microwave cavities. Also the risk of permanent physical damage is present in these devices whose reparation becomes difficult or even impossible after satellite launch [2, 7–9]. Due to the surface character of SEE processes, anti-Multipactor treatments should include the first surface layers of the treated material. For this reason, when interacting with low SEE treatments, additional difficulties arise regarding the power attenuation of the transmitted RF wave owing to skin effects [10, 11].

In the field of high-energy particle accelerators, electron cloud (EC) phenomena are a detrimental effect that takes place as a consequence of the SEE. In this case, the phenomenon is originated and sustained by SEE processes derived from the impact of accelerated photoelectrons on the walls of the accelerator beam pipe. If at certain point, the growing density of the present EC is high enough to influence the beam quality, detrimental effects would be induced up to its complete degradation[12]. Its discovery dates back to nearly 50 years ago [13, 14] and its study has been an important research of interest since then. In the particular case of the Large Hadron Collider (LHC) at CERN in which the mecesary magnetic dipole field requires the use of superconducting technology operating at low temperature below 20 K, EC phenomena leads to the increase of the heat load [15–17] of the cold dipoles resulting in their inefficient operation which limits the achievable machine performance.

Both Multipactor effect and EC phenomena are extremely sensitive to SEE and the probabilities for Multipactor or EC to take place strongly depend on the secondary electron yield (SEY) parameters of the materials exposed to primary electron bombardment. For this reason, special attention was paid on the understanding and modification of SEY of the materials used during the development of this thesis.

The aim of this work is the development of low SEY anti-Multipactor coatings by means of surface micro- and nano-structuring of technical materials for aerospatial applications, as well as the study of the phenomena involved in the modification of the SEY and their role on the Multipactor and EC mitigation. In Chapters 6 and 7, the strategies followed to achieve micro- and nano-structured surfaces of low SEY for technological satellite RF devices applications, and the most relevant results of the studies carried out will be presented. It will be shown that it is possible to achieve high aspect ratio roughness with highly improved SEY properties, without generating a significant increase on the power insertion losses (IL) due to skin effects. Intensive studies taken within an unprecedented energy range, regarding the SEY at very low primary energies (from 0 to 40 eV above the Fermi level) will be presented in Ch.8. Supported by simulation studies, it will be proved that the behavior of the low energy secondary electron yield (LE-SEY) plays indeed a critical role on the EC build up and the evolution of the heat load in the cold dipoles of LHC-CERN. The low SEY properties of sp^2 carbon has often led to the project of using graphitic carbon thin films for the reduction of the SEY and multipacting phenomena in

particle accelerators and in space devices by means of electron conditioning or Scrubbing [18–20]. Regarding the low SEE properties of sp^2 bonded carbon, the evolution of SEY and LE-SEY of graphite as a function of the amount of lattice damaging will be presented in Ch. 9. It will be shown that the level of structural quality plays an important role on the electronic properties of the material and consequently its effect on SEY and LE-SEY will be analyzed.

Chapter 2

Introducción

La emisión secundaria de electrones, (SEE por sus iniciales en inglés) es el proceso a través del cual, electrones ligados a un sólido, son emitidos al vacío debido al intercambio de energía producido por el impacto de electrones con ese sólido. SEE es extremadamente sensible al estado superficial del sólido en el cual tiene lugar y es la causa de numerosos fenómenos perjudiciales con respecto al crecimiento exponencial de la población de electrones presentes en sistemas de vacío bajo condiciones de resonancia electromagnética.

El crecimiento en forma de avalancha de la población de electrones en vacío debido a la emisión secundaria de electrones bajo condiciones de resonancia de radio frecuencia (RF) es conocido como efecto Multipactor. Fue originalmente observado y estudiado por Taylor Farnsworth en la década de 1930 [1]. El efecto Multipactor ha sido un importante objeto de estudio durante las últimas tres décadas debido a los efectos adversos que se originan en los dispositivos de las guias de onda de satélites. No sólo es un efecto perjudicial en cuanto a la funcionalidad de dispositivos de alta potencia de RF, sino que también representa un importante problema tecnológico debido a fenómenos perjudiciales que puede originar llegando incluso a la degradación y el fallo de sistemas [2–6]. En lo que respecta a las guías de onda de satélites, puede ser la causa de numerosos problemas relacionados con el aumento del ruido de la señal emitida y el desacoplo de cavidades de RF. Además existe el riesgo de originar daños permanentes en los dispositivos, cuya reparación es extremadamente dificultosa o incluso imposible tras el lanzamiento del satélite [2, 7–9].

Debido a la sensibilidad superficial de la emision secundaria de electrones, los tratamientos anti-Multipactor deben incluir las capas mas superficiales de los sólidos tratados. Por esta razón, al utilizar tratamientos de baja emisión secundaria, surgen dificultades adicionales en relación a la pérdida de potencia de la onda de RF transmitida debido los efectos peliculares de inserción o *skin effects* [10, 11].

En el campo de investigación de los aceleradores de partículas de alta energía, los fenómenos de nube de electrones (EC por sus iniciales en inglés) son efectos perjudiciales que tienen lugar como consecuencia de la aumento descontrolado de la población de electrones. En este caso el fenómeno esta originado y sostenido por procesos de emisión secundaria de electrones derivados del impacto de foto-electrones acelerados hacia las paredes del acelerador. En el probable caso de que la creciente densidad de la nube de electrones alcance a ser suficientemente alta como para influenciar en la calidad del haz, se podrian producir importantes efectos nocivos llegando incluso a su completa degradación [12]. Desde su descubrimiento en los años 50 [13, 14] ha sido un importante campo de especialidad de investigación. En el caso particular del gran colisionador de hadrones (LHC de sus iniciales en inglés) del CERN en el cual los dipolos magnéticos requieren del uso de tecnología de superconductores operando a temperaturas por debajo de 20 K, los fenómenos de nube de electrones, originan un incremento de la carga de calor [15–17] en los dipolos frios, resultando en un rendimiento ineficiente y la consecuente limitación de la operativilidad del sistema.

Ambos fenómenos, Multipactor y EC, son extremadamente sensibles a la emisión secundaria de electrones, y las probabilidades de que el Multipactor y la nube de electrones se desarrollen dependen de el coeficiente de emisión secundaria (SEY por sus iniciales en inglés) de los materiales expuestos al bombardeo de electrones primarios. Por esta razón, una atención especial ha sido depositada en la modificación y estudio del SEY de los materiales usados durante el desarrollo de esta tesis.

El objetivo que se persigue en este trabajo es el desarrollo de recubrimientos anti-Multipactor de bajo SEY por medio de la micro- y nano-estructuración de materiales técnológicos para aplicaciones en el ámbito aeroespacial, así como el estudio de los fenómenos implicados on la reducción del SEY y su papel en la formación de la nube de electrones y el efecto

Multipactor. En los capítulos 6 y 7 se presentarán las estrategias seguidas para lograr recubrimientos micro- y nano-estructurados de bajo SEY para aplicaciones en dispositivos de RF de satélites y los resultados mas relevantes de los estudios realizados. Se mostrará que es posible obtener superficies nano-estructuradas de alta relación de aspecto con una baja emissión secundaria, sin necesidad de generar un aumento significativo de las pérdidas de potencia por inserción. En el capítulo 8 se presentarán los resultados de intensivos estudios con respecto al SEY a bajas energías primarias (de 0 a 40 eV sobre el nivel de Fermi) con una resolución sin precedentes en dicha region de la energía primaria. Apoyado por estudios de simulación, se probará que el comportamiento del coeficiente de emisión secundaria a bajas energías (LE-SEY por sus iniciales en inglés) juegan un papel de importancia crítica en el desarrollo de la nube de electrones, y la evolución de la carga de calor en los dipolos fríos del LHC en CERN.

Las propiedades de bajo SEY del carbono en estado de hibridación sp^2 han establecido el uso de laminas grafíticas como una estrategia comunmente usada con fines anti- Multipactor en el ámbito de los aceleradores de partículas y dispositivos espaciales, por medio de el condicionamiento por bombardeo electrónico o *Scrubbing* [18–20]. En relación a las propiedades de baja emision decundaria de electrones del carbono, en el Capítulo 9 se presentarán los resultados experimentales obtenidos en relación a la evolución del SEY y LE-SEY de grafito en función de la cantidad de defectos cristalográficos presentes. Se mostrará el papel de la estructura cristalográfica en las propiedades electrónicas del material y consecuentemente su efecto en SEY y LE-SEY serán analizados.

Chapter 3

Background Knowledge

3.1 Secondary Electron Emission

When particles with sufficient kinetic energy hit the surface of a solid, this may emit photons, electrons, ions, atoms, or molecules. Strictly, secondary electron emission (SEE) refers to the case of electron emission upon impact of electrons [21]. Incident electrons are called primary electrons and those emitted, secondary electrons (SE). SEE phenomana was first discovered in 1902 by Austin and Starke [22], who found that a metallic target was able to emit a larger amount of electrons that it was receiving. If only mere electron reflection ocurred, a number of emitted electrons should be at the most, equal to that of the primary electrons, hence this observation was settled as a proof that the primary electrons liberated additional electrons to vacuum from the material itself.

3.1.1 Energy Distribution of Emitted Electrons

The amount of emitted electrons vary as a function of their emission kinetic energy for each primary energy E_0. The energy spectrum of emitted electrons is represented in Fig. 3.1 and often known as Energy Distribution Curve (EDC) [23–25].

It shows that emitted electrons can be classified into three different groups depending on their generation process resulting in different emission kinetic energy renges, i.e.

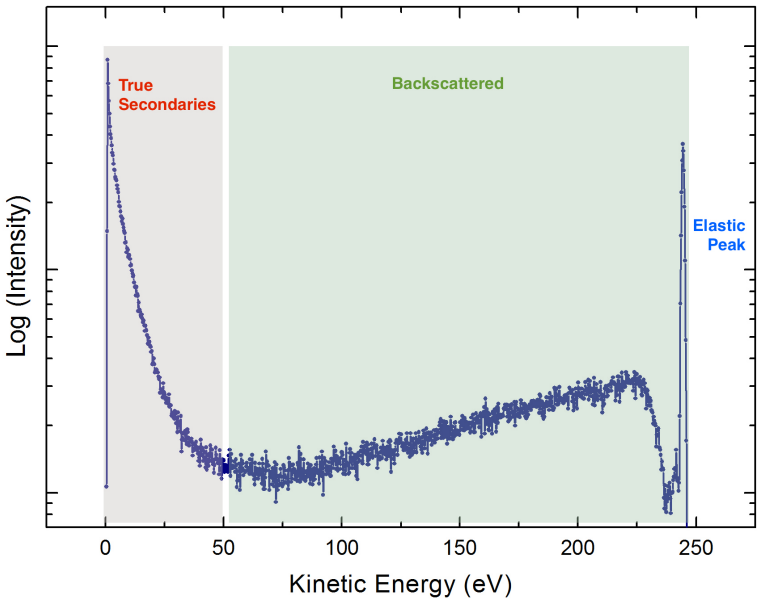

Figure 3.1: Secondary electrons EDC curve of a technical polycrystalline silver plated sample measured at a 245eV of primary energy

• **"True" secondary electrons.** They were bounded electrons of the material (energy below the Fermi level) which are emitted (freed to an energy above the vacuum level) by an energy loss of the primary electrons as they penetrate into the material [26]. For example, by means of plasmon decay [27]. A sudden increase above the vacuum level originates the characteristic EDC spectrum with a sharp asymmetric peak a low energies. As energy increases, the signal continue rising until reaching its maximum, typically located at 1-5 eV above the vacuum level, then a gradual reduction of intensity is observed. The full width at half maximum of the peak ranges between 5 and 15 eV. The decreasing tail at increasing energies can extend well over the inelastically backscattered electron energy range however with negligible small intensity. Thus, for practical purposes, it is convention that true secondary electrons extend from 0 to 50 eV kinetic energy, while backscattered ones extend from 50 eV to the primary energy, since both have very small intensity at 50 eV. However, this convention has no practical meaning for primary energies below 100 eV.

The kinetic energy of true secondary electrons is assumed to range between 0 and 50 eV [23]. This behavior in EDC spectra is quite universal for metals, and suggests that SE generation takes place through cascade processes [28], since only in this way, the amount of secondary electrons generated inside the sample can be multiplied so that the emitted current may even be higher than the incident current.

More clearaly for high primary energies ($>$ 500 eV), another special kind of secondaries

produce relatively sharp structures of low intensity, Auger electrons, characteristic of the chemical nature of the material (see Sec. 5.4.2.1), which, however, are not relevant for the Multipactor effect because of their low intensity.

.

• **Inelastically backscattered electrons.** They are primary electrons which lose certain amount of energy by interacting with the material and are re-emitted to the vacuum with a smaller energy [23].Their spectrum often show certain structure, (more intense and sharp for higher primary energy) corresponding to primary electrons energy losses of 0-50 eV. Their energy ranges from 0 eV to the value of the energy of the primary electrons.

• **Elastically backscattered electrons.** They are electrons that do not lose any amount of energy and are re-emitted to the vacuum with the same energy as the primary electrons. Such electrons typically suffer only a single collision with an atom of the substance.

3.1.2 Secondary Electron Yield (SEY)

The secondary electron yield, (SEY) defines the most relevant SEE properties of a material. This parameter relates the amount of electrons emitted, with the amount of impinging electrons as a function of the primary electron impact energy for a given primary incident angle (normal incidence, in default). Its magnitude is of critical importance in the development and sustainment of Multipactor [2, 7, 29, 30], as well as in its simulation and prediction [31–33]. SEY can be mathematically defined as the ratio of emitted current to the primary impigning current:

$$SEY(E_0) = \frac{I_{Emitted}}{I_{Impigning}} \tag{3.1}$$

Even though its simplicity, usually unimodal and well defined by few (2-4) parameters, this curve may be the result of a huge amount effects.

The SEE phenomenon has been widely studied. It is based on a complex process composed of three main steps or subprocesses [26, 34, 35]. a) Penetration or transport of primary electrons in the solid while interacting with it; in these interactions, primary electron can be elastically or inelastically scattered as well as these last can again be scattered,

b) in those inelastic interactions, plasmons, interband transitions, or knock-off processes [25, 27] can be produced which eventually can generate true secondary electrons (which were bound electrons of the solid), c) true secondary electrons can also as in (b) generate more secondary electrons in a SE cascade, and d) all those electrons can escape and be emitted into vacuum if their energy and directions allow them to overcome the WF or surface energy barrier [24, 36].

Fig. 3.2 shows the typical SEY dependance on primary electron energy. As shown in the figure, the SEY curve reaches a maximum value SEY_{Max} at certain energy $E_{0,m}$, and then starts to decrease. The value of SEY_{MAX} gives us very important information about the secondary emitting properties of the material, since the higher SEY_{MAX} is, the higher the amount of SE's emitted. As the primary energy increases there are more secondaries generated in the solid, and then SEY increases too. However as primary energy increases, primary electrons penetrate and generate secondaries deeper in the solid, which reduces the probability of SE's to be emitted, this effect makes SEY to start decreasing after reaching its maximum value [37]. Many pure metal surfaces usually have SEY_{Max} value of arround 1.50[38, 39], but surface impurities due to air exposure such as the typical carbonaceous contamination makes the SEY_{Max} increase to values higher than 2.0[39].

The simple qualitative explanation of the general behavior of SEY summarized above, is actually dominated by the true SE contribution. The elastically reflected component of SEY can be parametrized [40] representing a very small percentage of the contribution of the total SEY. No simple qualitative explanation exist for inelastic backscattered electrons, because the variety of processes involved with different energy ranges of importance also depending on atomic number[41–43].

The SEY curve can be decomposed in three components according to the nature of the electrons contributing to the total amount of the electrons released from the sample. Thus it can be expressed as

$$SEY(E) = \delta_{true} + \delta_{inelastic} + \delta_{elastic} \tag{3.2}$$

were δ_{true}, $\delta_{inelastic}$ and $\delta_{elastic}$ correspond to the true SE's (blue line in Fig. 3.2), inelastically backscattered electrons (green line in Fig. 3.2) and elastically backscattered electrons (red

line in Fig. 3.2) respectively. The inelastic backscattering emission coefficient $\delta_{inelastic}$ is always less than 0.5 and structureless [42]. It is either low and monotounusly decreasing with primary energy for low atomic numbers or higher and monotounusly increasing for high atomic numbers. On the other hand, the elastic backscattering emission coefficient $\delta_{elastic}$ is almost null for a wide range of primary energies, except for the very low primary energy region, tipically 0-200 eV. Thus total SEY reflects essentially the behavior of the true SEE at energies higher than the very low energy region. The SEY at primary energies below 50 eV is dominated by elastically scattered electrons, and special care must be taken when studying its behavior. LE-SEY results will be analyzed in detail in Chs. 8 and 9.

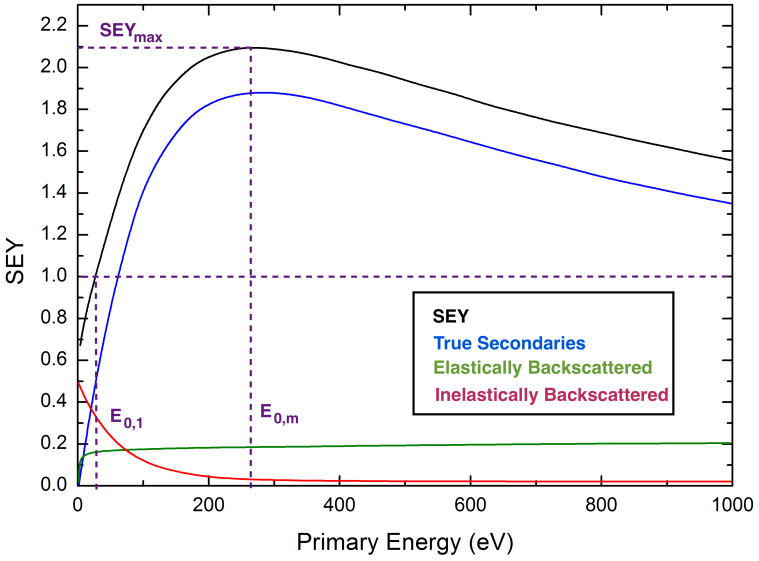

Figure 3.2: The SEY for Cu chemically cleaned but not in-situ vacuum-baked samples[44]. Calculated contributions of true secondaries, elastically backscattered and inelastically backscattered electrons [35].

For primary electrons at energies at which $SEY < 1$ there are more electrons impinging the surface than emitted, under this conditions the multiplication of electrons is not possible and there is a net absorption of electrons. On the other hand, for primary electrons with energies at which $SEY > 1$ there are more electrons emitted to the vacuum that those impigning on the solid. As shown in Fig. 3.2 $SEY = 1$ at two points, namely $E_{0,1}$ and $E_{0,2}$, at which the amount of emitted electrons is the same as those reaching it, known as first and second crossover respectively, and for all the values of the primary energy between them $SEY > 1$. It is this energy range, $E_{0,1} < E_0 < E_{0,2}$ of SEY which must be taken in consideration when dealing with detrimental effects related to SE multiplication such as Multipacing phenomena [2] which detailed description will be provided in the following sections.

3.1.3 Angular distribution of emitted electrons

The angular distribution of "true" SE's responds approximately to a cosine distribution according to Lambert's law [45] and is independent of the angle of incidence of the primary electrons [23, 46].

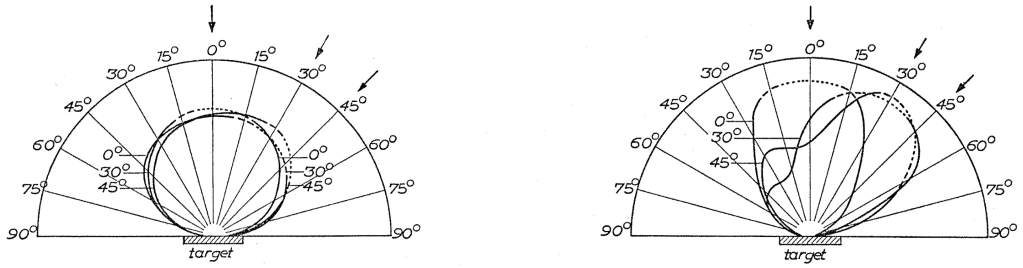

Figure 3.3: Angular distribution of the secondary the true (left panel) and backscattered (right panel) electrons emitted from polycrystalline nickel, according to [46]

However the angular distribution of backscattered electrons depends on the primary electron incidence angle. At normal incidence, angular distribution is still the Cosine function. As shown in Fig. 3.3 as incidence angle changes so does the angular distribution, showing an important component towards the opposite of the incidence angle and a second specular component which becomes grater as the angle of incidence rises [23, 47].

3.1.4 The dependance of SEY on primary electron angle of incidence

Secondary emission yield increases with primary electron energy under an oblique angle of incidence [23, 48]. When the angle of incidence increases, primary electrons still penetrate into the solid, but SE generation processes happen in a region closer to the surface inside the solid. If the penetration depth of electrons at normal incidence is R, the penetration depth at an incidence angle of θ would be $R \cdot Cos(\theta)$. As a consequence, fewer SE's are now absorbed before they reach the surface.

Also, this predicts that $E_{0,m}$ should increase, since R is an increasing function with the primary energy. However, because of the increasing straggling of the primary electron beam with penetration into the material, the fraction of escaping secondaries increases with primary energy and the SEY curve suffers not only a change of scale, but also, as

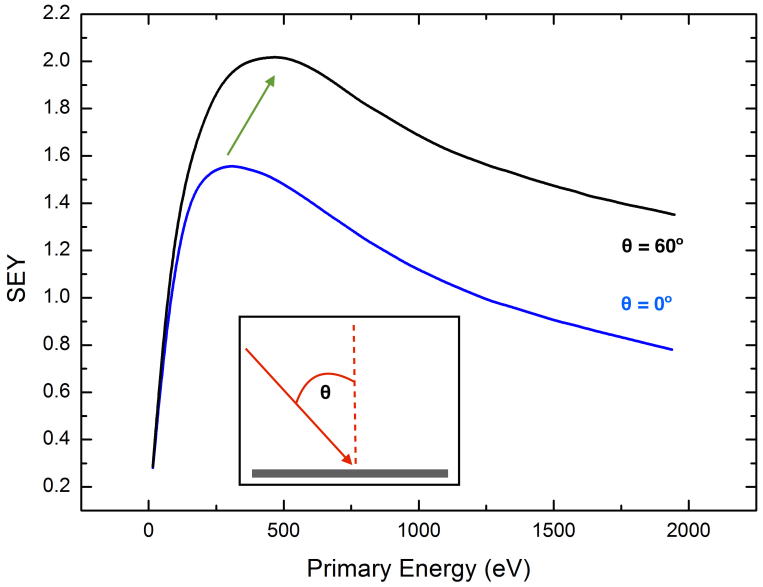

Figure 3.4: angular and energy dependance of SEY measured on Ag [49]

shown in Fig. 3.4, an increase on the primary energy energy at which SEY starts to decrease [49].

3.2 Theory of Secondary Electron Emission

Semiempirical theories of SEE were first developed by Salow and Bruining [23, 50] based on the assumptions that i) a distinction can be made between the production and escape mechanisms of SEs, ii) the energy distribution of internal secondaries is unimportant, and iii) the electron energy loss mechanism may be described in part by a simple law known as Widdingtons law, i.e. $dE/dx = -A/E(x)$ [51], where E is the energy of the electron traveling within the material, x is the depth into the material of the electron, and A is a constant characteristic of the material. A better agreement between theoretical and experimental values were later proposed by Lye and Dekker [52], replacing Whiddington's law by the idea that primary electrons lose their energies according to a power law of the form:

$$\frac{dE}{dx} = -\frac{A}{E^{n-1}} \tag{3.3}$$

where E is the energy of the electron penetrating into the material and $n > 1$ is the power law fitting coefficient. Further analysis were done by Dionne who investigated the effects of scattering on SEY proposing a constant loss of energy of primary electrons, and developed deeper analysis on SEY parameters interpretation [26, 53] .

Such constant loss model proposed by Dionne is based on the assumption that inelastic collisions, might change the direction of the trajectories of electrons traveling within the solid. In such case, due to angular scattering of primary electrons, the length of the path followed by the electrons, and hence their average loss of energy is independent of the depth reached inside the solid, i.e.

$$\frac{dE}{dx} = -\frac{E_0}{d} \tag{3.4}$$

where d is the electron range, and represents the total path length for one electron when its trajectory is straight, and no scattering processes take place. However, d is determined by primary electrons which do not undergo angular scattering and in that case, the energy loss of the primaries is governed by the power law described in Eqn. 3.3 [53]. This means that by integrating Eqn. 3.3, the expression for the electron range d can be determined as:

$$d = \frac{E_0^n}{n \cdot A} \tag{3.5}$$

3.2.1 Dionne's Theory

Dionne's theory is based on the original model of Lye and Dekker [52] in which it was assumed that secondary yield may be written in the form [26]:

$$SEY = \int_0^\infty n(x, E_0) f(x) dx \tag{3.6}$$

where $n(x, E_0)dx$ represents the number of SE's produced per incident primary electron of initial primary E_0 in a layer of thickness dx at a depth x and $f(x)$ represents the probability for a SE produced at x to arrive at the surface and escape, overcoming the WF barrier.

The average number of SE's produced is assumed to be proportional to the average energy loss per unit path length and may be related by

$$n(x, E_0) = -\frac{1}{\zeta}\left(\frac{dE}{dx}\right) \tag{3.7}$$

where ζ represents the average energy loss per generated SE. The function $f(x)$ can be expressed as

$$f(x) = p_e p_m(x) \tag{3.8}$$

$$p_e = B \equiv Escape\ probability \tag{3.9}$$

$$p_m = e^{-\alpha x} \equiv Migration\ probability \tag{3.10}$$

Where the parameter α is the SE absorption coefficient, equivalent to an inverse mean free path of SE's inside the solid before they are trapped or their energy falls below the vacuum level, irrespective of their energy. By substituting Equations 3.7 and 3.8 into 3.6, SEY can be expressed as

$$SEY = -\frac{B}{\zeta}\int\left(\frac{dE}{dx}\right)e^{-\alpha x}dx \tag{3.11}$$

The most relevant assumption of this secondary emission theory is, as previously explained, that the primary electrons suffer a constant energy loss defined by

$$\frac{dE}{dx} = -\frac{E_0}{d} \tag{3.12}$$

Which in combination with Eqn. 3.5 leads to

$$\frac{dE}{dx} = -(An)^{\frac{1}{n}}d^{\frac{(1-n)}{n}} \tag{3.13}$$

According to this fact, Eqn. 3.7 can then be expressed as

$$n(x, E_0) = \left(\frac{1}{\zeta}\right)(An)^{\frac{1}{n}} d^{\frac{1-n}{n}} \tag{3.14}$$

By substitution of Eqn 3.14 into Eqn 3.11, the SEY equation becomes

$$SEY = \left(\frac{B}{\zeta}\right) \int_{x=0}^{x=d} (An)^{\frac{1}{n}} d^{\frac{(1-n)}{n}} (e^{-\alpha x}) dx \tag{3.15}$$

Integrating the latter we obtain

$$SEY = \left(\frac{B}{\zeta}\right) \left(\frac{An}{\alpha}\right)^{\frac{1}{n}} (\alpha d)^{\frac{(1-n)}{n}} (1 - e^{-\alpha d}) \tag{3.16}$$

Where [26]:

$B \equiv$SE Escape Probability

$\zeta \equiv$ Average energy loss per generated SE

$\alpha \equiv$ SE Absorption Coeficient $\equiv \frac{1}{\lambda_{secondaries}}$

$A \equiv$ Primary Electron Absorption Coeficient

$d \equiv$ Primary Electron Range $\equiv$ Penetration Depth

$n \equiv$ Power Law Coefficient

A value of n=1.35 has been widely assumed since it has been proved to fit most of experimental data [26, 53, 54]. Expressions for SEY_{max} and $E_{0,m}$ can be obtained as a function of B, ζ, A and α resulting, for n=1.35 in [26]

$$E_{0,m} = 2.3 \left(\frac{A}{\alpha}\right)^{0.74} \tag{3.17}$$

$$SEY_{MAX} = 0.9 \left(\frac{B}{\zeta}\right) \left(\frac{A}{\alpha}\right)^{0.74} \tag{3.18}$$

This theoretical analysis provides results which enables us to find relationships between SEY and intrinsic electronic and chemical properties of the studied material. Equations 3.17 and 3.18 clearly show the dependance of $E_{0,m}$ and SEY_{MAX} on the electron absorption coefficient of the material, and how for higher δ_{MAX}, $E_{0,m}$ tend to increase too[26, 53]. Also B and ζ are shown to be affected by the state of the surface and the degree of contamination of the sample. In Sec. 4.3.2 this issue will be addressed in detail showing how SEY depends on the status of the sample surface, and how it is modified by surface contamination.

3.2.1.1 Furman's Reformulation

Based on Dionne's theory, a very interesting expression for Eqn. 3.16 can be obtained [24].

The SEE coefficient can be represented as SEY/SEY_{MAX} vs $E/E_{0,m}$. In this case we obtain a reduced form for the actual SEY curve in which maximum appears at the point (1,1) of the graph. This representation is extremely useful for fitting experimental SEY data. The formula proposed in this case to fit Dionne's SEY curve is [55]

$$D(x) = ax^{1-x}\left(1 - e^{-bx^n}\right) \tag{3.19}$$

where the paramter n is the power law coefficient, x represents the relation $E/E_{0,m}$ and $D(x)$ is $SEY(E)/SEY_{Emax}$. The values for a, b and s are constrained by the conditions $D(1) = 1$ and $D'(1) = 0$, which are, of course, chosen to ensure that SEY reaches a peak value SEY_{max} at an energy $\mathrm{E}_{0,m}$ resulting in:

$$a = \frac{1}{1 - e^{-b}} \tag{3.20}$$

$$n = \frac{1 - e^{-b}}{1 - (1 + b)e^{-b}} \tag{3.21}$$

which leaves b as the only independent parameter. This fact makes this formula to be a very easy and handy way to fit SEY data.

However ulterior studies, [35, 56] propose a simplest alternative form for D(x) that differs from 3.19 but satisfies Dionne's constant energy loss condition. Furman reformulation of the reduced SEY is expressed as

$$D(x) = \frac{nx}{(n-1+xn)} \tag{3.22}$$

Which also leaves only one independent parameter namely n, the power law coefficient.

In [35] Furman verified that Eqn. 3.22 can be obtained by defining the electron migration probability as $f(x) = (1 + x\alpha/2)^{-2}$ instead of the originally proposed $f(x) = exp(-x\alpha)$.

It is noticeable that both 3.19 and 3.22 have the same power law behavior at small and large primary energy, i.e.[35]

$$D(x) \propto \begin{cases} x & \text{as } x \to 0 \\ x^{1-n} & \text{as } x \to \infty \end{cases} \tag{3.23}$$

Eqn. 3.22 provides in some cases a better fit to the SEY data than 3.19, which would imply that the SE escapes probability function $f(x) = (1 + x\alpha/2)^{-2}$ describes the escapes more accurately than $f(x) = exp(-x\alpha)$. Fig. 3.5 shows SEY curves calculated with both Dionne's and Furman's formulas.

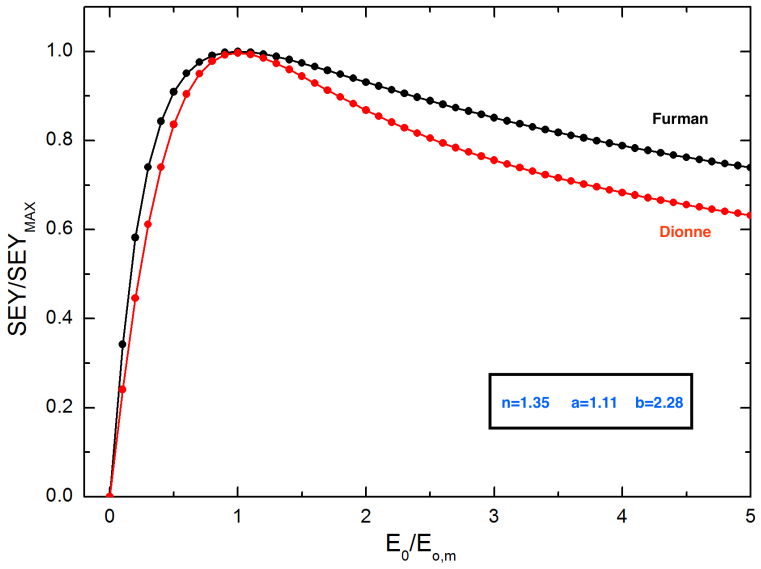

Figure 3.5: Comparison of the true secondary emission yield scaling function curves calculated by using Dionne's and Furman's equations

In fact Eqn. 3.22, has been widely employed in the performance of e⁻cloud build calculations as well as PyECLOUD and ECLOUD simulations programs of the large hadron collider (LHC) [57]. However, the validity of Furman's over Dionne's model can not still be certainly concluded.

3.2.2 Dennison's Theory

Despite the effectiveness of both Dionne's and Furman's models in correctly predicting SEY, they differ greatly in their predictions of the asymptotic dependence at high incident energy. A fundamental source of discrpancy is the way in which the incident electron penetration and energy dissipation inside the material are described, due to this fact, in [34] Dennison proposed a *Continious Slowing Down Approximation* (CSDA) for electrons energy loss, instead the constant loss theory assumed by Dionne and Furman [26], as a fitting strategy. In the CSDA, the effect of inelastic collisions on the incident particle is modeled as a continuous braking force that depends only on the current value of the energy. An expression for the electron range proposed by Mandell [58] is used in CSDA which implies a double power law

$$d(E) = b_1 E^{n_1} + b_2 E^{n_2} \tag{3.24}$$

with $n_1 < 1$ and $n_2 > 1$, from which the expression

$$-\frac{dE}{dz} = \frac{E}{b_1 n_1 E^{n_1} + b_2 n_2 E^{n_2}} \tag{3.25}$$

would be obtained for the stopping power. According to this expression the stopping power would reach its maximum at

$$E_{maxSP} = \left[-\frac{b_1 n_1 (n_1) - 1}{b_2 n_2 (n_2) - 1} \right]^{\frac{1}{(n_2 - n_1)}} \tag{3.26}$$

A comparison between Constant energy loss and CSDA stopping power curves is shown in Fig. 3.6, being the latter characterized by a strong peak near the maximum penetration

depth of the trajectory when the incident particle reaches the energy of the stopping power maximum.

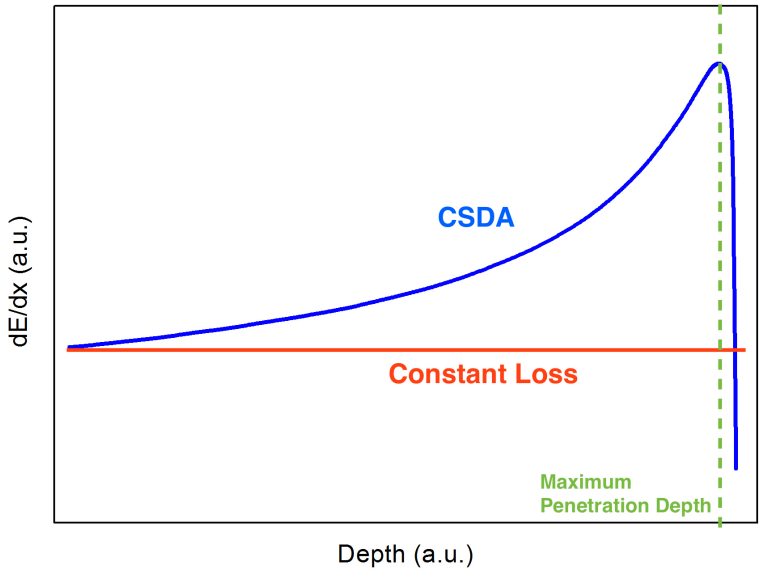

Figure 3.6: Stopping power versus depth, comparison between *Constant Energy Loss* (black line) and *CSDA* (blue line) approximations

In his work Dennison presented a fourth-order numerical method to compute Eqn. 3.6 in order to obtain, through certain fittings procedures, the expression to accurately fit SEY data. If the range of the electrons, at the energy at which the stopping power curve reaches its maximum i.e. $d(E_{maxSP})$ is larger compared to the scape length of SE's $\lambda = 1/\alpha$, then, the approximation $\lambda \to 0$ is applicable, which simplifies the integral of Eqn. 3.6. E_{maxSP} corresponds to the energy of the maximum yield and it is the variation of the stopping power with respect to the incident energy what determines the shape of SEY. In this case SEY can be expressed in its reduced form as

$$D(x) = (n_2 - n_1)[(n_2 - 1)x^{n_1 - 1} - (n_1 - 1)x^{n_2 - 1}]^{-1} \tag{3.27}$$

where, as in Eqs. 3.19 and 3.22 x represents the relation $E/E_{0,m}$ and $D(x)$ is $SEY(E)/SEY_{Emax}$ and $(n_1 - 1) > 0$ and $(n_2 - 1) < 0$ are the slopes of the low-energy (crescent) and high-energy (decrescent) asymptotes of SEY.

On the other hand, if $1/\alpha$ is larger than $d(E_{maxSP})$, then SEY continues to increase significantly for incident energy $E > E_{maxSP}$. and the shape of the SEY curve does depend on

the value of $1/\alpha$. In this case a higher order approximation to compute Eqn. 3.6 should be used.

3.3 Measurement of SEY

As previously explained[21, 23, 24], the SEY represents the amount of SE's emitted per incoming primary electron as a function of the primary energy. There are many ways to obtain electrons from a source and send them towards a sample with a given certain energy. Also in order to count the amount of electrons incoming and out coming from the sample one can use many strategies such as direct determination using spherical or hemispherical gridded shells or indirect determination of difference in currents [23] .

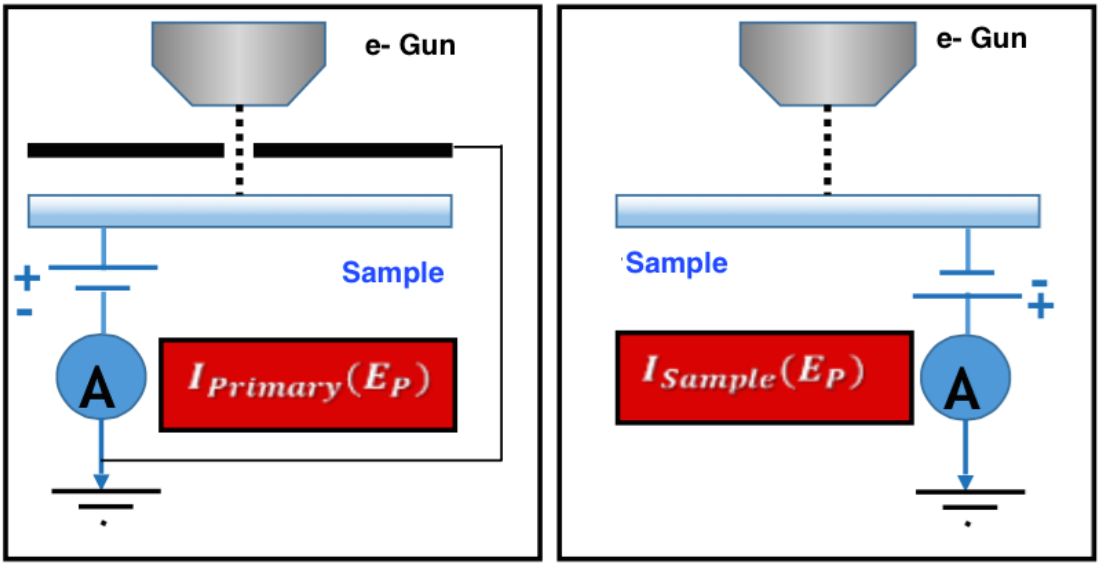

Figure 3.7: Scheme of the geometrical disposition of the equipment for SEY data acquisition; Left Image: I_p acquisition. Right Image: I_s acquisition

In this thesis SEY has always been determined by making use of the latter strategy. Electrons are emitted from an electron gun cathode by means of thermionic emission, and are accelerated towards the sample at different energies controlled by the grids of the gun. As shown in Fig. 3.7, An electrometer connects the sample to ground and measures the current through the sample. Since using indirect determination we only have access to sample currents, the value of $I_{Emitted}$ is not directly measurable. However, for a conductive

sample, $I_{Emitted}$ can also be written as $I_{Impigning} - I_{sample}$, hence we can rewrite Eqn. 3.1 into

$$SEY = \frac{I_{Impigning} - I_{sample}}{I_{Impigning}} = 1 - \frac{I_{sample}}{I_{Impigning}} = 1 - \frac{I_s}{I_p} \tag{3.28}$$

Measuring I_s and I_p at the same time is not something possible so the procedure to measure SEY is to make use of a positively biased Faraday cup in order to obtain an accurate measurement of all the electrons impigning the sample I_p, and then proceed to measure the sample current I_s. SEY value results from making the basic calculation explained in Eqn. 3.28. A more detailed description of the strategies carried out to measure SEY will be described in Sec. 5.4.1.1.

The uncertainity of this measurement obviously depend on the perturbations of each experimental setups. Nevertheless, intensive studies carried out in consortium with different institutions as CSIC, ONERA and ValSpaceConsortiom (VSC) in the framework of the project *EVEREST* [59], revealed an error $<5\%$ of the measured value, after comparison among data taken in all laboratories, in good agreement with error margins reported in provious works [48, 60, 61]

3.4 Electron Cloud in Particle Accelerators

The phenomenology of the e^- cloud formation is shown in Fig. 3.8 in which the most relevant basic concepts are pictorially analyzed. When the first proton buch appears in the dipole, it will be curved by the magnetic dipole field, emitting then sincrotron radiation. Sincrotron photons will then travel tangentially to the beam line surface ant hitting the accelerator walls with an impact angle of $\sim 1.5°$. Some of the absorbed photons will produce photoelectrons. When photoelectrons are emitted from the walls, they will interact with the beam being accelerated by Coulomb attraction. During such interaction, they will gain energy and impigne the opposite accelerator wall. SEE processes derived from such impact take place, revealing SE's into the beam pipe, which amount and energy distribution will mainly depend on the SEY of the material of the accelerator. Next bunches will not only create new photoelectrons, but also accelerate towards the walls the electrons present in

the vacuum system. For this reasons this can be assumed to be a resonant phenomenon. After certain number of bunch passages, the density of the present e^- cloud would be high enough to influence the beam quality, inducing detrimental effects up to its complete degradation [12].

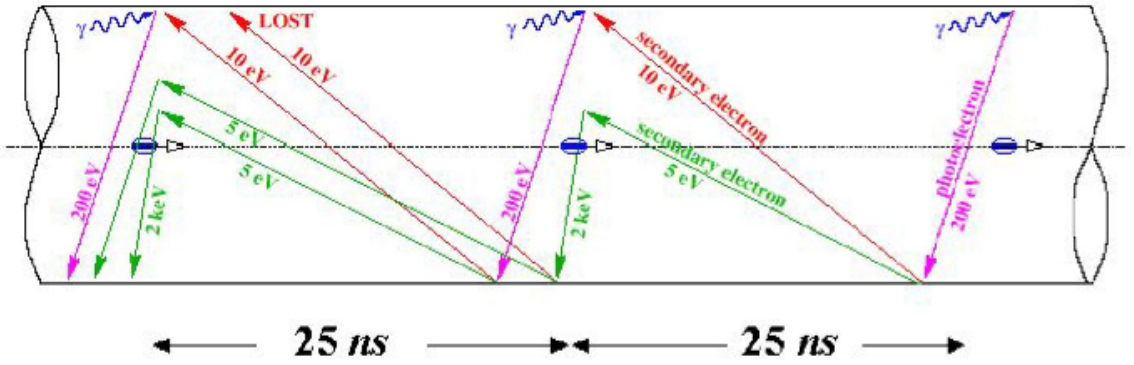

Figure 3.8: Schematic description of the e^- cloud process at LHC generated by F. Ruggero

In the particular case of the CERN LHC, the required magnetic dipole field and magnetic rigidity in the quadrupoles implies the use of the superconducting technology operating at cold temperature. The interior of the LHC dipoles consists on a cold bore held at 1.9 K [40, 62] protected from unwanted heat deposition caused by sinchrotron radiation by the so called "beam screen" which is held at temperatures between 5 and 20 K. During the LHC operation, sinchrotron radiation and specially electron resulting from e^- cloud phenomena increases the heat load [15–17] of the cold dipoles resulting in their inefficient operation and stimulating the desorption of gas molecules. The available beam screen cooling capacity is exceeded if the EC-induced heat load surpasses 1 to 1.5 W/m [63] in any of the two rings of the LHC, and in this case, the EC will limit the achievable machine performance.

3.5 Multipactor Effect in Parallel Plate Geometry

Multipactor effect consists on an oscillating cloud of electrons, built up and sustained by secondary emission that results from the impacts with the surfaces that is driven by and in synchronism with an RF field under vacuum conditions. It can occur both by single and double surface mechanism. In both cases, electrons are driven by the oscillating electromagnetic field to periodically impact the metallic surface of the device, generating an uncontrolled growth of SE's [2, 6]. Double surface configuration consisting on two parallel

metallic surfaces separated by an empty gap of distance d_g (see Fig. 3.9). The latter is the configuration of RF wave guides, end the one to be studied in this thesis.

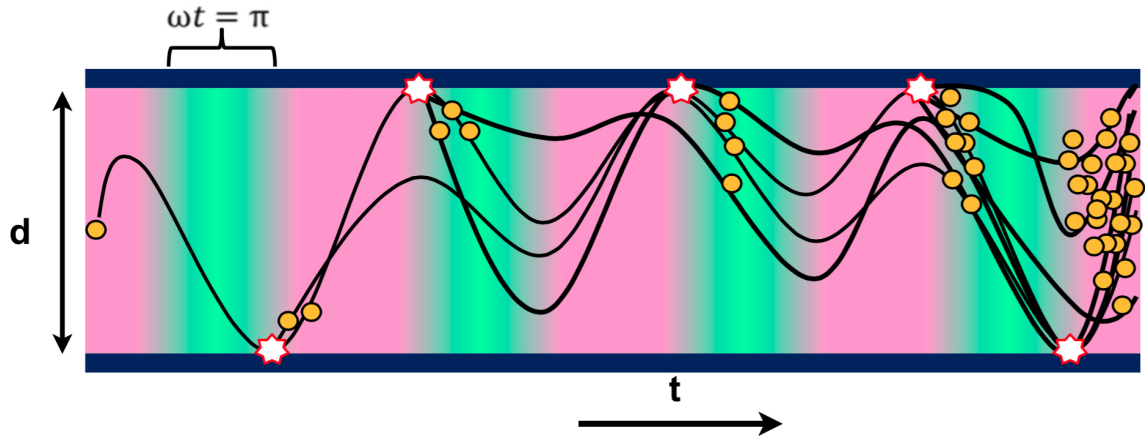

Figure 3.9: Multipactor effect. Schematic description of the exponential growth of electron population due to SE generation

When an external electric field is applied to an electron located at one of the surfaces that forms the waveguide, the electron will then move. If the field applied is oscillating in the form $\mathfrak{E}_0 Sin(wt)$, being $\mathfrak{E}_0$ the amplitude, w the frequency, and t the time, and the electron could reach the oposite surface by the time the electric field of the wave reverses direction at $wt = \pi$, generating then electrons by means of SEE, which would be accelerated towards the opposite surface increasing SE population within the waveguide. The latter are "resonant conditions" for multipactor discharge and include geometry and SEE properties.

3.5.1 Theory of Multipactor Discharges in Parallel Plate Geometry

RF satellite wavegiudes constitute a configuration described by the double surface parallel plate geometry. Resonant conditions for an electron in such configuration depend on several factors for multipactor to take place. In the simplest scenario, electrons under Multipactor resonance conditions must travel the distance d_g between both parallel plates, in a period close to the time needed for the RF Electric field changes direction, so that SE's generated at the surface are again accelerated towards the opposite surface [2, 4, 64]. Making use of the Lorentz law and the equations of motion of an electron in presence of an electromagnetic field

$$\frac{dv}{dt} = \frac{q}{m}(\mathfrak{E} + v\mathfrak{B}) \tag{3.29}$$

we can analyze this resonant conditions [64].

It is well known that for a wave propagating in the z direction with amplitude Eo, angular frequency w, and wave number k, the electric and magnetic fields are given by

$$\mathfrak{E} = \hat{x}\mathfrak{E}_0 Sin(k_z - wt) \tag{3.30}$$

$$\mathfrak{B} = \hat{x}\mathfrak{B}_0 Sin(k_z - wt) \tag{3.31}$$

Since the velocity of the electron is sufficiently smaller than c the magnetic field $\mathfrak{B}$ has a magnitude smaller than $\mathfrak{E}$ by a factor c, so the equation of motion for an electron moving in the x direction becomes

$$\frac{dv}{dt} = \frac{e}{m}\mathfrak{E}_0 Sin(wt) \tag{3.32}$$

integrating Eqn. 3.32 we obtain the next expressions for the electron velocity

$$v = vo + \frac{e\mathfrak{E}_0}{mw}(cos(\varphi) - cos(wt)) \tag{3.33}$$

and position

$$x = xo + \frac{v_0}{w}(wt - \varphi) + \frac{e\mathfrak{E}_0}{mw^2}[Sin(\varphi) - Sin(wt) + Cos(\varphi)(wt - \varphi)] \tag{3.34}$$

for a value of $wt = \mathfrak{n}\pi + \varphi$ electric field changes direction, and the Multipactor condition implies that the position of the electron in that moment must be d. So the multipactor condition for the Voltage in a double surface configuration is

$$Vo = \mathfrak{E}_0 \cdot d_g = \frac{m}{e}\frac{wd(wd - v_0\mathfrak{n}\pi)}{\mathfrak{n}\pi Cos(\varphi) + 2Sin(\varphi)} \tag{3.35}$$

For simplicity we can use the boundary conditions $v_0 = 0$, and $\varphi = 0$ and then Eqn. 3.35 becomes

$$Vo = \frac{4\pi m}{e}(f \cdot d_g)^2 \tag{3.36}$$

Eqn. 3.35 represents the Multipactor susceptibility of a double surface geometry. This theoretical analysis gives us an expression for the voltage needed to generate multipactor discharge as a function of the product of the frequency and gap distance. One of the most important conclusion derived from this analysis is that the Multipactor breakdown voltage is invariantt for a constant value of the product of the frequency and the gap distance $f \cdot d_g$, this means that if the size of the transmission line is doubled and the frequency of the wave is halved, the voltage at which breakdown occurs remains the same [4].

This expression however can become more complicated since in a more realistic analysis one should, not only take in consideration the values $v_0 = 0$, but also all the values of v_0 for which the increase of electron population by means of SEE is possible [2, 6]. this increase of population can only happen for certain energies for which SEY is grater than 1, i.e. primary energy values must be between first and second crossover $E_{0,1} < E_0 < E_{0,2}$. By using Eqn.3.33 one can find the direct relationship between the velocity and the energy of electrons within the waveguide. This means that the Multipactor susceptibility boundaries depend directly on SEY parameters. Hence as explained in Sec. 3.5.2, in a more realistic model, the relationship between the applied voltage and the frequency-gap product is not restricted to a simple curve but it expands to a region limited by certain boundaries [4, 65].

3.5.2 Multipactor boundaries

Multipactor boundaries set the limits of the Multipactor susceptibility. Many simulations studies have been developed using theoretical principles above explained [31–33, 66, 67]. Fig. 3.10 Shows a very illustrative example of the multipactor susceptibility diagram for different materials with different SEY curves.

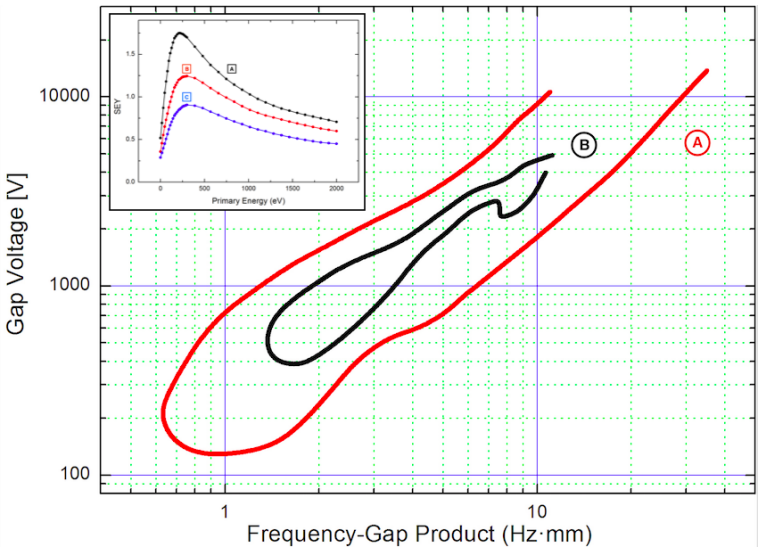

Figure 3.10: Multipactor susceptibility region for coatings of different SE emitting properties; Inset: SEY curves of the three different coatings.

The graphs were obtained by using the simulation software MEST [31]. It is remarkable the fact that for low SEY materials the Multipactor region shrinks. This phenomenon is the consequence of the reduction of the energy range between crossovers $E_{0,1}$ and $E_{0,2}$ as SEY_{MAX} decreases. Finally, no Multipactor region is observed for materials with SEYmax below 1.

3.6 Power Attenuation in RF Wavegides

The goal of RF satellite waveguides studied in this thesis, is to deliver RF power with minimal power attenuation. In an ideal case, the propagating waves in a waveguide suffer no attenuation as they travel down the waveguide. However, in a realistic model, the fields associated with the propagating waveguide modes produce currents that flow in the walls of the waveguide. Given that the waveguide walls are constructed from an imperfect conductor, the walls act like resistors and dissipate energy in the form of heat, which are known as *Power Insertion Losses* or *insertion losses*(IL) [68, 69]. RF waves must travel very long distances and wave guides must succes achieving this goal keeping IL as low as possible.

3.6.1 Skin depth

The large conductivity of metallic materials forming the RF waveguides makes it difficult for oscillating electromagnetic fields to penetrate into metals due to physical phenomena known as skin effects, the induced currents tend to shield the fields. Considering an oscillating electric field, for a conductor [70] we have

$$\frac{\partial^2 \mathfrak{E}}{\partial x^2} = \mu_0 \sigma \frac{\partial \mathfrak{E}}{\partial t} \tag{3.37}$$

Which differs from the known wave equation and is known as diffusion equation. It usually appears in transport phenomena [71], in this case this formula describes how electric field penetrates into a conductor for a given boundary condition. If a DC electric field is applied along a metallic surface, it would fully penetrate into the solid. This means that a DC field can be induced in a conductor since electric current is allowed to flow as current flows through conducting wires in electric circuits. It is however a very different case when an oscillating field

$$\mathfrak{E} = \mathfrak{E}_0 Cos(wt) \tag{3.38}$$

is applied into a conductor. Inside the conductor we can assume an ansatz for the electric field such as:

$$\mathfrak{E}(x,t) = \mathfrak{E}_0 e^{\gamma x} Cos(kx - wt) \tag{3.39}$$

Where γ is the spatial dumping factor. By substituting Eqn. 3.39 into Eqn. 3.37 we obtain:

$$\gamma = \sqrt{\frac{w\mu\sigma}{2}} \tag{3.40}$$

being the inverse of the damping factor the parameter known as skin depth [72, 73]:

$$\delta = \sqrt{\frac{2}{w\mu\sigma}} \tag{3.41}$$

where μ is the magnetic permeability in vacuum. According to Eqn. 3.41, at sufficient high frequencies, the induced currents are confined by the skin effect to a surface region in which, due to surface defects, electric currents may suffer scattering that results in poor conductivity, enhancing then IL.

3.6.2 Power Insertion Losses

In an RF waveguide, if the transmitted power is P_T and the received power is P_R, then the IL are expressed as

$$IL = 10log\left(\frac{P_R}{P_T}\right)dB \qquad\qquad IL \propto \alpha_c \tag{3.42}$$

The power attenuation measured in dB and is proportional to the so called attenuation constant α_c which has units of [dB/m]. For conductive metallic surfaces the attenuation constant is proportional to the RF surface resistance R_s and for a homogeneous non magnetic conductive solid at microwave frequencies it is expressed as [68, 69]:

$$R_s = \frac{1}{\sigma \cdot \delta} \tag{3.43}$$

Where σ is the conductivity of the material and δ is the skin depth defined in Eqn. 3.41. Hence to the attenuation constant α_c can be expressed as [72, 73]:

$$\alpha_c = \frac{2R_s}{b\eta\sqrt{1-(f_c/f)^2}}[GeometricalFactor] \qquad\qquad \eta = \sqrt{\frac{\mu}{\epsilon}} \tag{3.44}$$

Where η is the traveling wave impedance and f_c is the cut-off frequency at which power flowing through the system begins to be reduced (attenuated or reflected) and depends on the geometry the waveguide and the wave propagation mode. Besides the surface resistance,

the value of the attenuation constant also depends on the frequency of the traveling wave, and the geometry of the waveguide as expressed in Eq. 3.44 by the *Geometrical Factor*.

In summary, the amount of power dissipated by radio frequency IL, for invariant geometrical conditions, directly depends on the attenuation constant of the waveguides walls which value is determined by the surface resistance R_s of the walls.

3.6.3 Effect of Surface Roughness

According to the reviewed dependance of the attenuation constant of a waveguide, and hence the IL on the surface resistivity of metals, it results of crucial importance to study possible sources of surface resistance enhancement such as surface roughening.

The effect of roughness on the resistivity has been widely studied [10, 11, 74–78] and its known to depend on both the shape and the size of the roughness relative to the skin depth. Complicated numerical models of periodically grooved metal power losses have been copumputed by previous authors. Results about power losses as well as the local surface impedances for different cross section shapes such as rectangular, triangular, and semielliptical are available in the bibliography [76–78].

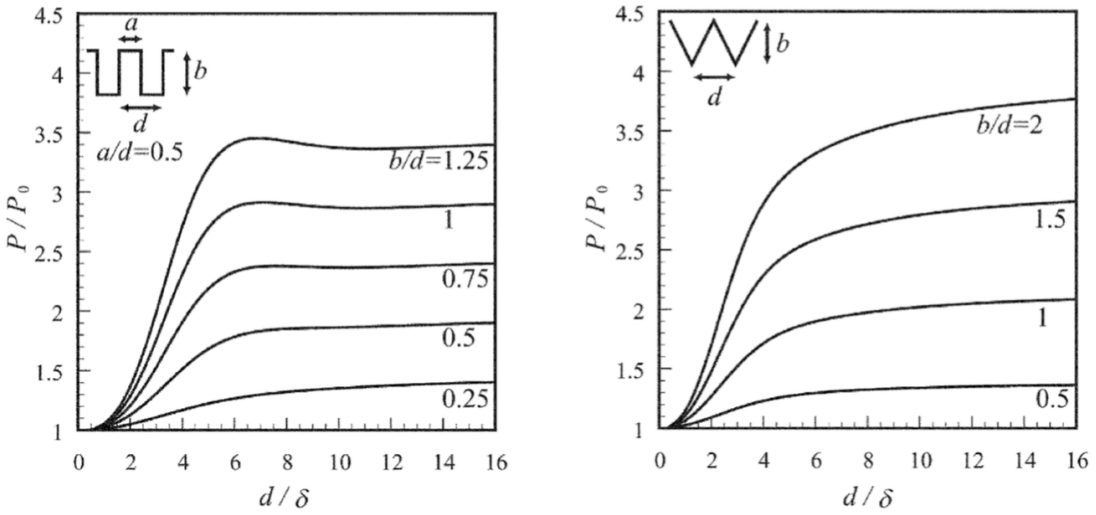

Figure 3.11: Power loss ratio for rectangular and triangular conductor grooves transverse to current flow as calculated in [78]

It has been proved and stablished that power losses, as well as the local surface resistance, are enhanced by roughness. Fig. 3.11 the results published in [78] representing the power

loss ratio P/P_0 as a function of the ratio of the period to the skin depth d/δ. The value of the abscissa is proportional to the square root of the frequency if the electric constants and period of the metal are fixed. It is clearly noticeable that the loss ratio is larger for deeper grooves. This ratio first increases and then becomes stable as the frequency is increased. In the case of rectangles, in which the behavior of the curve is quite asymptotic, a value of $d/\delta = 1$, results in a power loss ratio $P/P_0 \approx 3$ at high frequencies. This matches with the fact that current flows nearly along the surface, since the profile length of the surface is for this case $d + 2b = 3d$, 3 times larger than for the flat case. Fig. 3.11 is indeed very ilustrative and useful to understand how IL are enhanced by surface roughness. One can see that IL of high aspect ratio surfaces can be dramatically reduced as long as the size of topological structures are reduced to values comparable to the skin depth.

Chapter 4

Multipactor Mitigation Strategies

As mentioned, in Ch.3, Multipactor and e^- cloud effects are undesirable phenomenon concerning RF satellite devices and particle accelerators, and its avoidance has developed a wide field of research for many years. Many strategies are usually performed to mitigate Multipactor effect. Avoiding resonance conditions by modifying the RF devices geometry and diminishing the SEE of the walls or SEY reduction, are widely used in the field of RF satellite devices. Also Modifying the RF field by adding a DC magnetic field has been proved to be an extremely efficient e^- cloud mitigation technique in the field of particle accelerators.

4.1 DC Magnetic field

It has been proved that by applying a DC magnetic field, the trajectories of the undesired electrons can be disturbed in such a way that under specific conditions, the desired increase in the Multipactor threshold can be obtained [79–81]. This implies that, for space-borne microwave components, given any range of emission angles, it is possible to design the needed deflection angle using DC magnetic field that will result in the suppression of Multipactor. Using solenoid magnets to eliminate an EC is already a functional Multipactor Mitigation Strategy at LHC, in which case longitudinal solenoid magnetic field may confine electrons near the walls of the multipactor susceptible cavity, where they are created and therefore may reduce the EC density. Detailed simulations [80, 81] shown that even a

weak longitudinal solenoid field forces the electron of the cloud to move into circular orbits that hit the cavity walls after the half a period has been performed, which means that if the process is fast enough, the magnetic field can clear the electrons between two bunch passages.

4.2 RF Waveguide Geometry Optimitation

This mitigation strategy is based on making the geometry of the waveguide unfavorable for multipactor at the frequencies of interests [82], according to Eqn. 3.36 and always taking into account the shape of the multipactor susceptibility diagram of Fig. 3.10, one can see that for a given fxd value, the voltage at which multipactor happens, or multipactor threshold, directly depends on the geometry of the walls of the waveguide. Being d the gap between the walls, for a given frequency f, the larger the gap between walls, the higher the power needed to generate Multipactor discharge, Fig. 3.10. However this technique is obviously limited by the fact that waveguide gaps dimensions need to be within certain limits. Nevertheless, recent works [83, 84] show high multipactor threshold values obtained for filters of novel smooth profiles even using the same minimum mechanical gap as their classical counterparts . Unfortunately, even though more complicated geometries have been achieved in order to reach higher thresholds[80, 85–88], the geometry cannot always be changed in the desired way, since system geometries may have engineering constraints or may be fixed by the necessary boundary conditions. For this reasons other methods like SEY reduction must be employed to prevent multipactor. In any case, either because modification of the RF field is not possible or is not sufficient, reduction of SEY at critical parts is often the final strategy.

4.3 Low SEY coatings

The most commonly used and efficient Multipactor mitigation technique is the optimization of the surface properties by means of surface treatments and the application of low SEE coatings on the walls susceptible to develop Multipactor discharge. This technique

has been stablished to be the most promising method to avoid the increase of electron population and the consequent destructive phenomena. Also antimultipactor coatings must be stable under air conditions. Satellite devices must be installed and exposed to corrosion under atmospheric conditions for several months which enhances its degradation, and in most cases may change its SEE properties making them unfavorable to for antimultipactor interests [89]. Corrosion-protection surface treatments for aluminium alloys have been the reference anti-multipactor coating for the European Spatial Agency (ESA) and the space industry during decades [90, 91]. Among the coatings developed, *Alodine* presents a low SEY, very stable in atmospheric air [90, 91] . There are however certain inconveniences worth to be highlighted regarding the use of alodine coatings that must be always taken into account. As previously explained in section 3.6 antimultipactor coatings must have excellent superficial electric conductivity in order to avoid RF power losses, and *Alodine* carries a tremendous inconvenient related to its high superficial resistivity which as measured by our group [92, 93] is about 3 to 4 times that Ag plating for 4.5 to 9 GHz respectively and its consequent power loss, makes it unable to operate under the desired power conditions.

4.3.1 Based on the material physicochemical properties

Light metals have low SEY because of their low production of secondaries, low electron density (see Section 3.2.1) and high absorption of secondaries (high probability of electron-electron interactions in metals). On the contrary, their oxides and in general other strongly ionic compounds that might be formed after atmospheric exposure have long secondary diffusion lengths, and often present high SEYs [23, 94]. Details of the surface chemical state can affect intensely the surface escape probability. Some adsorbed molecules or radicals, like H_2O and OH, seem to supply surface energy levels to help SE's to escape hence usually increasing the yield [39, 89]. Magnesium for instance, is an excellent substitute for aluminium in space components because of its density and mechanical properties, however, magnesium oxidizes rapidly in air and the oxide has a high SEY depending of preparation [23]. In fact, Mg oxide is used in plasma display panels because of its high SEY. Moreover, SEY values of more than 7 have been reported for Mg oxide surfaces [95]. Therefore, in principle, it does not seem very attractive for RF components where multipactor discharge is possible. Materials like nitrides, carbides, or other compounds of transition metals like

Ti, V, Cr, and Nb as well as metallic alloys, have been often assumed to be favorable for anti-multipactor coating purposes [90, 91, 96–101]. These compounds are metallic but they have also some ionic bonding and thus are more resistant to oxidation than the pure metals.

4.3.2 Electron Conditioning (Scrubbing)

Electron conditioning or scrubbing was first developed in the framework of particle accelerator in which beam instability caused by SE clouds formed around beams is a serious problem [102, 103]. Some mitigating methods have been employed to control EC in accelerators and resulted in very good results [104, 105], such as the use of permanent magnets and solenoid coils. However as well as in satellite waveguides, reducing the electron emission from the exposed surface i.e. beam duct in this case, is one of the most effective methods. A very efficent way to reduce SEY of technical surfaces is by means of electron conditioning due to the effect that the prolonged electron irradiation has on the chemical state of the wall surface and that often produces a significant reduction of the SEY [18, 19].

Many pure metal surfaces usually have maximum SEY value of about 1.50 [38, 39], but surface impurities due to air exposure such as the typical carbonaceous contamination makes the SEY increase up to 2.0[39]. Extended electron exposure has been proved to reduce the value of SEY_{MAX} to values as low as 1.1 [106]. This SEY reduction effect of the electron conditioning on technical surfaces coincide with the formation of a graphitic surface film [20, 105]. Graphitic carbon-based materials, and specially graphite, are known to have low SEY [20, 38, 105, 107, 108], hence their electron emitting properties are convenient for anti-Multipactor purposes. According to this, the presence of carbon films reduces significatively the SEY of the metallic surfaces [107].

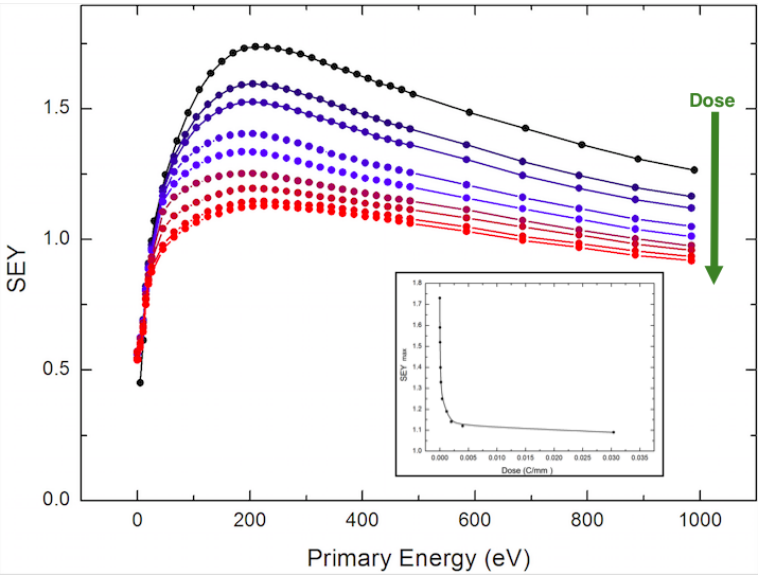

Figure 4.1: SEY curves measured during the development of this thesis for different doses at 500 eV electron impugning energy; Inset:SEY_{max} versus Dose for as received Cu at normal incidence.

Air exposed surfaces, are usually covered by contaminants containing a significant amount of C atoms. When irradiating contaminated surfaces with energetic electrons, contaminant C-H and C-O bonds tend to dissociate forming volatile compounds [109, 110] which would be desorbed from the surface. Carbon atoms rearrange then in honeycomb domains characteristic of the graphitic materials accompanied by sp^3 to sp^2 hybridization transition [106].

As shown in several previous works [20, 106, 111, 112], Scrubbing dosis or fluences can be defined as the electron dosis applied to a surface per unit area, it can be expressed as; F=I·t/$\mathfrak{A}$, and its value has units of [C/mm^2]. A clear example of the effect of the electron irradiation on technical surfaces is depicted in Fig. 4.1 where we can see [112] the dependance of SEY_{MAX} versus the electron dose at different primary energies. At certain dosis the curve reaches an asymptotic behavior indicating that the sample gets "fully scrubbed". Also the efficiency of scrubbing depend on the energy of the irradiating beams. Therefore the time required to obtain a fully scrubbed surface is consequently different especially when low energy electron beams are used.

4.3.3 Surface Roughening Effect on SEY

The SEE modification capabilities due to surface roughness were known since long time [23]. However, first attempts to simulate and explain this effect were not successful; it is not a simple effect to be explained with a simple SEE model. More recently, experimental results have been reported for deeply textured surfaces of diamond [113] and Cu [92, 114, 115] with maximum SEY around 0.5. These surfaces were formed by whiskers, dendrites, or ion- and chemical-etched columnar structures in the nano- or micro-meter scale. However, surface electrical conductivity was probably poor. Also recently, it has been confirmed that a more detailed model of SEE can explain a reduction of SEY due to deep surface roughness [116, 117]. Quailtative explanation for the SEY reduction phenomenon due to surface roughening is illustrated in the upper panel of Fig. 4.2. When a SE escapes through a smooth surface to the vacuum it reaches no obstacle but the WF barrier [23], being a very different case when there is a rough surface to pass through. In the latter case, a percentage of re-emitted electrons would hit an inner side of the groove and with some probability they will be absorbed, or they can generate further SE's [118].

Both experimental works and theoretical simulations have been carried out about this topic [92, 118] setting a clear background knowledge on the SEY reduction phenomenon due to surface roughening. Even though the inhibition or suppression of the SEE has been the most observed phenomenon, previous authors [47, 117]demonstrated that the effect of the modification of the surface morphology may result on SEY an increase of the SEY_{Max} values depending on the shape of the ripples or protuberances forming the roughness. As pictiorally explained in the bottom panel of Fig. 4.2, even though measurements are performed at normal incidence, the local injection angle of incidet electrons increases with the aspect ratio of the corrugated surface. According to what was presented in Sec. 3.1.4, the number of SE's released from the surface increases due to such oblicbous impact, and if the surface aspect ratio is not large enough and the SE reabsorption does not take place, an increase on SEY can be observed.

Remarkable challenges arise regarding the usage of surface roughening as a multipactor strategy. On one hand the morphology must be such, that SEY is mitigated instead of enhanced. On the other hand, the great inconvenient of this technique in the concern

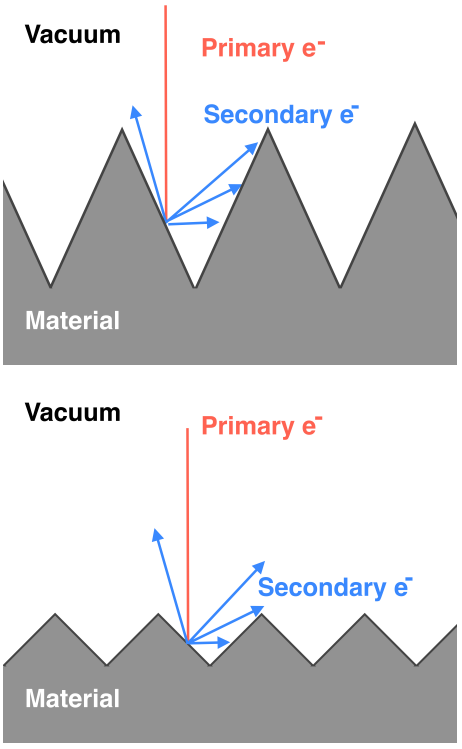

Figure 4.2: Graphical explanation of the origin of the variation of SEY of rough surfaces. **Upper panel:** Even thouh SEE might be ebhanced owing the oblique interaction of primaries with the solid, electrons are intercepted and reabsorbed by surrounding material. **Lower panel:** SEE is enhanced by the oblique interaction of primaries with the solid and electrons are not intercepted or reabsorbed by surrounding material.

of the RF satellite devices is the risk of increasing surface resistance and the consequent enhancement of RF power losses accordint to the overviewed in section 3.6.3. One can conclude that when dealing with rough surfaces as anti-multipactor coatings, the size of the high aspect ratio structures must be reduced to the minimum possible in order to find a compromise between diminishing SEE, and power loss enhancement minimization.

Chapter 5

Experimental Techniques

In this chapter the experimental techniques used in this thesis are described. A review of characterization techniques such as microscopies, photoemission or Raman spectroscopies is presented from a point of view of the study of the SEE of the materials analyzed, as well as the synthesis techniques developed to obtain them. Also, the technology used to achieve the desired vacuum conditions is explained, together with a detailed description of the set-ups and facilities in which this experiments were carried out.

5.1 Ultra High Vacuum (UHV)

Vacuum technology has advanced considerably over the last century, and very low pressures are nowadays relatively easy to obtain [119–121]. Vacuum environments can be splitted into three regimes regarding their range of pressures, these are; Low Vacuum (1mbar-10^{-2} mbar), High Vacuum (10^{-2}-10^{-8} mbar) and Ultra High Vacuum (10^{-8}-$< 10^{-12}$ mbar). The highest vacuum achieved in this thesis was $\sim 10^{-10}$ mbar. Vacuum environments are obtained inside vacuum chambers. They are rigid enclosures within which experiments are carried out. Vacuum chambers can be made out of stainless steel or in a more modern fashion, μ-metal. The latter is a nickel-iron alloy, which main distinctiveness is its high magnetic permeability, for magnetic screening in electron spectroscopies [122, 123]. In order to obtain UHV conditions, some special procedures are needed. Initially, the vacuum chamber will be pumped down to 10^{-2} millibar using a rotary pump. At pressures higher

than high vacuum, the inelastic mean free path of the gas molecules are still so small (hundreds of μm) that they interact with each other. This is, while gas is being pumped, the remaining molecules in the chamber *feel* the effect of the pumping due to the interactions between them. This is called *laminar regime*. Once high vacuum is reached, molecules mean free path range from hundreds of mm to several Km, and they no longer interact with each other except for occasional random impacts. This is called *molecular regime*. The pumping limits of rotary pumps are well defined since their working principles are subjected to the laminar regime of the gases. However their use is necessary for further vacuum achievements. I order to pass the laminar regime barrier and obtain high vacuum, turbomolecular pumps were used. These pumps work on the principle that gas molecules can be given momentum in a desired direction by repeated collision with a moving solid surface. In a turbomolecular pump, the blades of a turbinee rotor, rapidly spinning at $\sim$30-40 KRPM hit gas molecules from the inlet of the pump towards the exit at its rear side, in order to create and maintain a high vacuum environment. For their operation turbomolecular pumps need to be backed by a rotary pump, which maintains a $\sim 10^{-2}$ mbar pressure at the rear side. Combined with turbomelucar pumps ionic pumps can be used, in order to achieve even finer vacuums. Ionic pumps ionize the gas molecules within its vessel. They employ a strong electrical potential, typically $\sim$5 kV, which allows the ions to accelerate and finally strike a titanium cathode. Due to the impact of high energy ions into the titanium cathode, the latter is sputtered onto the walls of the pump, while bombarding ions are buried into the walls. The freshly sputtered titanium is extremely reactive and acts as a getter that then evacuates the gas by both chemisorption and physisorption resulting in a net pumping action. Turbomolecular and ionic pumps can achieve pressures as low as 10^{-11} mbar. This pressure correspond to a molecular regime, in which the pumping of each molecule is due to independent events. Molecules will then be pumped when they randomly reach the pump vessel. Hence by increasing the pumping area, the probability for a molecule to be pumped will also be increased. Despite the impeaccable effectiveness of turbomolecular and ionic pumps to maintain UHV environments, a baking procedure (or *bakeout*) must be carried out in order to achieve such low pressures when pumping vacuum chambers for first time, since the amount of molecules pumped out decreases with pressure, there is always a low limit to the achievable value due to any constant source of molecules (leaking or outgassing). After atmospheric exposure, contaminant (mostly

water) molecules are attached to the chamber walls. The extremely high vapor pressure of such contaminants (∼3KPa for water at room temperature), makes the molecules attached to the walls to slowly desorb which continuously maintain the chamber at pressures higher than desired. The bakeout by heating the chamber walls in order to accelerate the process. By doing so, the vapor pressure of contaminants will increase resulting in a rise of pressure in the chamber due to accelerated desorption. Once the walls get free of those contaminants desorbing at room temperature, the pressure starts to decrease again, and the temperature of the system should be gradually decreased to the room temperature. After system cool down, pressures down to 10^{-10} were achieved and maintained. In our set-up, electrical heating tapes were used by wrapping them around the different parts of the chamber. After that, everything was covered with aluminum foil for insulation and heat distribution. Special care was taken at delicates parts such as small weldings, feedthroughs and vacuum-integrated electronic devices, for these reasons baking temperature was always kept between 100 and 130 degrees Celsius. The pressure was measured by using commercial gauges, accurately calibrated by the manufacturer. There are different kinds of gauges regarding the pressure ranges in which their measurements is reliable, however, their functionality is based in the same principle. Either by thermionic emission, or by high voltage application, positive ions are produced inside the gauge vessel, The ions are attracted to a biased electrode known as the collector, which measures the current produced by the impact of those ions. The collector current depends on the amount of ions obtained, which is a function of the pressure in the system.

5.2 Experimental Set-up

The results presented in this thesis were obtained at two laboratories; *Laboratory of Surfaces and Materials for High Power RF in Space Applications of the Applied Physics Department at Universidad Autonomy de Madrid, Madrid, Spain* and *Research division of the Material Science Laboratory at Laboratori Nazionali di Frascati, Frascati, Rome, Italy* belonging to *Instituto Nazionale di Fisica Nucleare INFN*. In the following subsections, a detailed description of the equipments used is presented.

5.2.1 Set-up at LNF

A schematic description of the UHV set up of the Research division of the Material Science Laboratory at LNF-INFN is shown in Fig. 5.1. The equipment consists on three connected vacuum chambers; Introduction chamber (10^3 mbar - 10^{-8}mbar), preparation chamber (10^{-8} mbar - 10^{-10}mbar) and analysis chamber (10^{-10}mbar). Each chamber is equipped with independent vacuum pumps, and their vacuum enviroments are separated by gate valves, which allows to introduce and draw samples into the system without exposing the analysis chamber to atmospheric pressure.

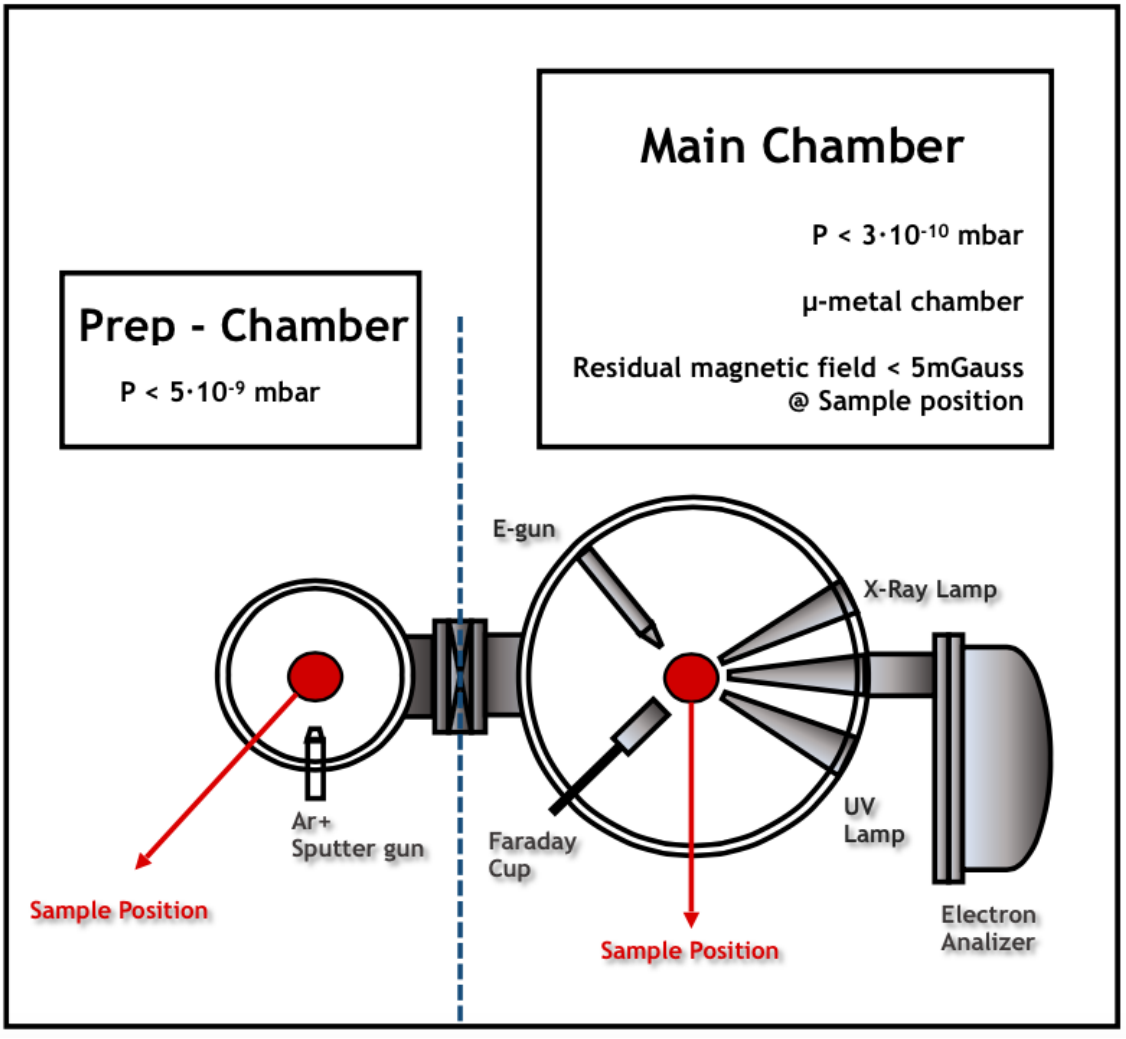

Figure 5.1: Schematic description of theset-up at LNF

Preparation chamber is equipped with an sputter ion gun for sample sputtering cleaning (see Sec. 5.3.1.1). It emits an unfocused ion beam in the range of KeV. Samples are

transferred to the analysis chamber by means of a magnetic transfer bar. Analysis chamber is equipped with an X-Ray lamp equipped with both Al and Mg non-monochromatic radiation, an Ultraviolet lamp and an hemispherical Omicron EA125 electron spectrometer, which were used to perform XPS and UPS photoemission spectroscopies (see Sec. 5.4.2). A Kimball electron gun is also installed which was used for SEE characterization and scrubbing experiments. The electron spectrometer, X-Ray lamp and Ultraviolet lamp are located at different level in height than the electron gun and faraday cup, which makes impossible the use of the electron gun and electron analyzer at the same time, hence EDC measurements are not possible to carry out.

An XYZθ high precision manipulator is installed on the top of the chamber in order to move the sample inside it, and to analyze at different positions. The manipulator is provided with electrical feedthroughs, and the precise electrical wiring, in order to measure sample electrical currents, apply bias voltages, etc. The analysis chamber is built in μ-metal which keeps residual magnetic field below 5 mGauss at sample position.

5.2.2 Analisys Set-up at UAM

A schematic description of the UHV Escalab 210 VG System of our laboratory *Laboratorio de materiales y superficies para alta potencia de RF en el espacio* at UAM is shown in Fig. 5.2.3. The equipment consists on two connected stainless steel vacuum chambers; Introduction-preparation chamber (10^3 mbar - $10^{-8} mbar$) and analysis chamber ($10^{-10} mbar$). Each chamber is equipped with independent vacuum pumps, and their vacuum enviroments are separated by a gate valve, which allows to introduce and draw samples into the system without exposing the analysis chamber to atmospheric pressure. Samples are transferred to the analysis chamber by means of a mechanical transfer bar.

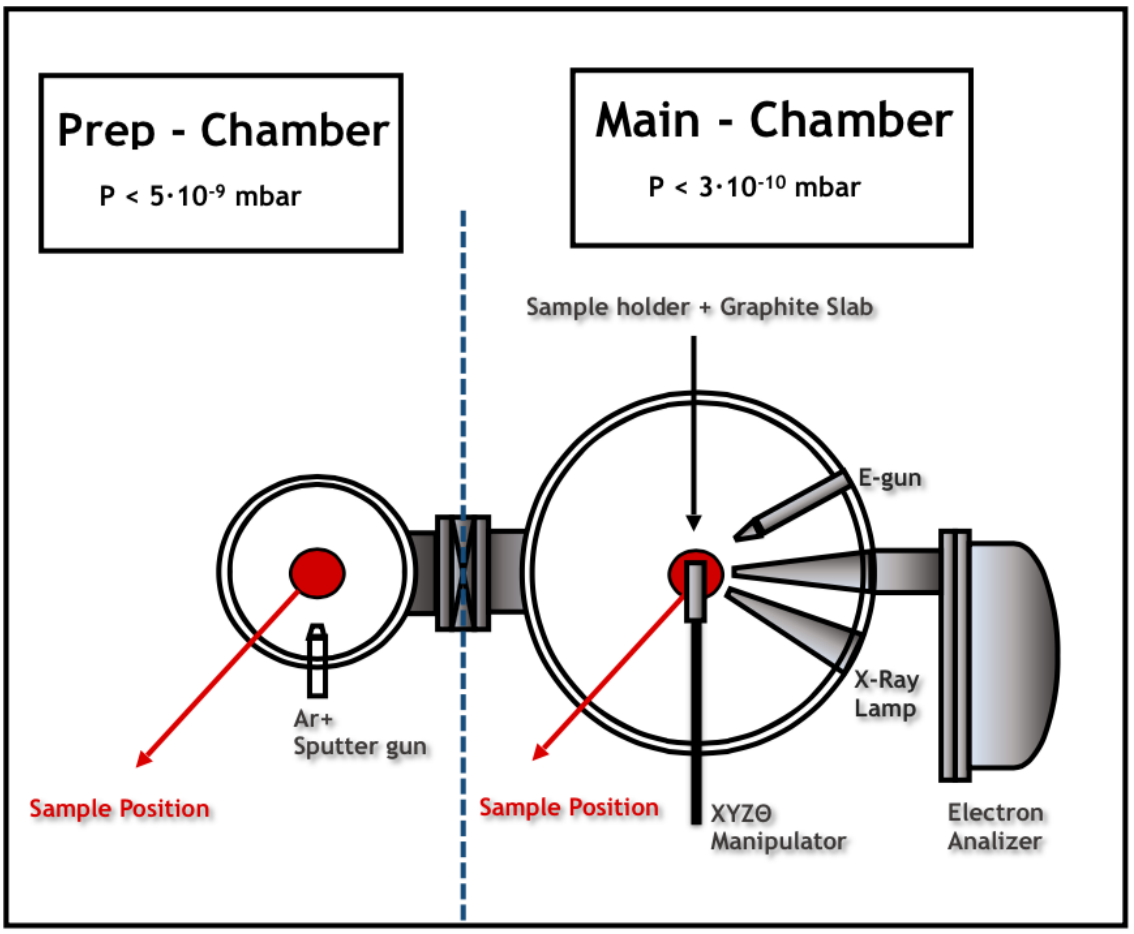

Figure 5.2: Schematic description of the analysis set-up at UAM.

The analysis chamber is equipped with an X-Ray lamp equipped with both Al and Mg non-monochromatic radiation, and an electrostatic sector spherical analyzer plus electron lens electron spectrometer, both manufactured by ESCALAB 210 VG (UK), which were used to perform XPS photoemission spectroscopies (see Sec. 5.4.2). A Kimball electron gun is also installed which was used for SEE characterization and scrubbing experiments. The electron spectrometer, is located at the same level than electron gun and, which makes possible the use of the electron gun and electron analyzer at the same time, hence EDC measurements can be carried out. An XYZθ high precision manipulator is installed at one side of the chamber in order to move the sample inside the it, and analyze at different positions of the sample. The manipulator is provided with electrical feedthroughs, and the precise electrical wiring, in order to measure sample electrical currents and apply bias voltages.

5.2.3 Sample Preparation Set-up at UAM

A schematic description of the HV sample preparation set-up of our laboratory at UAM is shown in Fig. 5.3. The equipment was designed and built by our laboratory and consists on an spherical vacuum chamber pumped by a turbomolecular pump, and a previous vacuum scroll pump. It is equipped with a MDC (USA) RF magnetron sputtering source (see Sec. 5.3.1.3), and a *Commonwealth* Kauffman ion gun (see Sec. 5.3.1.1), which emits a focused ion beam able to reach ion currents up 2.5 μA/mm^2 with energies ranging from 0.1 - 1 keV. The ion beam has normal incidence on the sample platform, while The magnetron is at 35° incidence angle on the sample platform. The flange and tube of the spherical chamber where the ion gun is installed are cooled by a fan. Gases are introduced into the chamber, through a high precision leak valve, which can keep high pressures of a few bars, separated from UHV pressures when closed. The leak valve introduce Ar gas into the chamber through an extremely small aperture. Gas conductance of the aperture is controllable, which makes very small fluxes of $\sim$ 5-10 mln/min (as measured with a Bronkhorst *EL-FLOW* flux-meter, appropriately calibrated for Ar) to be achievable. Ar gas was provided by commercial alluinum *minican*. Gas is stored at pressures of $\sim$15 bar, and dispensed to the leak valves through a metallic pipeline. Samples are introduced and taken out using an 8" Conflat port sealed with Viton gasket and after every working cycle the system vented with nitrogen.

The turbomolecular pump is connected to the chamber with a gate valve located between them. Also a bypass is installed which directly connects the chamber and the pump through a high vacuum valve. By shutting the gate valve, pumping speed can be controlled by the high vacuum valve located on the bypass. This mechanism, together with the high precision leak valve, allowed us to accurately control gas fluxes and achieve and maintain $\sim 10^{-3} - 10^{-2}$ mbar Ar environments, which are required for Plasma Based Sputtering Techniques (see Sec. 5.3.1). Substrates were placed in a disc of 7 cm of diameter located at the geometrical center of the chamber and electrically connected to ground. The disc was made of copper for thermal and electrical conductance purposes. In order to obtain the highest homogeneity possible during deposition the disc was mounted on a UHV rotary mechanical drive and coupled to an external electrical motor spinning at 30 rpm. For

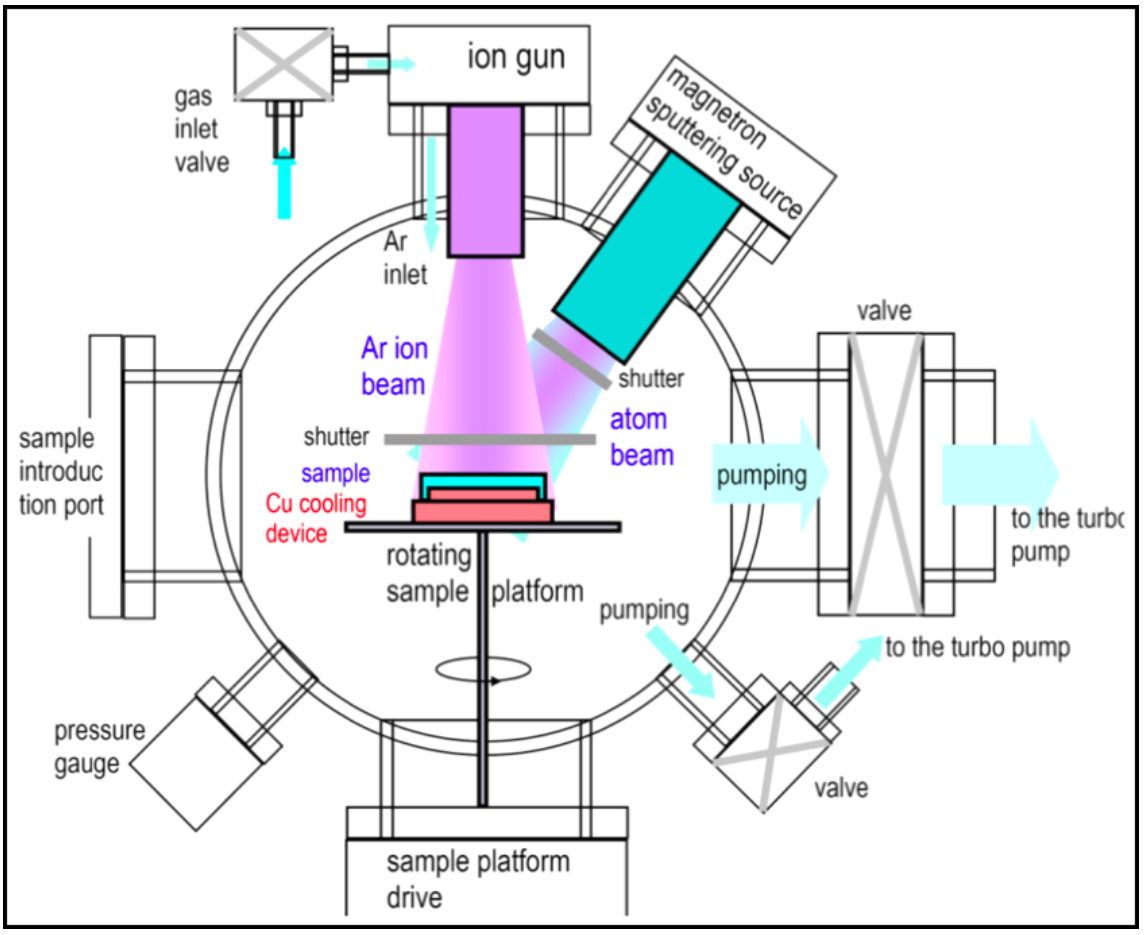

Figure 5.3: Schematic description of the synthesis set-up at UAM.

geometrical reasons, electrical currents at sample position were not available to obtain due to the technical limitations brought by sample holder rotation.

5.3 Synthesis Techniques

5.3.1 Plasma Based Sputtering Techniques

Anti-Multipactor coatings were obtained in this thesis by using ion etching and sputtering deposition techniques. Further analysis on the strategy followed will be done in Ch. 6.

Sputtering is the result of momentum transfer, i.e. surface atoms of the target are emitted when momenta of energetic incident particles are transferred to target surface atoms. For the sake of a better understanding, sputtering processes have commonly been compared with an "atomic pool" where the incident particle (cue ball) breaks up the close-packed

rack of atoms (billiard balls), scattering some backward (toward the player) [124]. It is known as a Physical Vapor Deposition (PVD) technique used to deposit thin films onto a desired substrate. PVD coating methods involve purely physical processes such as plasma sputter bombardment rather than involving a chemical reaction at the surface as in chemical vapor deposition (CVD). However, the great momentum transfers that take place in a sputtering deposition process, could eventually lead to surface atoms rearrangement and surface modification. Hence we can expect that high energy particle bombardment modifies surface topography, crystallography, and grain structure.

Ions are the most common particle used in sputtering processes, since due to their large masses, considerable large momenta can be transferred to the solid, for this reason sputtering processes were carried out using Ar^+ ions as bombarding particles in this thesis. The use of nobel gases bring extremely important advantages, since, surface modification can be obtained while the sample remains free of chemical modification. Reactive sputtering can be also developed in order to obtain compounds by sputtering from targets in the presence of a reactive gas usually mixed with an inert working gas.

The efficiency of the sputtering process is defined by the sputtering yield and can be defined as:

$$S = \frac{N_{sputtered\ atoms}}{N_{incident\ ions}} \tag{5.1}$$

And it depends on different physical constant of both incident ions and target atoms as well as the impact energy.

In order to develop sputtering experiments, the understanding of glow and plasma discharges is extremely important since all of the incident particles are originated in a plasma. A plasma can be defined as a quasineutral gas that exhibits a collective behavior in the presence of applied electromagnetic fields. Plasmas are weakly ionized gases consisting of a collection of electrons, ions, and neutral atomic and molecular species. The densities of glow discharges and arcs exploited in the industrial plasma processing applications range from $\sim 10^8 cm^{-3}$ to $\sim 10^{14} cm^{-3}$.

The application of a sufficiently high voltage between metal electrodes immersed in a low-pressure gas, and in presence of an electron emitting cathode, makes the emitted electrons collide with gas molecules, and then positive ions appear. The energy of the electrons should be higher than the ionization energy of the gas molecules. At the beginning of the discharge, the primary electrons from the cathode must be accelerated by an electric field near the cathode. The positive ions bombard the cathode surface, which results in the generation of SE's from the cathode surface. The SE's increase the ionization of the gas molecules and generate a self-sustained discharge [124]. The so called Townsend equation reveals that the discharge current i rises dramatically from i_0 because of the combined effects of impact ionization and SE generation, and is written as:

$$i = i_0 \frac{e^{\alpha d}}{1 - \gamma_e(e^{\alpha d} - 1)} \tag{5.2}$$

where i is the charge current, d is the distance between walls, γ_e is known as the Townsend SEE coefficient versus incident ion energy, which differs from SEY, and α is the Townsend ionization coefficient, and represents the probability per unit length of ionization occurring during an electron-gas atom collision.

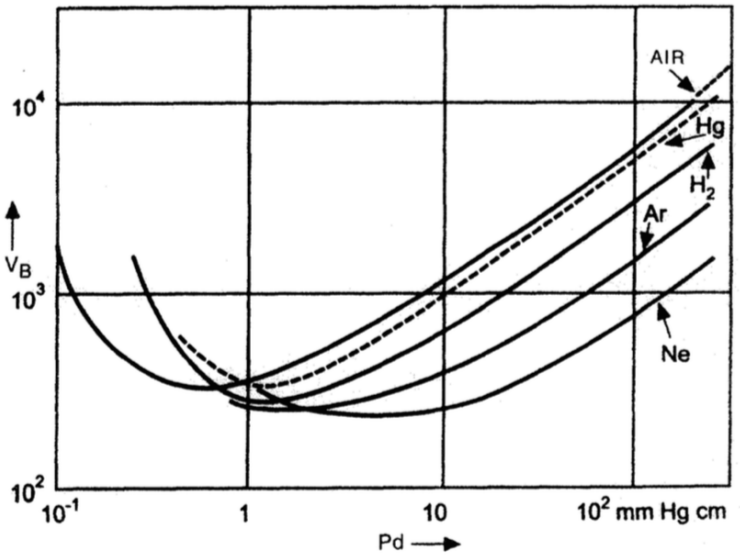

Figure 5.4: Paschen curves for a number of gases.

Breakdown is supposed to occur when the discharge current tends to infinite, i.e. $\gamma_e(e^{\alpha d} - 1) = 1$ in Eqn. 5.3. The breakdown voltage necessary to start a discharge or electric arc,

between two electrodes in a gas as a function of pressure and gap length comes given by the Paschen law, which expressed by

$$V_B = \frac{C_1 Pd}{ln(Pd) + C_2} \tag{5.3}$$

where P is the pressure, d is the distance between electrodes and C_1 and C_2 are constants. A plot of V_B versus Pd is shown in Fig. 5.4 and is known as Paschen curve. It is indeed very illustrative, since it can be seen that at low values of Pd there are few electron-ion collisions and not enough SE's are produced to sustain ionization in the discharge. Moreover, at high pressures there are frequent collisions and electrons do not acquire enough energy to ionize gas atoms, as a consequence, the discharge is dampen. In between, at typically a few hundred to a thousand volts, the discharge is self-sustaining.

5.3.1.1 Kaufman Sputter Ion Gun

In this work, a commercial *3cm-Type Commonwealth* Kaufman ion gun was used. Kaufman ion guns belong to the gridded ion sources type. A schematic diagram of a gridded Kaufman ion gun is depicted in Fig. 5.5. It consists on three key elements, i.e. discharge chamber, electron source or cathode and grids. Ions are generated in the discharge chamber through electron acceleration. A tungsten hot filament is the cathode, which emits electrons by means of thermionic emission when an electric current passes through it. Electrons will then be accelerated towards the anode, in order to ionize the present gas. Permanent magnets are located around the discharge chamber in order to increase the path length of the accelerated electrons by causing an helicoidal trajectory in their way to the anode, which increases the ionization efficiency of the gas. Ions created in the discharge chamber are then accelerated to high velocities with the source grids.

Grids are electrodes separated a few millimeters from each other. They are precision machined, made from thermally stable graphite. Each grid is formed by several small apertures that allow for extraction of ions. The grid located near the discharge chamber is known as screen grid, it contains the plasma and its potential depends on the plasma potential, which is determined by the discharge parameters. The outer grid is known as

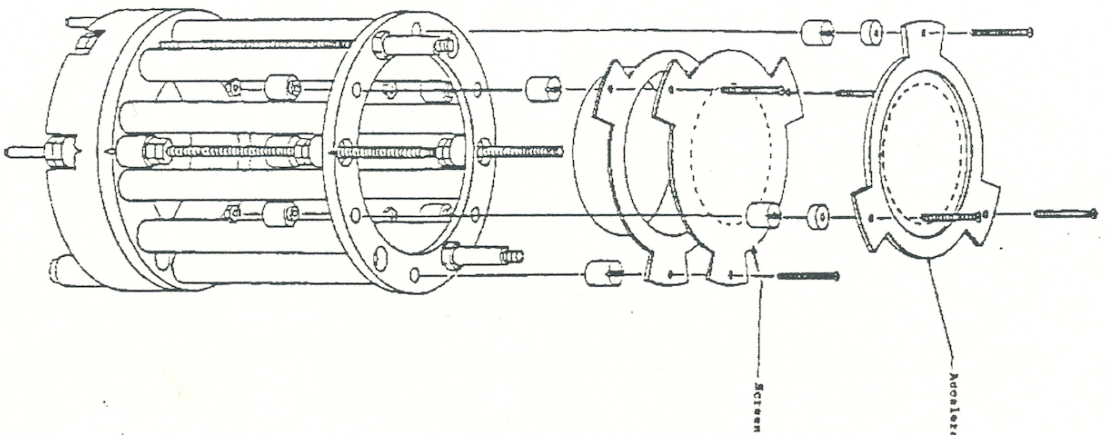

Figure 5.5: Assembly of the ion optics of the Kauffman ion gun .

accelerator, and assist the ion beam generation in two ways: a) it extracts the ions from the discharge chamber, and b) it determines the beam focusing. The ion gun assembly extracts ions from the discharge chamber by applying specific voltages to each grid. The electrical scheme of the Kauffman ion gun is shown in Fig. 5.6. The screen grid is biased positive and as a consequence, the plasma in the discharge chamber is also biased positive with respect to ground. On the other hand, the accelerator grid is biased negative with respect to ground. The established electric field makes positive ions present within the discharge chamber to drift out of the assembly. The energy of the ions emitted to the target is determined by the screen grid voltage or *beam voltage*, and the ion current available from the ion source are determined by the ion source parameters, such as gas pressure, cathode power, anode potential and geometry. In some cases, a neutralizer can also be placed downstream the source. By emitting electrons a balance of the number of positive ions which leave the source is achievable.

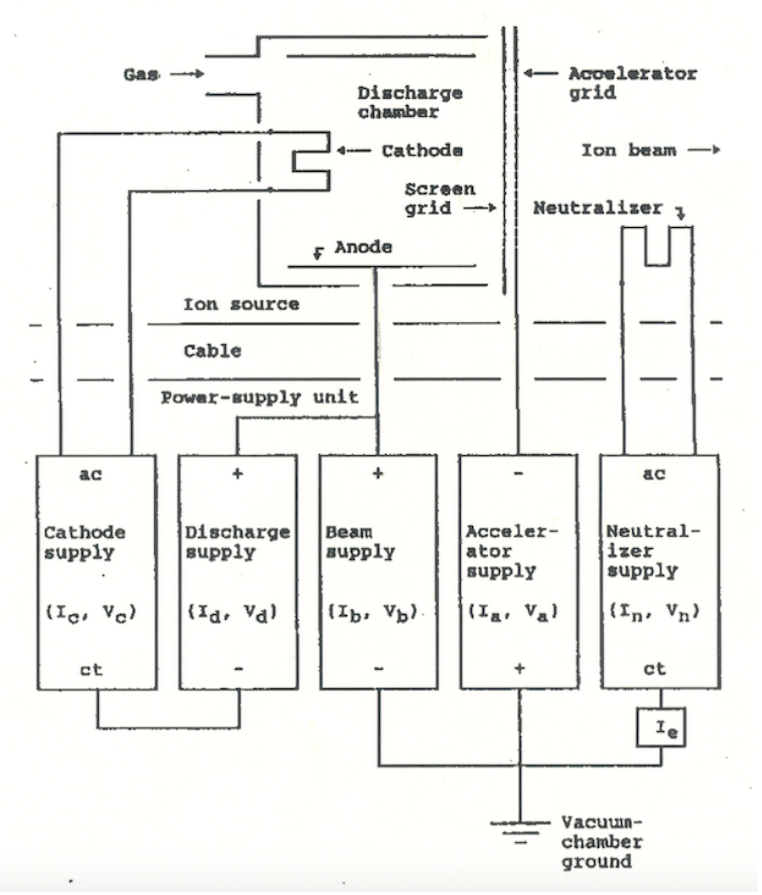

Figure 5.6: Schematic description of the electronic configuration of the kauffman ion gun and its power supply.

The beam voltage and beam current of a Kaufman ion source can be adjusted independently. Beam voltage is controlled directly by changing screen grid voltage. On the other hand, by changing the value of the accelerator grid voltage, one can vary the amount of ions drifted out of the ion gun assembly, which allows to control the ion beam current. By measuring the net current at the anode produced by drifted ions, an estimated value of the beam current can be obtained, however it is important to notice that the current value measured at the anode, does not equal the current at the sample position, i.e. *Sample Current*

5.3.1.2 Analysis of the Kauffman Ion Beam

As previously noted in Sec. (5.2.3), ion beam current is not measurable at substrate position while sample synthesis. However a series of measurements were carried out in the absence of a rotation of substrate platform or disc, in order to estimate intensity and

shape of the ion beam and understand its behavior under different conditions. A grid of 7 insulated electrodes was built for this purposes, whose schematic description is shown in Fig. 5.7. Each electrode was connected to a feedthrough, so that the electrical current could be measured. The totality of the electrodes was disposed in an area similar to that for the copper sample holder.

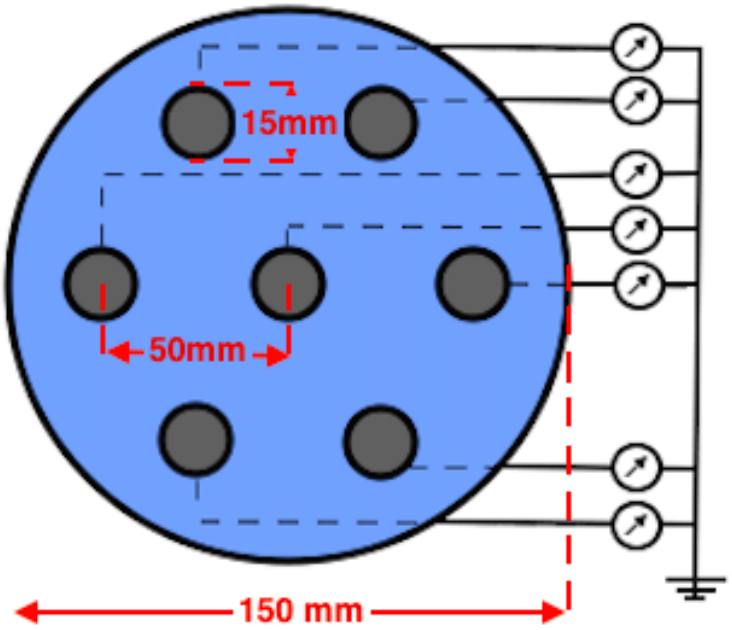

Figure 5.7: geometrical disposition of the seven anodes grid used to determine the intensity and shape of the ion beam produced by the kauffman gun.

Ion gun operation was carried out under a $3 \cdot 10^{-3}$ mbar Ar enviroment, which constitutes normal operation conditions. Ion beam energies were set at 450 eV, 700 eV and 900 eV and at each energy, ion beam currents measured at Accelerator Grid were set at 5 mA, 15mA and 30 mA, being 30 mA the maximum beam current disposable from the power supply. The currents measured at each electrode were recorded, and a graphically represented. The results obtained are shown in Fig. 5.8 and Table. 5.1. In a general way, it is clear that the increase of beam energy has a tremendous effect in the measured sample current, hence the set value of beam current, measured at ion gun anode, is proved to vary the amount of ions emitted, but it is important to note that its value is only indicative at each different beam energy applied.

As shown in the graphical representation, data obtained at 5 mA beam current, and 900 eV beam energy does not follow the general trend in intensity. This is an extreme case in

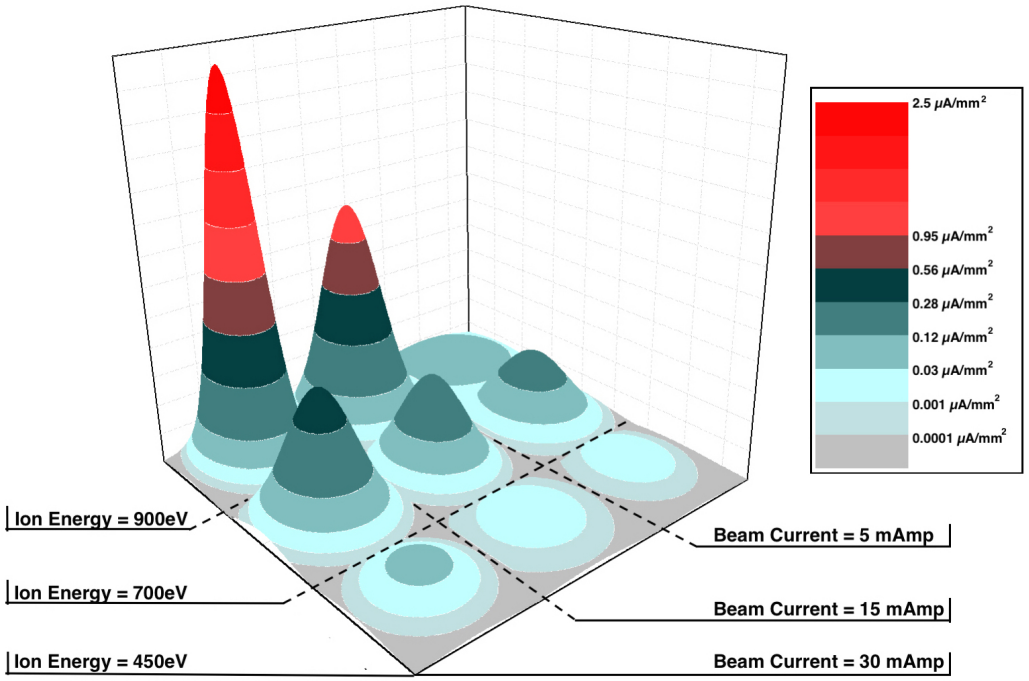

Figure 5.8: 3D representation of the results obtained on the analysis of the intensity and shape of the ion beam produced by the kauffman gun.

which anode voltages need to be weak in order to obtain beam currents as low as 5 mAmp. On the other hand, the screen voltage needs to be too high in order to obtain beam energies as high as 900 eV, hence anode voltages became negligible and the current obtained at the sample position is very low. For this reasons experiments should not be carried out under this conditions.

	Intensity(μA/mm^2)			FWHM (mm)		
	5 mA	**15 mA**	**30 mA**	**5 mA**	**15 mA**	**30 mA**
450 eV	0.14	0.25	0.50	188	110	103
700 eV	0.22	0.62	1.50	117	87	84
900 eV	0.16	0.85	2.51	87	87	70

Table 5.1: Results of the analysis of the Kauffman ion gun beam. Values of the Ion intensities measured at the sample position (left panel), and the FWHM of the gaussian Ion Beam (left panel), obtained at different beam energies and accelerator grid currents

Table 5.1 shows the quantitative results of the Kaufman ion gun study developed. The ion currents range from $\sim$ 0.15 to $\sim$ 2.51 depending on the set parameters. Also, it was demonstrated that the beam is distributed following a gaussian-like shape, which FWHM

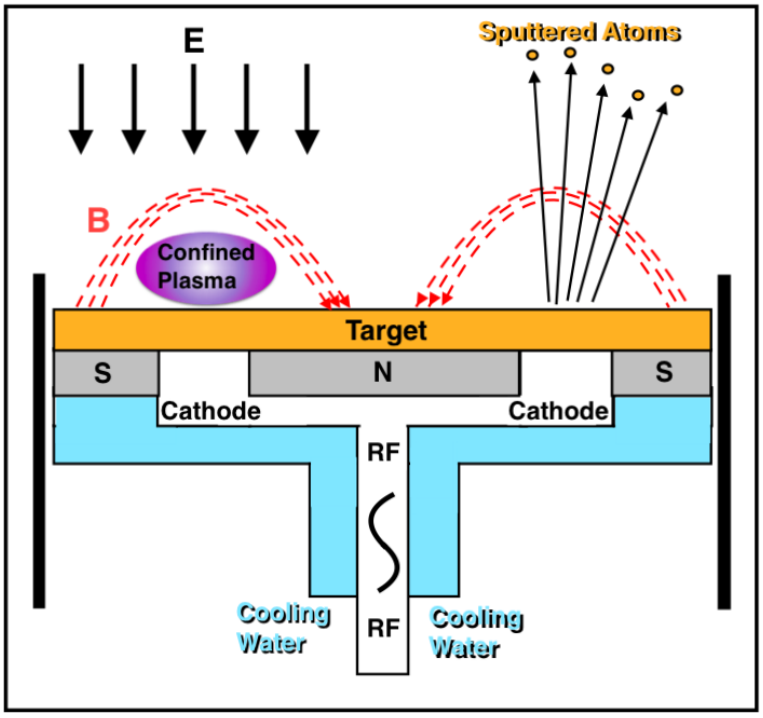

Figure 5.9: Schematics of a magnetron sputtering source.

depend on the beam energy as well as on the current used. In a general way, the FWHM of the beam tend to shrink for both higher set energies and beam currents. This analysis will be indeed very useful when developing anti-Multipactor coatings, which results are reviewed in Chs. 6 and 7.

5.3.1.3 Magnetron Sputtering Technique

Magnetron sputtering is one of the most popular deposition technique among a wide range of industrial possibilities. A schematic drawing of principle of magnetron sputtering can be found in Fig. 5.9.

Plasma is generated by applying an intense electric field between anode and cathode (target) which accelerates free electrons and ionize the present gas. Among all the geometrical configurations available, circular planar configuration is the most common, and the one used in this work. Magnetron sputtering sources, are equipped wiith permanent magnets located on the back of the target, in such a way that they do not interact with the generated plasma. Magnets exhibit a simple concentric geometry in which the center is one pole and the perimeter is the opposite, hence the center would be a very small round magnet surrounded by an annular ring magnet of the opposite polarity, with a gap in between. The

magnetic field lines bend over with a portion parallel to the target surface, and returns normal to the target surface into the south pole, completing the closure of field lines. The closed field lines form then a boundary "tunnel" which traps electrons near the surface of the target. This electron trapping improves the efficiency of the generated plasma and constrains the ion density, allowing higher current at lower gas pressure and achieves a higher sputter deposition rate. In addition, the increased ionization efficiency achieved within the magnetron tunnel allows the discharge to be maintained at typical operating pressures of 10^{-3}, which are lower than those required in absence of magnetic fields. A fundamental reason for these beneficial effects in magnetrons is the displacement of the Paschen curve minimum to lower Pd values relative to simple discharges. Therefore, for the same electrode spacing and minimum target voltage, a stable discharge can be maintained at lower pressures.

Plasma deposition techniques are complex preocesses, and their study requieres simulations, and a large number of devices to experimentaly check the plasma properties. This thesis relies in a well known configuration with a commercial RF equipment. However, an accurate knowledge of the generated plasma would require the use of a quartz micro balance, to check the deposition rate, however such task becomes very difficult when working with RF generated plasma.

A schematic description of the magnetron sputtering equipment used in this work is depicted in Fig. 5.10. A circular planar *2" Meivac-Mak Sputter head* was used, as a sputtering source. Plasma generation was achieved by means of RF exposure. RF was provided by a commercial *SEREN R301-Series RF Power Supply*. It is intended for use with radio frequency plasma processing systems and radio frequency processing applications. It provides a 13.56MHz, level-controlled radio frequency power output up to 300 Watts.

The power supply works in series with a *SEREN AT-3 Automatic Matching Network* used to deliver RF power to the Sputtering head.

This matching network can operate either in manual or automatic mode. However automatic mode is extremely accurate and its functionality is very precise. For this reason, automatic mode was always used in the experiments of this thesis.

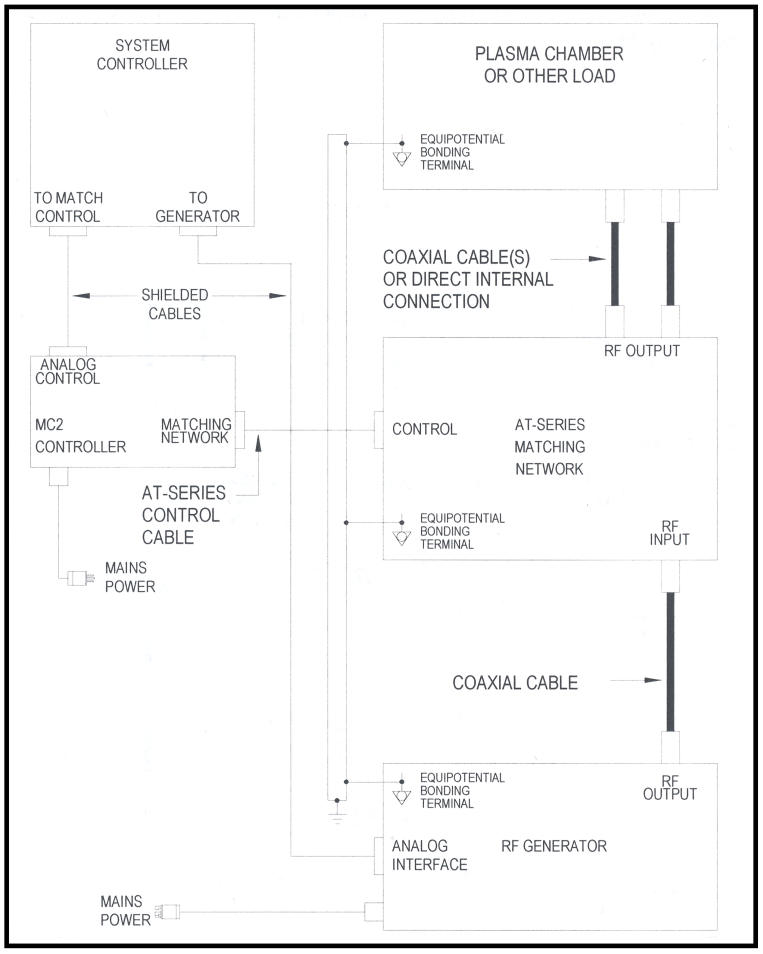

Figure 5.10: Schematic diagram of the SEREN R301-Series RF Power Supply, SEREN AT-3 Automatic Matching Network, and the SEREN MC-2 Matching Network Controller disposition used to carry out the magnetron sputtering performance during this thesis.

5.4 Characterization Techniques

5.4.1 SEE Characterization

In order to develop SEE measurements, a low energy ELG-2 electron gun from Kimball Physics was used as the source of primary electrons. A graphical description of the components and operation of the e^-gun is presented in Fig. 5.11. An electrical current flows through a metallic cathode which makes it to emit electrons by means of thermionic emission. Besides the cathode, the electron gun consists on the following elements that produce the electron beam: Grid, Anode, Focus and Deflection. The electrostatic lens system uses a triode configured electron source with a control grid aperture, and a four pole deflection system. The electron beam is accelerated, in the grid-anode section, and then focused by

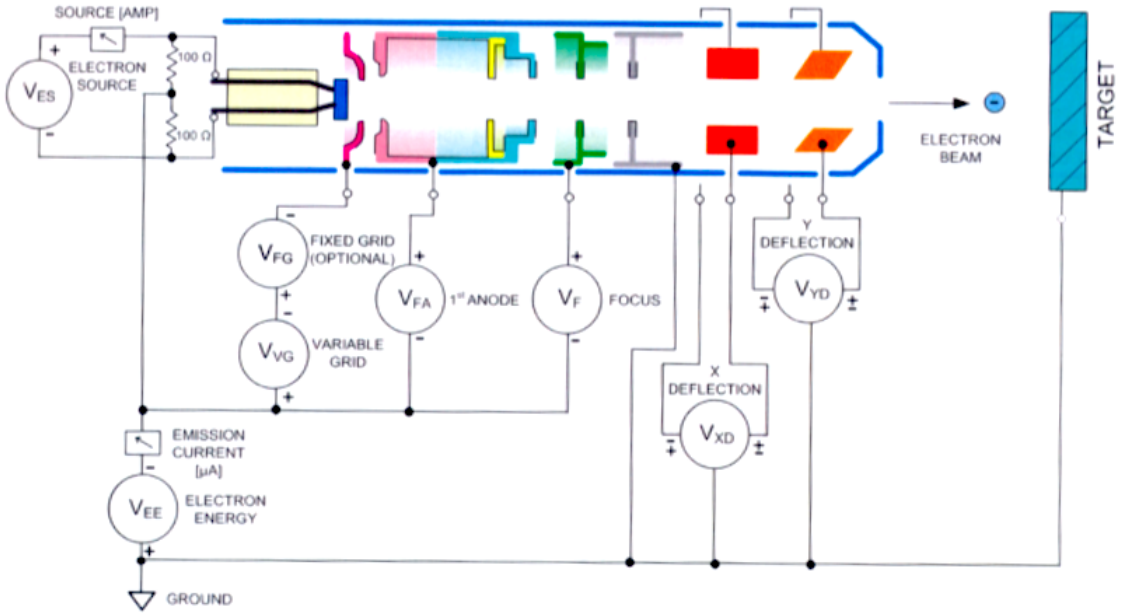

Figure 5.11: block diagram of the ELG-2 e^- gun used for the data acquisition in this thesis.

the focus voltages. Beam energy, beam current, and beam divergence are all directly controllable. It operates in an energy range from 5 eV to 2 keV however, intensive observations, showed that spot size and current behavior is neither stable nor controllable at energies below 25eV. The achievable electron current ranges from 1 nA to 1 μA. Spot size is also controllable, ranging from 0.5 mm to 2 cm. However, at each beam energy, the e^- beam adopts a different shape and size, for this reason, grid, anode, and focus voltages must be re-adjusted as beam energy evolves in order to maintain a constant sized spot. Prior to operation a warm up period of $\sim$2 hours must be respected in order to obtain a stable e^- current during a primary energy scan.

The EGPS-1022 power supply was used to control beam energy, anode and focus voltages. It consists of a group of modular power supplies that provides the necessary voltages to drive the e^- gun. The source, grid anode and focus power supplies are floated, while the energy and deflection supplies are referred to ground. A Model 6514 KEITHLEY electrometer was used to measure I_s and I_p. It makes current measurements from 10 pA to 21mA using 10 measurement ranges; 20 pA, 200 pA, 2 nA, 20 nA, 200 nA, 2 μA, 20 μA, 200 μA, 2 mA and 20 mA. fast measurements up to 1200 readings per second are possible to be obtained. There is the option of enabling damping functions which reduce the reading noise for current measurements. However, damping will also slow down the

response of the measurement.

5.4.1.1 SEY Experimental Details

SEY measurements were carried out both at UAM and INFN-LNF. As previously pointed out in sec. 3.3, the indirect determination of difference in currents strategy was used to obtain SEY coefficient in both laboratories. Eqn. 3.28 shows that SEY is mathematically obtained by operating with two values namely, I_s and I_p. To obtain the e^-gun primary curent; I_p, a positive and grater than 45 eV bias voltage is applied to a target in which the electrons will impact. The reason of doing so, is to avoid reemission of SEs, all of them with less of 50 eV energy, to the vacuum and hence be sure that one measures an accurate value of the primary current that reaches the sample at each primary energy set by the accelerating voltage of the e^-gun. Slightly different methods were used to measure I_p at each laboratory, however both methods, are valid for the measurement purposes.

The set up used at INFN-LNF, counts with a movable faraday cup, which is composed by three slots of different widths, 1 mm, 2 mm and 3 mm (left pannel of Fig. 5.12). A +75 V bias voltage is applied to the Faraday cup in order to ensure that practically all electrons, within an acceptable error, are kept within the slots. By using a computer controlled electric engine the position of the device can be changed and monitored with an accuracy of μm.

The use of this system is very convenient in two aspects: a) It avoids the scape of most of the electrons due to reemission, by making the electron beam penetrate into one of the slots, and b) by measuring the current detected inside the slots at different positions of the Faraday cup, an accurate measurement of the electron beam spot size can be obtained. By changing the e^- gun parameters, the size of the beam can be modified, so one a can choose the most convenient spot size depending on the experiments requirements. Right panel of Fig. 5.12 shows a very illustrative example of a beam width analysis. The peaks represent the increase on the current detected when electrons fall into the slots,. When the spot is smaller than the slot, very well defined peaks are obtained. The absence of a plateau on the top of the peaks is an indicative of a spot bigger than the slot used to measure the current, hence the slot never contains the entire spot.

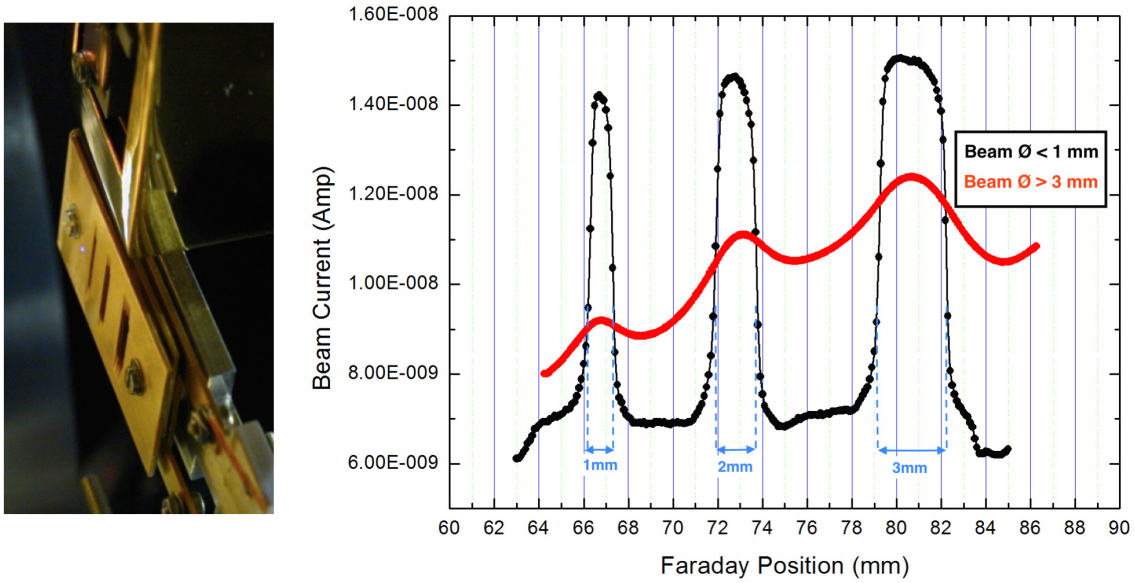

Figure 5.12: **Left:** Picture of the three-slot Faraday cup used to measure I_p during SEY data acquisition at LNF-INFN. **Right:** Results of a spot size and position analysis measured at the three-slot Faraday cup, prior to I_p acquisition. Comparison between spot size smaller than 1 mm in diameter (black line), and spot size grater than 3mm(red line). Note the lack of definition when the spot is bigger than the slots.

As previously noted, after warming up period, kimball gun is very stable and the dependance of current with primary energy is satisfactorily reproducible. However, the spot size of the beam, strongly depends on the primary energy set by the gun. For this reason the values for grids voltages need to be changed for each primary energy, in order to obtain a well focused spot of constant size, hence, the use of the faraday cup is indeed extremely useful.

At UAM Madrid, I_p is measured by applying a +50 V bias voltage on an graphitic carbon (g-C) slab, free of contaminants. g-C is a very convenient material for this purposes since it has a very low SEY around 1 [20, 38, 105, 107, 108, 125, 126]. By applying +50 eV bias one ensures all SE's to be kept within the solid [23], however the bias is not effective for highly energetic backscattered electrons, which might be free to leave the sample. It is known that backscattered electrons contribution to SEY of g-C can be considered constant and has a value of 0.1 within certain reasonable error [41, 42]. Taking this into account, Eqn. 3.28 can be rewritten in this case as:

$$SEY^{@UAM} = 1 - \frac{I_s}{I_p} = 1 - \frac{I_s}{I_{+50}^{g-C} \cdot (1 - 0.1)} \tag{5.4}$$

This method has been shown to result on reliable values of SEY using a much simpler set up than the one used at INFN. Nevertheless it is not possible to accurately determine the spot size which limits the versatility of the system. A $1cm^2$ square test sample coated with commercial *phosphor* [127] powder was used in order to determine the electron beam spot size at UAM. This method allowed us to ensure that the spot was not bigger than the test sample, and hence the whole beam reaches the target. At some points of the development of this thesis, SEY results were aquired by the same technique at the the *Departamento de Superficies y Nanoestructuras* at ICMM CSIC.

To obtain I_s, a negative bias is applied to the sample under study, -30 V at UAM and -75 V at INFN. By doing so, kinetic energy of electrons emitted from the gun would be reduced in a value equal to $\Delta E = e \cdot V_{Bias}$ at the moment of the impact with the surface. This is operationally convenient since the behavior of the e^-gun is neither stable nor controllable at very low energies, and a negative voltage allows us to work with landing energies close to zero still when the e^-gun works in an energy region where it is stable. Also the negative voltage is useful for other purposes such as avoiding space charge problems and repelling second generation electrons originated at neighboring parts of the set up, which could considerably affect the measurements.

Once I_s and I_p are measured, the use of Eqn. 3.28 is not straightforward due to the applied bias voltage, and the energetics of the SEY measuring technique should then be redefined. When measuring I_p, electrons reach the sample with an energy greater than that set by the e^-gun accelerating grid voltage, however, in this case the relevant information to be obtained is the number of electrons that are emitted when certain energy is set by the e^-gun accelerating grid, independently of their impact energy. On the other hand, since SEY depends on the energy of the primary electrons under the conditions at which secondary emission process are effective, i.e. in presence of negative or null bias voltage; it is necessary to take into account the bias voltage when measuring I_s, and correct the energy shift due to its slowing down effect, obtaining then:

$$SEY(E) = 1 - \frac{I_s(E)}{I_p(E_{gun})} \quad ; \quad E = E_{gun} - e \cdot V^-_{Bias} \tag{5.5}$$

Where E_{gun} is the energy of electrons set at the e^-gun. The currents used to measure SEY, should be of the order of a few nA in order to avoid surface modification due to

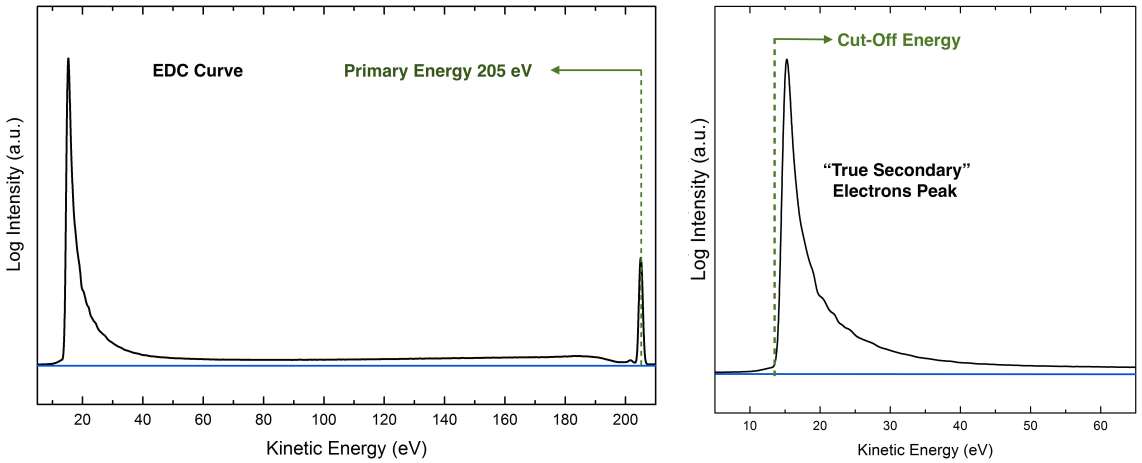

Figure 5.13: **Left:** EDC curve measured during the development of this thesis at a primary energy of 205 eV. **Right:** Magnification of the true SE's peak.

electron conditioning or scrubbing [20, 112]. A LabVIEW®software was developed to control the SEY data acquisition. Previous calibration of spot size was carried out so that values of e^-gun grids voltages can be automatically modified for each set energy. This allows to obtain an energy independent spot size. Unlike grids and accelerating voltages, source voltage and wehlnet values are fixed, and never change during SEY acquisition. The software controls both EGPS-1022 e^-gun power supply, and 6514 KEITHLEY electrometer, in such a way that a certain number of current measurements are recorded for each energy set at the e^-gun. Current signal measured by 6514 KEITHLEY electrometer is filtered and damped using different strategies depending on the requirements of each experiment.

5.4.1.2 EDC

Energy distribution curve (EDC) or SEE spectra is previously defined in Sec. 3.1.1. An example of an EDC curve measured during the development of this thesis is shown in Fig. 5.13, in which the "true secondary" electrons peak appears magnified in the right panel.

The measuring process is as follows. The electrons released from the sample to vacuum due to primary electron backscattering and secondary emission processes are collected by the hemispherical electron analyzer. The electron analyzer scans the whole electron kinetic energy range from 0 eV to the energy of the primary beam. As previously reviewed in Sec. 3.1.2,

The analysis of the EDC curve of certain material can bring extremely valuable information about the nature of the electrons contributing to SEY at each primary energy, as well as physical properties of the material under study. It is remarkable the observed behavior of the EDC at the true SE's peak cut-off curves at low energies. As it is clearly observable in Fig. 5.13, such cut-off represents the signal of the electrons with the lowest energy emitted from the sample. Electrons start escaping from the sample at energies higher than sample WF. However, In the case that any positive bias is applied, a retarding effect on the emitting electrons coming out the sample would make the true SE's peak cut-off to be measured at a kinetic energy:

$$E_K^{Cut-Off} = \Phi + e \cdot V_{bias} \tag{5.6}$$

where Φ is the sample WF, and $e \cdot V_{Bias}$ is, the retarding energy due to the applied bias voltage. The analysis of the position of the cut-off energy of EDC samples has been broadly used to perform WF measurements. A similar technique for WF determination is used in Photoemission Spectroscopies, in which after polarization of the studied sample, the peak of the SE's generated by the photoemited electrons, can be analyzed

[128–133].

Besides, a direct relationship EDC and SEY coefficient can be obtained. This analysis can bring extremely valuable information about the nature of the electrons contributing to SEY at each primary energy. The treatments carried out in this thesis have been meant to decrease the electron emitting properties of the materials under study (and hence their SEY coefficient) and good understanding of the physical processes involved in SEY modification could be achieved by analyzing EDC spectra and comparing with SEY.

Experimental Details EDC measurements were carried out in the ESCA-Lab 210 (VGS) analysis set up at UAM Madrid (see Sec 5.2.3). The geometry of the system was favorable allowing to make use of the electron spectrometer simultaneously with the KIMBALL e^-gun. The e^-gun is set at fixed energy while the e^-beam impinges in the sample. the amount of SE's is much higher than the amount of backscattered electrons, due to this, elastic peaks in EDC spectra are very small, for this reason, the electron

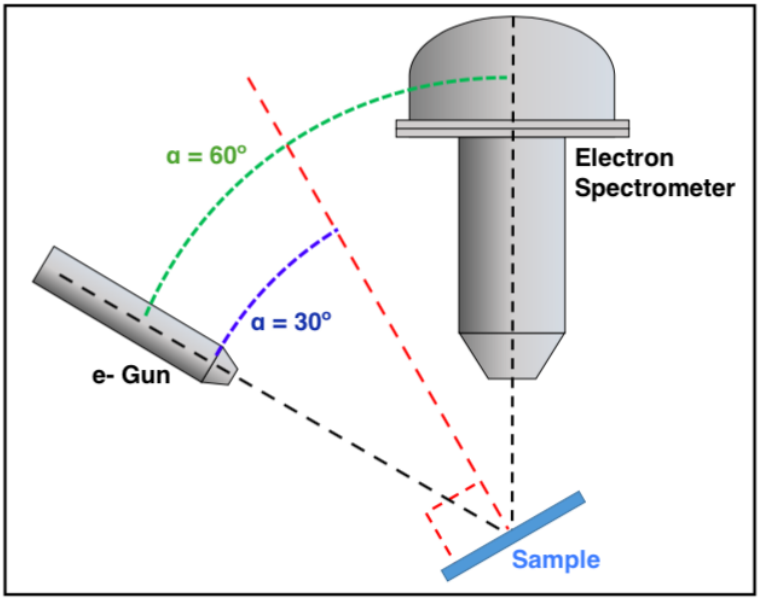

Figure 5.14: Schematics of the disposition and angular relation between e^- gun, sample and electron spectrometer used for EDC data acquisition.

analyzer was set in CRR mode (see Sec. 5.4.2). In CRR mode, the sensitivity of the spectrometer is proportional to the kinetic energy of the electrons, which makes the elastic peak to be amplified. However, when quantitative analysis is needed, and comparisons between spectra taken at different primary energies are needed, the spectrum signal must be corrected following the next formula.

$$I' = \frac{I}{E_{kinetic}} \tag{5.7}$$

Where $E_{Kinetic}$ is refered t the vacuum level, I is the measured intensity in CRR mode, and I' represents the intensity corrected. Primary electron energies were set between 100eV and 1keV.The same values of e-gun grid voltages, and source voltage used to measure SEY were applied for EDC measurements in order to obtain a similar electron beam, and operate under the same conditions. Since e^-gun and e^-analyzer positions are fixed, and it is only the sample holder which angular position can be freely changed, the relationship between the angle of incidence of the electrons, and the angle between the sample and analyzer (Fig. 5.14) is constrained by $\theta_{e^-gun} = 60° - \theta_{analyzer}$, hence for the sake of finding a compromise between both devices, a sample angle $\theta_{sample} = 30°$ was set, to obtain $\theta_{e^-gun} = \theta_{analyzer}$. As well as for SEY measurements, the sample was always connected to ground so that no charge effects are possible.

The accidental impact of analyzed electrons within the walls and lenses of the electron analyzer may originate new SE's within the same energy range of electrons emitted by the studied sample, in this case there would be two kind of secondaries, those emitted from the sample, and those generated within the analyzer, and the signal obtained would be the sum of both. This effect would carry the misrepresentation of the information as a consequence, since it would be impossible to differentiate between both kinds. For this reason, A negative bias voltage referenced to ground was applied to the sample so that spectra are shifted towards higher kinetic energies. By doing this, one can avoid the superposition of signals obtain an EDC spectrum of the sample under study free of systematic errors. One should always take into account the effect of electron conditioning, hence the acquisition time should be as low as possible so that the sample is not exposed to high scrubbing doses.

5.4.2 Photoemission Spectroscopies (PES)

Photoemission spectroscopies, (PES) include both core level and valence band surface-sensitive quantitative spectroscopy techniques based on the photoelectric processes. They are used to obtain information about the chemical composition, and chemical state of the elements present in the surface of the solid under study. Electromagnetic radiation penetrate into the solid reaching depths in the order of microns which is much greater than the inelastic mean free path of photoelectrons, this is why only electrons generated within the closer layers to the surface of the sample are emitted to the vacuum, being the depth sensibility of this technique not greater than 10 nm [134].

PES analysis require ultrahigh vacuum (UHV) conditions to be carried out. It is of critical importance to generate a high inelastic mean free path environment in order to avoid scattering of both electromagnetic radiation and photoelectrons. Also experimental equipments necessitate UHV to operate since they are composed of several filaments, anodes and electron analyzers which are very delicate and operation at pressures higher than the high vacuum range would expose them to irreparable damage. Minimization of chemical reactivity of the surface while data acquisition is another advantage that UHV environments bring to this technique.

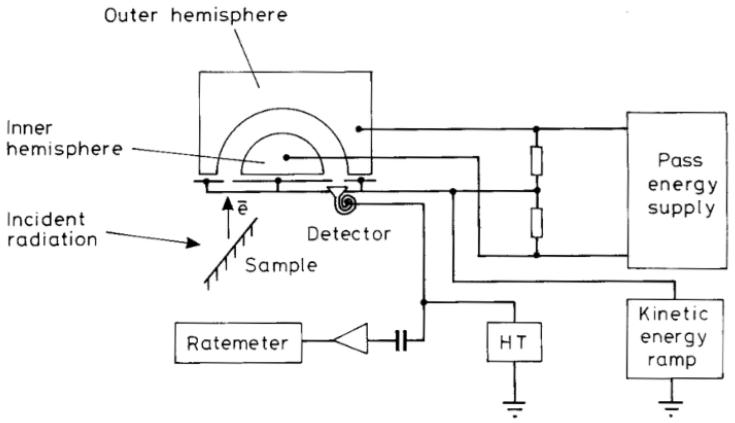

Figure 5.15: Schematic description of electron spectrometer used in this work.

Photoelectrons emitted from the sample must be collected and analyzed by an electron spectrometer, which would count the amount of electrons and analyze their energies. An electron spectrometer is an instrument used to allow the passage of only those electrons that have a given specific energy. In this thesis hemispherical deflection analyzers (HDA) were used. This analyzers consist on two metal hemispheres arranged in such a way that their centers are coincident, Fig. 5.15. By placing different voltages at each hemisphere an electric field is applied between the walls. Energetic electrons are injected into the gap between hemispheres through a slot which width can be adjusted in order to control the energy resolution and the amount of electrons reaching the gap between hemispheres. If the electrons are travelling very fast, they will impinge on the outer hemisphere. If they are travelling very slow, they will be attracted to the inner hemisphere. Hence only electrons in a narrow energy transmission function of gaussian-like shape, succeed in getting all the way round the hemispheres and make it to the detector. its central energy is known as pass energy. The spectral energy resolution is by geometry proporrtional to the pass energy, so that for small pass energies, more accurate values of the energy will be obtained but a small amount of electrons will be detected, diminishing then the intensity of the signal.

The lenses enable two operating modes - Constant Retardation Ratio (CRR), or Constant Analysis Energy (CAE).

When CRR operation mode is used, the electrons will be slowed down by an amount which is a constant ratio of the electron energy to be analyzed, i.e.

$$RR = \frac{E_k - \phi}{E_A} \approx \frac{E_k}{E_A} \tag{5.8}$$

Where E_k is the kinetic energy of the electrons refered to the Fermi level, E_A is the pass energy of the analyzer and ϕ is the WF of the electron analyzer. Throughout the scan range the pass energy of the analyzer is continuously varied to maintain a constant retard ratio, hence sensitivity is reduced at lower kinetic energies, since it is proportional to the pass energy. As a consequence, the intensity of the signal obtained depends on the kinetic energy of the electrons, as follows,

$$I' = I \cdot E_{kinetic} \tag{5.9}$$

Being I' the detected intensity, and I the intensity corresponding to the actual number of electrons emitted from the sample and entering the analyzer + lens system. The value of the constant retardation ratio can be chosen so that for lower values, the resolution of the spectrum obtained is decreased, and the intensity is increased.

When CAE operation mode is used, the retarding voltage is changed as kinetic energy of detected electrons varies so that the analyzer pass energy is kept constant, i.e.

$$E_p = (-q)k\Delta V \tag{5.10}$$

where q is the charge of the particle, the potential difference $\Delta V = V_{out} - V_{in}$ applied to the hemispheres, k is the calibration constant. The resolution obtained in CAE is constant throughout the whole kinetic energy range. Nevertheless the sensitivity, is inversely proportional to the kinetic energy and at lower kinetic energies is improved over that obtained with CRR. Even though the choice of weather work in CAE or CRR mode depend on the specific conditions and history of each experiment, CAE is typically used when energies in the range of 150-2000 eV of kinetic energy are to be analyzed, and CRR for kinetic energies within the range of 0-150 eV

5.4.2.1 X-ray Photoemission Spectroscopy (XPS)

X-Ray photoemission Spectroscopy, (XPS) is a surface-sensitive quantitative core level spectroscopy technique based on the photoelectric effect. Photoelectrons are excited from occupied states by incident X-rays. If the energy of the photons is larger than the binding energy of the electron, the excess energy is converted to kinetic energy of the emitted photoelectron. Since the incoming photon energy and the WF of the spectrometer are known, measurement of the kinetic energy via an electron analyzer makes it possible to calculate the binding energy. The equation describing the total energy conservation is writen as follows:

$$E_B = h\nu - E_K - \phi$$

Where $h\nu$ is the incident photon energy, E_B is the binding energy of the electron E_K is the kinetic energy of the emitted electron, andϕ is the WF of the sample. The electron analyzer will then scan the possible electron kinetic energies, and count the electrons detected for each energy providing a spectrum where electronic levels of the material are represented as peaks located at their corresponding binding energies, see Fig. 5.17. Photoemission peaks have the shape of a Lorentzian curve, with gaussian broadening due to instrumental factors, resulting in a combination of both curves. Usually they have asimetric shapes owing to plasmons or inelastic scattering.

The difference in electronegativity between two elements produces energetic displacements of the bounded electrons sharing the chemical bond and core levels. In XPS such displacement is manifested in a shift of the binding energy of the photoelectons called chemical shift, it ranges from 0.1 to 5 eV [135]and gives information about the chemical state of the element detected. As it can be observed in Fig. 5.17, the background signal of the spectra increases with binding energy, such phenomenon is due to the SE's generated by the inelastic collisions of the photoelectrons with the lattice in their path out of the solid. Different functions as those proposed by Shirley [136] and Tougaard [137] can be used to substract the background when performing quantitative analysis. The photoionization cross section, is given by the sensitivity factors which are tabulated from empirical values from each bound state of an element [138]. X-rays are generated by bombarding a metallic

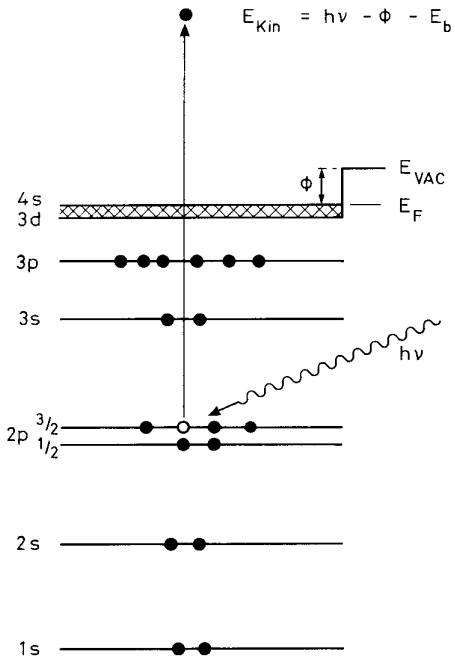

Figure 5.16: The electron transition involved in the photoemission of a $2p_{3/2}$ electron from Cu.

anode with high-energy electrons. In this case the energy of the emitted X-rays depends on the anode material, Mg and Al in our case, and beam intensity depends on the electron current striking the anode and its energy. Each anode emits non-monochromatic radiation being their main emission lines $E_{photon} = 1486.7$ eV for Al Kα X-rays, and $E_{photon} = 1253.6$ eV for Mg Kα X-rays. The atomic sensitivity factors depend on the energy of the excitation source, as well as on the incident angle, so that the radiation energy can be chosen depending on the requirements of the experiment. Appart from photoelectrons, signal derived from different physical process can also be detected by means of XPS. Among them there are shake-down and X-Ray satellites, ghost lines and Auger lines. The latter provide also relevant physical information of the studied sample. Auger effect is an electronic process resulting from the transitions between energy levels in an excited atom. Such an excitation is produced by the absorption of a photon in the case of XPS. Due to this excitation process the atom would reach an unstable state originated by the emission of an electron and the consequent hole generation. In order to reach the most stable state, the electrons of outer shells would de-excite and fill the core hole releasing an amount of energy equal to the difference between orbital energies. The energy released by this process can either result in the emission of a photon or be transmitted to another electron in an outer level that is emitted from the atom as a so-called Auger electron.

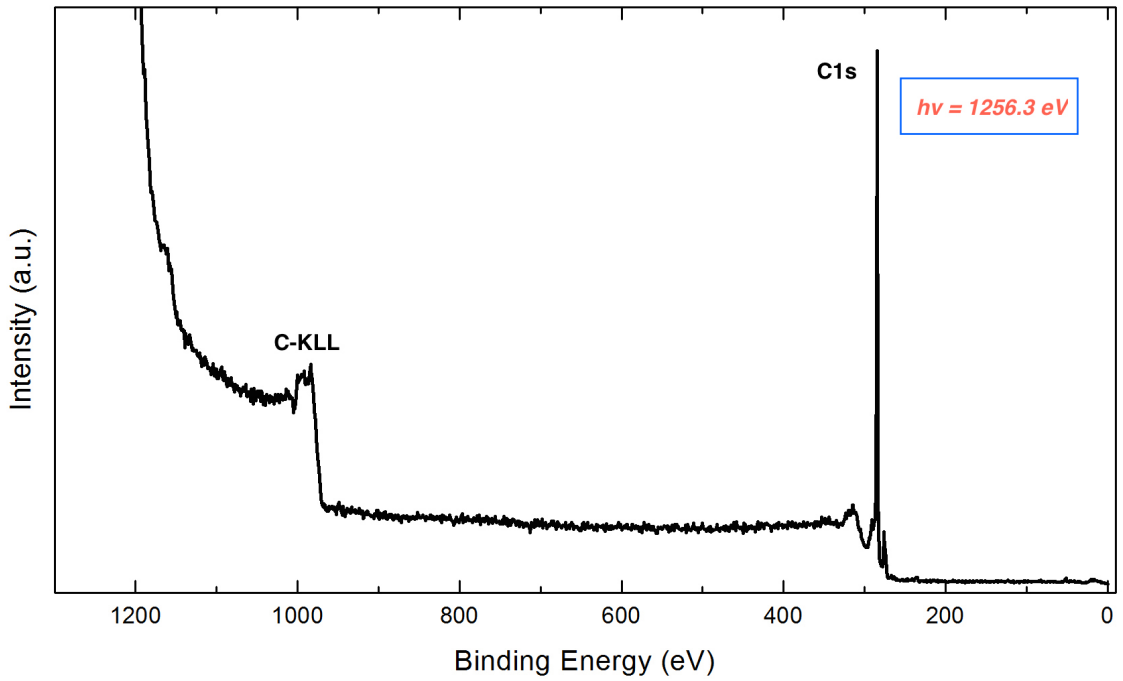

Figure 5.17: XPS survey spectrum measured on "as cleaved" HOPG during the development of this thesis. Both XPS C1s peak and XAES C-KLL are observable

More information about this commonly used technique can be found elswere [139]. In the following, aspects this technique of importance for this thesis performance will be presented.

Thickness quantification Apart from elemental detection and chemical state determination, XPS was used in this thesis to estimate the thickness of metallic thin layers deposited by means of magnetron sputtering techniques. Assuming a one layer material that has a constant and uniform and infinite thickness across the whole scanned area. The intensity of a peak corresponding to an infinitesimal slice is [139]:

$$d\Im = SNKexp\left(\frac{-x}{\lambda}\right)dx \tag{5.11}$$

where $\Im$ is the measured XPS intensity, S is the XPS sensitivity factor, N is the atomic concentration, λ is the inelastic mean free path (IMFP) of the photoelectrons traveling through the solid, and x is the depth from which those electrons are emitted from. In the presence of a homogenous overlayer of thickness d_{Thick}, covering the infinitely thick substrate, Eqn. 5.11 can be integrated to give

$$d\Im_{Layer} = \int_{d}^{Infty} SNKexp\left(\frac{-x}{\lambda}\right)dx = SNK\lambda_{Layer}\left[1 - exp\left(\frac{d}{\lambda_{Layer}}\right)\right] \tag{5.12}$$

$$d\Im_{Bulk} = \int_{0}^{d} SNKexp\left(\frac{-x}{\lambda}\right)dx = SNK\lambda_{Bulk}\left[1 - exp\left(\frac{d}{\lambda_{Bulk}}\right)\right] \tag{5.13}$$

hence after comparison of $\Im_{Layer}$ and $textfrakI_{Bulk}$ and making use of Eqns. 5.12 and 5.13, an estimation of the actual over-layer thickness is achievable. the accuracy of such estimation depends on the homogeinity and morphology of the over-layer.

Experimental Details The XPS measurements showed in this thesis were acquired at UAM and at LNF-INFN. in the equipments presented in Secs. 5.2.2 and 5.2.1. All spectra were taken in CAE mode. The surveys were aquired with a pass energy of 50 eV and a step of 1 eV, and the rest of the regions were aquired with a pass energy of 20 eV and a step of 0.5 eV. Mg (Kα = 1253.6 eV) anode was used for all the experiments

5.4.2.2 Ultraviolet Photoemission Spectroscopy (UPS)

Ultraviolet Photoelectron Spectroscopy (UPS) is the most powerful and versatile technique to study the electronic structure of the valence bands in atoms, solids and molecules, UPS can also be used to identify molecular species on surfaces by analyzing characteristic electron energies associated with the bonds of the molecules. In this technique, ultraviolet light is used to irradiate the sample and generate photoelectron processes. In this thesis ultraviolet Helium lamp was used, which could emit light at two energies; 21.2 eV, known as He I radiation, emitted from neutral atoms, and 40.8 eV, known as He II radiation, emitted by single ionized atoms. These lines were produced by cold cathode capillary discharge. They represent resonance fluorescence produced when the gas is excited in the discharge and then decays back to its ground state. Important differences exist between UPS and core electron photoemission spectroscopy such as XPS. As previously mentioned, the atomic sensitivity factors dependon the energy of the excitation source, hence for studying valence band states, low energy radiation, in the range of ultra-violet, are better suited than X-Ray sources, since the photoipnization cross-sections are higher and better resolutions can be

obtained. The energy of an electron in the solid depends on its momentum. Hence, by detecting photoelectrons emitted from a surface at different emission angles, the energy of the electrons as a function of the momentum vector may be determined. This process is known as "band mapping" and is a powerful probe of the electronic structure of crystalline materials. The measurements are usually to be compared with theoretical predictions.

Experimental Details UPS experiments were carried out at LNF-INFN in the set-up presented in Sec. 5.2.1. Photoelectrons were excited by the non monochromatic radiation of a HeII (40.8 eV), Spectra were acquired with an Omicron EA125 analyzer in CAE mode with a pass energy of 5 eV

5.4.3 RAMAN Spectroscopy

The content of this section is limited to offer a summary the theoretical background of this spectroscopic technique, oriented to the understanding of the results obtained in this thesis. More detailed information can be obtained elsewere [140, 141]. Raman spectroscopy is used to observe vibrational, rotational, and other low-frequency modes in a system [142]. It is based on the study of the inelastic or Raman scattering, of monochromatic light usually in the visible range of frequencies. Monocromatic radiation is usually obtained from a laser, which light interacts with molecular vibrations and phonons. Such interactions led to a shift in energy of the photons which gives information about the vibrational modes in the system. The resulting inelastically scattered photon which is emitted can be either of higher or lower energy than the incoming photon.

When the material absorbs energy and the emitted photon has a lower energy than the absorbed photon, the process is labeled as Stokes Raman scattering. On the other hand, If the material loses energy and the emitted photon has a higher energy than the absorbed photon, in this case the process is called anti-Stokes Raman scattering. It is important to notice that the energy difference between the absorbed and emitted photon is independent of the absolute energy of the photon, since it corresponds to the energy difference between two resonant states of the material. Raman shifts are reported in wavenumbers, which have units of inverse length (cm-1) and it can be expressed as

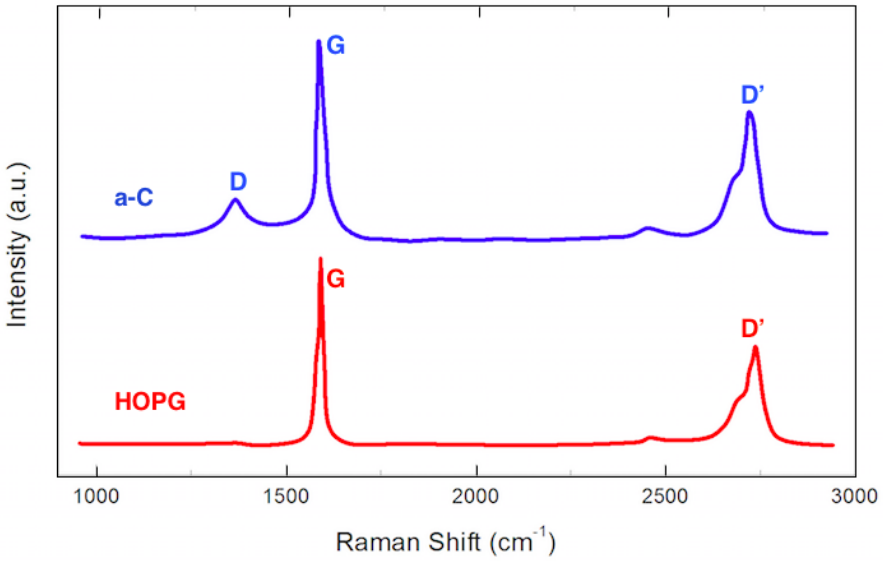

Figure 5.18: Raman spectra measured on "as cleaved" HOPG (red line) and atomically damaged amorphous carbon (blue line) obtained during development of this thesis.

$$\Delta w = \left(\frac{1}{\lambda_0} - \frac{1}{\lambda_1}\right) \tag{5.14}$$

where Δw is the Raman shift expressed in wavenumber, λ_0 is the excitation wavelength, and λ_1 is the Raman spectrum wavelength. Raman spectroscopy is an integral part of carbon based materials research, and provides insight into all sp2-bonded carbon allotropes. It is used to determine the number and orientation of layers, the quality and types of edge, and the effects of perturbations, such as electric and magnetic fields, strain, doping, disorder and functional groups. The Raman spectra oh highly oriented polycrystalline graphite (HOPG) is shown in Fig. 5.18 and it consist of a set of distinct peaks. The most characteristic peaks, namely G and D appear around 1580 and 1350 cm^{-1} respectively. The G peak corresponds to the E2g phonon at the Brillouin zone center. The D peak is due to the breathing modes of six-atom rings and requires a defect for its activation. It comes from transverse optical (TO) phonons around the K or K0 points in the first Brillouin zone.

The analysis of the D and G peak widths and their dispersions with excitation energy unambiguously discriminate between the two main stages of disordering incurred by such samples. We note that, by definition, our analysis only applies to defects able to activate the D peak in the Raman process. The G-band is the primary mode in graphite. It represents the sp2 configuration bonded, its position is independent of the excitation laser

frequency, and is a resonant band, which makes the intensity of peaks to be high. The position of the G-band is quite sensitive to doping and even very minor strain. The D-band is known as the disorder or defect band It is the result of a one phonon lattice vibrational process of the sp2 carbon rings. The band . The band is typically very weak in graphite. The intensity of the D-band is directly proportional to the level of defects in the sample. It shows a dispersive behavior, so there are a number of weak modes underlying this band and the choice of excitation laser energies will enhance different modes

Experimental Details The Raman spectra were measured ex-situ by using a Horiba XploRA Raman microscope system with a 100x objective at λ=532 nm. Low power was used to avoid heat induced sample damage or graphitization

5.4.4 Scanning Electron Microscopy (SEM)

Some of the techniques used for the study of the morphology of the coatings developed in this thesis were scanning electron microscopy (SEM), field emission scanning electron microscopy (FE-SEM), and energy dispersive X-ray spectroscopy (EDX). SEM and FE-SEM images are obtained through the signal of SE's emitted by the sample when its surface is bombarded by an electron beam at energies up to 30 keV. The electron beam is emitted by a hot filament through thermionic emission in the case of SEM. A more sophisticated technology is used in FE-SEM which allowed us to obtain high resolution images of the synthetized surfaces. In this case field a emission gun was used to produce a more coherent electron beam, smaller in diameter, and with a greater current density, which results in an better signal-to-noise ratio and spatial resolution than for SEM. A FE-SEM image of a nano-structure obtained in this thesis can be seen in Fig. 5.19. Electron microscopes generate two dimensional images of a sample surface, with a magnification as large as a few hundreds thousands 100,000X. However, these microscopes cannot measure the vertical dimension (z-direction) of the sample, the height (e.g. particles) or depth (e.g. holes, pits) of the surface features.

EDX is an analytical technique used for chemical characterization of a sample. When highly energetic electrons impact on a sample, the latter originate X-ray radiation characteristic

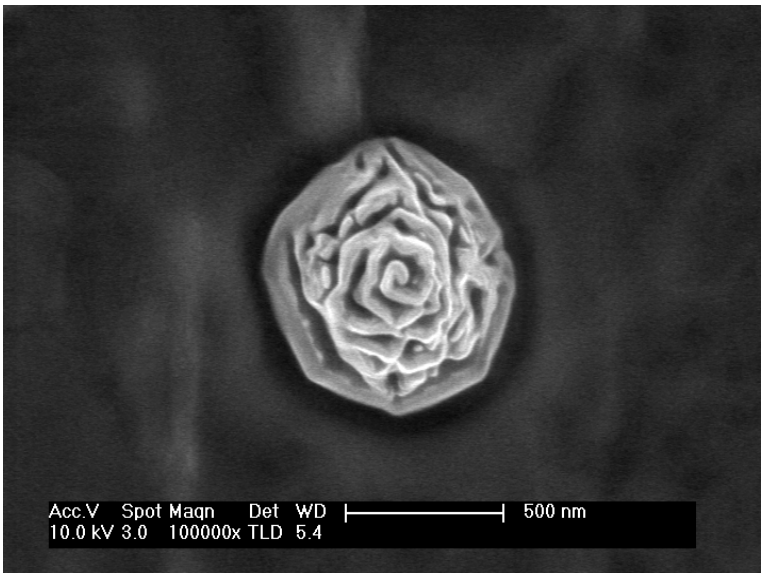

Figure 5.19: FE-SEM image of a rough silver coating obtained during the development of this thesis.

of the material, and by analyzing it, information about the chemical composition can be obtained. As a difference with photoemission spectroscopies, EDX is much less surface sensitive and gives information within a range of order of microns.

Experimental Details In this work SEM and FE-SEM microscopes from *Servicio Inter-Departamental de Investigacion* at UAM were used. SEM quipment is a scanning electron microscope *Hitachi S-3000N* With EDX analyzer from Oxford Instruments model INCA x-sight for sample exploration and EDX chemical composition. FE-SEM equipment is a Philips XL30 S-FEG Scanning Electron Microscope, with which we were able to observe structures of sites smaller than 20 nm.

5.4.5 Atomic Force Microscopy (AFM)

Also AFM techniques were used for the study of the surface morphology. AFM operation is based on the use of a tip of a few nanometers size located at the end of a cantilever, the tip, when attracted or repelled by the surface produces the deflection of the cantilever. This deflections are registered through a laser beam which is reflected at the extreme of the cantilever. The graphic of the position of the beam in the scanner, and the registered deflection by the laser produces a map formed by hills and valleys showing the morphology of the sample [143]. AFM microscopies work tapping the sample making the cantilever

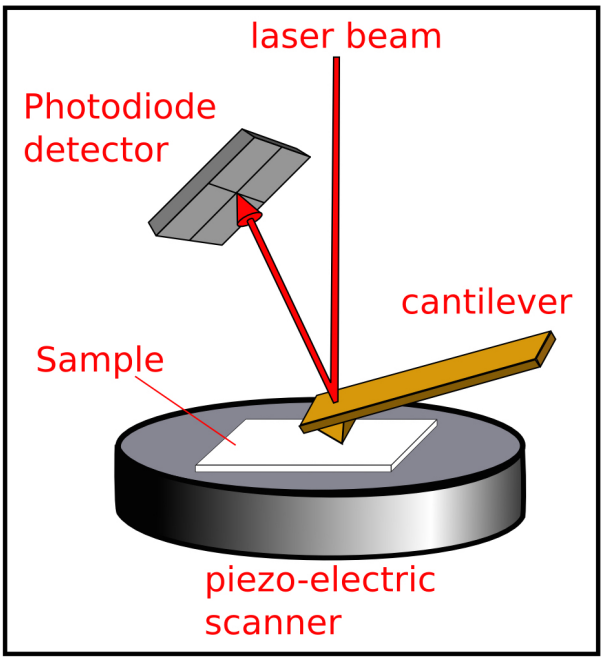

Figure 5.20: Schematic diagram of the operation of an Atomic Force Microscopy.

to oscillate, Fig. 5.20. The amplitude and frequency of this oscillations are registered and related with the topography of the sample. Once the tip is located manualy over the surface, the latter approximation is done automatically. A laser beam, a four quadrant photodiode, and the precise electronics, control the movements of flexion and torsion of the tip. During the scanning processes, vertical and horizontal movements of the sample are controlled by a cylindrical piezoelectric.

Unlike electronic microscopies, the measurement of an AFM is made in three dimensions, the horizontal X-Y plane and the vertical Z dimension. Resolution (magnification) at Z-direction is normally higher than X-Y. it is possible to image the surface topography with extremely high magnifications, up to 1,000,000X, comparable or even better than electronic microscopes

Experimental Details The measurements were obtained at the Istituto di Fotonica e Nanotecnologie del Consiglio Nazionale delle Ricerche (CNR-IFN) in Rome, using a AFM Veeco (Digital Instruments) D3100 with controller Nanoscope IIIa, in tapping mode.

Chapter 6

Surface Micro- and Nano-structuring of Technical Ag Plating by Ion Beam Techniques and SEE Properties

As explained in Sec. 4.3.3, the modification of the morphology of a surface, may result on important variations of the SE emitting properties of the treated material, being the reduction of the SEY parameters the most common effect when increasing roughness aspect ratio [21, 92, 114, 115]. In this chapter, observations of the SE's behavior under surface roughening conditions are presented, as well as a description of the strategies followed to achieve micro and nanostructure metallic surfaces under the aim of the SEY reduction and the consequent Multipactor effect avoidance.

6.1 Description of the samples

The experiments were performed on 10μm technical electrochemically silver plated Al samples manufactured by the company *TESAT Spacecom*. The same coating is applied on the technical RF satellite devices, described in Ch. 7, whose treatment and study will be the target of the ESA ITI project "Optimization of Surface Roughness of Anti-Multipactor Coatings for Low Insertion Losses and Secondary Emission Suppression for High Power RF Components in Satellite Systems" under whose framework this work has been carried

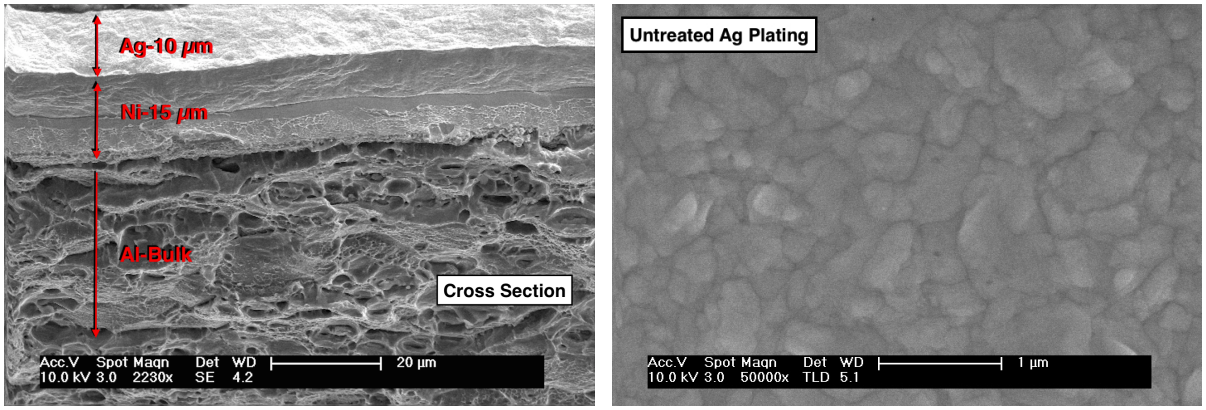

Figure 6.1: SEM images obtained from an untreated Witness**Left:** Cross section of the witness. Different layer forming the coating can be observed. **Right:** Surface morphology of the untreated witness.

out. The Ag coated Al samples have been denominated as *Witnesses*, since the knowledge obtained by their usage will be applied on the technical RF satellite devices, which are actually designed to be integrated in the correspondent satellite assembly. This fact makes possible the performance of Multipactor and IL measurements.

The cross section of a witness sample is shown in the left panel of Fig. 6.1. The sample was cutted into two halves by cryo-mechanical methods and SEM analysis showed the layered structure that form the witnesses samples. SEM analysis revealed an homogeneous 10μm thick Ag coating, which shows the accuracy of the Ag coating method used. EDX measurements performed on the cross section of the studied witness sample, brought to light the composition of each layer. As pictorially explained in the figure, the bulk of the sample is formed by Al, according to the specifications provided by the manufacturer. Besides a 15μm thick Ni layer was found located between the Al bulk and the Ag coating, which presence ensures an appropriate adherence of the Ag coating on the substrate [144].

SEM studies of the morphology of the Ag technical plating surface morphology, were also performed. The results, shown in Fig. 6.1, reveal a rather flat surface, formed by grains of different sizes characteristic of polycrystalline materials. The absence of pores is remarkable even at grain boundaries.

Fig. 6.2 show a comparison between SEY curves measured on untreated "as received" and atomically clean witness. The cleaning procedure consisted on repeated Ar^+ sputtering cycles of 1 h at 1.5 KeV in an Ar environment of $5x10^{-6}$ mbar. Surface cleanliness was determined by the absence of C and O signals in the XPS spectrum. A strong reduction

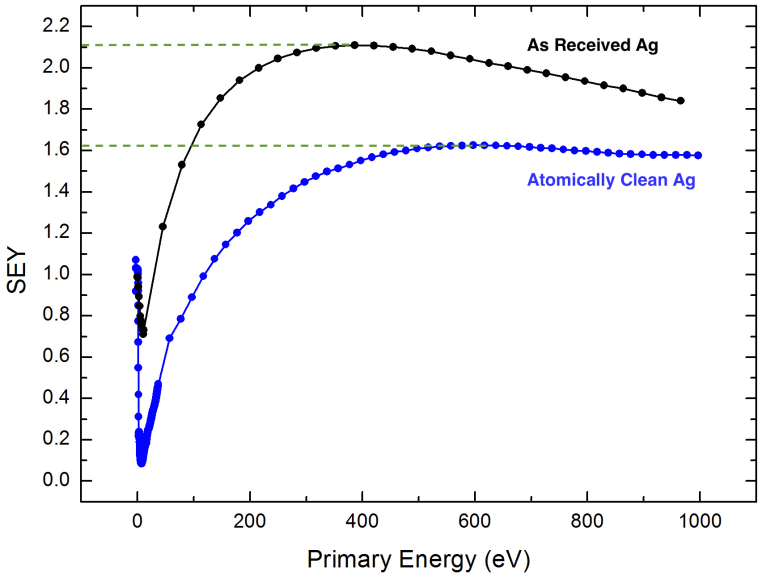

Figure 6.2: SEY measurements of untreated Witness "as received" (Black line) and after cleaning procedure (Blue line). Maximum values are marked with green dashed lines

of SEY is observed after surface cleaning, in good agreement with previous observations [39, 145]. However, all the SE studies of the samples after surface treatments were carried out under air exposed "as received" conditions, since those are in fact the conditions of interests for industrial applications, in which treated devices are exposed to atmospheric conditions for variable periods of time before satellite launch.

6.2 Effect of Ion Bombardment on Technical Ag Plating

Ion Beam Sputtering has revealed itself as a powerful technique to induce nano-structured surface morphologies [146, 147]. Resulting nano-structures are often produced in rather short processing times and, depending on the ion source capabilities, over relatively large areas, for a wide range of materials such as metals, being the latter in the scope of this thesis. In order to develop an appropriate strategy to achieve the desired nanostructured surface on technical Ag plating, the effect of 900 eV ion bombardment (see Table. 6.1) on technical Ag plating was studied by means of SEM which results are shown in Fig. 6.3. As previously described in Sec. 5.2.3 the kauffman ion gun is installed in such a way that ions bombard the sample at normal incidence. SEM analysis reveal the formation of isolated and disordered ripple-like formations due to ion bombardment. Unfortunately, quantitative studies of the aspect ratio were not achievable, however visual inspection reveal

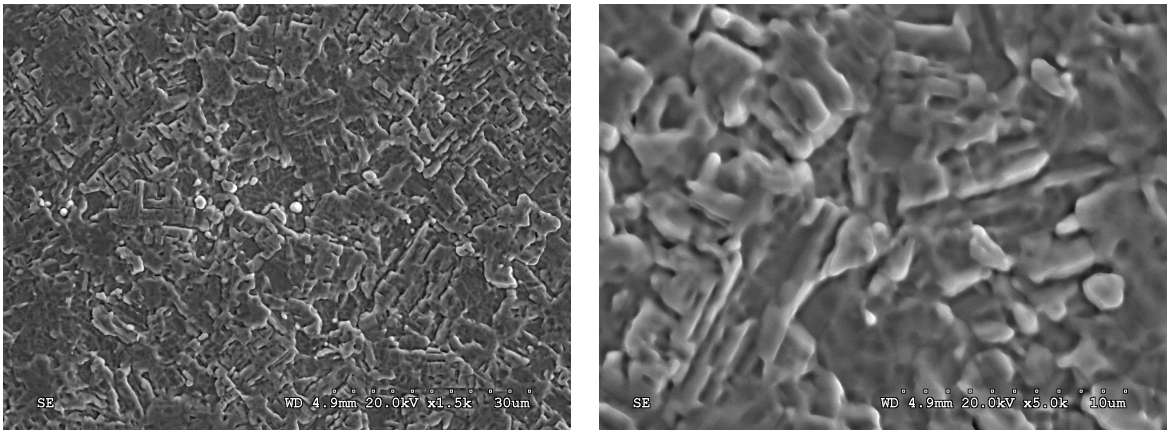

Figure 6.3: SEM images obtained from technical Ag coating suputtered at normal incidence, SEM analysis was carried out at a magnification of x4K and X15K.

that, despite a clear increase in the sharpness of the structure with respect the untreated sample due to the ripple-like structure formed, the absence of pores is remarkable even at grain boundaries, as it was the case for the untreated Ag technical plating presented in the right panel of Fig. 6.1.

Previous studies performed on monocristallyne Si revealed that low energy (E<10keV) ion bombardment at normal incidence do not produce remarkable surface morphology, remaining surfaces flat as the atoms are sputtered [148–151] . As the glazing angles increase, close packed ripple-like structures appear. This however seems to be in clear contradiction with the results shown in Fig 6.3. Nevertheless it is worth noticing the important role of the polycrystalline nature of the Ag technical coating in the ion induced erosion phenomena. Previous published studies [152–154] reported a remarkable dependance of the sputtering yield on the different orientations of the crystalographic domains, thus the structure observed is ascribed to the polycristalline nature of the plating and the preferential ion etching resulting from it [152].

Anti-Multipactor surfaces, for which multipactor discharge effects were completely mitigated, were performed prior to the work related to this thesis at UAM, [92]. According to such results Multipactor effect mitigation was achieved due to high aspect ratio surface morphology in the range of microns which acts as a multi-Faraday cage for the incoming electrons, resulting in a overall electron suppression effect. For this reasons, since differential sputtering due to the polycristalline nature of the technical Ag coating did not reveal

the formation of high aspect ratio porous surfaces, it was assumed to be insufficient for multipactor purposses and more sophisticated techniques are demanded.

	Beam Energy (eV)	Beam Current (mA)	Ar Pressure (mbar)	Δt (sec)
Normal Incidence Sputtering	900	20	$3.82{\cdot}10^{-3}$	1200

Table 6.1: Ion gun, pressure and time parameters used during the sputtering procedure.

6.3 Surface Treatment: Masked Ion Etching

The strategies followed in this thesis to obtain anti-Multipactor rough coatings were inspired in the preferential ion etching [146, 155–157] of a surface due to strong differences in the sputtering yield of different materials composing the samples under treatment. In all the cases, an Ar^+ ion beam of sufficient energy etches the surface of the Ag coated sample while Ti atoms (of lower sputtering yield) are simultaneously deposited over the surface and thus supposedly constituting an etching mask. Left panel of Fig. 6.4 shows the calculated sputtering yield of Ag, Au, and Ti, for Ar^+ ion energies ranging from 0 to 1000 eV based on empirical equations for sputter yields at normal incidence as presented in [158]. The figure clearly shows that, approximately 6 Ag atoms are sputtered for each one of Ti. As pictorially explained in the right panel of Fig. 6.4, in a simple approach of first order approximate explanation, the deposited Ti would randomly form separated islands which would protect the Ag substrate form being eroded by the ion beam. However, it is known that under those conditions, there are several other physical mechanisms apart from sputtering which produce mass flow leading to varied surface morphologies depending on different parameters of the process.

It was an important disadvantage that our particular case (a "soft" heavy substarte and a "hard" light mask, seed, surfactant or impurity) had scientifically not been studied; our research needed to move into new experimental specialized areas, and there was no sufficient time to perform the necessary experiments to clarify the influence of the different parameters or conditions of the process on the resulting surface roughness. Instead of exploring a range of values for each parameter, approximate optimization was obtained by a "trial and error method", by moving towards the optimum values. This has represented

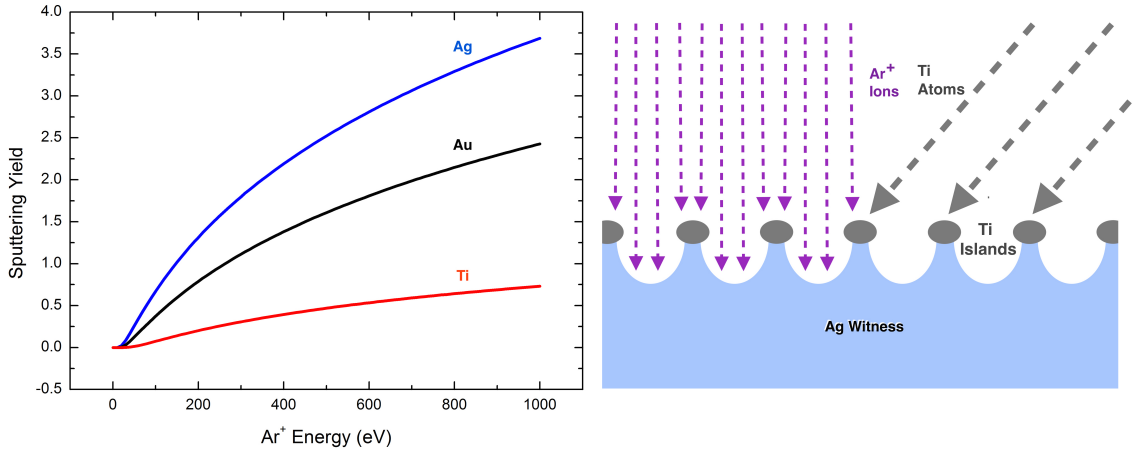

Figure 6.4: **Left:** sputtering yields of Ag (Blue line), Au (Black line), and Ti (Red line) for Ar^+ ions in the energy range form 0 to 1000eV . **Right:** Schematic description of the preferential ion etching and shadowing effects produced by Ti masking.

much more work than expected or planned. The witnesses treatment procedure is explained in detail in Appendix A

Each coating was applied simultaneously on two similar Ag witness samples. The morphology of the obtained coatings was studied by means of SEM microscopy. As it is well known, only a 2D quantitative study of the morphology of the structure can only be obtained, for this reasons, in order to obtain information about the depth of possible grooves and pores, the sample was cutted into two halves by using mechanical methods and explored from an angle perpendicular to the cross section, as previously explained in Sec. 6.1 and Fig. 6.1. Unlike SEM, AFM provides quantitative information about the depth of the the pores and grooves that form the surface under study, unfortunately, the morphologies obtained in this work were formed by structures too sharp and pores too deep to be measured by AFM. SEM analysis of the resulted samples are presented in the following subsections.

6.3.1 Titanium Cone Technique

A Ti truncated cone sputtering target is used during the performance of this technique as a source of Ti in order to achieve preferential ion etching [146, 155–157]. This experimental arrangement was first developed for the same purpose (low-SEY coatings) by Curren et al in the 1985-95 decade at NASA [159]. The technique is based on the simultaneous sputtering of both the Ti of the walls of the cone and the sample under treatment by the same ion

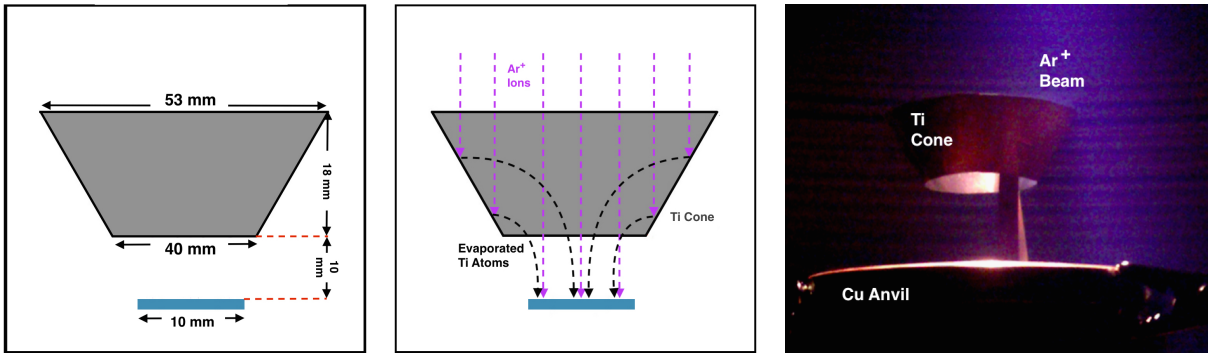

Figure 6.5: **Left:** Ti cone geometrical description and disposition. **Center:** Schematic description of the simultaneous Ag ion etching and Ti sputtering in the Ti cone technique configuration. **Right:** Photo of theactuall Ti cone used in this technique. The cone is misaligned in order to appreciate the ion beam and its interaction with the cone.

beam as shown in the central panel of Fig. 6.5. Under this conditions, special care must be taken in order to find the perfect balance between beam current beam energy and cone dimensions in order to obtain the adequate J_{Ion}/J_{Ti} ratio on the treated sample and hence produce the desired surface morphology. Many parameters regarding beam current, beam energy and cone shape and size play a crucial role and are to be optimized when using this technique, for that reason intensive trials were developed in order to find the needed conditions. The optimal ion gun working parameters were found to be *Ion Beam Current* = 20 mA and *Ion Beam Energy* = 900 eV, which according to the analysis performed in Sec. 5.3.1.2 generates ion beam with a gaussian current distribution which FWHM ranges between 70 and 90 mm. It is important to remind that the ion beam current value does not represent the actual current applied on the surface but an orientate value measured at the accelerating grids of the gun. The optimum geometry and disposition of the cone was also found. A geometrical description of the cone-sample conjunct is graphically presented in the left panel of Fig. 6.5.

For its build up a 0.1 mm thick 99.999% pure Ti foil was used. The whole cone has a surface of 29 cm^2, the areas of both apertures are 38.5 mm^2 and 12.5 mm^2. According to the estimated value of the gaussian FWHM of the ion beam, it was assumed that the beam interacted with the whole area of the Ti cone, while a 32 % passed trhough the smaller apperture reaching the substrate without obstaculzation. The Ti cone is located at a height of ∼1 cm with respect the sample. A photo of the actual cone used to treat the samples here presented is shown in the right panel of Fig. 6.5. In order to be able to observe the ion beam and the shadowing effect resulting from the interaction of the beam and the cone,

the later was misaligned with respect the ion beam center. When the sample and the cone are adequately located inside the chamber, and the desired pressure has been obtained, the ion gun is then set on, rising slowly current and energy until the desired values of beam current and beam energy are reached, while watching electrical leakage in grids. Once the kauffman ion gun parameters are set, platform shutter is set off and processing time starts. During the process all the parameters, pressure, ion current, ion energy intensively watched and readjusted if needed in order to keep steady values. When the procedure is finished, sample platform shutter is set on again and the ion gun is set off. The sample is then maintained in vacuum for 24 hours in order to let ensure a complete cooling down of the sample. Only 2 coatings, *W-1* and *W-2*, prepared by using this technique are here presented.

6.3.1.1 Coating *W-1*

The morphology of the surface of Coating *W-1* after the Ion etch masking treatment and the ion gun parameters set during the procedure are presented in Fig. 6.6 and Table 6.2 respectively. The two figures in the upper panel of the figure were obtained at normal incidence while the two figures in the lower panel were obtained at a glazing angle of 30°.

A roughness formed by elongated grains of is observed. The protuberant grains are separated from one another an estimated average distance of ~ 0.3 μm by small chasms. These protuberances, appear bunching together in clusters of sizes ~ 10 μm, forming a second order coarser roughness also of high aspect ratio. Such behavior seem to be the result of lateral coalescence of conical grains. Which result on a large inhomogeneity in the surface density of those clusters producing microscopic different shades or variations of darkness. According to the bottom panels of Fig. 6.6, the height of the clusters has been estimated to range between 10 and 20 μm

	Beam Energy (eV)	Beam Current (mA)	Ar Pressure (mbar)	Δt (sec)
Masked Ion Etching	900	20	$3.82{\cdot}10^{-3}$	1200

Table 6.2: Ion gun, pressure and time parameters used during the ion etch masking procedure of *W-1*.

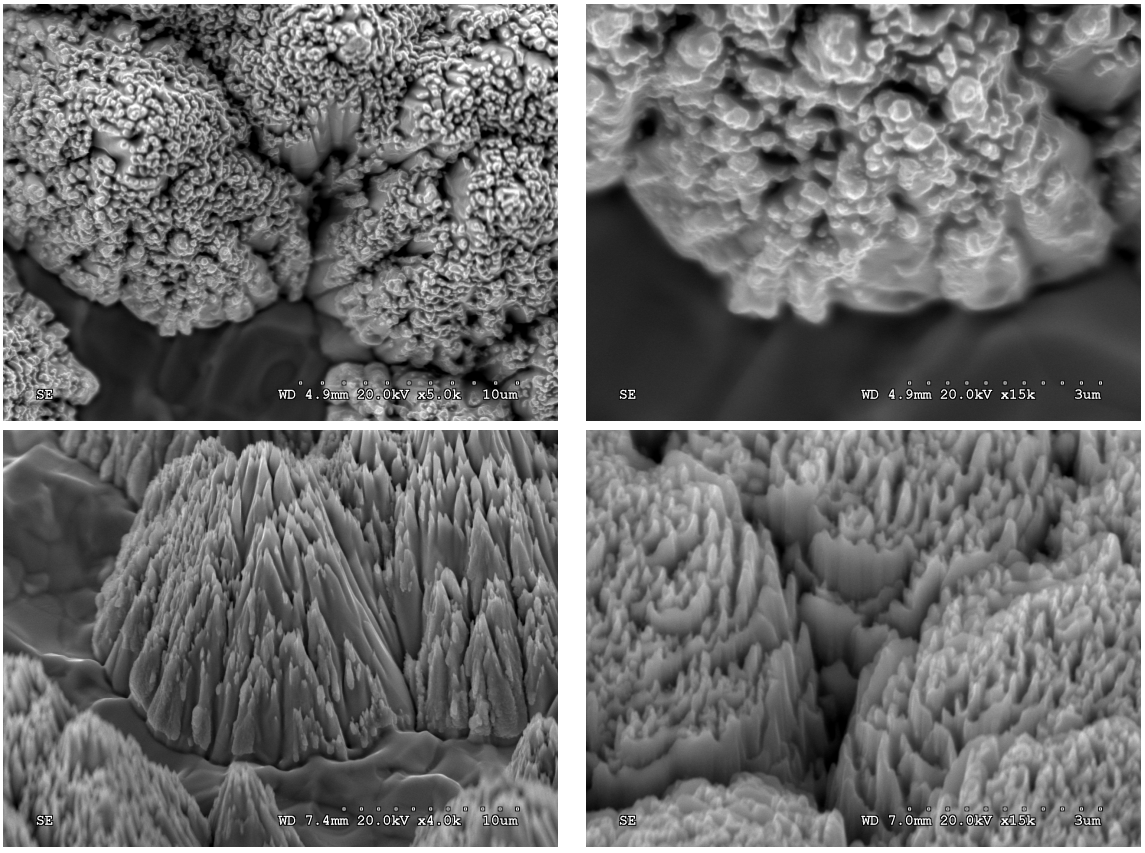

Figure 6.6: **Upper panel:** SEM images obtained from Coating *W-1* at normal incidence, SEM analysis was carried out at a magnification of x4K and x15K. **Right:** SEM images obtained from Coating *W-1* from an angle of 30° with respect the normal incidence. SEM analysis was carried out at a magnification of x4K and x15K.

6.3.1.2 Coating *W-2*

The same Ti cone technique, under the same ion beam parameters was applied on Coating *W-2*. in this ocasion, the deposition time was reduced from 1200 sec to 900 sec. The morphology of the surface of Coating *W-2* after the ion etch masking treatment and the ion gun parameters set during the procedure are shown in Fig. 6.7 and Table 6.3 respectively. The same roughness formed by elongated grains with average separation distance ~ 0.3 μm observed in Coating *W-1* is also present. However, in this case, due to a reduction in the time of exposure, these elongated grains do not appear bunching together in clusters and unlike for Coating *W-1* a second order roughness is not formed, which result on a highly homogeneous surface.

SEY results of both samples are presented in Sec. 6.17. Briefly, The SEE of Coating *W-1* was dramatically reduced to values of SEY_{max} below 1, while the reduction was smaller for Coating *W-2*. Such difference was ascribed to the large aspect ratio of the coarser second

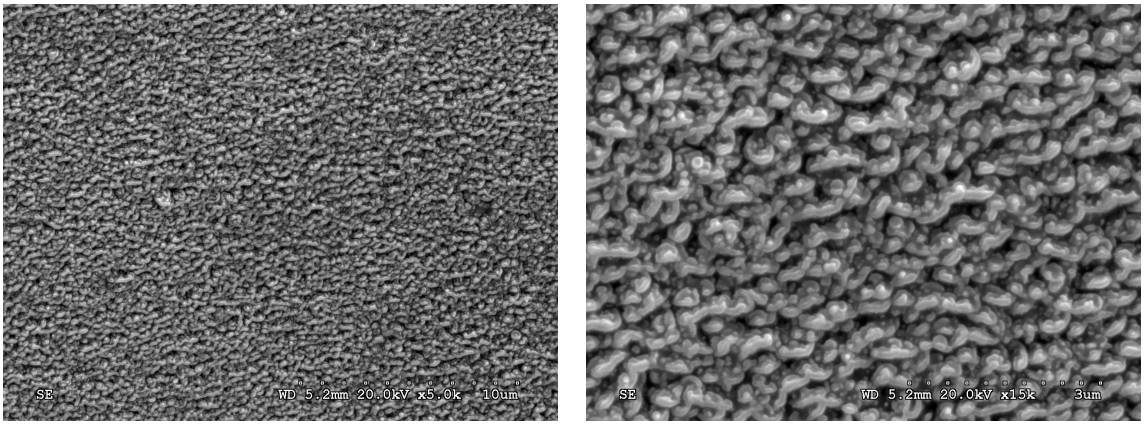

Figure 6.7: SEM images obtained from Coating *W-2* at normal incidence, SEM analysis was carried out at a magnification of x4K and X15K.

	Beam Energy (eV)	Beam Current (mA)	Ar Pressure (mbar)	Δt (sec)
Masked Ion Etching	900	20	$3.82{\cdot}10^{-3}$	900

Table 6.3: Ion gun, pressure and time parameters used during the ion etch masking procedure of *W-2*.

order roughness of Coating *W-1*, which impedes the scape of SEs, in a more efficient way than the smaller sized roughness of which Coating *W-2* is uniquely composed. However, despite the extremely low SEY results obtained for Coating *W-1*, which constitute a very convenient anti-Mutipactor property, according to the results obtained in previous projects [92] the IL are expected to be high, due to the large sizes of the second order roughness clusters (see Sec.7.1.1).

For this reason, the work carried out in this thesis aimed to the development of more homogeneous surfaces as it is the case of Coating *W-2*, whose reduction of SEY is still remarkable, and IL are expected to be lower than those for coatings similar to Coating *W-1*.

6.3.2 Magnetron Sputtering Assisted Technique

A RF magnetron sputtering head was used during the development of this technique as a source of Ti. Unlike for the Ti cone technique, the amount of Ti atoms reaching the sample surface can be controlled by varying the magnetron power used n the sputtering deposition, while independently, ion flux and energy can be set. This results in a higher versatility of the method which allowed to obtain different morphologies in a wide range of shapes and sizes, the most relevant shown in the following subsections.

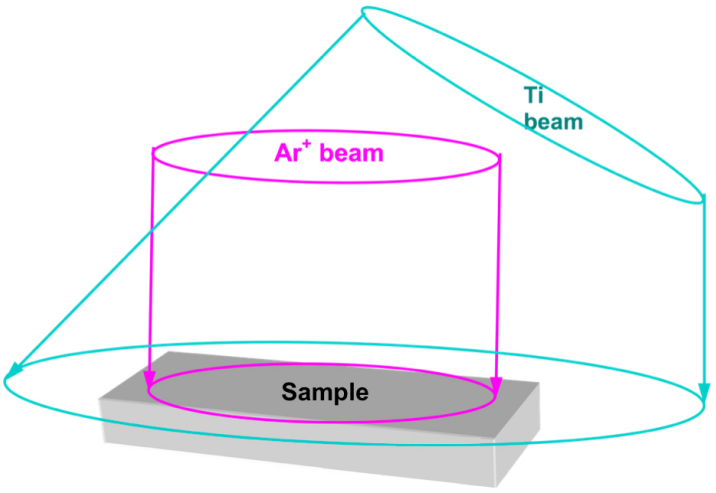

Figure 6.8: Schematic description of the geometrical disposition of the ion assisted magnetron sputtering technique.

A schematic description of the geometry of this technique is shown in Fig. 6.8. As previously explained in Sec. 5.2.3 the magnetron sputtering head is located in such a way that Ti atoms reach the surface with an incidence glazing angle of 35.5 °, while the incidence of the Ar^+ ions remained perpendicular to the surface. Being the operation pressure range of the kauffman ion gun limited at 10^{-3} mbar, and the the operation pressure range of the magnetron sputtering head ranging between 10^{-4} and 10^{-2} mbar, the simultaneous operation of both plasma based devices was possible to carry out at an Ar pressure of 3-4x10^{-3} mbar. The same pumping speed used for the Ti cone technique was maintained. Some related works were found in which masked co-deposition techniques were used to achieve nano-structured morphologies [146, 155–157, 160, 161]. However, this improved experimental arrangements, were RF magnetron sputtering is used for a more controllable preferential sputtering technique for surface nano-structuring, is for our knowledge, original of this Thesis.

A total of 3 coatings, *W*-3, *W*-4 and *W*-5, performed by using this technique are here presented. Each coating was applied simultaneously on two similar Ag witness samples. SEM analysis of the resulted samples are presented in the following subsections.

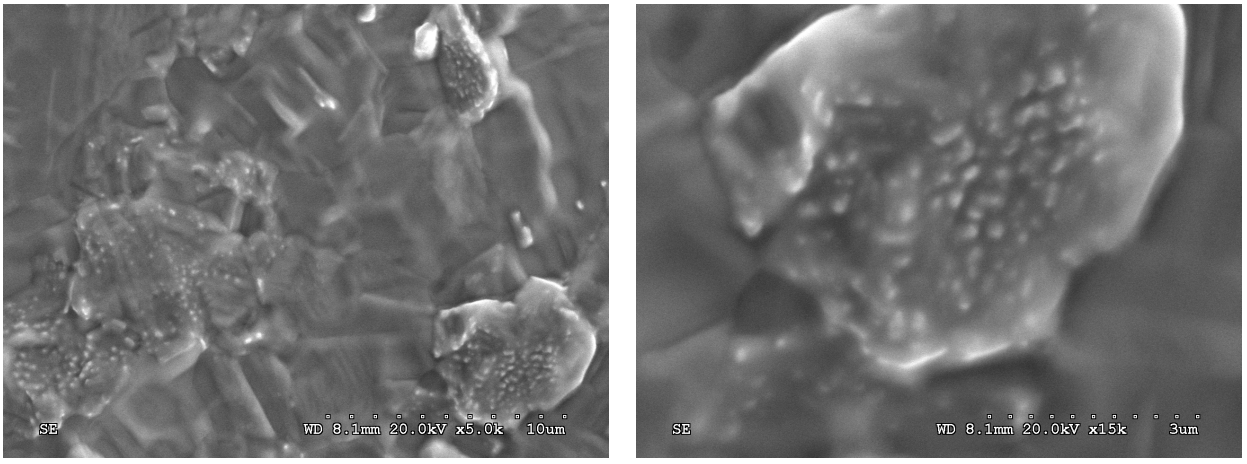

Figure 6.9: SEM images obtained from Coating *W-3* at normal incidence, SEM analysis was carried out at a magnification of x4K and x15K. **Table:** Ion gun, magnetron sputtering, pressure and time parameters used during the ion etch masking procedure.

	Beam Energy (eV)	Beam Current (mA)	Magnetron Power (W)	Ar Pressure (mbar)	Δt (sec)
Masked Ion Etching	900	20	80	$3.82{\cdot}10^{-3}$	900

Table 6.4: Ion gun, magnetron sputtering, pressure and time parameters used during the ion etch masking procedure of *W-3*.

6.3.2.1 Coating *W-3*

The morphology of the surface of Sample W-3 after the Ion etch masking treatment, as well as the ion gun and magnetron sputtering parameters set during the procedure are shown in Fig. 6.9 and Table. 6.4 respectively. The same ion gun parameters used for Coating *W-2* during the same period of time were set for the performance of Coating *W-3*, The figures exhibits a surface characterized by a low aspect ratio surface, typical of polycristalline ion bombarded technical Ag plating shown in Fig. 6.3. In the right panel of Fig. 6.9 a scarce amount of soft shaped rounded protuberances can be seen, revealing that no significant roughness was obtained after the treatment.

This could be explained by an insufficient dose (fluence) of Ti relative to the Ar ion one, hence the consequent strong ion erosion brought out the initial roughness due to the poly-crystalline structure. In some regions however, Ti dose was just right to initiate the growth of grains or protuberances which are supposed to grow into conical shape.

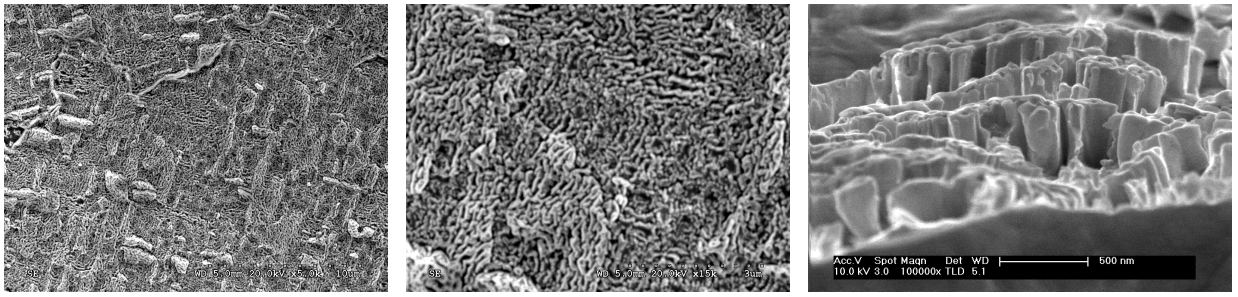

Figure 6.10: **Left:** SEM images obtained from Coating *W-4*.**Left** and **Center:** At normal incidence and magnification of x4K (Left) and x14K (Center). **Right:** SEM images of a 90° cross section of Coating W-4.

	Beam Energy (eV)	Beam Current (mA)	Magnetron Power (W)	Ar Pressure (mbar)	Δt (sec)
Masked Ion Etching	900	20	125	$3.82{\cdot}10^{-3}$	900

Table 6.5: Ion gun, magnetron sputtering, pressure and time parameters used during the coating of *W-4*.

6.3.2.2 Coating *W-4*

In order to increase the amount of deposited Ti and to favour the formation of rough coatings, the sputtering magnetron power was increased from 80 to 125 W during the deposition procedure of Coating *W-4*, avoiding the lack of rough structure due to an excess of ions obtained on Coating *W-3*. The morphology of the surface of Coating *W-3* after the Ion etch masking treatment, as well as the ion gun and magnetron sputtering parameters set during the procedure are presented in Fig. 6.10 and Table 6.5 respectively.

The surface exhibits in this case a micro-patterned rough surface characterized by elongated curly structures, separated by pores of an average pore area of about 0.11 μm^2 (see Table. 6.6). After SEE analysis was carried out, the samples were cut by means of cryo-mecanical procedures in order to analyze the cross sections of the obtained structure.

The SEM analysis of the cross section of Coating *W-4* is shown in the right panel of Fig. 6.10 which revealed an average pore depth of 390 ± 25 nm. The free proffesional software *ImageJ* was used to analyze the rough surfaces. By using the *Threshold* tool [162], one can automatically or interactively set lower and upper color threshold values, segmenting grayscale images into features of interest and background, and hence obtain valuable information about the shape and size of the features of interest. Fig. 6.11 shows the result of applying the *Threshold* tool on Coating *W-4*. Once the color threshold has been set correctly, the image is composed by two colors uniquely i.e. black and white, and then the desire analysis on the shape and size of the structures of each color can be carried

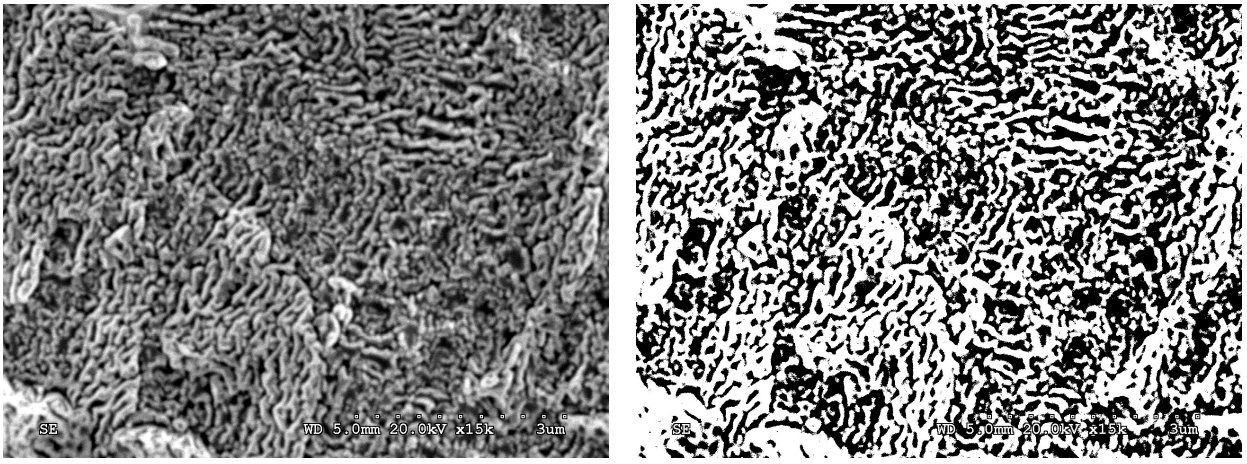

Figure 6.11: **Left:** SEM images obtained from Coating *W-4* at normal incidence and magnification of x14K. **Right:**SEM images obtained from Coating *W-4* at normal incidence and magnification of x14K after threshold color analysis.

	Pore Density (Pore/μm^2)	Porosity %	Average Pore Area (μm^2)	Max Pore Area (μm^2)	Min Pore Area (μm^2)
W-4	4.5 $\pm$ 0.2	52 $\pm$ 3	0.110 $\pm$ 0.005	2.2 $\pm$ 0.1	0.0020 $\pm$ 0.0001

Table 6.6: Summary of the values obtained after analysis of the morphology of the surface by means of the threshold color technique on Coating *W-4*

out. The numerical results obtained after *Threshold* color analysis are shown in Table. 6.6. After repeated measurements, the accuracy of this method has been estimated to be 5% of the measured value.

The micro-patterned structure observed in the left and central panels of Fig. 6.10, appears overimpressed on a typical morphology of polycristalline ion bombarded technical Ag plating as shown in Fig. 6.3 across the whole surface, such composition reveal a double surface pattering effect on the treated sample in which preferential sputtering takes place due to; i) due to the masking effect of the deposited Ti [155–157], and ii) due to the polycristalline nature of the technical Ag plating [152–154], which results on a second order coarser structure.

This effect was ascribed as well as for Coating *W-3* to an excess of ion dose applied on the sample, hence by reducing the beam current of the ion gun, the second order behavior of the formations due to crystalline preferential ion etching is expected to be mitigated. Unlike for Coating *W-1*, the second order structure constitutes a low aspect ratio roughness whose effect on the surface resistivity of the samples is expected to be negligible comparing to that for Coating *W-1*. Nevertheless, an improvement in homogeneity is desirable in order

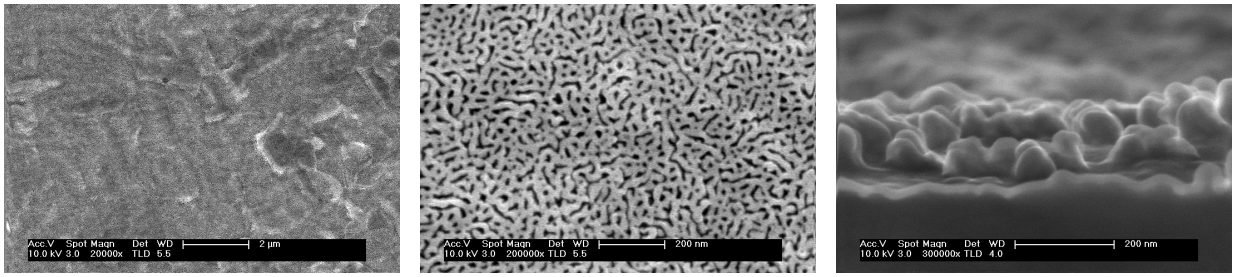

Figure 6.12: **Left:** SEM images obtained from Coating *W-5* at normal incidence and magnification of x4K. **Center:** SEM images obtained from Coating *W-5* at normal incidence and magnification of x14K.

to obtain a rough coating which, when applied to RF satellite waveguide components, the IL enhanced by the surface structure are reduced to its minimum.

6.3.2.3 Coating *W-5*

In order to obtain a rough surface more homogeneous than those previously presented, the beam current was reduced from 20 mA to 15 mA, keeping magnetron power at 125 W as used for Coating *W-4*. The morphology of the surface of Coating *W-3* after the Ion etch masking treatment, as well as the ion gun and magnetron sputtering parameters set during the procedure are presented in Fig. 6.12 and Table. 6.7 respectively.

Once again similarly to the results shown in the left and central panels of Fig. 6.10 of Coating *W-4*, the low aspect ratio morphology typical of polycristalline ion bombarded technical Ag plating as shown in Fig. 6.3 is observed as a second order coarser structure. Nevertheless, the surface exhibits in this case a nano-patterned rough surface characterized by close packed pores of an average area of 440 $\pm$ 44 nm^2 (see Table. 6.8), much smaller than that of Coating *W-4* as revealed after color threshold treatment of the SEM image shown in Fig. 6.13. After SEE analysis was carried out, the samples were cut by means of cryo-mecanical procedures in order to analyze the cross sections of the obtained structure. The SEM analysis of the cross section of Coating *W-5* is shown in the right panel of Fig. 6.12 which revealed an average pore depth of 65 $\pm$ 7 nm. The numerical results obtained after Threshold color analysis are exposed in Table. 6.8

The porosity of Coating *W*-5 has been estimated to range between the 26% and 34% of the total area analyzed, while for Coating *W-4* this value ranges between 42 % and 53%, revealing a lower probability of incoming primary electrons to penetrate into the pores for

	Beam Energy (eV)	Beam Current (mA)	Magnetron Power (W)	Ar Pressure (mbar)	Δt (sec)
Masked Ion Etching	900	15	125	$3.82{\cdot}10^{-3}$	900

Table 6.7: Ion gun, magnetron sputtering, pressure and time parameters used during the coating of *W-5*.

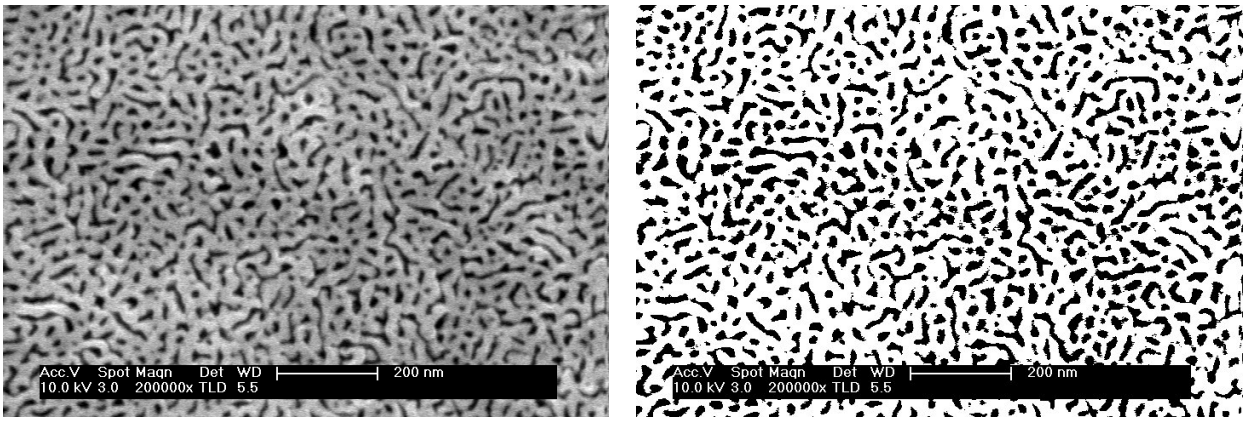

Figure 6.13: **Left:** SEM images obtained from Coating *W-5* at normal incidence and magnification of x14K. **Right:**SEM images obtained from Coating *W-5* at normal incidence and magnification of x14K after threshold color analysis.

	Pore Density (Pore/μm^2)	Porosity %	Average Pore Area (nm^2)	Max Pore Area (nm^2)	Min Pore Area (nm^2)
W-5	743 ± 35	30 ± 2	436 ± 21	1222 ± 60	22 ± 1

Table 6.8: Summary of the values obtained after analysis of the morphology of the surface by means of the threshold color technique on Coating *W-5*

	Typical Pore Size			Min	Max	Porosity
	Width (nm)	Length (nm)	Depth (nm)	Aspect Ratio	Aspect Ratio	%
W-4	100 ± 5	600 ± 60	350 ± 35	1.0 ± 0.1	3.5 ± 0.3	50 ± 5
W-5	15 ± 0.7	30 ± 2	70 ± 4	2.0 ± 0.1	4.5 ± 0.2	30 ± 2

Table 6.9: Pore size analysis of Coatings *W-4* and *W-5*

the former, and hence, the reduction of SEY is expected to be lower for Coating *W-5* than for Coating *W-4*. Also the average pore depth of Coating *W-5* was reduced to the 16% of the value of Coating *W-5*.

A dramatic reduction of the average pore area was observed for Coating *W-5* comparing to Coating *W-4*, being the area of the later $\sim$ 250 times larger than that for the former leading to a larger number of pores per unit area for the former surface.

The studies revealed an aspect ratio slightly higher for Coating *W-5* than for Coating *W-4* (see Table 6.9). This fact, together with the observed homogeneity of its surface, and according to the exposed in Sec. 3.6 makes Coating *W-5* a good candidate for low surface resistance coatings, which SE emitting properties will be discussed in the following sections.

In a general way, it has been observed, that the size and the disposition of the pores obtained depend on the time of exposure of the sample under the treatment and the intensity of the ion flux applied as well as the amount of the Ti evaporated over the sample. Regarding this last point, a strong dependance of the pore size on the J_{Ion}/J_{Ti} was observed, being pore areas smaller as the ion fluxes decrease with respect the amount of incoming Ti atoms . As the ion current increases the pores broaden and the porosity increases. When the ratio J_{Ion}/J_{Ti} gets larger than certain threshold, as it is the case of Coating *W-3*, the excessive erosion due to the ion etching impedes the deposition of Ti atoms, and no pores are obtained (see Fig. 7.19 in Sec.7.4.1.5).

6.3.3 Role of Temperature in Surface Morphology

As previously pointed out, every coating was applied on two samples at the same time in order to observe possible dependencies of the morphology obtained on unexpected parameters. Two very different morphologies, shown in Fig. 6.14, were obtained on both samples treated under the procedure of Coating *W-2*. In this case the origin of such discrepancy was found to be on the thermal contact of the samples. The sample analyzed in Sec. 6.3.1.2, which from now on will be labeled as Coating *W-2-A*, was properly installed on the sample holder, while the second sample, from now on labeled as Coating *W-2-B*, was accidentally installed in such a way that thermal contact was efficient only in two points of the sample, avoiding the dissipation of the heat through the copper anvil of the sample holder, as a result, an increase of (thermal) diffusion could be expected.

In situ temperature measurements of the substrate can not be performed in the Sample Preparation Set-up at UAM during the coating procedure, since the rotation of the sample holder impedes the constant thermal contact of the temperature meters on the substrates. For this reason in order to elucidate the thermal evolution of the samples under treatment, and the effect that a bad thermal contact can have on the substrate, temperature measurements were carried out without sample rotation. As graphically explained in the left panel of Fig. 6.15, the experiments were performed on two witness samples, in two geometrical dispositions simultaneously. One of the samples,(Sample *A*) was installed in a non conventional way, separated from the refrigerating Cu anvil in order to avoid heat dissipation.

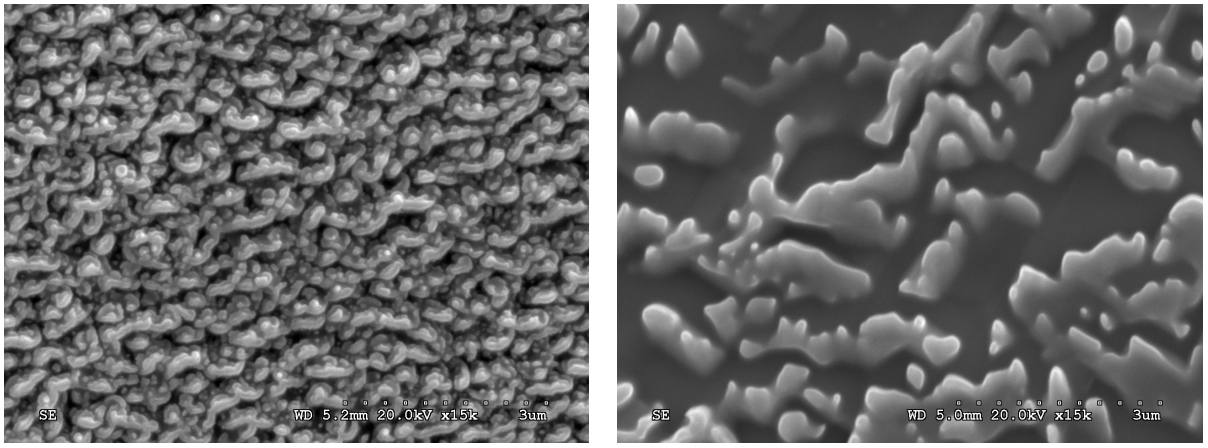

Figure 6.14: the effect of substrate overheating in roughness formation. **Left:** SEM images obtained from Coating *W-2-A* at normal incidence and magnification of x14K. **Right:**SEM images obtained from Coating *W-2-B* at normal incidence and magnification of x14K.

	Beam Energy (eV)	Beam Current (mA)	Magnetron Power (W)	Ar Pressure (mbar)	Δt (sec)
Thermal Experiment	900	20	125	$3.82{\cdot}10^{-3}$	900

Table 6.10: Ion gun, magnetron sputtering, pressure and time parameters used during the thermal evolution experiment.

Another sample, (Sample *B*) was installed in a conventional way with a proper thermal contact in order to favor heat dissipation. A Type K [163] thermocouple was installed on each sample, ensuring; i) A proper contact between the thermocouple junction and the sample. ii) The thermocouple junction is never exposed to the ion beam.

The ion gun, magnetron sputtering, pressure and time parameters used during the experiment are presented in Table. 6.15. The evolution of the temperature during the experiment is shown in the right panel of Fig. 6.15. As it is clearly observed, the temperature of the isolated Sample *A* drastically rises to values up to 300°C after 15 min while Sample B remains at values aroung 50 eV revealing a strong dependance of the temperature of the substrate with the quality of the thermal contact and its consequent heat dissipation. It was assumed that a similar thermal evolution took place during the performance of Coating *W-2*, and that overheating due to a poor thermal contact of Coating *W-2-B* is at the origin of the morphological differences with respect Coating *W-2-B*.

SEM results reveal that overheating of samples under treatment may ruin the rough morphology. This effect, according to experimental results found in the literature [164–167] was ascribed to an increase on the thermal energy of the atoms at the sample surface, which results on an increase of their mobility, making them to rearrange, avoiding the desired

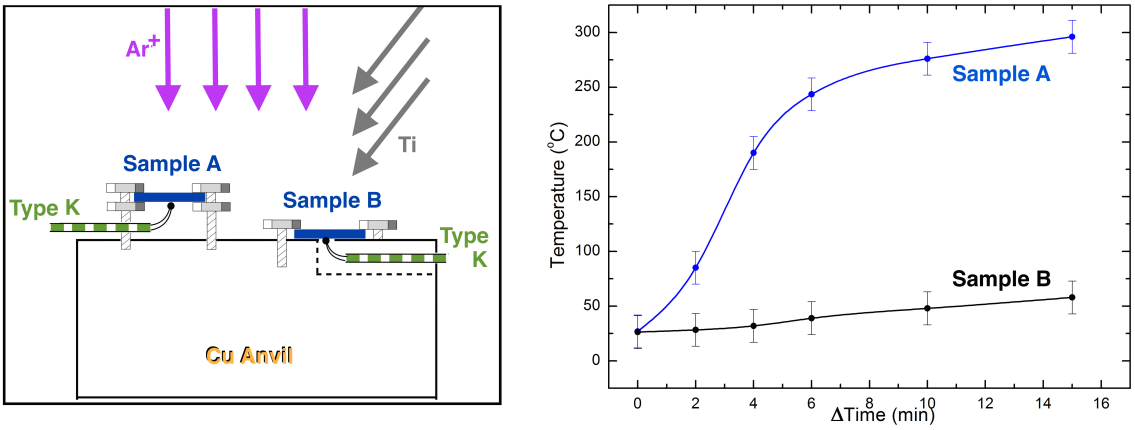

Figure 6.15: **Left:** Schematic description of the geometrical composition of the temperature evolution experiment. **Right:** Results of the temperature evolution experiment.

granular growth. One conclusion is that preferential sputtering and shadowing effects alone cannot explain the dynamics of the roughness formation, and the role of the temperature is an important parameter to take into acount. This accidental result must be assumed as a first step towards a future investigation focused on the thermodinamical aspects related to the micro- and nano-structurization of treated samples.

6.3.4 Dynamics of Roughness Growth

This research was oriented toward technological goals in the shortest time and costs in a trial-and-error methodology, as a consequence, it lacks necessary series of data on the independent influence of different parameters of the surface treatment procedure in order to elucidate possible physical mechanisms in the evolution of the roughness growth. Besides, the samples obtained were not analysed in detail for different roughness parameters, only SEM photos at normal and oblique view were routinely obtained. In spite of it, one may try to compare the results obtained with other analogous cases studied with more scientific rigor found in the literature. Recently, there has been an increased interest on self-organized nanopatterning by ion beam sputtering techniques, also called surfactant sputtering or ion etch masking [146, 147]. In our case the surfactant (Ti) is of lower sputtering yield, higher cohesive energy, and higher surface tension.

In those studies, several effects or driving forces have been proposed as an explanation for the dynamics of those processes and from the scarce and unconnected data available, the

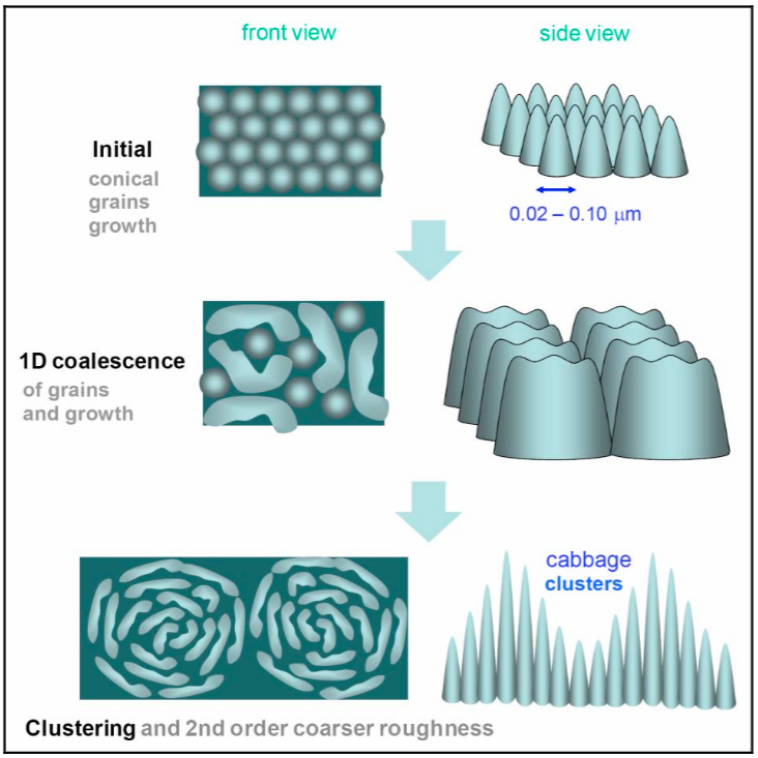

Figure 6.16: Preliminary hypothesis on the kinetics of roughness growth in sputtering-mask-assisted ion etching. Main steps in the evolution of the surface morphology under Ar ion etching while sputtering deposition of Ti (mask)

proposed working hypothesis for the evolution (and dynamics) of the surface roughness is (see also summary in Fig. 6.16):

i The first steps of the roughness formation consist on the nucleation of dots growing into conical protuberances or mounds as it can be observed in the Fig. 6.9 for Coating *W-3* by preferential sputtering [146, 155–157], chemical effects on sputtering yield and selective deposition and shadowing effects [151, 168, 169].

ii The growth of the initial morpholgy (possibly enhanced by an increase on the suftractant Ti) and lateral coalescence (coarsening), produces elongated mound ranges which tend to maintain a minimum distance or gap among them by an enhancement of preferential sputtering, shadowing effects and chemically driven thermal and ion induced diffusion [170–172], leading to components segregation and new phases formation [172–175]. Both mound width and gap width as well as their length seem to be characteristic of the roughness despite their relative variations.

iii As the procedure time increases, the growth in height is enhanced, while clustering of ranges into bunches or ripple heap structures. Nucleation of overlapping larger

coarser roughness takes place, and as a consequence second order roughness scales appear as clearly shown in Fig. 6.6.

iv Such behavior evolves until ripple heap structures become isolated on a flat background or substrate due to thermal and ion induced diffusion effects on surface morphology as presented in Sec. 6.3.3.

As it will be reviewed in the following subsections, during the whole surface roughness evolution (i-iv), the SEY appears to decrease; however, RF surface resistance is supposed to increase significantly during stages (iii, iv) because the size scale becomes μm. Thus, processing should be stopped just after stage (ii). Then, the roughness obtained is of high aspect ratio (2-10), smooth (only one size scale), uniform, not ordered patterns, nor random, rather chaotic patterns with short-range order.

6.4 SEE Analysis

The study of the SE emitting properties of the treated samples is presented in this section. The variation of SEY parameters after each treatment were analyzed, as well as the contribution of true secondaries and backscattered electrons to the EDC spectra measured on the treated witness samples. The understanding of the processes that take place in the SEE reduction is of crucial importance for controlling and understanding the nature of the Multipactor mitigating effect that those treatments may lead to.

6.4.1 SEY Analysis

Fig. 6.17 shows the SEY reults measured on the coatings obtained. The results obtained for each technique are presented in different graphs. The left panel shows the results obtained after SEY analysis of Coatings *W-1* and *W-2* obtained by using the Ti cone technique and the right panel shows the results obtained after SEY analysis of Coatings *W-3*, *W-4* and *W-5* obtained by using the ion assisted magnetron sputtering technique. Before measuring SEY the samples were extruded from the synthesis set-up chamber and kept under atmospheric conditions for a period of one week, in order to recreate the "as received"

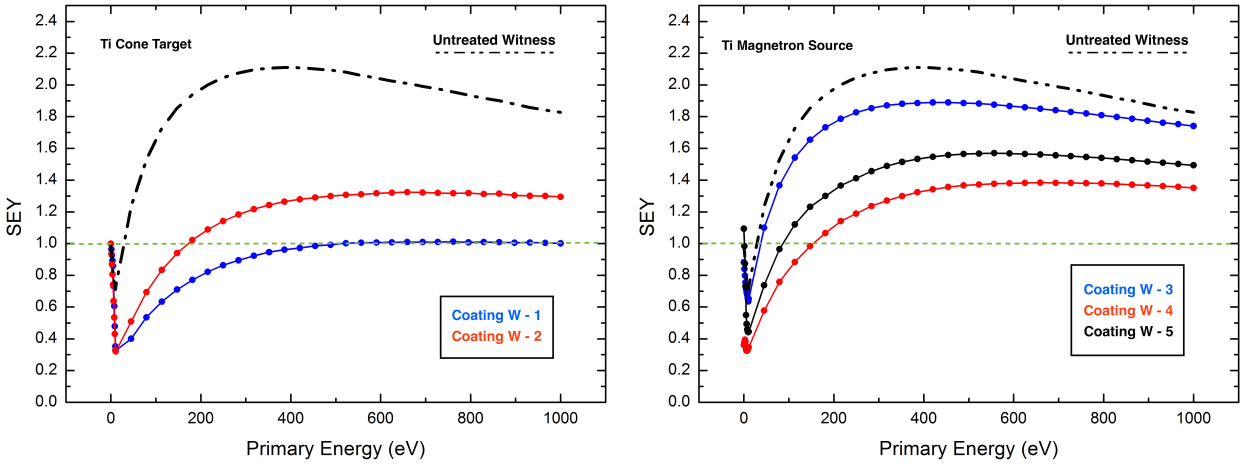

Figure 6.17: **Left:** SEY results measured on Coating *W-1* (Blue line) and Coating *W-2* (Red line) in comparison with the untreated witness (Dashed line). **Right:** SEY results measured on Coating *W-3* (Blue line), Coating *W-4* (Black line) and Coating *W-5* (Red line) in comparison with the untreated witness (Dashed line).

conditions, since those are in fact the conditions of interests for industrial applications, in which treated devices, are exposed to atmospheric conditions for variable periods of time before satellite launch.

A clear reduction of SEY with respect the untreated Ag plated witness was observed for all coatings. In the case of the Ti cone technique the effect of the second order coarse roughness of Coating *W-2* was manifested showing a dramatic reduction of SEY, remaining its maximum slightly bellow 1. according to the exposed in Sec. 3.5.2, this coating applied on an RF satellite waveguide component would avoid the Multipactor breakdown. SEY of Coating *W-1* however show a fainter reduction with respect the untreated witness being its SEY_{max}= 1.32, which also constitutes an important reduction down to the 63% of SEY_{max} of the untreated sample.

The measurements performed on the ion assisted magnetron sputtering technique coatings show a smaller reduction of SEY than for the Ti cone technique with respect the untreated witness, however the results obtained are still promising, being the minimum SEY_{max} obtained at a value of 1.37 for Coating *W-4*, very similar to that for Coating *W-2*. This coincidence is in well agreement with the SEM analysis previously discussed since the SEY suppression effect depend on i) pore aspect ratio, and ii) pore total area fraction (%). Both very similar for W-2 and W-4.

Despite the slightly higher aspect ratio estimated for Coating *W-5*, its total pore area

ratio was smaller and thus SEY analysis revealed that its maximum value was reduced to a higher value than for Coating *W-4* remaining at $SEY_{max} = 1.56$. This behavior is explained by the fact that, the porosity is smaller for of Coating *W-5* than for Coating *W-4*, the probability of electrons to penetrate into the pores is limited resulting in a higher value of its SEY_{max}.

As expected, SEY measured on Coating *W-3* showed the faintest reduction among all the treated surfaces due to the absence of pores of its surface observed after SEM analysis. However SEY_{max} was reduced to the 85% of the value for the untreated witness revealing that its characteristic polycrystalline morphology slightly etched out by ion erosion, also present in Coating *W-4*, does have some SEE mitigation effect.

6.4.2 EDC Analysis

EDC analysis was performed on the Coating *W-1* and *W-2* and compared with the untreated as received witness. All measurements were performed, within the same working cicle. Equipments were never turned off and on again between two measurements, hence the values of the analyzer WF beam current and bias voltage were assumed to remain steady during the whole measuring period. The EDC spectra were acquired at 205, 405 and 1006 eV in order to study the behavior of emitted electrons at different points across the SEY energy range. The spectra were acquired following the procedure explained in Sec. 5.4.1.2. At each primary energy stage, the e^- gun was stabilized, and then EDC spectra of all the samples were acquired without changing e^- gun parameters, in order to avoid any possible source uncertainty on of the value of the primary electron energy, so that comparisons between coatings at certain primary energy are reliable. As explained in Sec. 3.1.1 bias of 10 eV was applied on the sample in order to avoid SE's produced inside the electrometer walls to interfere with the electrons emitted from the sample.

Fig. 6.18 shows the results obtained on the samples at different primary energies. As it can be seen, a clear reduction of the intensity of the EDC spectra is observable for treated samples with respect the untreated witness. The reduction of the intensity is in good agreement with the reduction of SEY being the lowest intensity of all the spectra corresponding to Coating *W-1* and followed by Coating *W-2*. As shown in Fig. 6.18 this

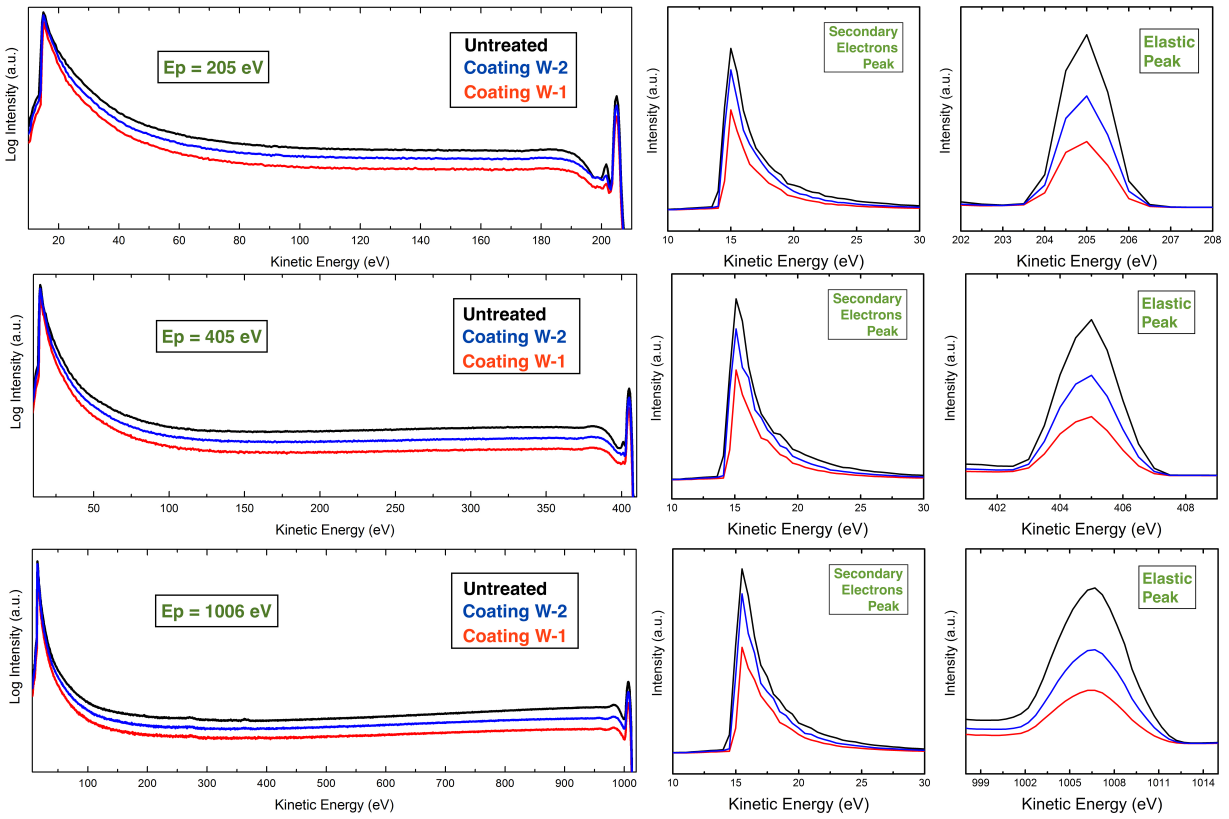

Figure 6.18: EDC curves measured on the untreated witness (Black line), Coating *W-1* (Red Line), and Coating *W-2* (Blue Line). Center and Right panels show the True SE's and the elastic peaks respectively. **Upper:** EDC measured at 205 eV of e^-gun energy. **Center:** EDC measured at 405 eV of e^-gun energy. **Bottom:** EDC measured at 1006 eV of e^-gun energy. Note the logarithmic scale for the full spectra and the linear ones for the insets

trend is observable at all the regions of the spectra, i.e. True SEs, Backscattered electrons, and Elastically backscattered electrons.

EDC spectra were normalized at the intensity of the elastic peak, in order to understand the effect of the surface roughness on different kind of electrons. Fig. 6.19 shows the results obtained, which are indeed very instructive.

It is clearly noticeable that after normalization, the true secondary peak presents a trend opposite to that observed in Fig. 6.18. Such effect, according to results reported reported in the past [117], reveals that surface roughening has a stronger suppression effect on backscattered electrons than on true SEs. This effect does not mean that reduction of SEY after surface roughening is due to a reduction of backscattered electrons uniquely, since a reduction of secondaries has been proved in Fig. 6.18, but clearly shows that backscattered electrons are more susceptible to be trapped within the formed pores of the surface than true secondaries. This effect is in good agreement with the well known dependance of the

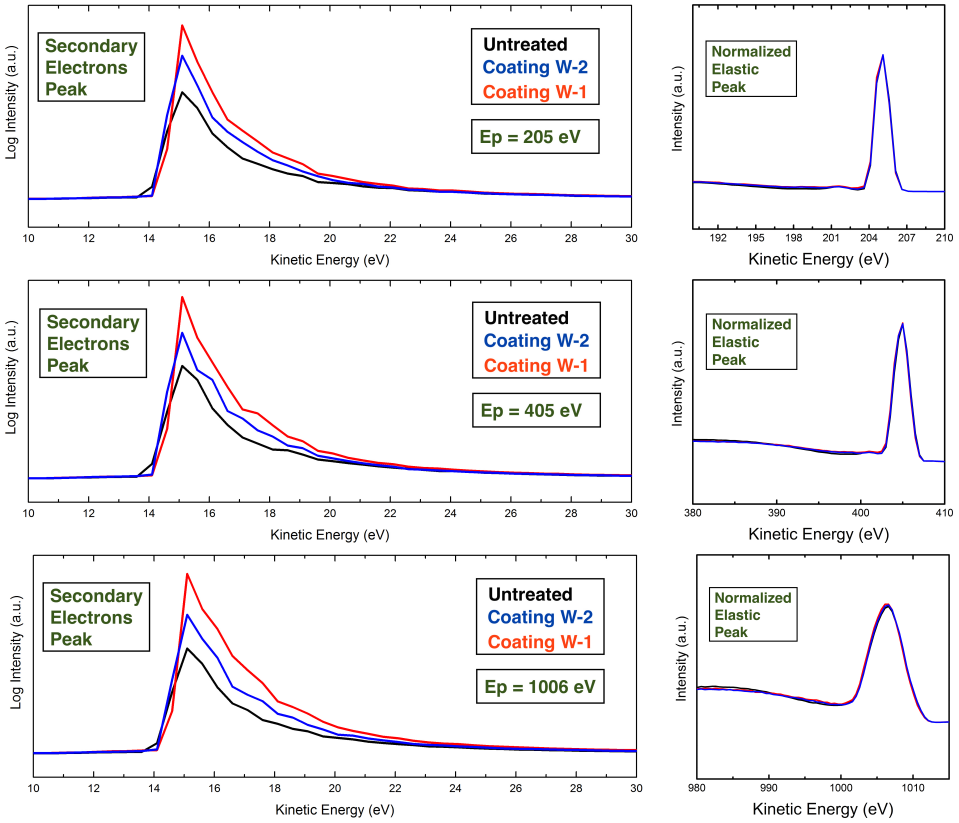

Figure 6.19: True SE's peaks from EDC curves measured on the untreated witness (Black line), Coating *W-1* (Red Line), and Coating *W-2* (Blue Line) after normalization to the elastic peak. Insets show the normalized elastic peaks. **Left:** EDC measured at 205 eV ofe^{-}gun energy. **Center:** EDC measured at 405 eV of e^{-}gun energy. **Right:** EDC measured at 1006 eV of e^{-}gun energy.

	Untreated		**Coating *W-1***		**Coating *W-2***	
	True Secondaries (%)	**Backscattered Electrons (%)**	**True Secondaries (%)**	**Backscattered Electrons (%)**	True Secondaries (%)	**Backscattered Electrons (%)**
200 eV	93.56	6.43	94.44	5.55	94.95	5.04
400 eV	91.35	8.68	93.04	6.95	93.87	6.12
1000eV	88.27	11.72	90.16	9.83	91.37	8.62

Table 6.11: Percentages of the contributions of true secondaries and backscattered electrons to the total are of the EDC spectra, at each primary energy, measured on the untreated witness, Coating *W-1*, and Coating *W-2*.

directionality of electrons on the nature of their emitting process. As it has been explained in Sec. 3.1.3, the angular distribution of "true" SE's responds approximately to a cosine distribution and is independent of the angle of incidence of the primary electrons [21, 46], while the angular distribution of backscattered electrons depends on the primary electron incidence angle. This fact makes the direction of the emitted backscattered electrons to be more confined to certain limits, which enhances the probability of being reabsorbed by the neighboring structure of the surface.

Table. 6.11 shows the percentage values of the areas (integrated intensity) measured under the EDC spectra in two different energy ranges. from 0 to 60 eV, which represents the the

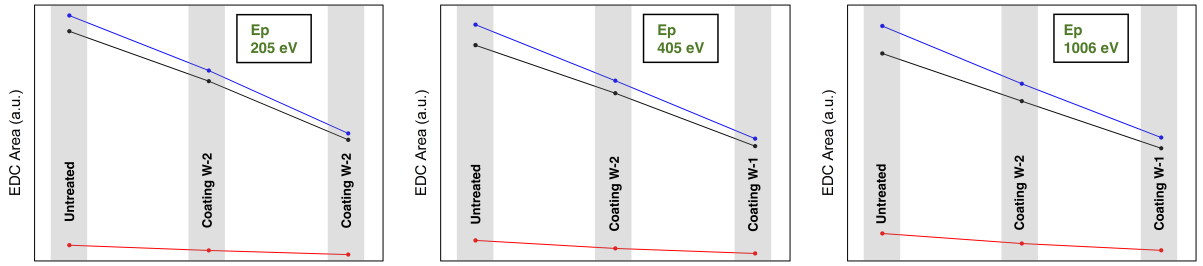

Figure 6.20: Evolution of the areas under the EDC curves for (Black line) in comparison with the contributions from the true SE's (Blue line) and the Backscattered electrons (Red line) . **Left:** Results obtained from the EDC measured at 205 eV of primary energy. **Center:** Results obtained from the EDC measured at 405 eV of primary energy. **Right:** Results obtained from the EDC measured at 1010 eV of primary energy.

energy range of true SE's (50 eV plus 10 eV due to the applied bias) and from 60 eV to the value of the primary energy, confirming that reduction of the emitted electrons is more efficient for backscattered electrons than for true SEs. However this result represents no contradiction with the fact that the effect that surface roughness have on the amount of the emitted true secondaries plays a crucial role in the SEY reduction. As Shown in Table. 6.11 a vast percentage of the emitted electrons is constituted by true secondaries, hence even though their reduction due to surface roughening is less efficient than for backscattered electrons, they still have a predominant effect on the resulting SEY curve.

In Fig. 6.20 the actual measured values of the EDC areas are represented, together with the contributions of the true secondaries and the backscattered electrons. As it is clearly observable the reduction of the total area of the EDC curve is dominated by the effect of the true secondaries.

6.4.2.1 WF Changes on Rough Surfaces

It is remarkable the observed behavior of the EDC at the true SE's peak cut-off curves at low energies. As perviously explained in Sec. 5.4.1.2, such cut-off represents the signal of the electrons with the lowest energy emitted from the sample, i.e. the kinetic energy corresponding to the WF of the material. In this case however the applied +10 V positive bias have a retarding effect on the emitting electrons, hence the electrons coming out the sample at the true SE's peak cut-off are measured with a kinetic energy:

$$E_K^{Cut-Off} = \Phi + e \cdot V_{bias} \tag{6.1}$$

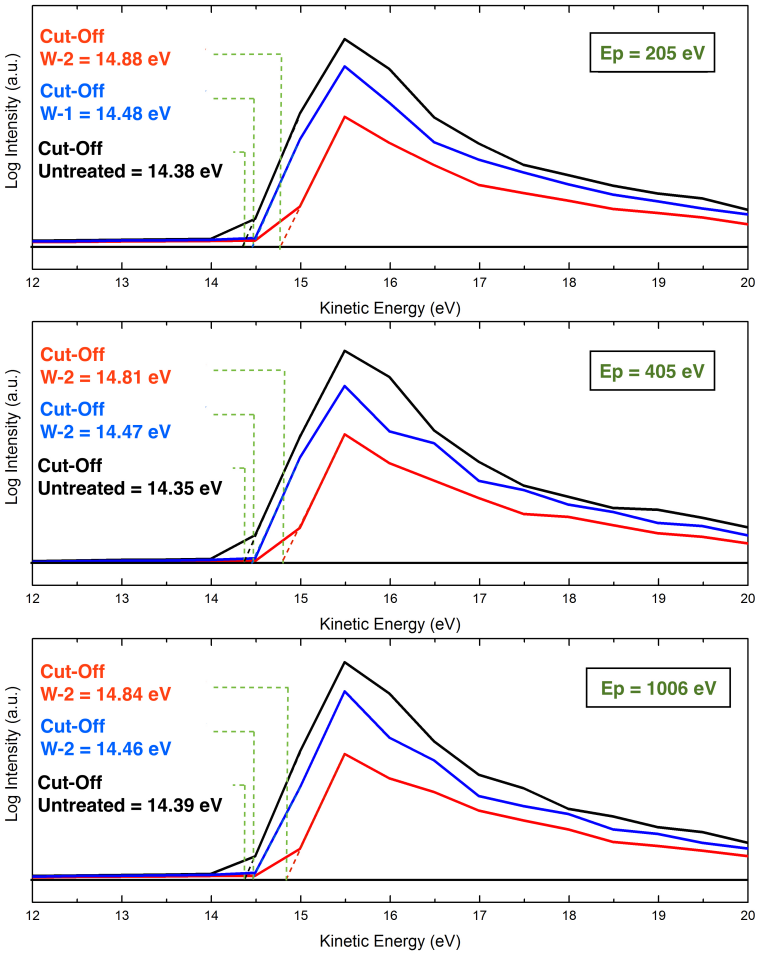

Figure 6.21: Magnification of the true SE's peaks from the EDC spectra measured on the untreated witness (Black line), Coating *W-1* (Red Line), and Coating *W-2* (Blue Line) in which the evolution of the cut-off energy is observable. **Left:** EDC measured at 205 eV of primary energy. **Center:** EDC measured at 405 eV of primary energy. **Right:** EDC measured at 1010 eV of primary energy.

where Φ is the sample WF, and $e \cdot V_{Bias}$ is, in this case, 10 eV. Fig. 6.21 shows a magnification of the cut-off region of the measured EDC spectra. It is clearly observable that the position of the cut-off of the treated witnesses shifts towards higher kinetic energies. Since V_{Bias} was kept constant during the whole period, this behavior is ascribed to an increase of the sample WF, due to the treatment applied. The results were validated to be free of any artifact related to the instability of the battery box which provides the 10 V bas voltage, since all samples were first measured at each primary energy and the same effect was observed at all energies, following the same trend for all the samples.

The estimated values of the WF are presented in Table. 6.12. This values present a clear trend, which is repeated at all energies. The WF of the untreated Ag witness was estimated to be 4.37 $\pm$ 0.07 eV in good agreement with data found in the bibliography [176–179].

	$Ag3d_{5/2}$	$Ti2p_{3/2}$	I_{Ag}/I_{Ti}
Coating *W-1*	0.91	0.63	18.27
Coating *W-2*	1	1	12.61

Table 6.13: Intensities of the $Ag3d_{5/2}$ and $Ti2p_{3/2}$ XPS peaks measured on Coating *W-1* and Coating *W-2*, normalized to the value of the most intense peak, i.e. Coating *W-2*. The right column shows the I_{Ag}/I_{Ti} ratio obtained for each Coating.

	Untreated Φ **(eV)**	**Coating *W-1*** Φ **(eV)**	**Coating *W-2*** Φ **(eV)**
200 eV	4.38 ± 0.25	4.88 ± 0.25	4.48 ± 0.25
400 eV	4.35 ± 0.25	4.81 ± 0.25	4.47 ± 0.25
1000eV	4.39 ± 0.25	4.84 ± 0.25	4.46 ± 0.25

Table 6.12: WF values of the untreated witness, Coating *W-1*, and Coating *W-2* estimated after SE cut-off energy analysis.

WFs of treated samples appear to be larger than for the untreated witness being 4.46 ± 0.07 eV for Coating *W-1* and 4.46 ± 0.10 eV for Coating *W-2*.

Two different phenomena may be at the origin of this behavior, i.e. A change in the chemical composition of the treated surfaces and a change in the scape probability of SE's due to surface roughening. As it has been mentioned, the coatings have been developed by depositing Ti on the surfaces of the samples, hence the presence of residual Ti was proposed as a possible cause of change of the sample WF. XPS measurements, shown in Fig. 6.22, were studied in order to study the amount of residual Ti present on the treated samples. The survey spectrum shown in the left panel of Fig. 6.22 reveal intense peaks corresponding to the Ag spectra lines, which means that, even though roughness has been formed, the sample was not covered by the evaporated Ti. On the other hand, no signal of Al or Ni from the substrates was observed, revealing that the effect of the ion etching did not erode the sample in excess.

The spectrum of the Ti2p is shown in the upper-right panel of Fig. 6.22, together with the Ag3d doublet, bottom-right panel of Fig. 6.22. $Ti2p_{3/2}$ appears at a binding energy of 458.4 eV corresponding to TiO_2 [180, 181]. The absence of structure at lower binding energies reveals a total oxidation of the present Ti, due to air exposure.

There is a large uncertainity regarding the accuracy of the value, and the confidence with which one can assume to know the actual values of the WF of certain materials due to the experimental difficulties related to its measurement procedure. Moreover, it is well known that WFs depend on the configurations of atoms at the surface of the material and

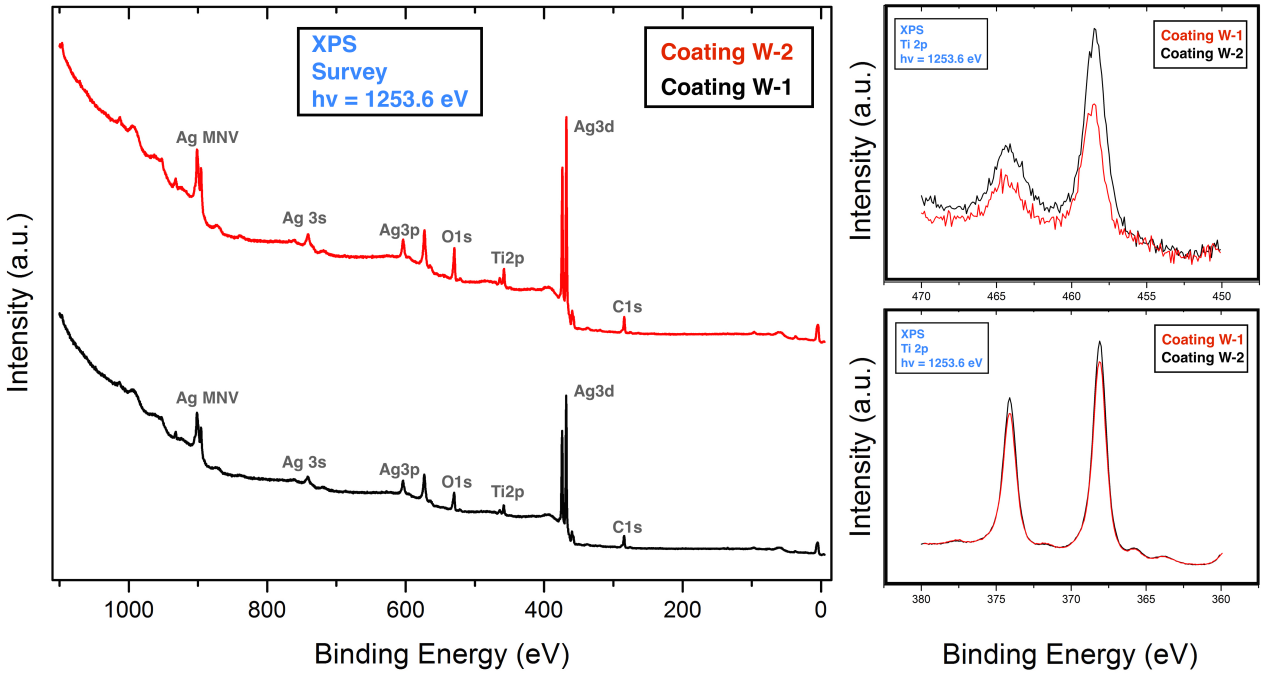

Figure 6.22: XPS spectra measured on Coating *W-1* (Black line) and Coating *W-2* (Red line) **Left:**Survey spectra. **Upper right:** Spectra measured in the Ti2p region. **Bottom right:** Spectra measured in the Ag3d region.

varies for different crystal orientations [176, 177], hence such uncertainity becomes larger when dealing with polycrystalline samples as it is the case of this work. Reported values of WFs found in the literature range from 4.14 to 4.74 eV for Ag [176–179] , while TiO_2 WF values appear to vary from 4.13 to 4.40 eV [179, 182–185]. According to this, the difference between both materials WF values is in fact smaller than the uncertainity related to them, and the behavior of the shift of the cut-off energy observed in the EDC spectra, can not be confidentially ascribed to the presence of TiO_2 on the Ag surface.

The intensity of the $Ag3d_{5/2}$ was measured to be dramatically larger than $Ti2p_{3/2}$ for both Coating *W-1* and Coating *W-2* as presented in Table. 6.13. As well as the resultant I_{Ag}/I_{Ti} ratio, the table also shows the values of the intensities of $Ag3d_{5/2}$ and $Ti2p_{3/2}$ peaks measured on both samples and normalized to the values of Coating *W-2*. Some conclusions can be obtained from this analysis. It can be observed that the amount of residual Ti is larger for Coating *W-1* than for coating Coating *W-1*, which is in contradiction with the assumption that the presence of residual Ti is the responsible of the observed increase of the WF of the treated witnesses with respect the untreated, since such increase is stronger for Coating *W-1* than for Coating *W-2*, revealing that the trends of both parameters evolve in the opposite direction.

Studies on the relationship of surface roughness and WF of metals were carried out in the past [186–188] , showing that WF was dependent on the surface roughness of metallic samples in such a way that a rougher surface had lower constraint for electrons to escape from peaks, resulting in lower WF. This results are clearly in contradiction with the observed behavior of our samples, which WF is increased after surface roughening treatment. However other experimental results obtained by different authors,[189] showed that the change in WF with roughness was not linear, increasing and decreasing at different stages of the roughness formation. In this thesis, it was supported the idea that the relation between WF and surface roghness may not only depend on the value of the surface roughness, but also the shape of the grooves forming it. As previously explained the reported, decrease of WFs due to roughness, is ascribed to a reduction in the constraint for electrons to escape from peaks [186–188], in which electrostatic *point effects* play an important role. However point effects are enhanced by sharp edges and peaks, which the samples obtained during this work lack. It is reasonable to take into account the idea that such difference in shape could be at the origin of the discrepancy found. It has been assumed that more detailed studies must be carried out in the future regarding the dependance of sample WF on surface morphology, taking into account a wider range of parameters including shape size and porosity of the surfaces under study, in order to explain the increasing behavior of the WF observed in this work, and crosscheck wether surface morphology is actually involved in that phenomena.

It is known, that variations in the WF may affect the SE emitting properties of the materials, [190–194] in such a way that, as observed in the results here presented, an increase of WF would result in a reduction of SEY. Accordingly, in [193] the energy distribution of low-energy SE's emitted from metals has been calculated by using a simple model, in which the use of an analytical expression for the energy-dependent mean free path of excited electrons in the calculations leaded to good agreement with experimentally obtained EDC curves.

In such model a complicated analytical expression was found to accurately describe the behavior of the EDC intensity as a function of the SE's kinetic energy. As a result the authors concluded that the shape of the EDC curve is entirely determined by the factor

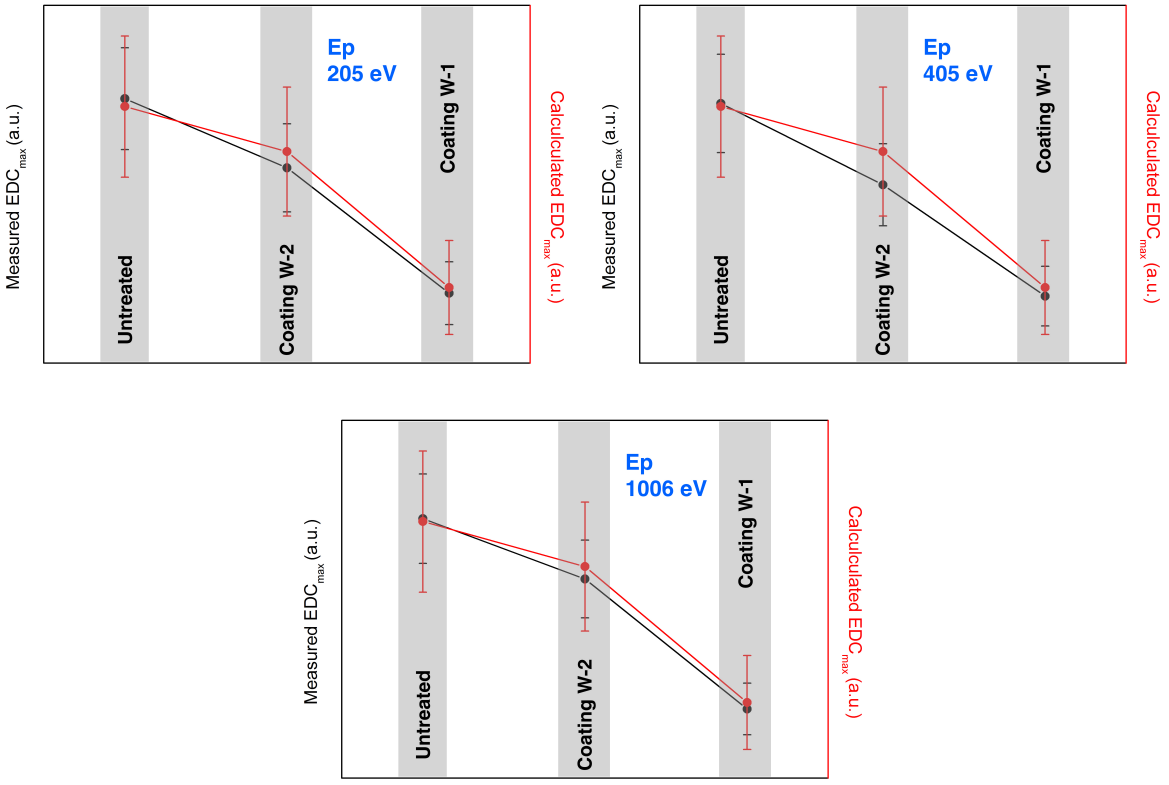

Figure 6.23: Comparison between measured (blak line) and calculated (red line) EDC_{max}. **Left:** Values obtained for a primary energy of 205 eV. **Right:** Values obtained for a primary energy of 405 eV. **Bottom:** Values obtained for a primary energy of 1010 eV.

$$f(E) = \frac{(E - E_f - \phi)}{(E - E_f)^4} \tag{6.2}$$

the maximum of the true SE's peak should occur at a value E_m that maximizes $f(E)$. This value is easily found by differentiating Eqn. 6.2 with leads to

$$E_m = E_f + \frac{4}{3}\phi \tag{6.3}$$

Thus combining Eqns. 6.2 and 6.3 we obtain

$$EDC_{max} \propto \phi^{-3} \tag{6.4}$$

which provides a value proportional to the maximum of the EDC curve as a function of the WF of the material studied. By making use of the theory above exposed, the values

for EDC_{max} were estimated according to the measured WF of each coating. As it can be observed in Fig. 6.23, the calculated values are in good agreement with the experiments.

6.5 Summary

Two different masked preferential ion etching techniques were developed and presented in this section, i.e. *Ti cone technique* and *ion assisted magnetron sputtering technique*. SEM results revealed morphologies of high porosity which originates the reduction of SEY. A hypothesis was presented to explain the dependance of such morophology with the time of exposure to thetreatment, and its dependance with the substrate temperature was manifested. EDC studies were carried out in order to elucidate the degree of influence of the surface morphology on the different kinds of emitted electrons. An increase of the WF with the surface roughness was observed, and after XPS analysis it was concluded that such behavios could not be explained by a change in the surface chemical state.

Chapter 7

Multipactor Mitigation in Aerospatial RF Devices

In this chapter, the results obtained in the ESA ITI project "Optimization of Surface Roughness of Anti-Multipactor Coatings for Low IL and Secondary Emission Suppression for High Power RF Components in Satellite Systems" are presented, as well as a detailed description of the used synthesis end testing procedures. This project constitutes the continuation of a previous project (AO 4025 CCN-02) in which practical control of Multipactor Power Threshold was achieved by means of surface roughening of technical Ag plating [92].

7.1 Description of the Samples

The samples under study used in this project are corrugated RF 12.8 GHz K_u-*Band low pass filters* of the harmonic type *Waffle Iron Filter*[195–197] designed by TESAT Spacecom. The devices were manufactured in two shells from Al alloy. Each shell was silver plated as explained in Ch. 6 in the description of the electrochemically silver plated Al witnesses.

Briefly, those RF filters are satellite waveguide components which constitute an important element among satellite devices, enabling the required frequencies to be passed through the RF circuit (pass band), while rejecting those that are not needed (stop band). According to the characteristics of their band pass, four types of filter can be defined, i.e: *Low pass*

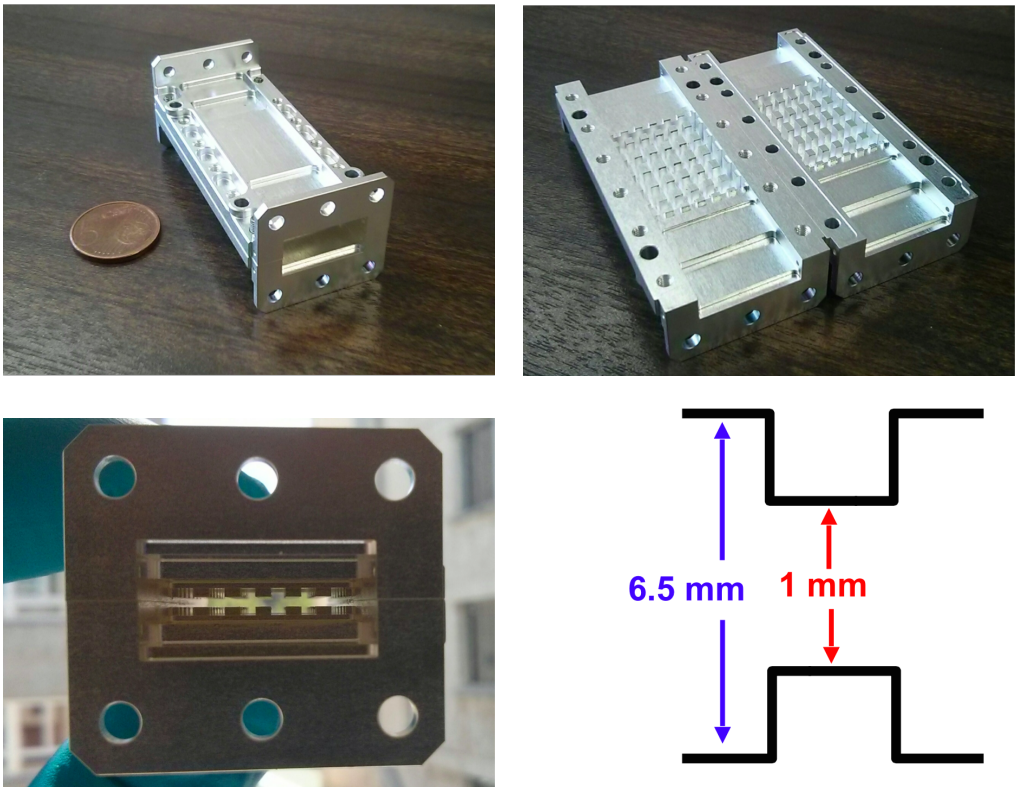

Figure 7.1: **Upper left:** Photo of the K_u-Band Low Pass Filter used in this work. The filter appears "as mounted" in the waveguide assembly.**Upper right:** Photo of the K_u-Band Low Pass Filter used in this work. The filter appears open with both shells showing their corrugated inner part. **Lower left:** Photo of the K_u-Band Low Pass Filter used in this work. The filter appears "as mounted" in the waveguide assembly. The gap between both surfaces can be observed. **Lower right:** Schematic description of the inner part of the K_u-Band Low Pass Filter used in this work, in which the distances between both shells is depicted.

filter which only allows frequencies below its so called cut off frequency f_c through. *High pass filter* which only allows frequencies above its f_c through. *Band pass filter* which allows frequencies within a given pass band through. *Band reject filter* which rejects signals within a certain band.

An ideal filter, would exhibit no loss within the pass band. Then outside this frequency band, (within the stop band) the filter will reject all signals. However In reality it is not possible to achieve the perfect pass filter and there is always some loss within the pass band, and infinite rejection is not achievable in the stop band. As pictorially explained in Fig. 7.1, the harmonic *Waffle Iron Filter* type consist on a series of corrugations located at the inside of both the top and bottom surfaces shells. The corrugation of the filters used in this work is formed by rectangular ridges of about 2 mm side, which are aligned with each other but do not meet in the middle, being the largest gap between shells is of 6.5 mm while the shortest is of 1 mm.

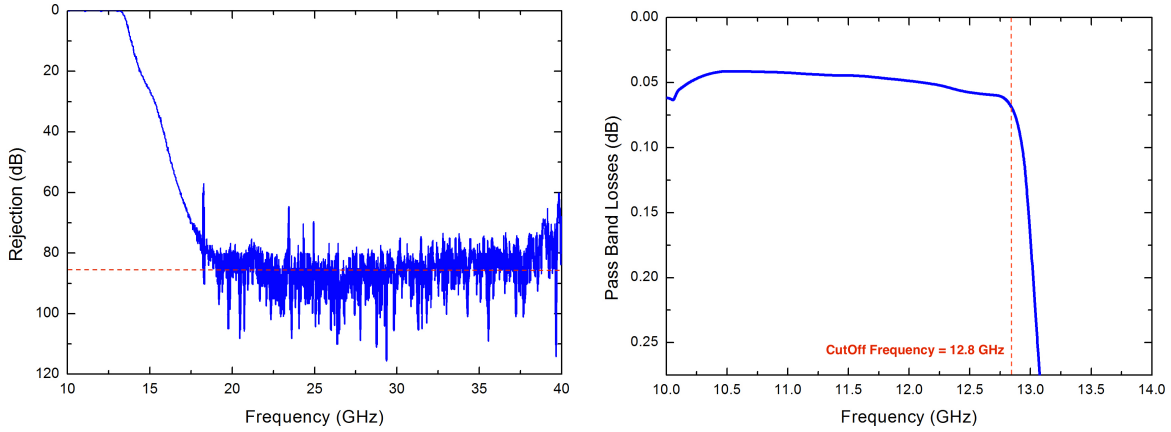

Figure 7.2: **Left:** Stop Band rejection of the waffle iron harmonic low pass filters as measured by the manufacturer TESAT Spacecom. **Right:** Pass Band Loss of the waffle iron harmonic low pass filters as measured by the manufacturer TESAT Spacecom.

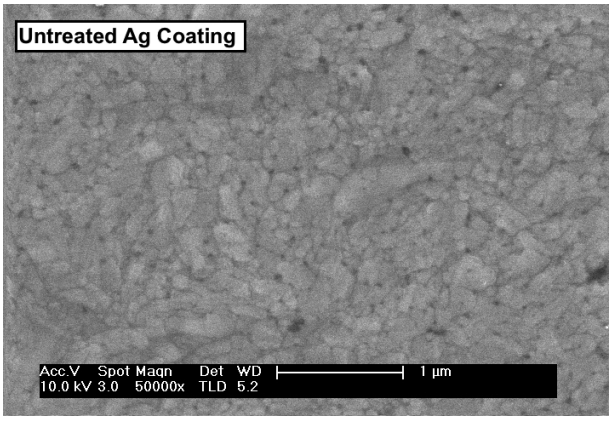

Figure 7.3: SEM image of the morphology of the untreated surface of the *K_u-Band Low Pass Filters* manufactured by TESAT Spacecom.

The main characteristic of waffle iron filters is that the number of rows of ridges affects the stop band attenuation, being possible then to achieve high rejection at the stop band. Fig. 7.2 left panel, shows the rejection of our samples as a function of the frequency, revealing an extremely good behavior within the stop band. Results on pass band losses test shown in Fig. 7.2 right panel, constitute also an extremely good value, typically < 0.10 dB. It is noticeable the behavior of the band pass loss curve, which drastically drops at a frequency of 12.8 GHz, revealing a favorable sharp transition between the pass band and the stop band. SEM studies of the morphology of the Ag technical coating morphology, shown in Fig. 7.3, reveal a rather flat surface similar to the untreated witness coatings, formed by domains of different sizes characteristic of polycrystalline materials. The absence of pores is remarkable even at grain boundaries.

The SEE yield was also measured on the untreated *K_u-Band Low Pass Filter*. The SEY

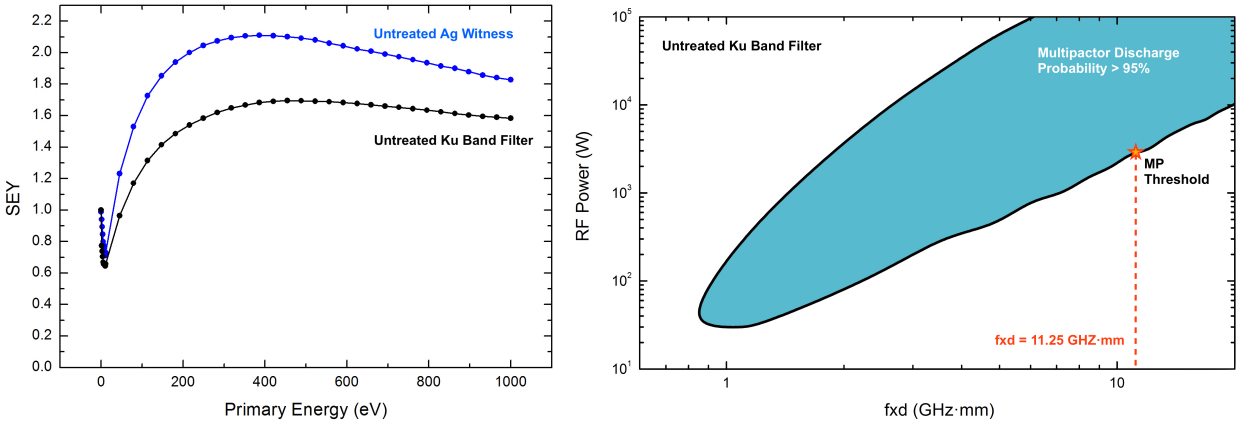

Figure 7.4: **Left:**SEY results measured on the untreated witness defined in Ch. 6 (Blue line) and the untreated *K_u-Band Low Pass Filter* (Black line). **Right:** Multipactor susceptibility region of the untreated *K_u-Band Low Pass Filter* simulated according to the measured SEY values by using MEST software

measurements of the filters were carried out at the *Departamento de Superficies y Nanoestructuras* at ICMM CSIC through the same measuring technique used at UAM explained in Sec. 5.4.1.1.

The left panel of Fig. 7.4 show a comparison between SEY curves measured on untreated "as received" witness and untreated "as received" filter in which a strong reduction of SEY is observed for the filter. Such behavior was ascribed to the presence of the characteristic rectangular ridges, which constitutes a macroscopic high aspect ratio corrugated surface. Due to the inhomogeneity of the inner part of the filter shells, the beam width was set to its maximum, being the spot diameter $\sim$ 1cm, as estimateded by using a *phosphor* powder screen. By doing so an average of the top and the bottom of the corrugated structure was measured, hence SEY values were avoided to depend on the spot position. Several SEY measurements were carried out on the filter at different spot positions, resulting on a constant value of $SEY_{max} = 1.69$, which means that under such spot size conditions the sample can be assumed to be homogeneous.

Multipactor tests were carried out on the untreated *K_u-Band Low Pass Filter* at the ESA European High Power Laboratory in Valencia (Spain), following the procedure explained in Sec. 7.2. The tests performed at 11.25 GHz revealed a Multipactor discharge at RF input power $P = 2900$ W.

The simulation software MEST (see Sec. 7.4.3.1), was used to estimate the Multipactor susceptibility region of the untreated *K_u-Band Low Pass Filter*. Multipactor effect has

been defined to happen when an initial small population of low energy "seeding" electrons clearly increases exponentially with time. No multipactor occurs when it clearly decreases exponentially. The transition occurs in a narrow border line, sharper in the upper limit than in the lower limit. The right panel of Fig. 7.4 shows the results obtained after the simulation within the limits of interest, were the conditions under which Multipactor threshold measurements were performed are included, i.e. $f\text{x}d_{Th}$ = 11.25 GHz·mm. The simulations were carried out in agreement with the Multipactor threshold measurements obtained at the ESA European High Power Laboratory. resulting in a threshold of $P \sim 2900$ W at $f\text{x}d_{Th}$ = 11.25 GHz. According to Eqn. 3.41, under the Multipactor measurement conditions, the skin depth of the a RF wave travelling through K_u-*Band Low Pass Filter* has been estimated to be δ= 610 mn.

7.1.1 Objectives of the Project and Motivation

Practical control of Multipactor Power Threshold was achieved in previous project (AO 4025 CCN-02) by surface roughnening of the Ag plating and Au overlayer in which six devices showed 4 - 13 dB improvements over the untreated state and two of them did not show any discharge [92]. However, regarding the necessities of the aerospatial industry, the main goal of the present project was to decrease IL to moderate values ($<$ 50% increase) by diminishing surface roughness size and thus surface resistance. The challenge was to achieve it maintaining the high Multipactor threshold. A large number of experiments were carried out, among which, a total of 5 K_u-*Band Low Pass Filter* labeled as #0512, #0500, #0497, # 0517, #0489 are presented here, since they constitute the most relevant results obtained. The working hypothesis was based on minimizing roughness size (main parameter for RF surface resistance) maintaining high roughness aspect ratio (main parameter for SEY suppression). Several technical strategies were envisaged in the project proposal and then studied for this project. Two most reliable, a physical technique based on ion beams and sputtering were selected for this work, i.e. Ti Cone technique, and ion assisted magnetron sputtering technique. The technical data of the K_u-*Band Low Pass Filter* and objectives of the project are presented in Table 7.1

Even though in previous project (AO 4025 CCN-02) chemical etching technique was proved to be an efficient procedure to obtain low SEY rough coatings and achieve practical control

Property	Typ. Value	Goal Value	Previous Work	Unit
MP Threshold	2900	> 6000	>15000	W
IL	0.050	0.065	0.15	dB
Stability under air exposure				

Table 7.1: Objectives of the ESA ITI project "Optimization of Surface Roughness of Anti-Multipactor Coatings for Low IL and Secondary Emission Suppression for High Power RF Components in Satellite Systems"

Filter		RF behavior at 12 GHz		Goal
	Type	IL [dB]	IL Enhancement [%]	IL Enhancement [%]
Ku0-Untreated	**Transformer**	0.150		<50
Ku0-Treated		0.52	247	
Ku0-Untreated	**Transformer**	0.215		<50
Ku0-Treated		0.630	193	
Ku0-Untreated	**Transformer**	0.281		<50
Ku0-Treated		0.786	180	
Ku0-Untreated	**Transformer**	0.359		<50
Ku0-Treated		1.067	197	
Ku0-Untreated	**Corrugated Low Pass**	0.178		<50
Ku0-Treated		0.422	137	
Ku0-Untreated	**Ridged Low Pass**	0.065		<50
Ku0-Treated		0.137	111	

Table 7.2: Comparison between the intrinsic IL of the untreated K_u*-Band Low Pass Filter* (Blue Line) and the IL of measured after the trueatment appied in the previous project (AO 4025 CCN-02) (Red line). Black dots represent the maximum power loss enhancement acceptable for industrial use.

of Multipactor power threshold [92], a vast enhancement of the IL was observed, which constitute a major problem for the functionality of RF devices.

The IL results obtained in the previous project (AO 4025 CCN-02) are presented in Table. 7.2. It is remarkable that the in the best case the IL were enhanced in a 111% of the initial value, being the 247% the highest enhancement achieved, which represents in all cases an extremely high value in comparison with the 50% imposed by the objectives of the project. The data presented in Table. 7.2 shows the ambitious challenge that the objectives of this project represent, since the enhancement of the IL must be drastically reduced with respect those measured in the previous project.

7.1.2 The Surface Treatment

For the *Ku Band Low Pass Filter* coatings, both techniques, Ion beam assisted Magnetron sputtering technique and Ti cone technique, previously presented in Ch. 6 were used. Despite the fact that the coating was applied on the same technical electrochemical silver coating for both technical *witness* samples and *Ku Band Low Pass Filters*, one must take into account the differences in volume between both samples, which can possibly lead into drastic differences in the requirements of each followed procedure. As previously showed in Sec. 6.3.3 the temperature of the sample during the coating process due to the continuous

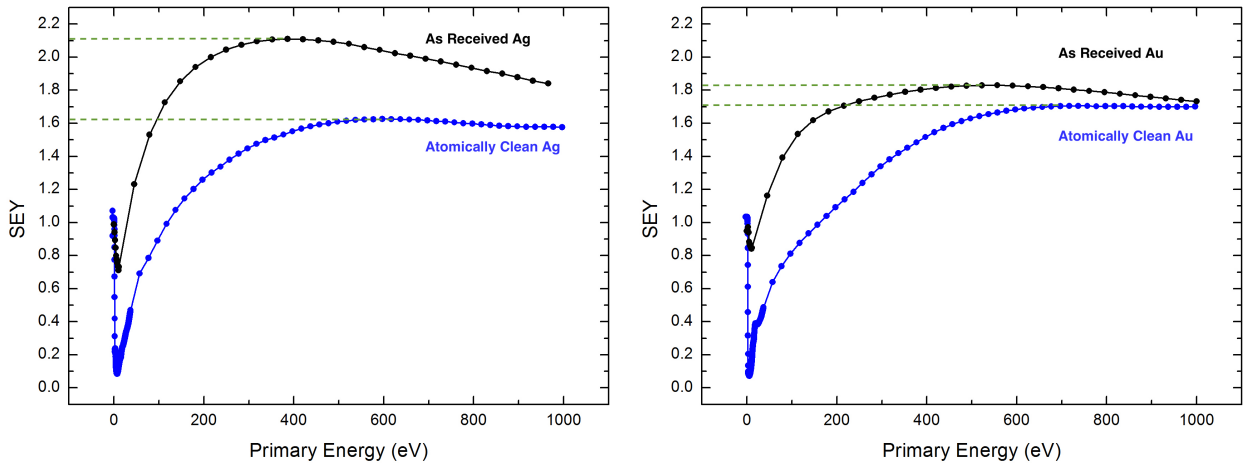

Figure 7.5: **Left:** SEY results measured on atomically clean (Blue line) and as received (Black line) electrochemically deposited polycrystalline Ag. **Right:** SEY results measured on atomically clean (Blue line) and as received (Black line) electrochemically deposited polycrystalline Au

flux of ions plays an important role in the roughness formation. The *K_u-Band Low Pass Filter* is more bulky than technical *witness* samples. Precisely, the weight of *Ku Band Low Pass Filter* is approximately 45 times higher than for technical *witness* samples, and for this reasons, the way that heat dissipates within their bulk is expected to differ from the witnesses to the filters. On the other hand, the area in contact with the copper sample holder, through which the heat dissipates, compared with the area exposed to the ion beam, is much smaller for the *Ku Band Low Pass Filter* than for the witness samples, being $\mathfrak{A}_{Exposed}/\mathfrak{A}_{Dissipation} = 1$ for the latter, and $\mathfrak{A}_{Exposed}/\mathfrak{A}_{Dissipation} = 70/4$ for the former. For this reasons, based on the results and knowledge obtained on technical witnesses, a number of trials were carried out in order to observe relevant differences in the results obtained due to the difference between the properties of each treated sample, and then obtain the most convenient coating.

The rough coating procedure for the *K_u-Band Low Pass Filters* consists on two main stages. In the first stage, surface roughness is formed on the Ag plated filter, at the central part of its inner surface, following the treatment procedures explained in detail in Appendix B. Briefly, due to the small contact area of the filter with the copper sample holder, a copper cooling device or anvil correctly fitting on the back of the filter is laid on the center of the copper disk. It is formed by a copper right rectangular prism located at the top of the copper cylinder of 75 mm diameter and 19 mm height used for witness samples and moderates filter temperature while strong ion bombardment, maintaining it well below 100°C.

In the second stage of the surface treatment, the etched Ag plated surface was coated by means of magnetron sputtering with an Au overlayer in order to passivate the surface and avoid oxidation upon exposure to air according to the requirements of air exposure stability imposed by the objectives of the project. Au is known to be the most inert among nobel metals, for this reason, the Au coating is of crucial importance to mitigate the detrimental effects of corrosion after atmosphere exposure [198–200], previously explained in Sec. 4.3. Besides, and most important, it has been proven that a Au overlayer lowers significantly the SEY at low energies (< 500 eV) of roughened Ag [92]

Fig. 7.5 shows SEY measurements performed on both as received and atomically sputtered clean Ag and Au in order to observe the effect of air exposure on the SE emitting properties of both metals. A different behavior of Au and Ag SEY curves after air exposure was manifested. While SEY of clean Ag is lower than that for Au, As received Ag increases its maximum SEY in a 30% reaching a value of $SEY_{max}^{Ag} = 2.11$, while air exposed Au maximum SEY increases in a 7% remaining in value of $SEY_{max}^{Au} = 1.83$, well below SEY_{max}^{Au}.

7.1.3 Thin Passivating Au Overlayer

The main restriction concerning the Au overlayer is related to its thickness for two main reasons. Firstly, even though Au has an extraordinary electrical conductivity of $4.10 \cdot 10^7$ S/m, it is still lower that the $6.30 \cdot 10^7$ S/m of silver [201], being the latter ~ 1.5 times grater than the former, which means that, since the power attenuation of a wave within a waveguide due to IL is proportional to the attenuation constant α_c, (see Sec. 3.6.2), being R_s the surface resistance of the material forming the waveguide and according to Eqn. 3.44, we have that

$$\alpha_c \propto R_s \tag{7.1}$$

and using Eqns. 3.43 and 3.41

$$R_s \propto \sqrt{\frac{1}{\sigma}} \tag{7.2}$$

hence, if the thickness of the applied Au coating is larger than the skin depth, the IL could be enhanced up to 22%.

Secondly as shown in Sec. 6, ion assisted magnetron sputtering technique, allowed us to obtain rough surfaces with pore sizes around 50 nm in diameter, much smaller than those obtained by means of chemical etching techniques, which means, that Au coatings of $\sim 2\mu m$ thick applied to rough surfaces in previous works [92] would now ruin the small sized roughness, eliminating then the low SEY properties of the sample. By achieving thin Au coatings of the order of nm the subjacent rough structure would be respected, and moreover, since according to Eqn. 3.41 the skin depth for Au at 12 GHz is $\sim 0.72\mu m$ (two orders of magnitude greater than nm) the IL enhancement due to skin effects produced by the conductivity reduction due to the presence of Au, would be negligible. In order to achieve this chalenging target a new Au coating strategy, different than that used in previous part of the project [92] is mandatory. The strategy was again to use ion assisted Magnetron sputtering deposition. It has been reported [165–167] that the ion-to-metal arrival rate ratio J_{ion}/J_{Metal} at the substrate plays a very important role on the morphology of the thin film, in such a way that by increasing the value of J_{ion}/J_{Metal} the thin film growth might change from a columnar morphology with a highly underdense microstructure to dense films with a more equiaxed grain structure due to renucleation. In this part of the coating procedure, the kauffman ion gun was set to low ion fluxes and low beam energies so that the achieved small sized roughness is not modified due to sputtering induced by the Ar^+ ions. While Au is deposited by means of magnetron sputtering, the Ar^+ ions enhances the mobility of incoming Au atoms on the surface providing them enough energy to rearrange in an homogeneous overlayer avoiding the growth in form of islands, but insufficient for damaging the surface morphology by ion mixing or etching.

In order to find the optimal conditions a total of four trials were performed on Coating *W-5* previously analyzed in Ch. 6. SEM analysis of Coating *W-5* is shown in Fig. 7.6. According to the results presented in Sec. 6.4.1, $SEY_{max} = 1.57$ for Coating *W-5* and the average pore area is 436 ± 20 nm^2, which makes it a good candidate for both high multipactor threshold, and low IL coating for K_u*-Band Low Pass Filter*. SEM analysis of the morphology of the samples after each of the gold coating obtained is shown in Fig.

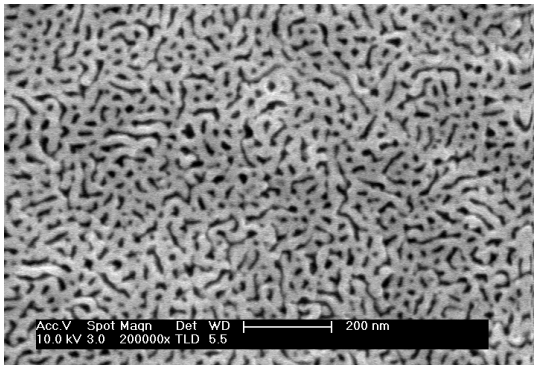

Figure 7.6: SEM image of Coating *W-5*, previously described in Ch. 6, on which four different Au coating treatments were carried out.

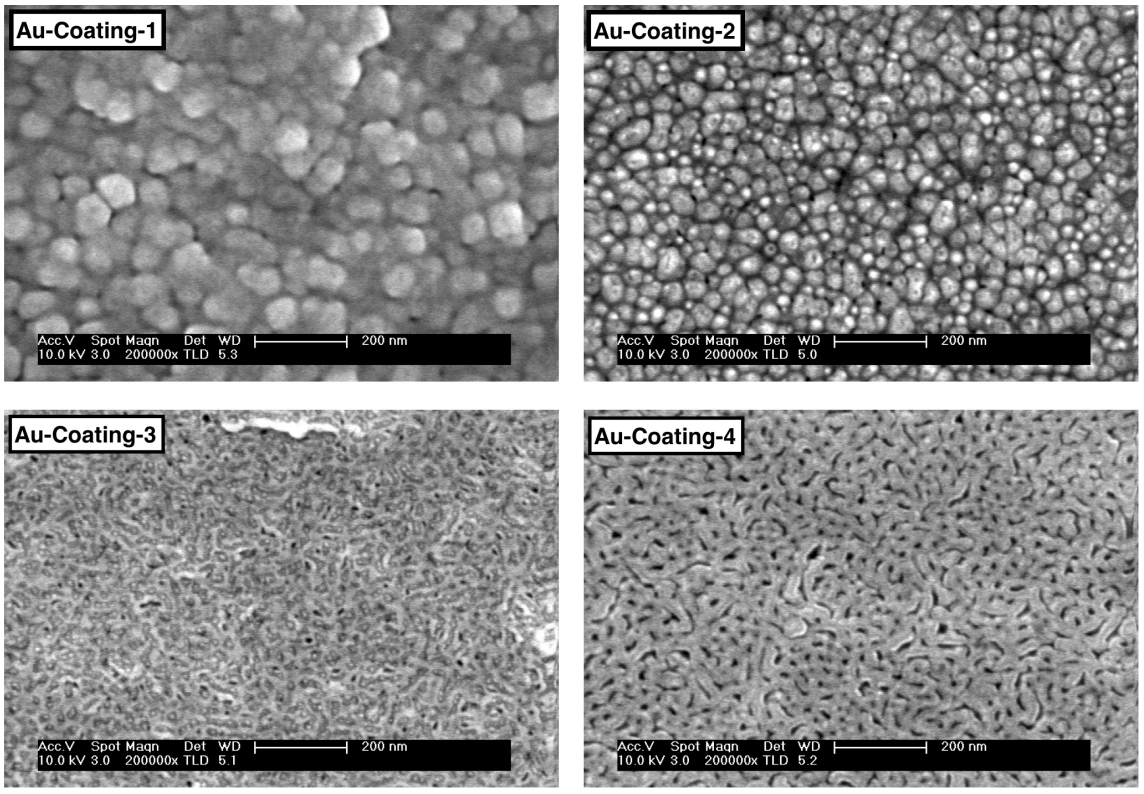

Figure 7.7: Comparison of the four Au coatings trials carried out on sample Coating *W-5*.

7.7. For each coating, different parameters of ion gun and magnetron sputtering source, presented in Table 7.3, were used.

Visual inspection of SEM images of Fig. 7.7 reveals that the rough structure of the Ag-Ti substrate becomes completely covered by over-grown Au grains after Coating-1. In this case during 60 seconds, the ion gun was set at 450 eV and 15 mA, while magnetron sputtering was working at 200 W. By reducing the beam energy and beam current to the half of the

	Beam Energy (eV)	Beam Current (mA)	Magnetron Power (W)	Ar Pressure (mbar)	Δt (sec)
Au-Coating-1	450	15	200	$4.0{\cdot}10^{-3}$	60
Au-Coating-2	900	15	100	$3.6{\cdot}10^{-3}$	90
Au-Coating-3	450	15	100	$4.0{\cdot}10^{-3}$	90
Au-Coating-4	450	15	50	$4.0{\cdot}10^{-3}$	90

Table 7.3: Summary of the beam energy, beam current and magnetron sputtering power parameters used on each Au coating treatment on Coating *W-5*.

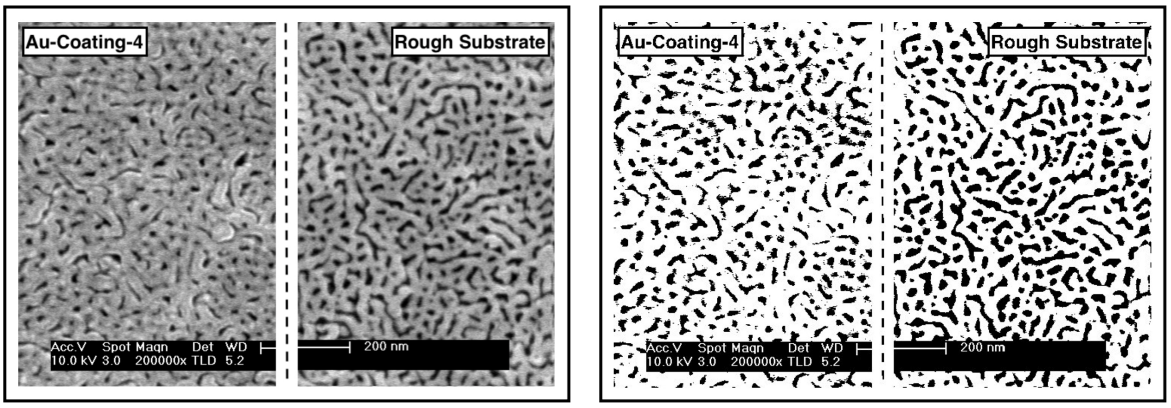

Figure 7.8: **Left panel:** Comparison between the morphology of Coating *W-5* prior to Au-Coating 4 and the Au-Coating 4. **Right panel:** Comparison between the morphology of Coating *W-5* prior to Au-Coating 4 and the Au-Coating 4 after color threshold image processing.

needed to originate rough structures a non destructive effect of the ions was expected. A very different structure from the substrate can be observed, characterized by conglomerated grains of $\sim 50 - 100nm$. We validated the idea that the amount of gold deposited over the substrate was grater than the required in order to obtain the appropriate balance between Ar^+ ions and Au flux, hence Au was deposited in excess. It is worth noticing that as depicted in Fig. 6.4, Au is an extremely soft metal, and its sputtering coefficient is ~ 3.5 times grater than for Ti [158], hence a bigger amount of material is evaporated for the same magnetron power. In the procedure of Coating-2, magnetron power was set to the half of the value used for Coating-1, and a smaller amount of Au was expected. Beam energy was increased up to 900 eV, so that excess of gold deposition could be avoided. Fig. 7.7 reveals this time, as well as for Coating-1, a very different structure comparing with the substrate. However in this case a new self-orgnized patterned surface is obtained by ion enhanced mixing of all the components, i.e. Ag, Ti, and Au. Ion induced diffusion allows different patterning forces (chemical and ballistic) to built a new surface morphology. The latter denotes that independently from the amount of gold deposited, the high energy of the Ar^+ ions, not only avoids the formation of a conformal Au overlayer, but on the contrary destroys the original substrate roughness. The resultant structure is a rough surface formed by rounded protuberances with sizes ranging from 20 to 100 nm.

During the performance of Coating-3, based on the observed results of Coating-2, a reduction of the destructive effect of high energetic Ar^+ ions is demanded. Ion beam energy was set back to 450 eV, while magnetron power was kept at 100 W. The results shown in Fig. 7.8 left panel reveal a total absence of Au grains, characteristic of the excess of over laying Au. However even though certain structure of similar shape than the substrate can be observed, no sharp structure is present except for some scarce randomly located pores, and the original pores seem to be covered by a thick conformal Au over layer. Visual inspection of Coating-4 reveal a very similar structure comparing with the rough substrate. To achieve this result, the amount of deposited Au was further reduced by setting magnetron power at 50 W, by doing so, the original surface roughness was maintained. Fig. 7.8 shows a close comparison between the rough substrate before and after the Au coating. The shape of the structure is maintained, however the size of the pores was visibly reduced. The same color threshold image processing explained in Ch. 6 was carried out. The resulting images are depicted in Fig. 7.8 right panel, and the numerical analysis is shown in Table. 7.4. A very small difference between the number of pores of each sample of $\sim 4.5\%$ of the measured value was obtained. However, the area is constituted by pores, for the pre-coated rough Ag, is ~ 1.6 times larger than for the Au coated sample. The average pore size has also been calculated for both samples revealing that pores of the pre-coated sample have an area 1.75 times larger than those for the Au coated sample.

	Pore Density (Pore/μm^2)	Porosity %	Average Pore Area (nm^2)	Max Pore Area (nm^2)	Min Pore Area (nm^2)
Pre-Coated	743 ± 35	30 ± 2	436 ± 21	1222 ± 60	22 ± 1
Au-Coating-4	703 ± 35	18 ± 1	249 ± 12	1117 ± 55	20 ± 1

Table 7.4: Summary of the values obtained after analysis of the morphology of the surface by means of the threshold color technique on Coating *W-5*.

XPS analysis on the Au coated rough sample was performed in order to crosscheck the presence of gold over the substrate, analyze the effectiveness of the method and quantify the amount of gold deposited. Before XPS analysis was carried out, the sample was exposed to air for a period of 24 hours. The XPS survey spectrum presented in the left panel of Fig. 7.9 shows the characteristic intense $Au4f$ doublet and other structure such as $Au4d$ doublet and $Au4p_{3/2}$ peak, confirming that Au was deposited on the substrate. Weak signal corresponding to Ag substrate is also present, precisely $Ag3d$ doublet and Auger $AgM_{4,5}N_1V$ transition can be observed. It is worth noticing the very small contributions

of O and C corresponding to surface hydrocarbon contaminants after air exposure, core level O1s the peak can not even be resolved out from the background noise, confirming that the Au overlay applied has, as expected, a passivating effect on the surface, avoiding oxidation after air exposure.

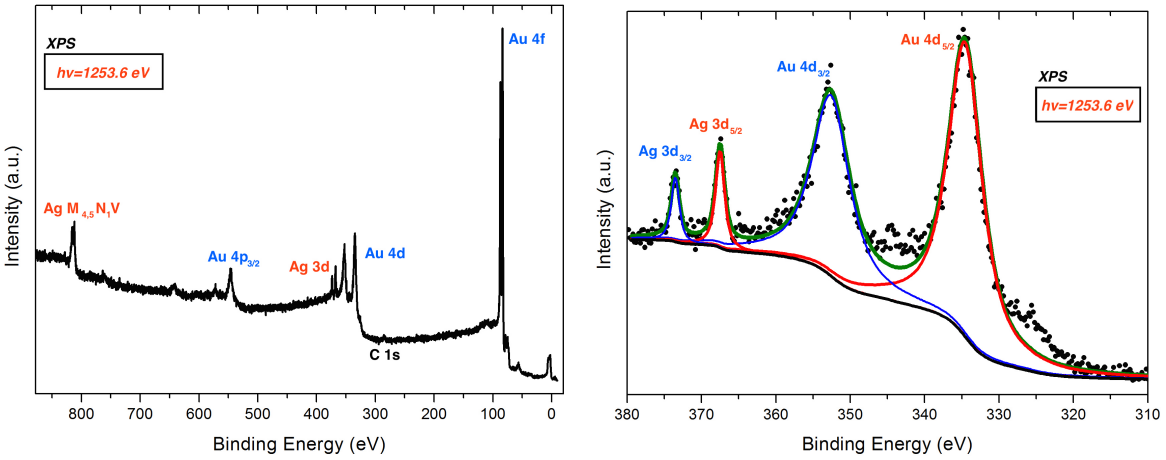

Figure 7.9: XPS analysis measured on Au-Coating 4. **Left panel:** Survey XPS spectrum. **Right panel:** Detailed XPS spectrum in the $Ag3d$ and $Au4d$ region

The Survey spectrum reveals that Ag signal is attenuated and only a small amount of electrons are able to scape to vacuum, according to that one a can conclude that the Au overlay thickness is actually larger than the inelastic mean free path of the photoelectrons traveling through Au. In the case of $Ag3d$ photoelectrons, which kinetic energy is $\sim$ 885 eV the IMFP was estimated to be $\sim$ 1.13 nm as calculated from the Tanuma, Powell, and Penn TPP2M formula in [202] . According to the exposed in Sec. 5.4.2.1, an orientative value of the actual over-layer thickness is achievable by comparing both Ag and Au peak intensities.

Right panel of Fig . 7.9 shows the detailed XPS spectrum in the $Ag3d$ and $Au4d$ region. A comparison between Au an Ag intensities resulted in a calculated ratio $[\Im(Au4d_{5/2})]/[\Im(Ag3d_{5/2})] = 11.35$. By making use the methodology presented in Sec. 5.4.2.1 and Eqns. 5.12 and 5.13, the relationship between $Ag3d$ and $Au4d$ intensities can be expressed as[139, 203, 204]:

$$\left(\frac{\Im_{Au4d_{5/2}}}{\Im_{Ag3d_{5/2}}}\right) = \left(\frac{S_{Au4d_{5/2}}}{S_{Ag3d_{5/2}}}\right)\left\{\frac{1-exp\left(-\frac{d_{Thick}}{\lambda^{Au}_{Au4d5/2}}\right)}{exp\left(-\frac{d_{Thick}}{\lambda^{Au}_{Ag3d5/2}}\right)}\right\} \tag{7.3}$$

Where $\lambda^{Au}_{Au4d5/2}$ is the IMFP of $Au4d_{5/2}$ photoelectrons traveling through Au, and $\lambda^{Au}_{Ag3d5/2}$ is the IMFP of $Ag3d_{5/2}$ photoelectrons traveling through Au. In this special case for the bilayered system that our sample constitutes, since NAu/NAg ~ 1[205]. A value of $d_{Thick} \sim$ 3.2 nm was obtained by applying Eqn. 7.3 which is consistent with the results depicted in Fig. 7.8 right panel. It is important to highlight that due to the strong corrugation of the surface studied, the value of the Au overlay thickness is subjected to a large error margin, since there might be areas where the gold deposition is more efficient than others. in any case, the dominant presence of Au on the surface of the sample has been crosschecked, while substrate roughness has been maintained, within certain acceptable limits.

7.2 Multipactor Testing Methods and Procedure

The Multipactor tests were run at the European High Power Laboratory in Valencia (Spain). The measurements were carried out in a class 10000 (ISO8) clean room, according to the procedure stablished in the official document ECSS-E-20-01A [206]

The devices under study (DUT) are kept under a vacuum of 10^{-5} mbar for arround 60 hours. In order to initiate a multipactor discharge it is necessary to have sucffient free electrons present in the test chamber and, in particular, in the vicinity of the device under test. Diagnostic tests performed by ESA [206] have shown this to be a necessary condition in order to obtain reliable data on discharge thresholds. To achieve such a condition, a ^{90}Sr radioactive β^- source and one UV lamp must be employed simultaneously during the test near to the DUT, to ensure the presence of free electrons within it. The radioactive source is constructed in such a manner that contamination of the DUT is not possible. Two thermocouples are connected to the DUT, in order to evaluate the increase of temperature during the test. An schematic of the measurement equipment is shown in Fig. 7.10, where all the detection systems are depicted.

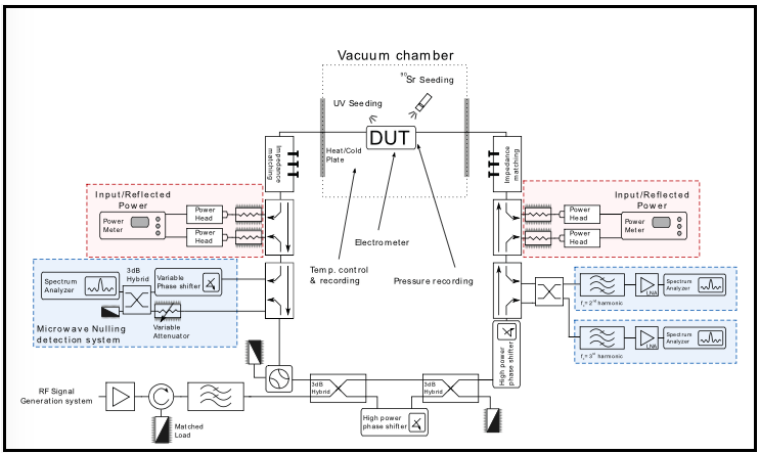

Figure 7.10: Schematic of the single carrier Ku-band Multipactor test configuration.

Before starting the test, the system was validated using a thru transmission line as DUT. All the test conditions were reproduced, and it was demonstrated a discharge free operation of the system up to the maximum RF power at the correspondent test frequency. This procedure was repeated once the test was completed to ensure the discharge free operation of the test bed during the DUTs testing phase. The test bed was run under the parameters parameters displayed in Table 7.5:

Frequency (GHz)	Pressure (mbar)	Temperature (°C)	Pulse Width (μs)	RF Power (W) (max)
11.25	$1.5{\cdot}10^{-5}$	RT	20	15000

Table 7.5: Summary of the test parameters under which the test bed at European High Power Laboratory the was run.

There are several methods to detect multipacting RF breakdown, which can be classified as global and local detection methods, each method has its conveniences and defects limited by the direction of research and test of device and instruments. Global methods are able to detect wether or not multipactor has occurred somewhere in the system. Nevertheless, through this method the specific location of the discharge can no be obtained. This kind of method is most commonly used for flight hardware test, in which the goal is to completely avoid multipactor discharge. Local methods however, are used to find out where the multipaction appears. This methods allow to monitor a certain area inside the hardware without taking the entire system into account, so that it is possible to identify the parts of the device that need redisign. This methods are most commonly used during the hardware

development phase. For all methods, the procedure is to apply a RF wave to the DUT and step by step, increase the input power, until discharge is detected.

7.2.1 Global Methods

Second/Third Harmonic Detection Method: This detection method is one of the most reliable detection methods in use and is based in the fact that multipactor discharge spreads energy over the spectrum, resulting in increased power in the harmonics. For optimum operation good coupling of the generated harmonic components is required.

Nulling of Forward/Reverse Power Detection Method: In this detection system a proportion of transmitted and reflected power is coupled into a phase and amplitude-matching network. Once the system is balanced the two signals produce a null, which is very sensitive to amplitude and phase variations within the system. Multipactor discharge creates an imbalance and a loss of the null.

7.2.2 Local Methods

Electron Probe Detector: An electron probe measures the electron current and provides temporal measurements of the multipactor electron current with respect to the microwave pulses. This method relies on the ability of a small positively charged probe to attract free electrons generated as a result of a discharge. A high impedance amplifier connected to the probe provides impedance transformation to 50 Ohm. An oscilloscope or voltmeter may then be used to monitor the probe current.

Optical Detection:A very efective detection method is to detect photons that are released during RF break- down, either from the surface of the material or by ionising the residual gas molecules present within the vacuum system. An optical fibre is placed through a small hole in the RF component as near as possible to the photo-multiplier outside the chamber. Any output from the photo-multiplier is displayed on an oscilloscope and also triggers a RF breakdown occurrence detector.

According to to the procedure stablished in the official document ECSS-E-20-01A [206] at least two detection methods must be used to determine Multipactor threshold, and one of them must be a global method. in this work, Second/Third Harmonic Detection Method, Nulling of Forward/Reverse Power Detection Method and Electron Probe Detector were used, and the results are shown in the following subsections.

7.2.3 Surface Treatment Procedure

Before starting the syntesis procedure, the system is vented with nitrogen, in order to open it and introduce the *Ku Band Low Pass Filter*. Once the filter half shell is installed over the copper cooling device, and located at the center of the chamber, the introduction port is closed and the procedure explained in Sec. 6.3.2 is followed. When the procedure is finished, sample platform shutter is set on again and the ion gun and magnetron sputtering are set off. The sample is then maintained in vacuum for 24 hours in order to ensure a complete cooling down of the sample. The system is then vented with nitrogen, and the second half shell of the *Ku Band Low Pass Filter* is installed into the equipment following the same procedure as done for the first half shell. The treated sample half shell in the mean time is covered on aluminum foil and located inside the vacuum chamber, in order to keep it under vacuum conditions, away from the effects of the ion gun and the magnetron sputtering. In the second stage of the procedure, before starting the Au coating of the roughen filters, the system is vented with nitrogen, in order to open it and introduce the two half shells *Ku Band Low Pass Filter* without the cooling device. After the Ti target is replaced by the Au target the introduction port is closed and the system pumped, then, the procedure explained in Sec. 6.3.2 is followed.

7.3 Ti Cone Technique Results

In this section, the results obtained after the Ti cone coating technique applied on the *Ku Band Low Pass Filter* #0514 are presented. The ion beam was set at 900 eV with a beam current of 30 mA, as those were the conditions used to obtain the rough coating presented in Sec. 6.3.1, which as previously explained constituted a very homogeneous

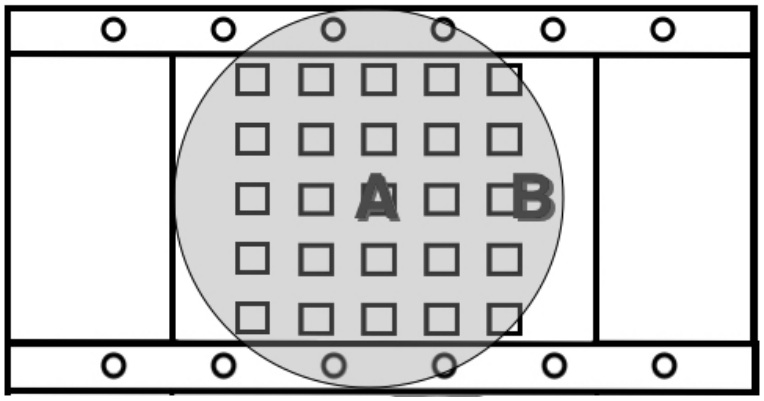

Figure 7.11: Schematic description of the *Ku Band Low Pass Filter* in the Ti cone technique configuration. Shaded area represents the area of the region exposed to the ion beam. Regions A and B, where SEM and SEY analysis were carried out are indicated.

rough surface of low SEY. An schematic description of the disposition of the cone and the filter is pictorially shown in Fig. 7.11, in which two regions marked with the letters A and B represents the regions where SEM and SEY analysis were carried out. In Fig. 7.12 and Table. 7.6, SEM analysis of the rough coating obtained is presented. It is noticeable the dramatic difference between the surface obtained on region A and Region B. Such a difference has been assumed to be due to the lack of homogeneity of the technique used. Region A shows a rough surface formed by rounded protuberances of an average size of $\sim$ 3.5 μm in diameter, separated from one another by deep pores covering distance that range from 1 to 10 μm. Such round protuberances constitute a second order roughness, similar to that found for Coating *W-1* in Ch. 6, which as observed in detail in the left panels of Fig. 7.12, are constituted by elongated wave like structures with a periodicity in the range of nm around the coarser protuberances in a coaxial disposition.

The morphology obtained in region B, unlike that for region A, exhibits a single ordered homogenous rough surface, formed by protuberances of tenths of μm in size, more than one order of magnitude bigger than the second order roughness on region A. By visual inspection of Fig. 7.12 bottom right panel, surface roughness seems to be of smaller aspect ratio and less abrupt and pore area is also smaller. Hence it was determined that pores constitutes a small percentage of the coated area. The presence of pores in region B could not be accurately determined, however at this point, such value did not constitute an information of crucial importance to reach solid conclusions about the coating obtained.

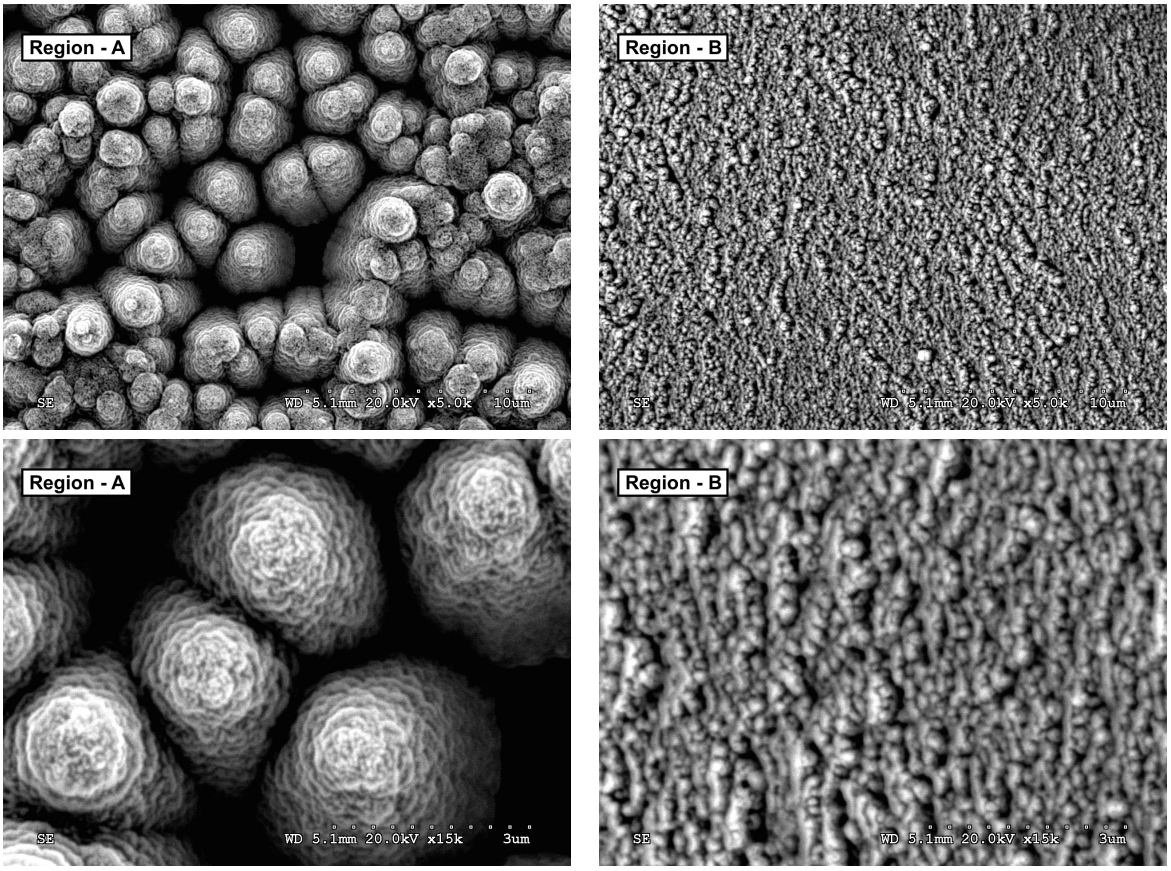

Figure 7.12: **Left:**SEM images acquired on region A of the surface of Filter #0512 after Ti cone technique treatment. **Right:** SEM images acquired on region B of the surface of Filter #0512 after Ti cone technique treatment.

	Beam Energy (eV)	Beam Current (mA)	Magnetron Power (W)	Ar Pressure (mbar)	Δt (sec)
Ion Etching	900	30	–	$3.85{\cdot}10^{-3}$	720
Au-Coating	450	15	50	$3.6{\cdot}10^{-3}$	90

Table 7.6: Summary of the beam energy, beam current and magnetron sputtering power parameters used on the treatment of Filter #0512

Two extremely different coatings were obtained on the same sample under the same technique conditions. Pore sizes were not comparable between both regions, also, the second order roughness of region A can not be due to the same cause that formed roughness on region B. The very different coatings reveal that Ti cone technique does not provide an homogenous source of Ti over the whole coated surface, resulting on an unpredecible behavior of the resultant morphology. A wide range of uncontrollable deposition conditions can take place, depending on the location of the roughness formed on the sample, for the same ion gun working parameters.

According to SEM results presented in Fig.7.12 it was assumed that the ratio I_{Ar^+}/I_{Ti} was too small in Region A, resulting in sharp protuberances surrounded by deep wide chasms. Such excess of Ti is in good agreement with the fact that region A is located

on the region were all the directions of the incoming Ti atoms sputtered from the Ti cone converge. On the other hand, due to the proximity of region B to the Ti come, the contribution of Ti to be restricted to its neighbouring areas uniquely, thus I_{Ar^+}/I_{Ti} ratio was assumed to be much smaller than for region A, which resulted in a more compacted small sized rough surface. Since previous experiments, in which this technique was applied, were carried out on small sized samples (1-1.5 cm^2) this dishomogeneity was not observed until larger ares were coated, $\sim$25 cm^2 in this case. It is remarkable the difference observed between the obtained coating in region A of Filter#0512 and Coating *W-2*, despite the same conditions, at the same geometrical location were used for both coatings. In fact region A of Filter#0514 is more similar to Coating *W-1*, even though the times of exposure differed from one another. Such effect was ascribed to a dramatic change in the heat dissipation capabilities of both kind of treated samples, which as demonstrated in Sec. 6.3.3 can play a crucial role in the morphology of the resulting surface.

SEY was measured on both regions A and B. The results are presented in Fig. 7.13. As expected from the sharp structure observed in region A, the high aspect ratio pores acted as faraday cups retaining emitting electrons, and avoiding them to scape to vacuum. The resulting SEY remained below 1 at all primary energies, finding a maximum value of $SEY_{max} = 0.96$. Such value represents an extremely good anti-Multipactor result, since SEY_{max} below 1 represents an almost null multipacting probability at any RF power. On the other hand, SEY measured on region B has a maximum value of $SEY_{max} = 1.38$, which also constitutes an important reduction comparing with the untreated filter.

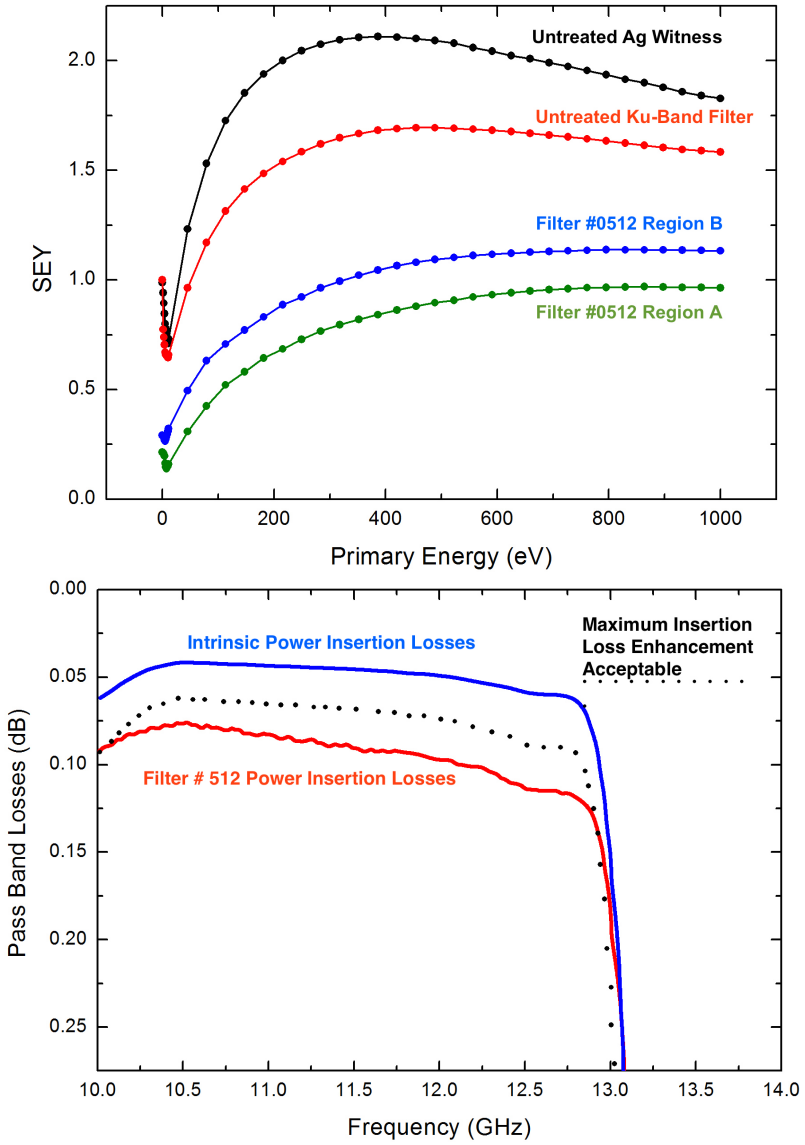

Figure 7.13: **Left:** SEY results measured on the treated filters (blue and green lines) compared withe the untrated filter (red line) and the untreated witness (black line). **Right:** Comparison of the IL results measured on the untreated filter (black line), and in Filter#0514 (red line). Black dots represent the maximum power loss enhancement acceptable for industrial use.

Despite the successful reduction of SEY obtained after exposing the *Ku Band Low Pass Filter* to the surface roughening procedure, the IL measurements developed by *TESAT Spacecom* reveal unfavorable results regarding the requirements of the project under which framework this thesis has been carried out. As depicted in Fig. 7.13 the IL were enhanced in $\sim$ 100% of the intrinsic value, being the 50% the maximum accepted enhancement, represented by black dots in the figure, see Sec. 7.1.1. In summary, Ti cone technique was proved to be an efficient procedure to obtain low SEY rough coatings. However a vast enhancement of the IL has been observed, which constitute a major problem for

the functionality of RF devices. Further attempts to reduce IL were not focused in this thechnique since the procedure was far to be controllable, being the resulting coatings extremely inhomogeneous, which limits the reproducibility of the coatings impeding its use as an industrial strategy.

7.4 Ion Assisted Magnetron Sputtering Technique Results

Due to the experimental inconveniences found for the Ti cone technique, the ion assisted magnetron sputtering technique described in Sec. 6.3.2 was used in order to find optimum anti-Multipactor coatings. A total of four filters: #0500, #0947, #0517 and #0499 used for this purposes are presented here. For simplicity the were named as Filter #1,#2, #3 and #4 respectively. In this section, the results obtained after the ion assisted sputtering coating technique applied on the K_u *Band Low Pass Filters* are presented. The ion beam was set at 900 eV while varying beam current in order to find the optimum conditions, to obtain rough coatings as favorable as those presented in Sec. 6.3.2, which as previously shown constituted a very homogeneous rough surface of low SEY.

7.4.1 Surface Morphology

An schematic description of the *Ku Band Low Pass Filters* is pictorially shown in Fig. 7.11, in which the central area has been magnified. Three regions marked with the letters A, B and C represents the regions on which SEM analysis was carried out. it has been found, that the ridges that form the *Waffle Iron Ku Band Low Pass Filters* have a shade effect on the incoming evaporated Ti atoms. Since the magnetron sputtering head is installed forming an angle of 32.5°, Ti atoms trajectories are hampered by the ridges, being able to reach the bottom surface of the inner part of the shell, only when they align with the free space between ridges rows during sample rotation. On the other hand, ion flux is not affected by the macroscopic intrinsic corrugation of the filters, since the ion beam is applied at normal incidence, the same amount of ions reach the sample on the three regions.

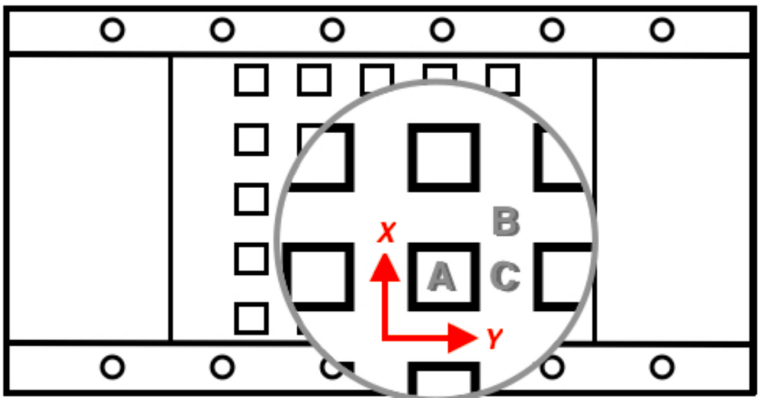

Figure 7.14: Schematic of the single carrier Ku-band Multipactor test configuration.

Region A is located at the top of the ridges, where no shade effect takes place, and Ti atoms find no obstacles to reach the surface. Region B is located at the bottom part of the surface, where Ti atoms reach the surface when their trajectories align with both directions X and Y shown in Fig. 7.14. Region C is located at the bottom part of the surface, where the amount of Ti atoms reaching the surface is reduced considerably being constrained t the condition of aligning with Y uniquely. In the following subsections, SEM images obtained accompanied with the ion gun and magnetron sputtering parameters are presented. For this reasons the morphology of the surface was analyzed in both the bottom and and the top of the ridges.

7.4.1.1 Filter # 1

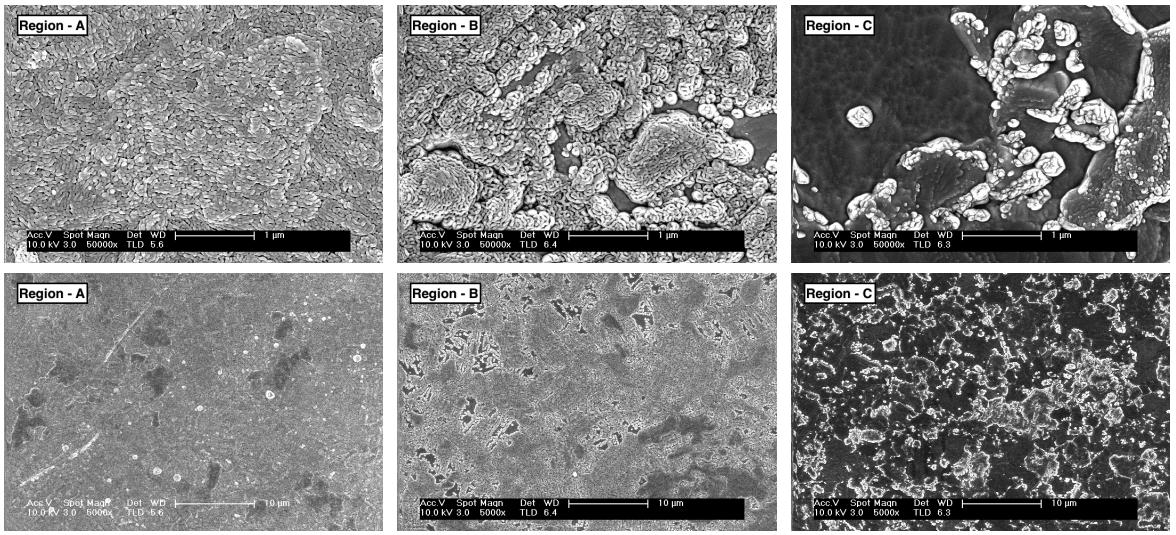

Figure 7.15: **Left:**SEM images acquired on region A of the surface of Filter #1 after ion assisted magnetron sputtering technique treatment. **Center:**SEM images acquired on region B of the surface of Filter #1 after ion assisted magnetron sputtering technique treatment. **Right:**SEM images acquired on region C of the surface of Filter #1 after ion assisted magnetron sputtering technique treatment.

7.4.1.2 Filter # 2

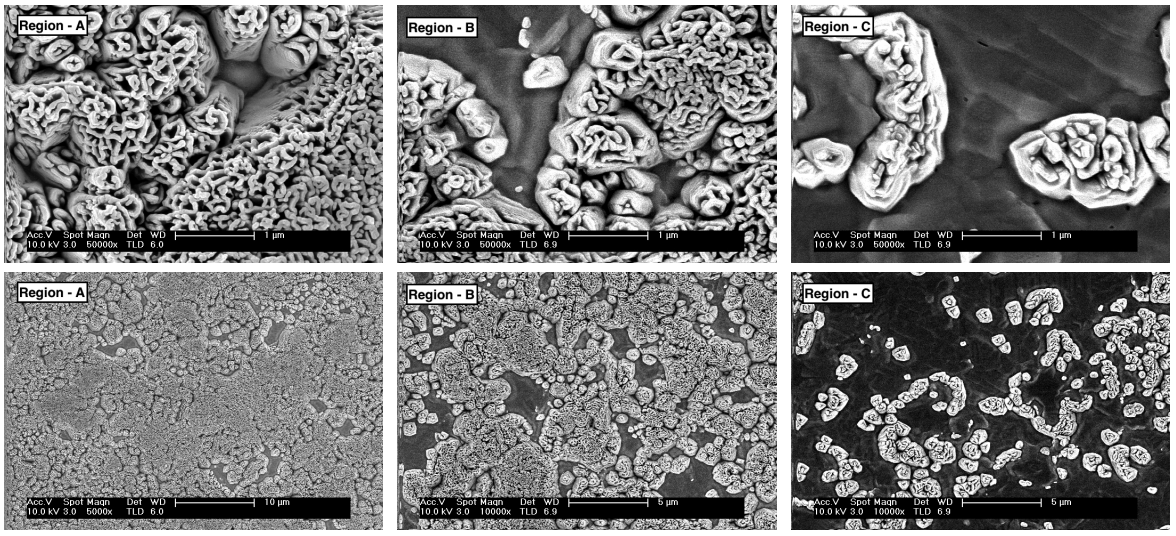

Figure 7.16: **Left:**SEM images acquired on region A of the surface of Filter #2 after ion assisted magnetron sputtering technique treatment. **Center:**SEM images acquired on region B of the surface of Filter #2 after ion assisted magnetron sputtering technique treatment. **Right:**SEM images acquired on region C of the surface of Filter #2 after ion assisted magnetron sputtering technique treatment.

7.4.1.3 Filter # 3

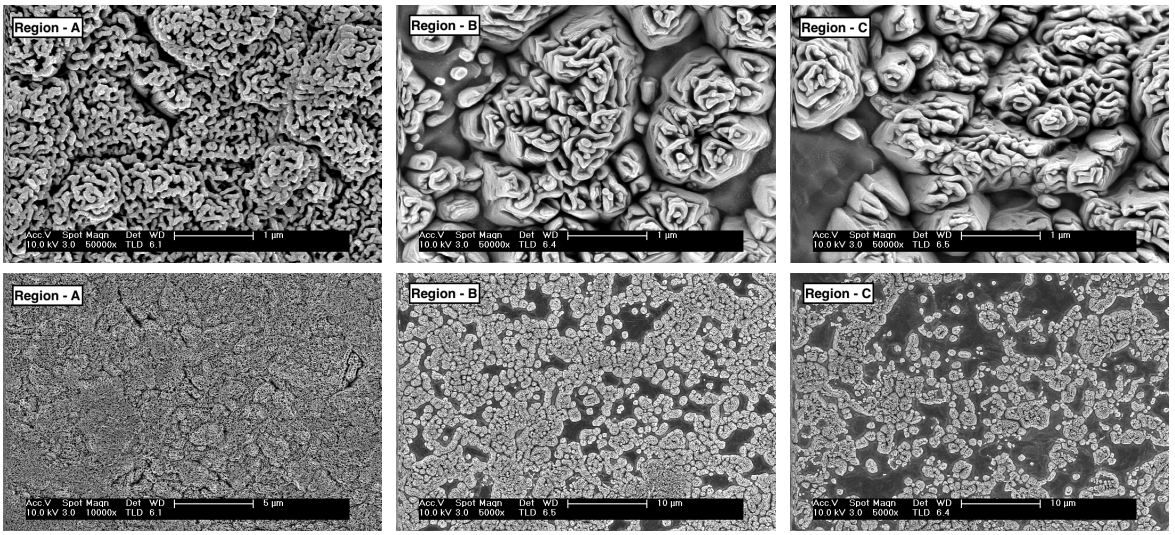

Figure 7.17: **Left:**SEM images acquired on region A of the surface of Filter #3 after ion assisted magnetron sputtering technique treatment. **Center:**SEM images acquired on region B of the surface of Filter #3 after ion assisted magnetron sputtering technique treatment. **Right:**SEM images acquired on region C of the surface of Filter #3 after ion assisted magnetron sputtering technique treatment.

7.4.1.4 Filter # 4

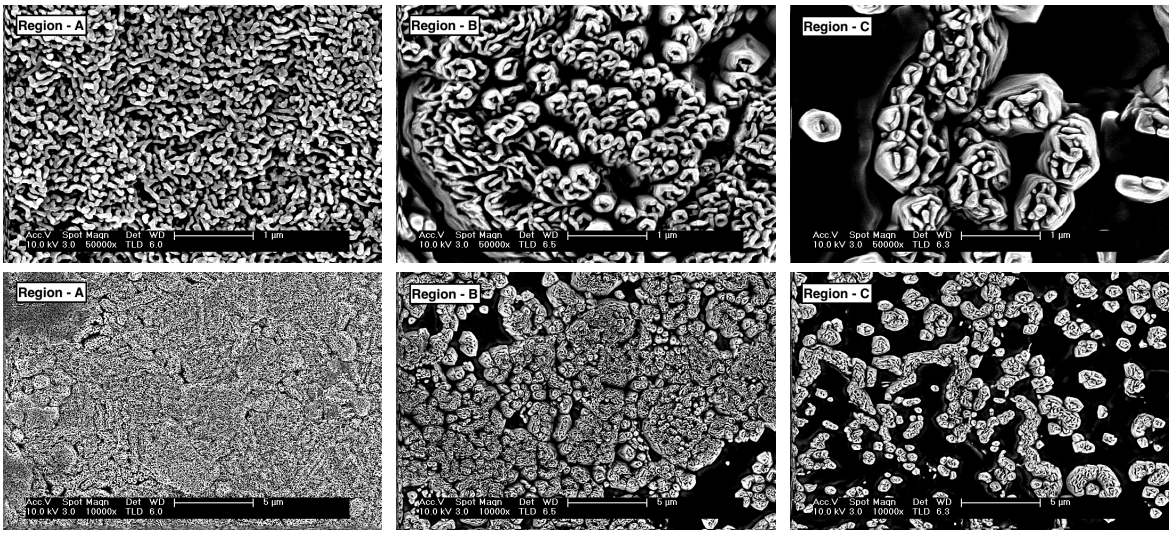

Figure 7.18: **Left:**SEM images acquired on region A of the surface of Filter #4 after ion assisted magnetron sputtering technique treatment. **Center:**SEM images acquired on region B of the surface of Filter #4 after ion assisted magnetron sputtering technique treatment. **Right:**SEM images acquired on region C of the surface of Filter #4 after ion assisted magnetron sputtering technique treatment.

		Beam Energy (eV)	Beam Current (mA)	Magnetron Power (W)	Ar Pressure (mbar)	Δt (sec)
Filter #1	**Masked Ion Etching**	900	15	125	$3.85{\cdot}10^{-3}$	720
	Au-Coating	900	15	100	$3.6{\cdot}10^{-3}$	90
Filter #2	**Masked Ion Etching**	900	30	125	$3.80{\cdot}10^{-3}$	900
	Au-Coating	900	15	100	$3.6{\cdot}10^{-3}$	90
Filter #3	**Masked Ion Etching**	900	20	125	$3.82{\cdot}10^{-3}$	900
	Au-Coating	900	15	100	$3.6{\cdot}10^{-3}$	90
Filter #4	**Masked Ion Etching**	900	22.5	125	$3.82{\cdot}10^{-3}$	900
	Au-Coating	900	15	100	$3.6{\cdot}10^{-3}$	90

Table 7.7: Summary of the beam energy, beam current and magnetron sputtering power parameters used on the treatment of Filter #1, #2, #3 and #4

7.4.1.5 Summary

In a general way, the SEM analysis of the surface morphology of the treated filters reveal an important effect of the Ti shadowing due to the presence of the macroscopic ridges, which is common for all the treated filters. As observed on the SEM analysis, the surface morphology on the top of the ridges is a rather close-grained coating, while regions B and C, are characterized by the presence of both isolated coated areas formed by clusters of protuberances and gaps among them, and uncoated patches, where the strong ion erosion impeded roughness formation. This effect increasing in the direction A $<$ B $<$ C. The shadowing of the Ti atoms resulted in an increase of the J_{ion}/J_{Ti} ratio, which has important effects on the morphology of the resulting coating on the shaded regions. Similarly to the surface morphology observed in Fig. 6.9 correspondent to Coating *W-3*, the excessive flux of ions on this regions impedes the formation of a continious rough coating, resulting in the appearance of uncoated patches, with the characteristic morphology of ion bombarded polycristallyne Ag shown in Fig. 6.1. The formation of such uncoated patches, where the rough coating can not be achieved, is predominant at region C were, as explained above, the shadowing is more effective. Magnetron power was kept in a constant value of 125 W since it was proved that such conditions guarantee the most stable and controllable performance of the magnetron sputtering head under the desired conditions of pressure. Unlike for the magnetron sputtering head, controlling and tuning the ion fluxes was straightforward due to the versatility of the kauffman ion gun, and hence its parameters were adjusted and optimized in order to achieve an optimum coating. Table 7.8 summarize the results of the quantitative study carried out on the morphology of each surface.

According to the exposed in Sec. 3.5.1, when an electromagnetic wave of certain frequency travels along the filter, at the points where the gap between the walls reaches its minimum, multipactor discharge is more likely to happen [2, 4, 64]. Is for this reason that the analysis of the morphology was focused on the top of the ridges, previously labeled as region A.

It is clearly noticeable that pore sizes (and correspondingly, prouberance sizes) directy depend on the ion fluxes applied on the sample. In this manner the average pore area of Filter#1, during which treatment the beam current was set to 15 mA, has been calculated to be $\overline{P_{Area_{\#1}}} = 5.9 \cdot 10^{-4} \mu m^2$, representing the smallest pore size value. However the measured porosity was $\sim 5.4\%$ which represents a very low value, and hence a very low probability for electrons to interact with the present pores is expected. For these reasons, the effect on SEY is not expected to be sufficient to reduce its maximum to a convenient value, for anti-Multipactor purposes.

		Uncoated Area (%)			Coated Area in Region A		
Filter	Beam Current (mA)	Region A	Region B	Region C	Porosity %	Average Pore Area (μm^2)	Coefficient of Variation (%)
#1	15	0	6.0 ± 0.3	–	5.0 ± 0.2	$5.9 \cdot 10^{-4}$	60
#2	30	5.0 ± 0.	20 ± 1	74 ± 4	40 ± 2	0.012	220
#3	20	0	14 ± 1	53 ± 3	34 ± 2	0.012	240
#4	22.5	0	10 ± 1	60 ± 3	38 ± 2	0.010	106

Table 7.8: Summary of the results obtained after color threshold analysis performed on the treated K_u-*Band Low Pass Filters*

As the beam current was increased, the average pore area of the treated surface increased accordingly, reaching values of $\overline{P_{Area_{\#2}}} = 1.2 \cdot 10^{-2} \mu m^2$ for Filter #2 during which treatment the beam current was set to 30 mA. The porosity in this case increased up to 40 %. It is worth noticing that in the latter case, the appearance of non-rough patches in region A, which constitutes ~ 5 % of the total area. This result clearly denotes an excess in the ion flux, which not only produces pores of larger pore area, but also in some regions, avoids the formation of close-grained roughness. Beam current was set on intermediate values of 20 mA and 22.5 mA for Filter #3 and Filter #4 respectively which resulted in a porosity of 34% for Filter #3, and a 38 % for Filter#4. Average pore areas were found to be $\overline{P_{Area_{\#3}}} = 1.2 \cdot 10^{-2} \mu m^2$ and $\overline{P_{Area_{\#3}}} = 1.0 \cdot 10^{-2} \mu m^2$ remaining invariant in these last two cases, and no uncoated patches were found resulting in well close-grained rough structures. It is remarkable the effect that the beam current set at the Kauffman ion gun has on the

porosity, revealing a strong dependance of the resulting morphology on the intensity of the ion flux.

In Ch. 6 a hypothesis, based on the SEM analysis, for the temporal dependance of the roughness growth was presented. In such model it was stablished that a minimum amount of Ti was needed for the roughnes structure to start growing and when Ti fluxes remain bellow such threshold the effect of the Ar^+ was predominant. The effect of the Ti shadowing due to the presence of the macroscopic ridges was in fact extremely usefull to crosscheck this fact, and analize the effect that the variations in the J_{ion}/J_{Ti} ratio have on the resultant surface morphology. Fig. 7.19 shows a schematic description of the dependance of the morphology with an increasing J_{ion}/J_{Ti} ratio, which was observed to be as follows; **A)** An excess of Ar^+ fluence avoids the formation of protuberances and the morphology resulting in a smooth surface which morphology comes determined by the preferential erosion of different crystalline domains (see Fig. 6.9 of Coating *W-3*). **B)** An decrease on the J_{Ar^+}/J_{Ti} ratio facilitates the formation of isolated protuberance clusters formed by protuberances and gaps (see Region C in Figs. 7.15-7.17 of Filters #1-#4). **C)** The morphology evolves towards a close-packed rough surface with the presence of scarce uncoated areas (see Region A in Fig. 7.16 of Filter #2). **D-E)** An appropriate J_{Ar^+}/J_{Ti} ratio results in a close-packed rough surface absent of uncoated areas as it can observed in the cross section SEM figures of Coatings *W-4* and *W-5* the depth of the pores of the surface decreases as the amount of sputtered Ti increases wit respect Ar^+ fluences. Also a decrease of the pore areas with J_{Ar^+}/J_{Ti} ratio is manifested. **F)** Such decrease of the pore areas dramatically enhanced as the ammount of sputtered Ti predominates with respect Ar^+ fluences as it can be observed in Fig. 7.17 of Filter #4.

Outside of the general trend observed and above presented, there are the results regarding Filter #514. As previously mentioned, the huge difference observed between the coatings obtained in region A and Region B (see Fig. 7.12) were ascribed to a significant difference in the amount of deposited Ti, resulting J_{ion}/J_{Ti} smaller for the central Region A. In this case the surface morphology is dominated by rounded protuberances of an average size of ~ 3.5 μm in diameter, separated from one another by deep pores covering distance that range from 1 to 10 μm which is in clear contradiction with the case **F)** in Fig. 7.12. The fact that the technique used for Filter #514 differs from that used for the rest of the

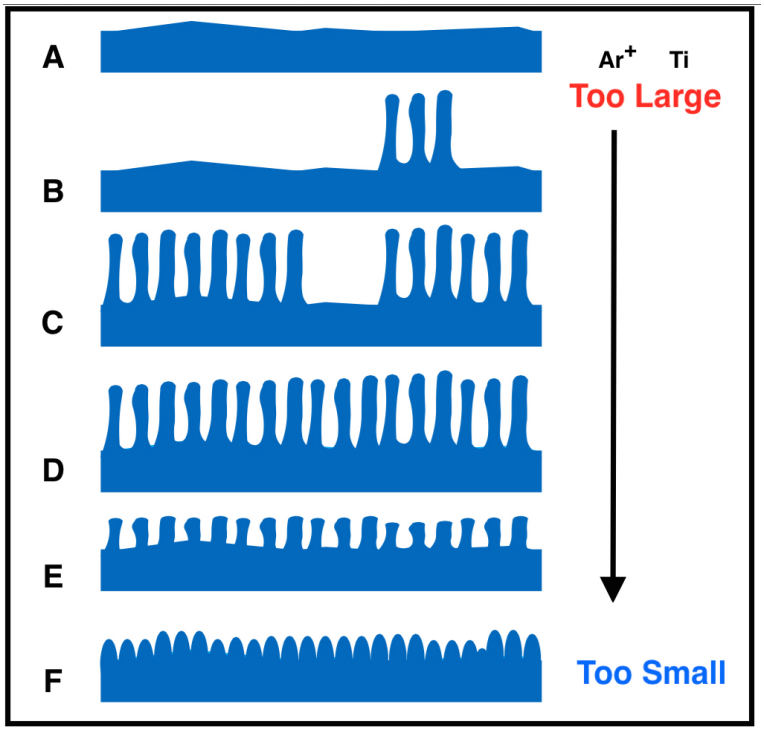

Figure 7.19: Model proposed for the evolution of the surface morphology under masked ion etching treatment, according to SEM observations presented in Chs. 5 and 6.

analyzed surfaces has been assumed to be at the origin of such discrepancy, revealing a strong dependance on the technique used.

It is important to emphasize in the limitations of our experimental set-up due to which a qualitative analysis was not possible to carry out, and unfortunately only qualitative studies are here presented according to our observations. Nevertheless this results constitute an important previous step in the understanding of our system and the perfectioning of the techniques to be used in a near future.

7.4.2 SEY Results

SEY measurements were carried out on all the treated samples. The results, depicted in the left panel of Fig. 7.20, show that in all cases SEY was reduced and first crossover $E_{0,1}$ was increased due to the roughness formed after treatments, in good agreement with the expected from the morphological analysis. The values of the SEY parameters obtained are presented in Table. 7.9. *SEY* curve measured on Filter #1 reveals an important increase on the SEY first crossover, being $E_{0,1}$= 150.5 eV which contributes positively to

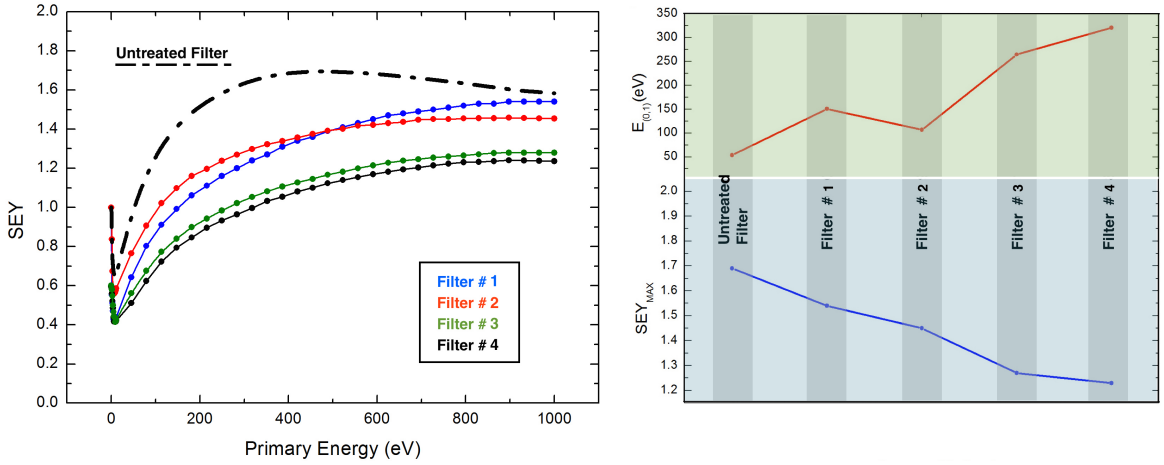

Figure 7.20: **Left:** Comparison between the SEY results measured on the untreated *K_u-Band Low Pass Filter* (Black dashed line) and the SEY results measured after the ion assisted magnetron sputtering trueatment applied on Filters #0500, #0497, #0519 and #0489 (Colored lines) . **Rightl:** Evolution of $E_{0,1}$ (Red line) and SEY_{max} (Blue line) of each of the *Ku Band Low Pass Filters* studied.

Multipactor effect avoidance, see Sec. 3.5.2. However its behavior at primary energies above 400 eV is characterized by a continuous increase up to $SEY_{max} = 1.54$, resulting on a slight decrease of SEY_{max} of the 8.9% of the untreated sample. Accordingly to the expected from SEM analysis, reduction of SEY after surface treatment of Filter #2, was more effective than the resulting after treatment of Filter #1, in good agreement with the increase of the porosity. Such effect increased the probability of primary electrons to suffer the effect of the surface corrugation, accompanied by the corresponding avoidance of the emitting electrons to scape into the vacuum. As a result SEY_{max}= 1.45 was obtained which represents a reduction in a 14,2 % of the value for the untreated sample. However, an important decrease on the value of the first crossover with respect Filter #1 was observed, being $E_{0,1} = 106.6$ eV, still higher than for the untreated filter. As shown in the right panel of Fig. 7.20 this value is clearly outside of the general trend of the SEY behavior for all filters.

The determination of the origin of such behavior is not straighforward. On one hand SEM analysis of Filter #2 shown in Fig. 7.17, Region A revealed the anomalous presence of uncoated patches on Region A due to an excess in the ion flux. The detrimental effect of such morphology on SEY is clear since electrons escaping to vacuum through uncoated regions find no obstacle as it happens for the untreated sample. Being this morphology an exceptional case among all the treated filters, it has been suggested as a possible cause for the anomalous decrease $E_{0,1}$ on Filter #2. On the other hand, due to the special conditions

Filter	SEY_{max}	$E_{(0,m)}$ (eV)	$E_{(0,1)}$ (eV)
Untreated	1.69 ± 0.08	488 ± 1	53.5 ± 1.0
1	1.54 ± 0.07	> 1000	150.8 ± 1.0
2	1.45 ± 0.07	> 1000	106.6± 1.0
3	1.27 ± 0.06	> 1000	264.4± 1.0
4	1.23 ± 0.06	> 1000	320.5± 1.0

Table 7.9: Values of SEY_{max}, $E_{0,m}$ and $E_{0,1}$ of each of the *Ku Band Low Pass Filters* studied

of spot diameter and sample macroscopic morphology under which the data was acquired the possibility of the behavior of $E_{0,1}^{\#2}$ to be result of certain experimental error must not be discarded. Moreover, it is also worth taking into consideration the possibility of an excess of surface contamination with respect of the rest of the filters, originated by certain uncontroled phenomenon.

Filter #3 and Filter #4 follow a similar behavior characterized by a diminishment of their SEE yield with respect to both filters previously analyzed. Such similar behavior in shape and magnitude of the SEY curve is in good agreement with SEM results, which reveal a porosity, similar both filters. The larger porosity facilitates the reduction of SEY down to values of $SEY_{max} = 1.27$ and $SEY_{max} = 1.23$ for Filter #3 and Filter #4 respectively.

7.4.3 Multipactor Test Results

The Multipactor tests were carried out in different steps or stages. Fig. 7.21 show the evolution of the RF power applied on the Filter under study. In the first stage the RF power is set at $\sim$ 1200 W, and kept at that level for $\sim$ 10 minutes. After each stage the RF power is increased $\sim$ 1000 W and kept during another 10 minutes. If a discharge was observed at any stage of the test, the power was reduced to the previous step in order to extinguish the discharge. Then the power was increased again to restart the test. In case of a second event was observed, testing was stopped. If no discharges were observed up to 14000 W, before switching off the RF power, the power level was increased progressively to 15000 W which represents the maximum power value dispensable by the testing set-up. Then, the test was stopped.

Multipactor results obtained are presented in Table. 7.10. It is noticeable that second discharges happen at higher RF power than first discharges which means that after a multipactor discharge has taken place, the threshold tends to increase. Such result is in good agreement with previous observations regarding electron conditioning or *Scrubbing*.

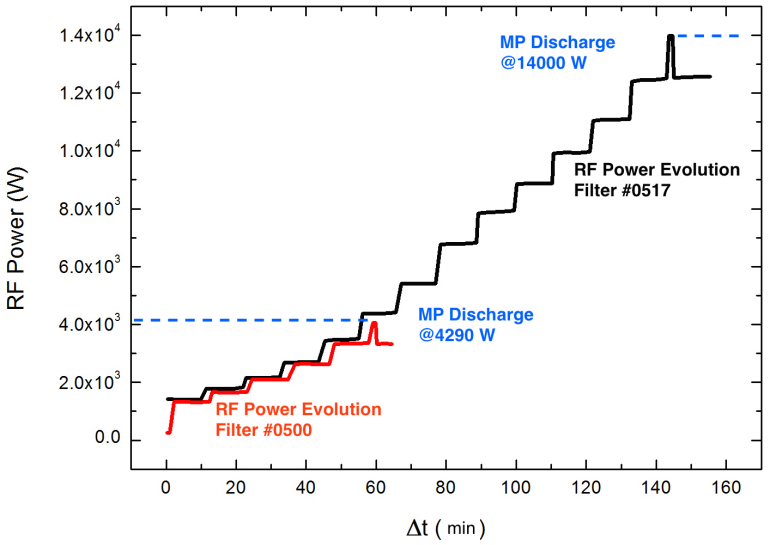

Figure 7.21: Evolution with time of the power applied on the *Ku Band Low Pass Filters* #3 (Black line) and #1 (Red line) during the Multipactor threshold measurement procedure.

Filter	RF Power		Detection technique				
	1^{st} MPT [W]	2^{nd} MPT [W]	Nulling	2^{nd} Harm.	3^{rd} Harm.	EM1	EM2
Untreated	2900	2900	yes	yes	yes	yes	yes
#1	4290	3520	yes	–	yes	–	–
#2	5570	7020	–	–	–	–	yes
#3	14000	14000	yes	–	–	yes	yes
#4	14800	>15000	yes	–	yes	yes	yes

Table 7.10: Summary of the results of the Multipactor test performed on the treated *Ku Band Low Pass Filters*. Threshold values are presented as well as the detection technique through which the discharge was observed.

As pointed out in Sec. 4.3.2 in the field of particle accelerators, the intentional e^- cloud discharge generation is often a very efficent way to reduce SEY of technical surfaces by means of electron conditioning [20, 106, 111]. The effect that electron irradiation has on the chemical state of the wall surface, often produces a significant reduction of the SEY [18, 19], whose reduction is known to be favorable for multipactor threshold increase and even Multipactor mitigation.

In our case, a close relationship between SEY and multipactor thresholds is observable. As shown in the left panel of Fig. 7.22, the evolution of the Multipactor thresholds is strongly correlated to the value of SEY_{max} of each filter, being the value of the former, larger as the latter decreases, as expected from previous studies [31, 33, 66] . The left panel of Fig. 7.22 show the relationship existent between the Multipactor thresholds and the value of $E_{(0,1)}$ of each filter. In this case, according the expectations, a correlation is observed, showing a tendency of the discharge threshold to increase with $E_{(0,1)}$. However a singular behavior is also observed corresponding to the anomalous value $E_{(0,1)} = 106.6$ of Filter #2 which origin was briefly discussed in Sec. 7.4.2.

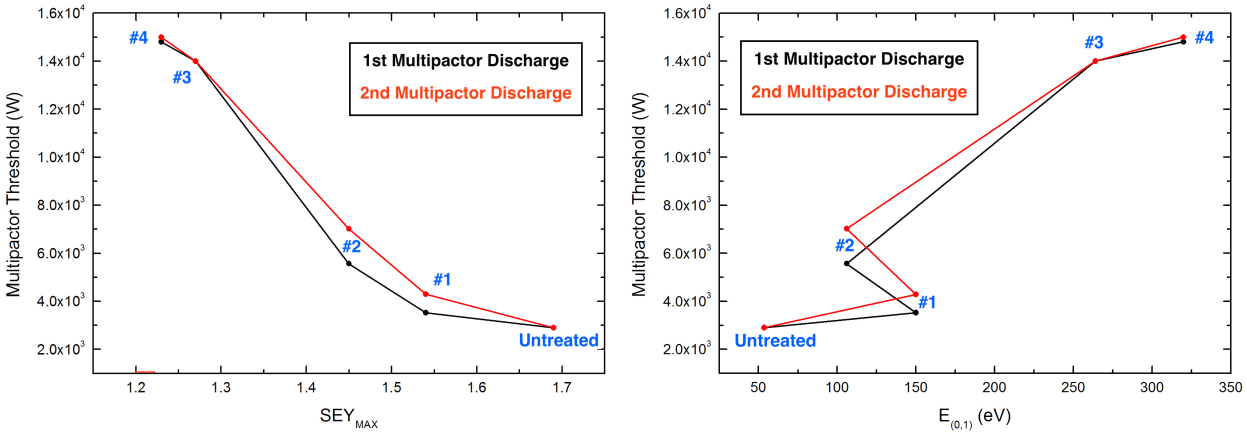

Figure 7.22: **Left panel:** Multipactor threshold measured on the treated *Ku Band Low Pass Filters* as a function of SEY_{max}. First Multipactor test (Black line), and second Multipactor test (Red line) results are shown . **Right panel:**Multipactor threshold measured on the treated *Ku Band Low Pass Filters* as a function of $E_{0,1}$. First Multipactor test (Black line), and second Multipactor test (Red line) results are shown

Clearly, the observed behavior of the SEY parameters confirm the well known fact that Multipactor thresholds strongly depend on the SE emitting properties of the coating material of the filter, being larger, as the number of SE is decreased, i.e. low SEY_{max} and large $E_{(0,1)}$. However despite the good correlations often achieved between SEY parameters and Multipactor thresholds, it is important to take into account that, even though quantifiable SEY parameters could be extremely useful to obtain some close expectations of what Multipactor susceptibility could be, it is necessary to make use of simulation softwares in order to obtain quantitative reliable predictions. In this thesis Multipactor susceptibility simulations were carried out by using the software MEST [31], which was developed within the framework of a project sponsored by the European Space Agency (ESA), as a tool to predict the occurrence of multipactor discharge in a simple radio frequency (RF) device modeled as parallel plates and includes a detailed Monte Carlo model of the SEE process in the plates.

7.4.3.1 MEST Simulation Results

The simulator has been validated using experimental data gathered at ESA and the Universidad Autonoma de Madrid and helped in the selection of material coatings for the mitigation of Multipactor effect in RF transmission lines on-board satellite payloads.

The system performs Montecarlo simulations where each electron is individually tracked. A discrete-event approach is followed, where the events are the collisions of electrons with the waveguide walls. The impacting electron can be absorbed, elastically or inelastically reflected, or true secondaries can be produced. In the latter case, the generated electrons are incorporated to the simulation and individually tracked in their turn. Materials are described by using the usual SEY parameters, i.e. SEY_{max}, $E_{(0,1)}$, $E_{(0,m)}$ and $E_{(0,2)}$ complemented with a more detailed model, where the contributions due to true secondary, backscattered or elastically reflected electrons are used. The contribution of inelastically backscattered electrons elastically backscattered electrons and by true SE's is modeled according to theoretical models available in the literature, with the atomic number Z as main control parameter.

The simulator generates V vs $f\text{x}d_{Th}$ maps of the Multipactor discharge detected in the simulations within the desired range of $f\text{x}d_{Th}$ values. However data obtained from the Multipactor thresholds tests carried out at the European High Power Laboratory are expressed in units of input power. Such discrepancy is due to the difference of suitability of each method. While the input power is a well known and controllable parameter facilitated by the measurement set-up at the laboratory, obtaining the value of the power between the walls at each section of the wave guide using MEST simulation software is not straightforward. The voltage applied within the filter walls is known to be related to the wave input power as follows:

$$P \propto (V)^2 \tag{7.4}$$

were the constant in the latter relationship depends on many unknown parameters such as waveguide impedance or geometry, hence the accurate calculation of the applied wave input power, starting from the voltage in a waveguide section, is a very advanced problem that remains outside of the scope of this thesis. Nevertheless, in order to be able to compare MEST simulation results, and measured Multipactor thresholds, certain calibrations can be done. The calibration procedure is simple. Knowing the SEY parameters of certain reference sample, which Multipactor threshold was previously measured, MEST simulation results are obtained by using its SEY parameters, and those related with the material

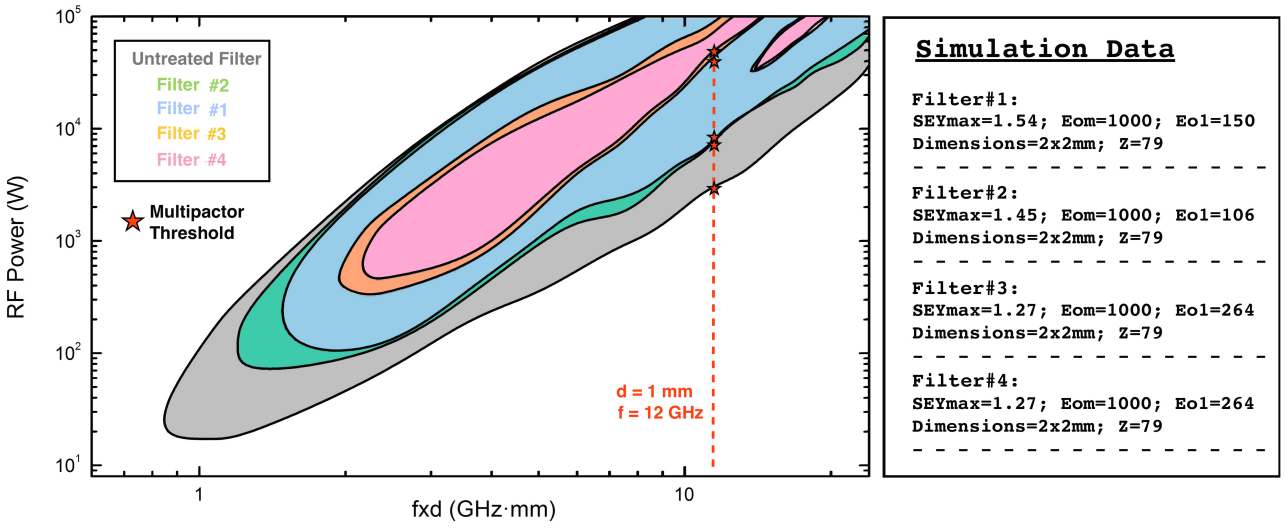

Figure 7.23: Multipactor susceptibility regions obtained after MEST simulations according with the SEY parameters presented in Table. 7.9.

properties of the sample coating. Then in order to obtain the correspondent *Power* vs fxd_{Th} map, and making use of Eqn. 7.4 the following expression is used to calculate the corresponding ordinate axis power values:

$$P = P_{Ref}\left(\frac{V}{V_{Ref}}\right)^2 \tag{7.5}$$

Where P_{Ref} is the measured Multipactor threshold, V is the simulated value of the voltage applied within the parallel plates of the waveguide to be converted and V_{Ref} is the simulated value of the voltage applied at the value of fxd_{Th} chosen according to the conditions of the threshold measurements. Simulations presented here were carried out by using the untreated filter as a calibration sample, which Multipactor threshold was measured at 2900 W for an input frequency of 11.25 GHz.

Infinite and finite parallel plates in the xy plane can be considered, with the RF electric field unidirectional in the z coordinate. For the simulations carried out in this thesis finite parallel plates were considered, corresponding to the actual shape of the waffle iron filter. Taking into account the dimensions of the ridges reported in Sec. 7.1.

Mest simulation were performed by using the SEY parameters presented in Table. 7.9 as input values, and the Multipactor susceptibility regions are shown in Fig. 7.23 after

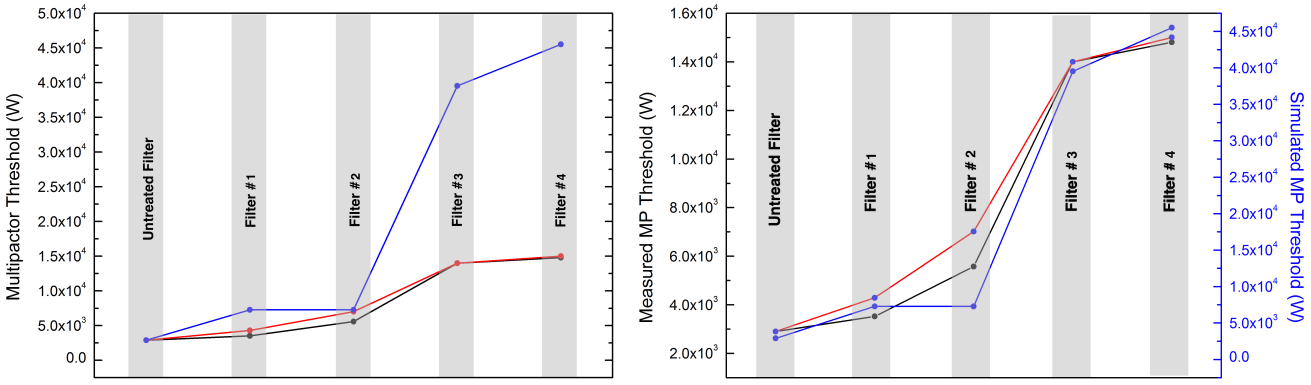

Figure 7.24: **Left:** Evolution of the Multipactor threshold values obtained experimentally (Black and red lines) and after MEST simulations, of each of the *Ku Band Low Pass Filters* studied. **Right:** Evolution of the Multipactor threshold values obtained experimentally (Black and red lines) and after MEST simulations, of each of the *Ku Band Low Pass Filters* studied. Simulated results have been rescaled in order to appreciate that the evolution of the Multipactor thresholds is similar for the simulated and the measured values in absolute terms.

power calibration procedure. Multipactor thresholds at the fxd_{Th} value corresponding to the parameters used at the European High Power Laboratory are indicated.

It is noticeable how not only Multipator thresholds increase, but also the whole susceptibility region shrinks for all values of fxd_{Th}. The left panel of Fig. 7.24 depicts a comparison between the Multipactor thresholds measured, and those obtained after simulation, which numerical results are presented in Table. 7.11. A clear discrepancy is observed between both kinds of data. As it is logical, the value of the multipactor thresholds obtained by both ways, experimental and simulated, are coincident for the untreated filter, since the calibration of the power values described by Eqn. 7.5 was subjected to that boundary condition.

However, as multipactor threshold increases the discrepancy becomes larger remaining simulated values always larger than those obtained experimentally. Such behavior was ascribed to certain source of inaccuracy in the calibration method. The behavior observed in the left panel of Fig. 7.24, is in fact in good agreement with the fact that, as pointed out in Sec. 7.1 the SEE results are drastically affected by the presence of the intrinsic macroscopic corrugation characteristic of the *Waffle iron filter*, and the SEY obtained corresponds to average values between the top and the bottom of the ridges, while Multipactor simulations were carried out using a value of 1mm for the gap between walls, which corresponds to the top side of the ridges uniquely. According to the analysis shown in Fig. 7.4 the actual SEY at the top of the ridges, where multipactor is more likely to happen is expected to

	RF Power		
Filter	**1^{st} MPT [W]**	**2^{nd} MPT [W]**	**MEST-MPT [W]**
Untreated	2900	2900	2900
#1	4290	3520	7275
#2	5570	7020	7275
#3	14000	14000	39525
#4	14800	>15000	45512

Table 7.11: Experimental and simulated Multipactor threshold values .

be higher than the measured which makes simulated Multipactor thresholds appear higher than the measured values. Nevertheless, despite the inaccurate calibration, both sets of data maintain the same relationship among each other and the evolution of the Multipactor thresholds is similar for the simulated and the measured values in absolute terms, as shown in the right panel of Fig. 7.24.

It is remarkable, that the simulated Multipactor susceptibility region is wider for Filter #2 than for Filter #1, which means that even though $SEY_{max}^{\#2}$ is smaller than $SEY_{max}^{\#1}$, the fact that the trend that their $E_{0,1}$ values follows are inverted, results in a strong effect in the Multipactor dependance on the SEY of our samples. Once again, the obtained value for Filter#2 appears outside of the general observed trend revealing a great discrepancy with the measured Multipactor threshold value. Such discrepancy, according to the abnormal behavior related to the SEY of Filter#2 previously observed in Figs. 7.22 and 7.20, has been finally ascribed to a lack of accuracy in the measurement of the SEY of Filter#2 due to an uncontrollable and eventual error related to the surface contamination of the surface. In this way MEST simulations confirms the premise settled by previous authors [31, 33, 66, 207], supporting the idea that $E_{0,1}$ plays an major role in the Multipactor susceptibility region.

7.4.4 IL Results

Last but not less important, power IL measurements on the treated filters were performed. As previously noted in Sec. 7.1.1, among the objectives of the ESA ITI project "Optimization of Surface Roughness of Anti-Multipactor Coatings for Low IL and Secondary Emission Suppression for High Power RF Components in Satellite Systems", in which framework this work was developed, there is the requirement of maintaining power IL enhancement of the *Ku-Band Low pass filters* bellow 50% of their initial value. Results of the RF power IL measured on the untreated filter were previously shown in Sec. 7.1. The value of the power

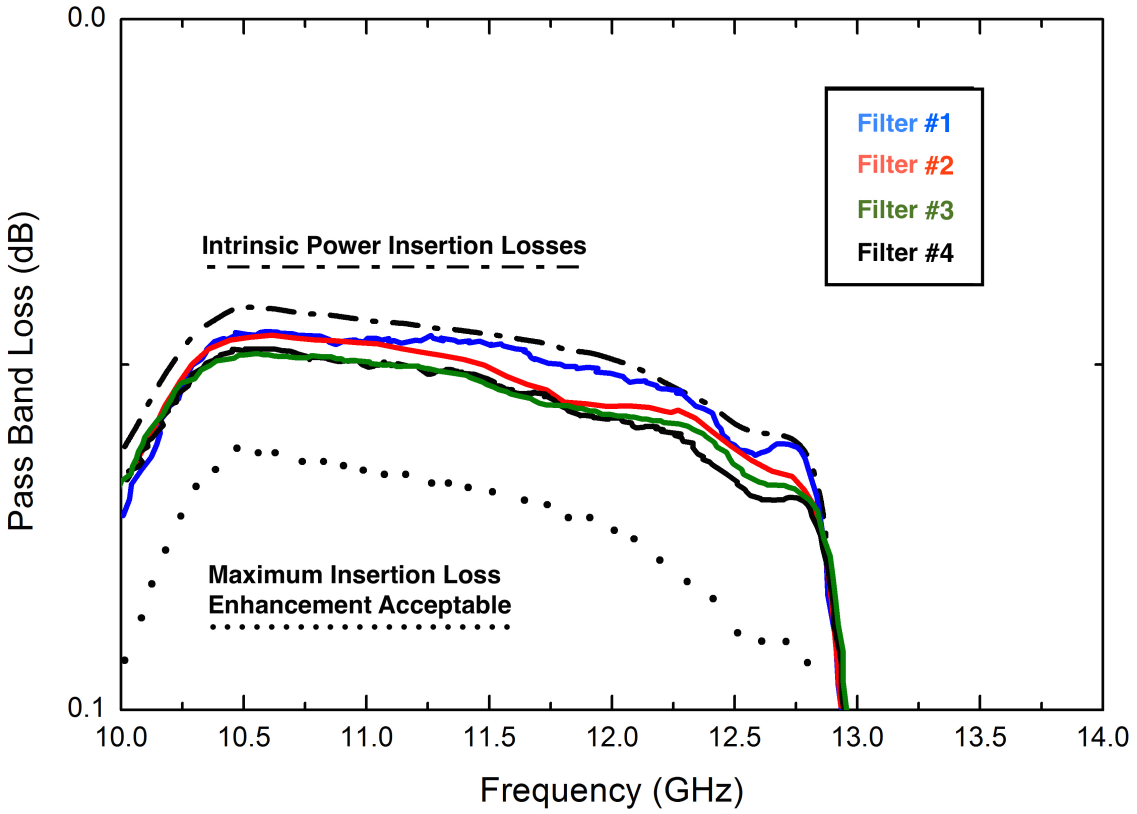

Figure 7.25: Comparison between the initial IL of the untreated K_u-*Band Low Pass Filter* (Black dashed line) and the IL measured after the ion assisted magnetron sputtering trueatment applied on Filters #1, #2, #3 and #4 (Colored lines). Black dots represent the maximum power loss enhancement acceptable for industrial use.

IL enhancement resulted to range between 0.04 and 0.06 dB across the whole band pass, as obtained by using Eqn. 3.42. Also IL results of filter #1 on which the Ti cone technique was applied, were previously presented in Sec. 7.3. The IL enhancement of filter #0514 resulted to range between 0.09 and 0.11 dB, which represents an increase of $\sim$ 100% of the initial value. Similar studies were developed on the filters on which the ion assisted magnetron sputtering technique was applied. The results compared with the intrinsic IL of the untreated filter are presented in Fig. 7.25. Black dots represent the IL enhancement limit set by the objectives of the project exposed in Sec. 7.1.1.

Measurements reveal extremely favorable results. The highest values of the IL enhancement correspond to Filter #2, and range between 0.047 and 0.067. The latter suppose an increase corresponding to the $\sim$ 18% of the intrinsic value, well within the limits imposed in the objectives of the project. Such a small power loss enhancements confirms the stablished fact that power losses, as well as the local surface resistance, which are indeed enhanced by surface roughness, can be dramatically reduced as long as the size of surface structures

are reduced to values smaller than the skin depth, i.e. 750 and 610 nm for Au and Ag at 12 GHz respectively.

7.5 Summary

The results obtained in the framework of the ESA ITI project "Optimization of Surface Roughness of Anti-Multipactor Coatings for Low IL and Secondary Emission Suppression for High Power RF Components in Satellite Systems" were exposed in this chapter. Both techniques presented in Ch. 6 were applied to the *K_uBand low pass filters* and only the *Ti cone technique* was found to fulfill the requirements of the project. Those were focused on the reduction of the SE emitting properties of the *K_uBand low pass filters*, in order to increase their Multipactor threshold up to an input power of 6000 W while keeping IL enhancement below the 50 % of the intrinsic value, which represent a considerable challenge taking into account the results obtained in previous projects. The Au passivating overlayer treatment was explained, and the results confirmed an overlayer thicknes in the range of nm. According to the morphological results obtained a hypothesis of the roughnes growth based on the J_{Ar^+}/J_{Ti} was given. MEST simulations were also performed revealing a strong effect on the intrinsic corrugation that the ridges of the filter constitute. Three of the four filters showed a Multipactor threshold higer than 6000W and one of them revealed an IL enhancement larger than the 50% of the intrinsic value.

Chapter 8

Low Energy SEY

The low energy part of the SEY spectrum, (LE-SEY), is known to play a major role in determining the performances of many scientific systems and devices but its detailed structure is still under debate[9, 207]. The understanding of the behavior of low energy secondary electrons is of crucial importance for multipactor effect prevention [207], as well as for EC oriented accelerator studies where most of the electrons present in the e^-cloud are of very low energy in nature, and have shown to have peculiar properties in terms of scrubbing [12, 20, 39, 106, 208, 209]. On the experimental side, the difficulty that the measurements at very low energies is clear since it is an intrinsically complicated region to be investigated [210, 211], and that, especially at E_0 very close to zero, space charge, electromagnetic fields, beam energy resolution etc. may act on the very low energy electron beam potentially affecting any detailed experimental SEY determination.

Previous detailed studies [40, 111, 212, 213] on SEY of Cu technical surfaces presented new observation reporting, for the first time, the tendency of SEY not only to reach 1 as E_0 approaches 0 eV, but also to stay significantly above 0 for a quite extended energy region, having a minimum SEY of about 0.5-0.7 at E_0 as high as 10-20 eV. However a strong warning was given against the extrapolation of such results as being a general property of SEY since this low energy behavior was clearly stated to be relative to the actual technical Cu surface studied. Based on experimental findings taken from the literature [214–219], it was also suggested [220] that the observed behavior of LE-SEY is somehow due to experimental artifacts, since the SEY value at zero impinging energy is and must be zero

or close to zero and the SEY curve should nearly monotonically decrease to this value. Also, some theoretical computations predict a very low SEY at low E_0 tending to zero at zero impinging energy and show a very good agreement between simulated SEY and experimental data [215] for the case of clean Al. On the other hand, different works [221], reported simulation results which are consistent with an increase on the electron reflectivity R_{el} (up to R_{el}=1 for E_0 ~0 eV) and with a significantly non-zero SEY for E_0 below 10-20 eV. Such simulations are consistent with the data presented and discussed in [40, 212, 213] and support not only that R_{el} at zero landing electron energy can be close to 100 % but also that SEY value at low impinging energies (from zero to some tens of eV) may have values significantly higher than zero.

Due to the discrepancies found in the literature, quantitative estimation of the confidence with which one can measure the LE-SEY in general, was the motivation of this work, and more specifically analyze the LE-SEY of metallic surfaces to investigate its effects on e^-cloud and Multipactor avoidance and prediction.

8.1 The Energy Scale

As an essential step to understand the measured data, it is necessary to clarify the energy scale and reference concerning our experiments. The energetic of our system is schematically described in Fig.8.1. As clearly discussed in previous publications, [190, 221], the energy of the different metals and systems (detectors, samples, guns etc.) align at the Fermi level, while the kinetic energy of any emitted electron is referenced to the vacuum level of the material from which it has been emitted, being the WF the distance between the Fermi level and the vacuum level for each sample. Any applied voltage, to the gun lenses or to the sample, will then accelerate (or retard) the e^-beam. According to this, electrons emitted by the gun will reference their kinetic energy to the cathode work function, WF_g plus additional, when present, applied gun lens voltages, while electrons interacting with the sample will reference their energy to the sample work function (WF_s) for metals.

In our set up, as previously explained in Sec.5.4.1.1, a negative bias voltage of Vbias 75 eV, was applied to the sample which allowed us to eliminate space charge problems on the sample and also to work with landing energies close to zero using the e^- gun in an

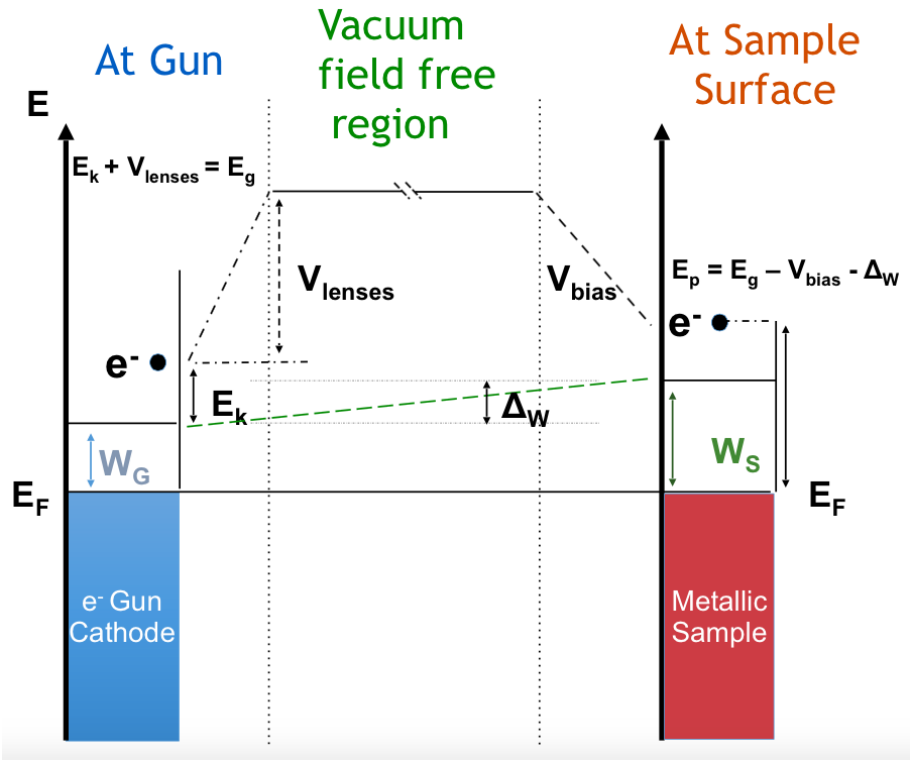

Figure 8.1: Schematic of the energetics of our experimental set-up. The energy levels are aligned to the equilibrium Fermi level E_F. The symbols used are: WF_g is the e^- gun Cathode work function; WF_s is the sample work function ΔWF is the difference between WF_g and WF_s ; E_k is the kinetic energy of the electron just emitted from the cathode; V_{lenses} are the voltage potentials accelerating electrons emitted from the cathode; E_g is the Energy of the electron emitted by the gun into Vacuum; V_{bias} is the retarding voltage applied to the sample; E_0 is the landing energy (above E_F) of the electrons at the surface, as defined in the text.

energy region where it is stable. The landing energy E_0 is then the energy of the electrons emitted by the gun (E_{gun}) minus the contribution of the negative applied sample bias voltage (eV_{bias}) plus the difference between the e^- gun cathode and sample WF so that:

$$E_0 = E_{gun} - eVbias + \Delta W \tag{8.1}$$

As graphically explained in Fig.8.1 all electron energies are referred to the Fermi Energy level E_F , which is the common and sample-independent reference for the entire system. With this energy reference, for an atomically clean metallic surface, the minimum energy of a primary electron interacting and producing a measurable I_s is the WF which value is not affected by surface contamination and for copper is known from literature to be WF_{Cu}=4.65 eV [178].

In this work we set E_0 (above E_F)= 4.65eV when $WF_s = E_{gun} - eV_{bias} - WF_{gun} = 0$. This implies that, in all spectra, the measured E_0 corresponding to the onset of electrons interacting with the solid, is an accurate measurement of the surface WF WF_s of the new sample under analysis with respect to WF_{Cu}.

8.2 On the Capability of Measuring LE-SEY

The e^-gun emits electrons by thermionic emission and the beam emitted has then an energy broadening related to temperature at which the gun emitter works, see Sec.8.5.1. In general terms such thermal broadening, indicated by the beam Full Width Half Maximum $FWHM_g$, can be assumed to be Gaussian in shape and is known to be $\sim 0.6 - 1.0$ eV, depending on the actual operating gun current and emitter type. Fig.8.2 shows an instructive analysis of the intrinsic difficulties of dealing with low energy landing energies E_0, when they are comparable with $FWHM_g$. Obviously, for energies $E_g \leq V_{bias} - \Delta W - FWHM_{g/2}$ all electrons impinging on the surface will be reflected by the higher negative bias voltage, resulting in an $I_s \sim 0$, and, consequently, a value of $SEY = 1$ will be obtained (Fig.8.2 left panel). However, it is not correct to assume this to be valid in absence of any V_{bias} and for all WF values, since, obviously, $E_0 < 0$ is unphysical. With this reasoning in mind, we plot all our measured SEY starting from 1 at $E_g \leq eV_{bias} - \Delta W - FWHM_{g/2}$. On the other hand, when $E_g \geq eV_{bias} - \Delta W + FWHM_{g/2}$ all the electrons reach the surface without being repelled by the bias, then they will interact with the surface, and SEY is measured correctly (Fig.8.2 right panel). Due to the finite energy width $FWHM_g$ of the e^-gun beam, when $eV_{bias} - \Delta W + FWHM_{g/2} \leq E_g \leq eV_{bias} - \Delta W - FWHM_{g/2}$, only some of the electrons reach the surface, having an energy $E_g \leq eV_{bias} - \Delta W$, while some other, having an energy $E_g \leq eV_{bias} - \Delta W$ are repelled by the sample bias (Fig.8.2 central panel). It follows that the measured SEY is inaccurate, since the value of I_p used in Eqn. 5.5 measures the total number of the electrons emitted by the e^-gun, while I_s only refers to those electrons reaching the surface with energy $E_{gun} \geq eV_{bias} - \Delta W$, which will be only a percentage of the ones emitted and measured by the Faraday cup. Their actual number strongly depends on the shape of the energy distribution of the emitted beam.

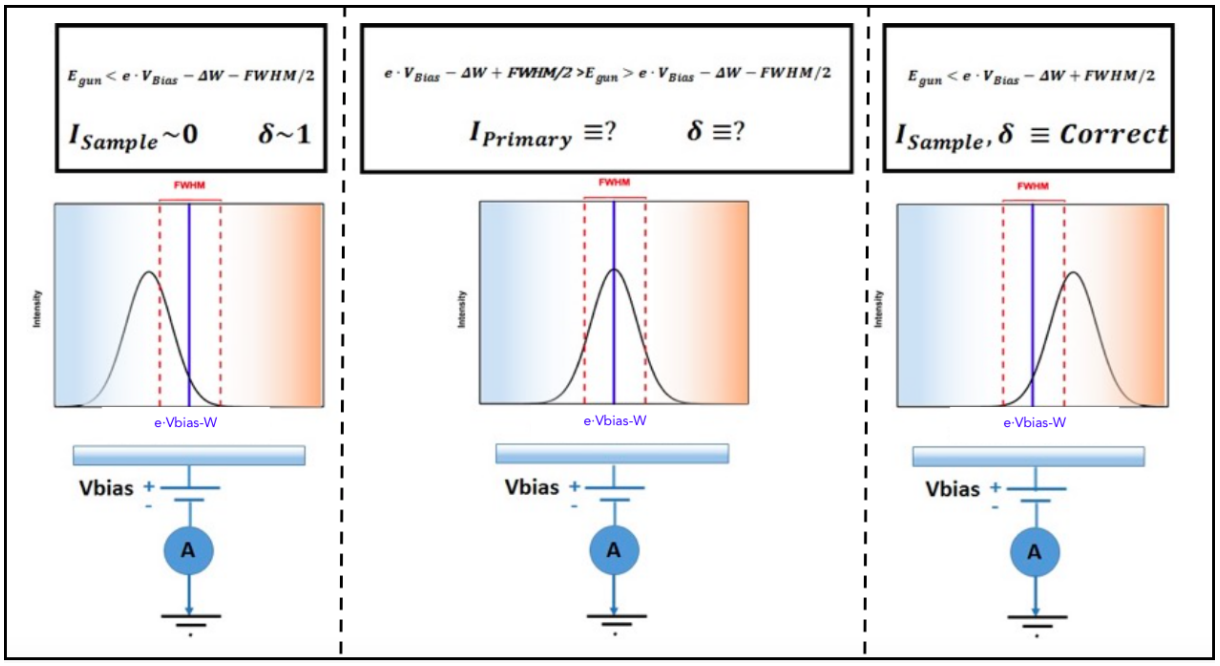

Figure 8.2: Schematic of the experimental set-up at E_G close to V_bias to analyze potential artifacts of the measuring method. In figure we assume that the e^- beam is Gaussian in nature with a certain FWHMg..

In conclusion, the LE-SEY we measure should consist of three regions: • at low energy, $E_{gun} < eV_{bias} - \Delta W$, when all impinging electrons are repelled by the biased sample, $\delta = 1$; • at high energy $E_{gun} > eV_{bias} - \Delta W$, when all impinging electrons interact with the sample, δ is measured correctly; • at $E_{gun} \sim eV_{bias} - \Delta W$,when some of the impinging electrons are reflected and some interact with the sample, δ cannot be accurately measured. The width of this region will measure the e^- gun line width if no other experimental artifacts are affecting our experimental set-up.

8.3 LE-SEY of Oxygen-Free High thermal Conductivity (OFHC) Copper

In this section experimental results that allowed us to confidently validate our experimental technique and compare the different literature results are presented. To address such issue we compared different as received Cu technical surfaces before and after having been atomically cleaned by ion sputtering, as checked by XPS analysis. We mention that the geometry and all other experimental conditions were kept constant during the acquisition

of the different set of data. The analysis of atomically clean Cu will help us validating the technique and then confidently discussing the LE-SEY of technical Cu. The experiment was carried out at LNF-INFN following the procedure explained in Sec.5.4.1.1

8.3.1 Atomically Clean OFHC sample

The clean surface was obtained after repeated Ar^+ sputtering cycles of 1h at 1.5 keV in an Ar pressure of 10^-6 mbar. Surface cleanliness was determined by the absence of C and O signals in the XPS spectrum. The SEY measured on an OFHC polycrystalline Cu sample cleaned by ion sputtering is shown in Fig. 8.3. It shows a $SEY_{max} = 1.4$ at around $E_{0,m} = 640$ eV, consistent with literature results [12, 106, 212]. The curve shape is similar to that of other clean metals [214–219, 222], with SEY values approaching zero when E_0 decreases to zero.

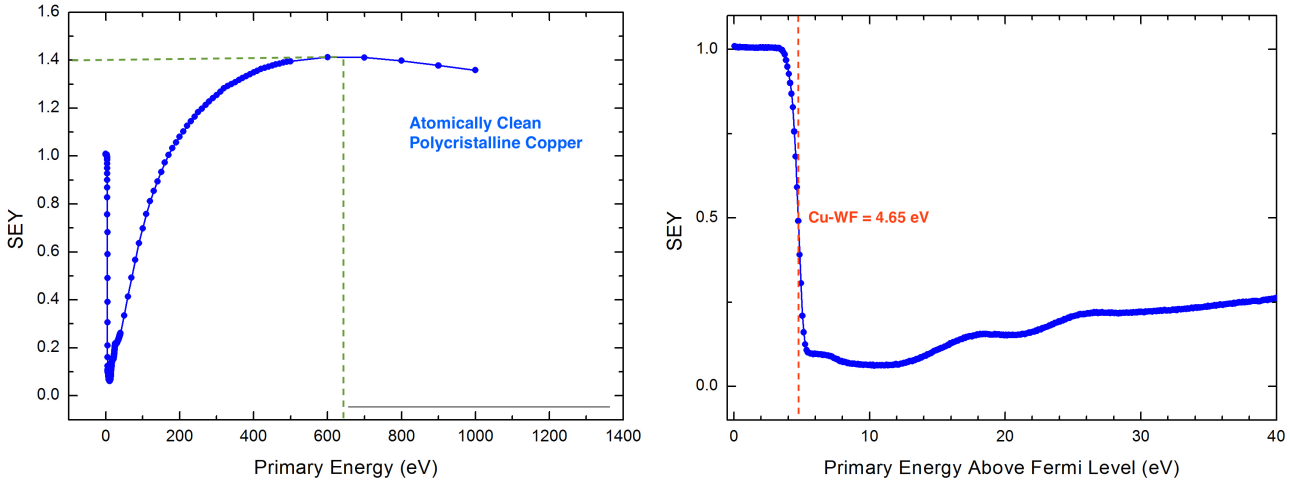

Figure 8.3: **Left:** SEY measurements on Clean OFHC in the energy region between 0 and 1000 eV above E_F. **Right:** LE-SEY measurements on Clean OFHC in the energy region between 0 and 30 eV above E_F.

A magnification of the very low energy region, shown in the inset of Fig. 8.3, is indeed very instructive. As expected from Fig.8.2 and from the previous discussion, the LE-SEY starts at 1, then, very sharply decreases to less than 0.1 and slowly increases to higher SEY values. As previously discussed, the threshold energy where such decrease takes place has been set at $E_0 = \mathrm{WF}_{Cu} = 4.65$ eV, being E_F our energy reference. The width of the transition region is consistent with the expected thermal broadening deriving from the Ta disk of the Kimball gun, and represents a "blind region" in which the actual value of LE-SEY can not

be measured. Further study of such "blind region" will be addressed in Sec. 8.5. These data, taken within an unprecedented energy range, spanning over all the low energies of interest, are consistent with previously published data [214, 215, 217–219], on atomically clean samples and with the calculations performed on clean Al [222]. This suggests that clean metals actually tend to have LE-SEY values approaching zero at landing electron energies approaching WF_s and to have low LE-SEY values for this entire energy interval. Structures at ~ 2 and 14 eV above the WF_{Cu} are clearly visible and their nature, which will be studied in detail in Ch. 9 can be ascribed the interaction of incoming electrons with the unoccupied states of the conduction band, and to plasmon collective exitations occurring in the solid [222, 223]. Moreover, and perhaps more importantly, the data confirm the capability of our system to measure with great accuracy LE-SEY values as low as 0.1 at impinging energies limited by a small blind region above WF_s.

8.3.2 "As Received" OFHC Samples

SEY and High resolution LE-SEY curves were measured on several as-received OFHC Cu samples before cleaning them by ion sputtering. The as-received samples were rinsed in ethanol and deionized water before being inserted into vacuum. Since the "as-received" and the clean Cu were actually the same sample, before and after sputtering, the difference in the measured signal cannot be ascribed to any difference in sample positioning or dimensions. SEY results are shown in Fig. 8.4 in which a comparison between one of the "as-received" samples, and the atomically clean OFHC sample is depicted. As received SEY curve exhibits a value of $SEY_{max} \sim 2$ at $E_{0,m} \sim 350$ eV in good agreement with literature results. The difference between the "as received" and the clean Cu sample is even more evident in their LE-SEY zoomed regions showed in Fig. 8.4. Clearly, the "as-received" surface exhibits a WF higher than WF_{Cu}, and does not seem to have a very well defined value.

The decrease of the LE-SEY value in the "blind region" of our apparatus is much reduced. The measured reduction from SEY=1 to its first flexus, is much wider (more than 4 eV in width) and cannot be ascribed to the experimental $FWHM_g$ broadening. It could also be difficult to assign it to the presence of disomogeneous areas with different work funcions

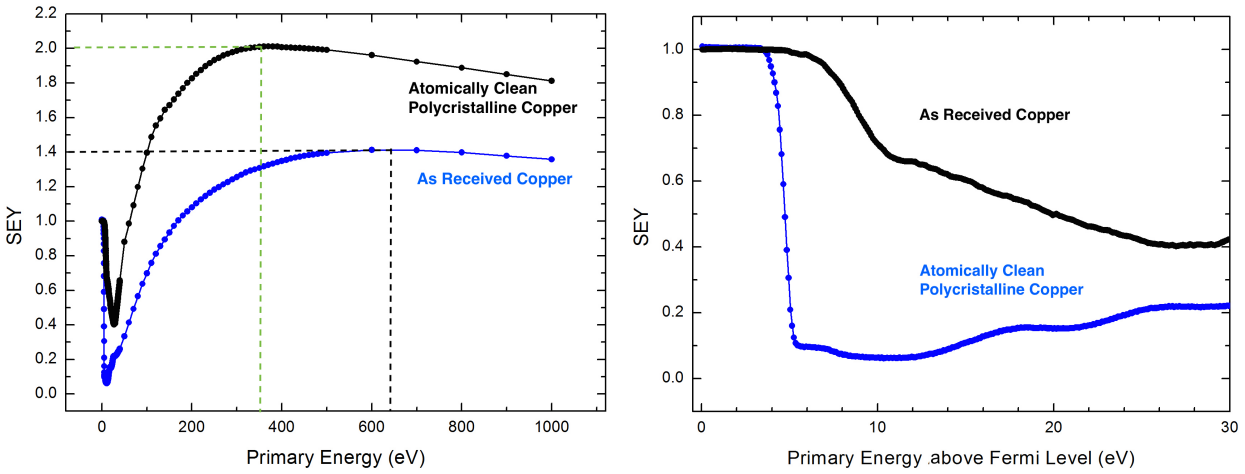

Figure 8.4: **Left:** SEY measurements of Clean OFHC (black line) and "as received" OFHC (blue line) in the energy region between 0 and 1000 eV above E_F. **Right:** LE-SEY measurements of Clean OFHC (black line) and "as received" OFHC (blue line) in the energy region between 0 and 30 eV above E_F.

since 4 eV is an enormous value for such WF variation. We ascribe this behavior to the enhanced ability of the "as received" surface to reflect low landing energy electrons. In fact, what the data here clearly shows is, that, for this "as received" sample, the reflectivity at landing energy close to WF can be assumed to be close to unity and the SEY value in the entire LE region is always higher than 0.5 at variance with respect to the clean Cu. This observation, toghether with the certified confidence that our experimental method is indeed able to correctly measure LE-SEY up to Ep values less than 1 eV higher than the WS, clearly indicates that the dramatic difference of the LE-SEY curves is due to the presence of the contaminant layer of the "as received" Cu.

8.3.2.1 The Indetermination of the "As Received" Sample Chemical State

It is remarkable the fact that "as received" is not a well defined chemical state, and actually, it is expectable to obtain different results for diverse "as received" samples, since their chemical composition and degree of contamination strongly depend on their different origin and history, which could result in drastic differences in their measurements. Results obtained on SEY of two different "as received" samples are shown in Fig. 8.5. A clear difference between both curves is observed, being the SEY represented by a red curve more close to the atomically clean copper exhibited in Fig. 8.4 than the one represented by a black curve, probably due to a different degree of contamination. It is outside the scope of

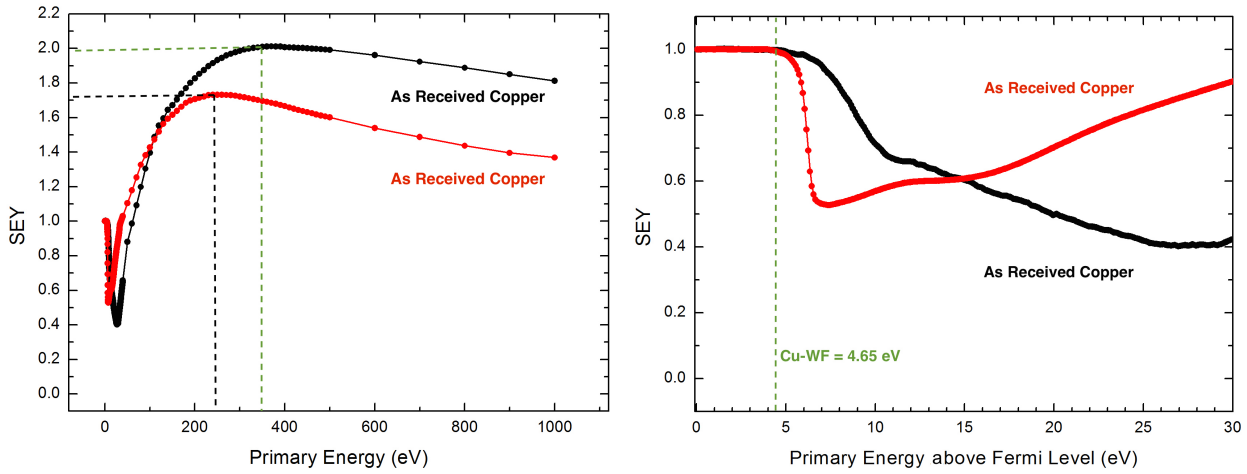

Figure 8.5: **Left:** SEY measurements of two different as received polycrystalline Cu in the energy region between 0 and 1000 eV above E_F, showing different values of SEY_{max} and E_0, m. **Right:** LE-SEY measurements of two different as received polycrystalline Cu in the energy region between 0 and 30 eV above E_F, showing different behavior within the blind region and the entire LE-SEY part.

this thesis to analyze such differences and understand their origin. Here it is only worth noticing that by "as received" we can not identify a specific surface composition and this obviously reflects in the noted differences in the detailed structure and shape of their SEY.

LE-SEY results of two different "as received" samples are shown in Fig. 8.5. As for SEY curves, LE-SEY spectra reveal a dramatic discrepancy between the values of both WFs as well as their shape within the entire low energy region. This observation, together with the certified confidence that our experimental method is able to correctly measure LE-SEY up to E_0 values less than 1 eV higher than the WF_s, clearly indicates that the dramatic difference of the LE-SEY curves is due to the presence of the contaminant layer of the as received Cu. This observation clarifies the apparent discrepancy of literature data which can be simply ascribed to the different samples cleanliness, and actual composition and metallicity of the outermost layers, which significantly alter the reflectivity at zero landing energies.

8.4 LE-SEY of Polycrystalline Technical Ag and Au

In order to confirm the results obtained from clean Cu data for the behavior of LE-SEY in metals, LE-SEY and SEY measurements on clean Ag and Au were also carried out. The samples were 5μm electrochemical technical platings on Al substrate manufactured

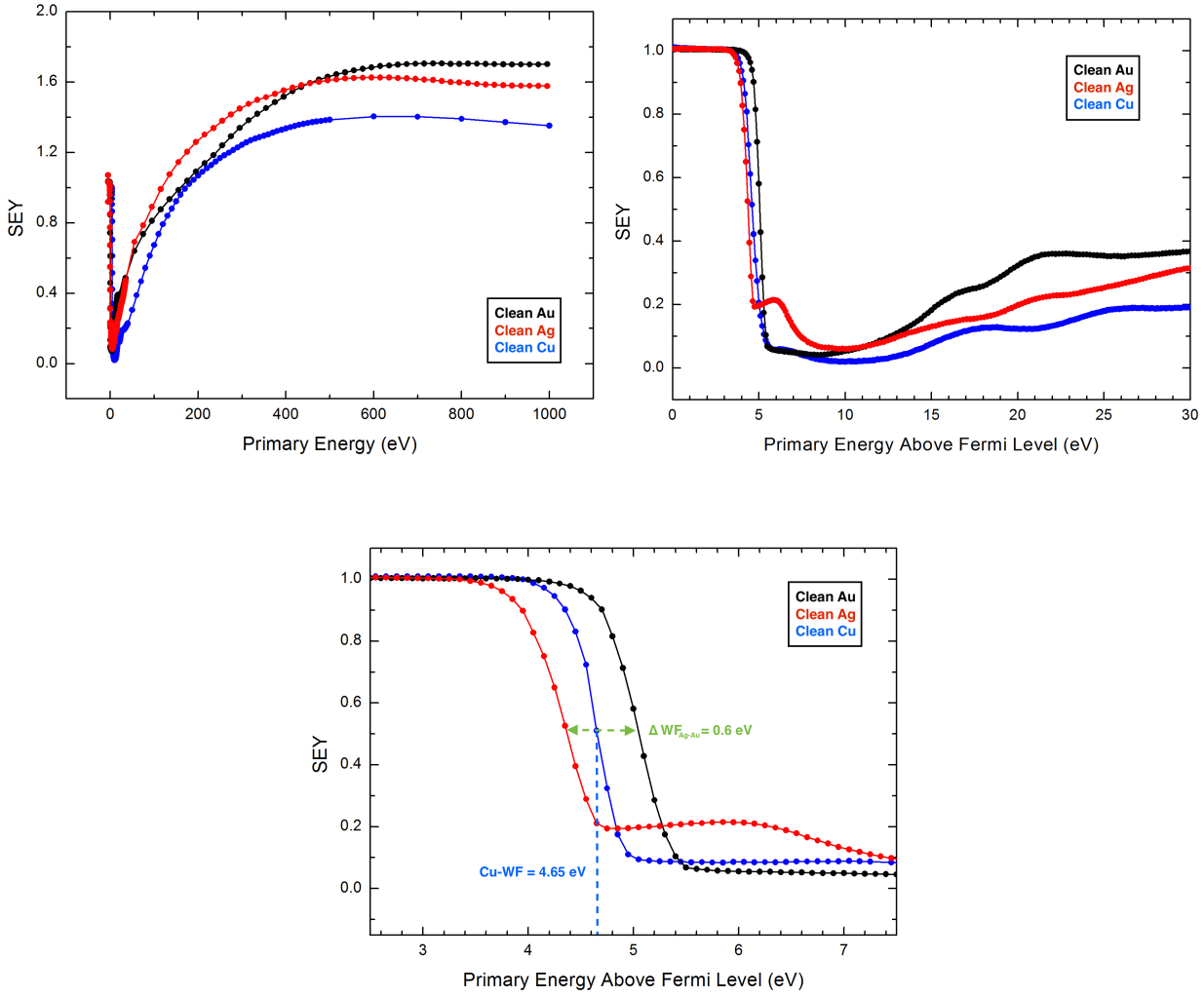

Figure 8.6: **Left:** SEY measurements of clean polycrystalline Au (black line), Au (red line) and Cu (blue line) in the energy region between 0 and 1000 eV above E_F. **Right:** LE-SEY measurements of clean polycrystalline Au (black line), Au (red line) and Cu (blue line) in the energy region between 0 and 30 eV above E_F. **Bottom:** LE-SEY measurements of clean polycrystalline Au (black line), Au (red line) and Cu (blue line) in the blind region. A difference of 0.6 eV between Ag and Au WFs is observed.

by *TESATSpacecom* as described in detail in Ch. 6. Results obtained, together with the spectrum previously obtained for clean Cu, are shown in the upper panels of Fig. 8.6 . The same tendency to zero for very low energies is observable for Ag and Au. Ag data shows an intense hump at primary energies ∼6eV above Fermi Energy, reaching values up to 0.3, however the behavior of the low energy tail of such hump, reveals a confirmed tendency towards zero within the blind region see Sec. 8.5.2. Each spectrum show a different shape formed by a number of humps and valleys. Such structure, was ascribed to the empty density of states of the conduction band of the sample, as well as to collective excitations characteristic of each metal see (Ch. 9).

However, due to the polycrystalline nature of the samples, the contribution of the empty

levels of the conduction band is assumed to be rather weak, since their interaction with incoming electrons strongly depend on the angular orientation of the crystalline network of the metal, which is not well defined for a polycrystal. Several measurements of LE-SEY, not shown here, confirm that the spectra are highly reproducible, and that different structure observed for each metal, is actually due to the physical properties of the material and not to experimental artifacts. Also the spectra reveal a WF difference between Ag and Au of $\Delta W_{Ag-Au} \sim 0.6$ eV which is consistent with the values expected from literature [178]. However as depicted in the bottom panel of Fig. 8.6 their individual values are not consistent with literature when setting them according to the fermi level previously stated for Cu LE-SEY spectrum. In order to understand this discrepancy it is important to notice that even though all the spectra were taken by using the same battery box, and the same e^-gun settings, there are other sources of uncertainty affecting the measurements. Under different uncontrollable conditions, the bias voltage provided by the battery box, and more importantly the intrinsic error of the e^-gun Energy set reading provided by the electronics of the $EGPS - 1002$ power supply system, can vary from one measurement to another, for different functional cycles of the e^-gun, i.e. when it is turned off and on again. Hence, since Ag and Au LE-SEY spectra were taken under the same conditions within the same e^-gun functional cycle, e^-gun energy offset was assumed to be constant for all the measurements and the value $\Delta W_{Ag-Au} \sim 0.6$ eV is indeed reliable and free of artifacts. On the other hand, a trustable comparison with WF_{Cu} is not obtainable. This reveals a very important limitation in the method used to measure WF differences, and hence a more accurate determination of the e^-gun energy offset and bias voltage is needed in order to obtain values of WF with an error smaller than 0.5 eV independently of the functional cycle of the e^-gun. It is important to notice that such differences in e^-gun offsets are never larger than $\sim$1 eV, and hence, the huge variation on the WF observed for the "as received" samples in Sec. 8.3.2.1 can not be ascribed to a change in the e^-gun energy set parameters.

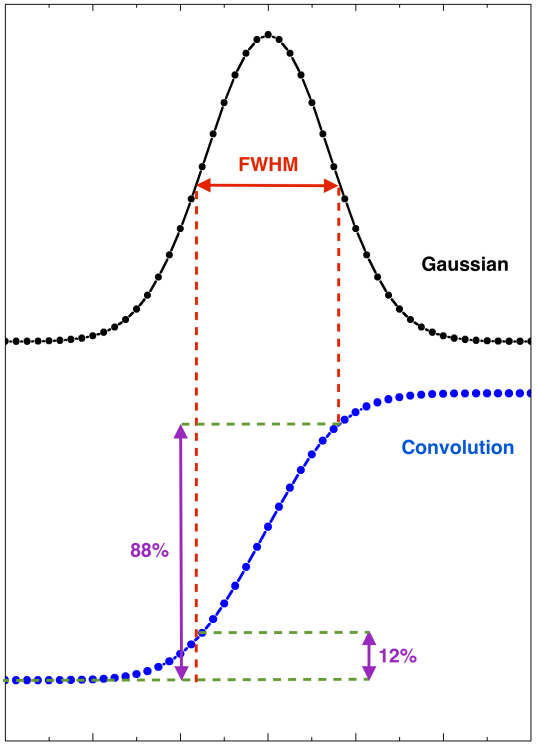

Figure 8.7: A gaussian curve (black line) and its convolution (blue line). The points at the convoluted curve related to the gaussian FWHM are highlighted.

8.5 Over the blind region

As previously noticed in Sec. 8.3.1 in this blind region the width of the e^- beam impedes us to measure the actual number of electrons impinging the sample. When the very first electrons, corresponding to the tail at high energies of the gaussian distribution, overcome the WF barrier, they interact with the sample. As the gaussian centroid position moves towards higher energies, the interaction becomes more important, in such a way that the spectrum observed corresponds with the convolution of the gaussian beam shape, until finally the whole beam interacts with the sample, and δ is measured correctly. Fig. 8.7 shows a gaussian curve, and its convolution. It is known that for the convoluteion of a gaussian distributions the distance between the 12% and the 88% intensity points, indicated in Fig. 8.7, corresponds to the $FWHM$ of the gaussian profile [224].

According to that, a value of $FWHM_g = 0.85$ eV was obtained for the e^- beam. Obtaining such value is of crucial importance in order to develop further analysis regarding the behavior of LE-SEY within the blind region, (see Sec. 8.5.2).

8.5.1 FWHM$_g$ Dependance on e$^-$gun Cathode Temperature

A noticeable dependance of $FWHM_g$ with cathode temperature has been observed. As previously noted in Sec. 8.2, electrons are emitted to vacuum by means of thermionic emission, since electrons are elementary particles classified as fermions, their energy distribution of occupied states is given by the Fermi-Dirac function:

$$f_{FD} = \frac{1}{1 + e^{(E-E_F)/k_B T}} \tag{8.2}$$

where k_B is the Boltzmann constant, and T is the temperature of the cathode. Fermi-Dirac function represents the probability for an electron to have certain energy, depending on the temperature of the system. Fig. 8.8 pictorially shows the dependance of the shape behavior of the Fermi-Dirac function on the temperature, for T= 500, 1150 and 1500 K being 1150K the typical value by the manufacturer for the cathode temperature under normal conditions. As it can be seen, as the temperature increases the distribution broadens, increasing then the probability for electrons to be in an energetic state higher than the fermi level. When the thermal energy given to the electrons overcomes the WF of the e$^-$gun cathode, there is a probability $P > 0$ for electrons to be emitted. The emission probability increases, for high temperatures producing a higher energetic broadening of the e$^-$ beam and consequently, a higher $FWHM_g$. The blind region measured on atomically clean polycrystalline Cu at different cathode temperatures is shown in Fig. 8.8.

A clear broadening of the blind region corresponding to a broadening of gaussian e$^-$beam $FWHM_g$ is observed as the temperature increases. Even though, due to technical limitations, the temperature of the cathode was not measured, it was controled by the *Source Voltage* e$^-$gun parameter.

8.5.2 LE-SEY At the Blind Region

In the so called blind energy region, the value of I_p, as measured by the Faraday cup, does not provide the correct number of electrons reaching the surface with energy $E_0 = \mathrm{WF}_s$ (above E_F). We can analyze the data in light of this discrepancy, and calculate the actual

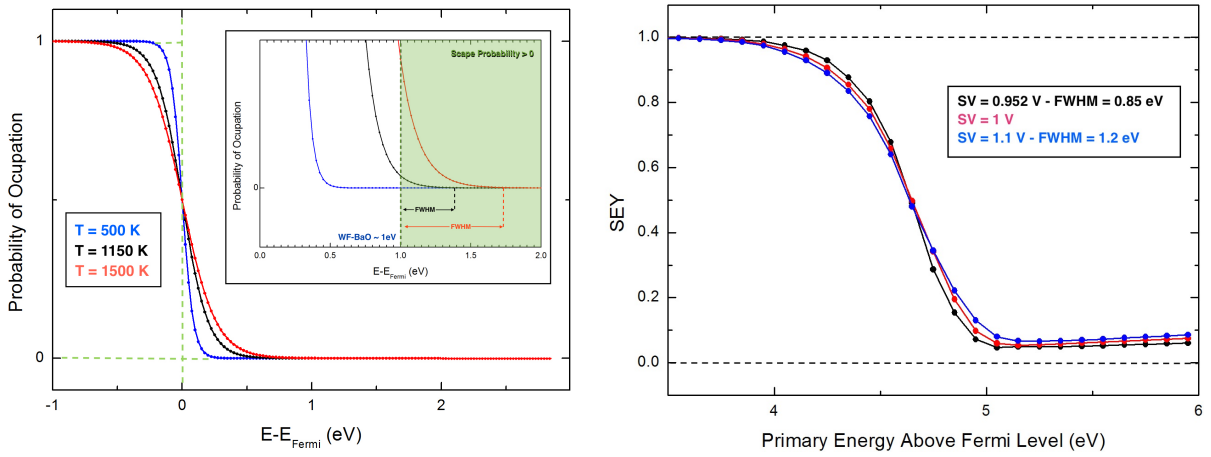

Figure 8.8: **Left:** Representation of the Fermi-Dirac distribution at 500 K (blue line), 1150 K (black line) and 2000 K (red line). **Inset:** cathode WF zoomed region in which the thermionic emission process is pictorially explained. When temperature is high enough, the tail of the Fermi-Dirac distribution overcomes the cathode WF, and electron emission is possible. **Right:** Experimental evidence of the e^- beam gaussian profile broadening with the increasing cathode temperature.

primary current I_p^c by convolving the measured I_p (which is nearly flat and negative in the small LE region of interest) with the impinging e$^-$beam assumed to have a Gaussian profile with $FWHM_g = 0.85$ eV. Such analysis is presented for clean Cu in the left panel of Fig. 8.9, where a comparison of the measured Ip with I_p^c is shown. As expected, I_p^c is zero when all electrons are repelled (as in Fig. 8.2 left panel); it is negative and equal to I_p when all electrons interact with the surface (as in Fig. 8.2, right panel); and, in the intermediate region (as in Fig. 8.2 central panel), it is the convolution of a Gaussian with a step function, being exactly 1/2 of I_p at $E_0 = W_s$. In the right panel of Fig. 8.9 we then compare the measured SEY with the one calculated by using I_p^c in Eqn. 5.5. Some peculiarities have to be clarified for a better understanding of the analysis of such corrected SEY.

The first regards the region where I_p^c is zero. In this region, SEY is not a defined quantity and has not been plotted. The other aspect regards the energy scale of the horizontal axis of both panels of Fig. 8.9. Such horizontal scale represents the centroid of the Gaussian beam of width FWHMg = 0.85 eV. This does not imply that we have SEY = 0 at impinging energy less than WF$_s$ but that, when the centroid of the Gaussian is below WF$_s$ there will still be some electrons of energy above WF$_s$ interacting with the surface, and generating the measured I_S. Finally, the error bars on the corrected SEY have been estimated as due to the decreasing current value we obtain approaching low centroid energy positions. In this region, I_s and I_p^c decrease down to few picoAmperes and the consequent error in the

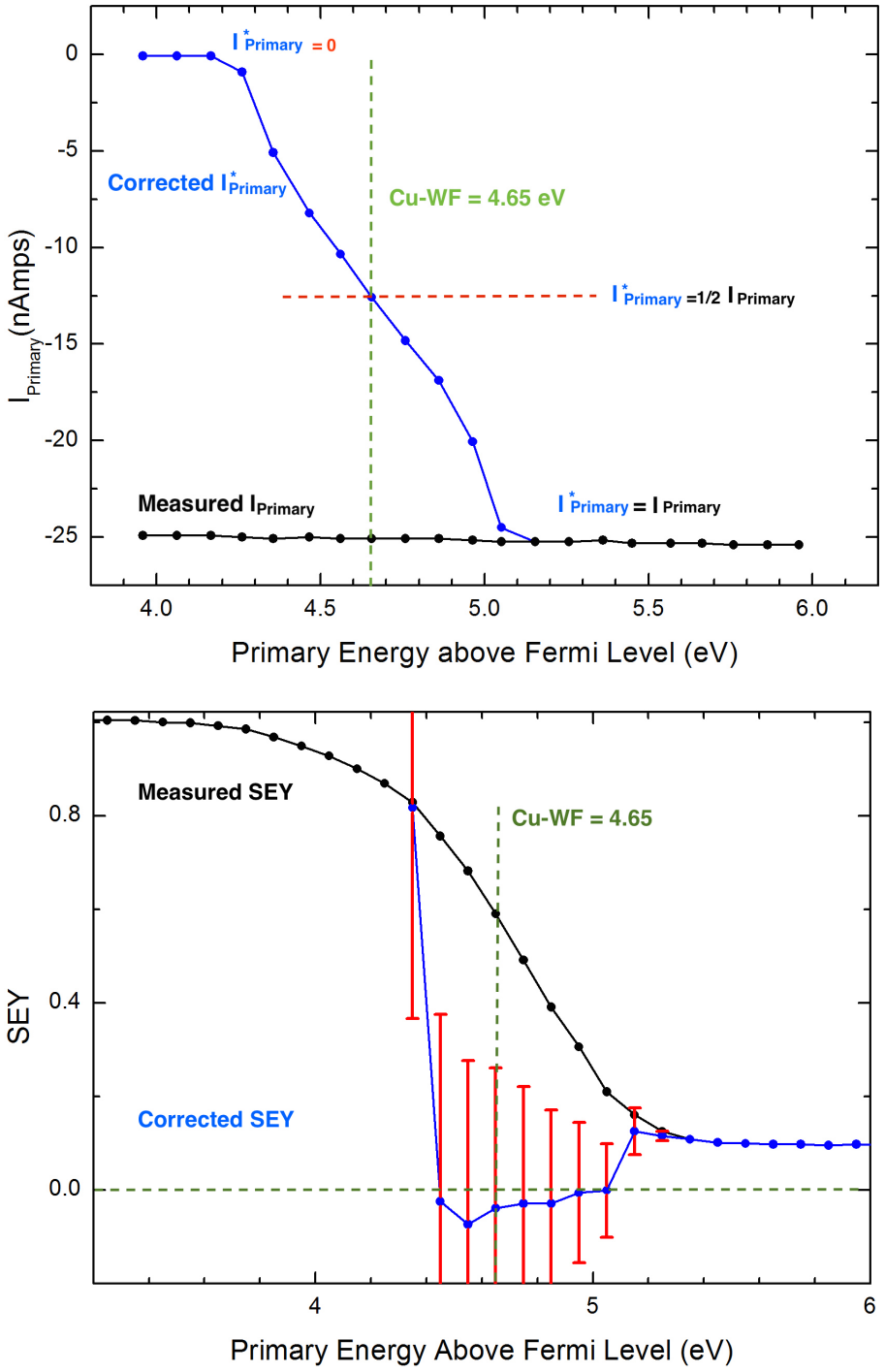

Figure 8.9: **Top:** Comparison between the measured I_p (black line) with the one obtained by using the corrected $I*_p$ (blue line) obtained by convoluting I_p with the Gaussian profile of the e^- beam of FWHMg = 0.85 eV. **Bottom:** Comparison between LE-SEY data within the blind region as obtained using I_p (black line) with SEY obtained by convoluting $I*_p$ with the Gaussian profile of the e^-beam of FWHMg = 0.85 eV.

SEY increases correspondingly. With this in mind, we see that we may extract significant information also from the so called blind region. Just by assuming a given $FWHM_g$ the corrected I_p^c is, within the error bar, very close to the measured Is, hence the SEY is close to zero also in the blind region suggesting that no electron reflectivity rise is occurring for clean Cu even at energy less than 1 eV from WF_s. A similar analysis on the clean Ag and Au polycrystalline samples is shown in Fig. 8.10, and confirms the tendency for clean metallic surfaces to have LE-SEY tending to zero at energy less than 1 eV from WF_s.

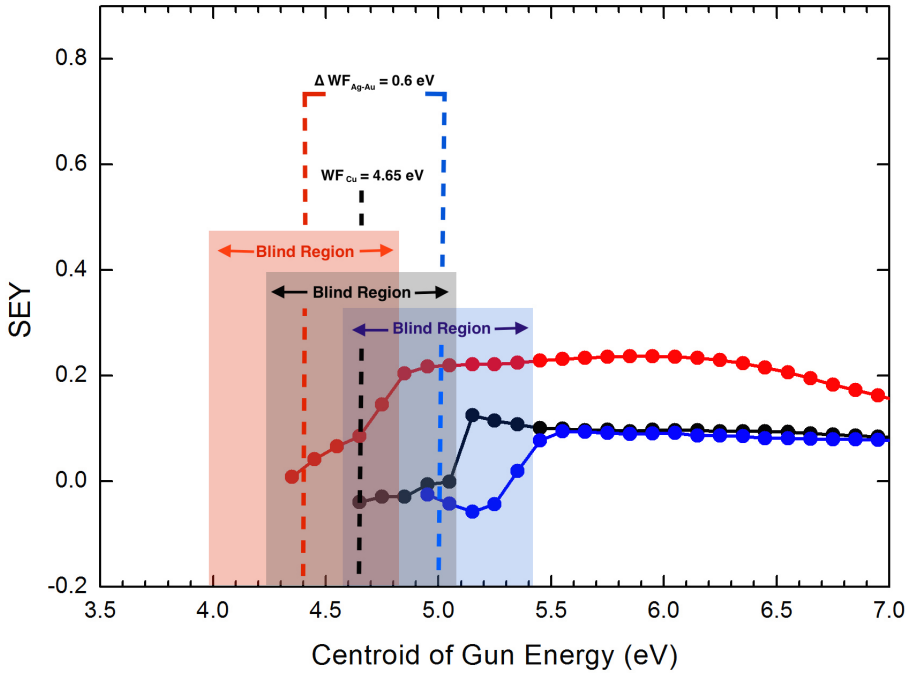

Figure 8.10: LE-SEY curves of Cu, Ag and Au within the blind region, obtained by using the corrected $I*_p$ after convoluting I_p with the Gaussian profile of the e^- beam of FWHMg = 0.85 eV. A difference of 0.6 eV between Ag and Au WFs is observed.

With this it is shown that, the blind region can still be studied and reduced by analyzing the measured data in light of the finite width of the e$^-$beam and confirm, also in this region not directly accessible from the as measured data, the same trend as discussed for the entire LE-SEY region.

8.6 Simulations

In order to get some hints on what may be the impact of the measured LE-SEY on the e^- cloud buildup [12] for the LHC, PyECLOUD simulations [225–227] have been performed for

the LHC dipole magnet for the nominal beam at injection energy and chamber parameters.

PyECLOUD is a code for the simulation of the EC (EC) build-up in particle accelerators. It has been broadly employed for benchmarking the EC observations in the Large Hadron Collider (LHC). Thanks to its capacity of running EC simulations with bunch-by-bunch length and intensity data from machine measurements, the scrubbing process of the LHC beam pipes could be reconstructed from heat load measurements in the cryogenic dipoles (see details in [227]). The goal of such investigation is to analize possible significant differences in simulated e-cloud effects due to small changes in the 0-20 eV SEY region could. After that and according with the results obtained, introduce in the simulation code a more refined and realistic model would be the ultimate solution taking care of all the experimental details of the SEY curve, including its LE part parametrization of the actual experimental LE-SEY curve

The model for the SEY for perpendicular electron incidence as a function of primary energy $SEY(E)$ used for the calculations is based on a parametrization of $SEY(E)$ derived from extensive laboratory measurements, which were carried out on the copper surface of the LHC beam chambers at CERN and in other research institutes [12, 40, 111, 228].

In the adopted model the curve $SEY(E)$ is decomposed in two main components, as shown in Fig. 8.11:

$$SEY(E) = \delta_{elas}(E) + \delta_{true}(E) \tag{8.3}$$

where $\delta_{elas}(E)$ and $\delta_{true}(E)$ correspond respectively to electrons which are elastically reflected by the surface and to the so called "true secondaries".

The Furman reformulation of Dionne's formula previously presented in Sec. 3.2.1 [35, 56] as:

$$\delta_{true}(x) = SEY_{max}\frac{sx}{s-1+x^s} \tag{8.4}$$

was used to parametrize the true SEY component of the of $\delta(E)$, which values were derived from extensive laboratory measurements, where $x = E/E^*_{max}$, with the value $s \approx 1.35$ as obtained from several measured data sets [40, 229]. In this model, as previously noted, there are only two free parameters, namely the energy at which the true yield is maximum, $E_{0,m}$,

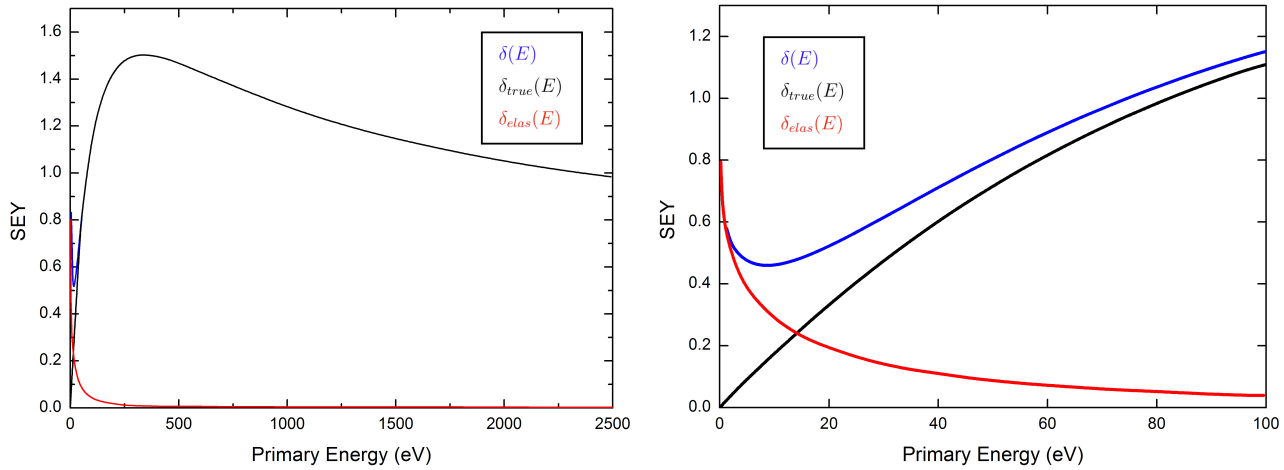

Figure 8.11: **Left:** SEY curve δ(E) for SEY_{max} 1.7 (blue curve), its elastic component δ_{elas}(E) (red curve) and its true secondary component δ_{true}(E) (black curve). **Right:** zoom on the low energy region.

which has been set to $\approx 332eV$, as found in measurements, and the effective maximum secondary emission yield SEY_{max}.

The elastically reflected component on the other hand can be parametrized in different ways in order to obtain different contribution to the LE part of SEY. As previously explained in Ch. 8 elastically reflected electrons strongly contribute to the results obtained at LE SEY of the studied samples. Supporting this idea, the elastically reflected component of SEY is normally parametrized [40] as:

$$\delta_{elas}(E) = R_0 \frac{(\sqrt{E} - \sqrt{E + E_0})^2}{(\sqrt{E} + \sqrt{E + E_0})^2} \tag{8.5}$$

which as shown in Fig. 8.11 its contribution to the total SEY is almost null except for the low energy region (from 0 to 100 eV). The latter parametrization depends uniquely on two fit parameters E_0 and R_0. In particular, R_0 is the reflectivity at zero impinging energy. In the following R_0 will be taken to be equal to 0.8.

The expression for δ_{elas} introduces a minimum in the total SEY curve, as it is seen in Fig. 8.12 and a value of $\delta(0) = R_0$.

In the following the parametric form of SEY is modified introducing differently distributed LE parts on otherwise unchanged curves and parameters. The usual parametrization described by Eqn. 8.5 together with the other two LE distributions studied in this work are shown in Fig. 8.12:

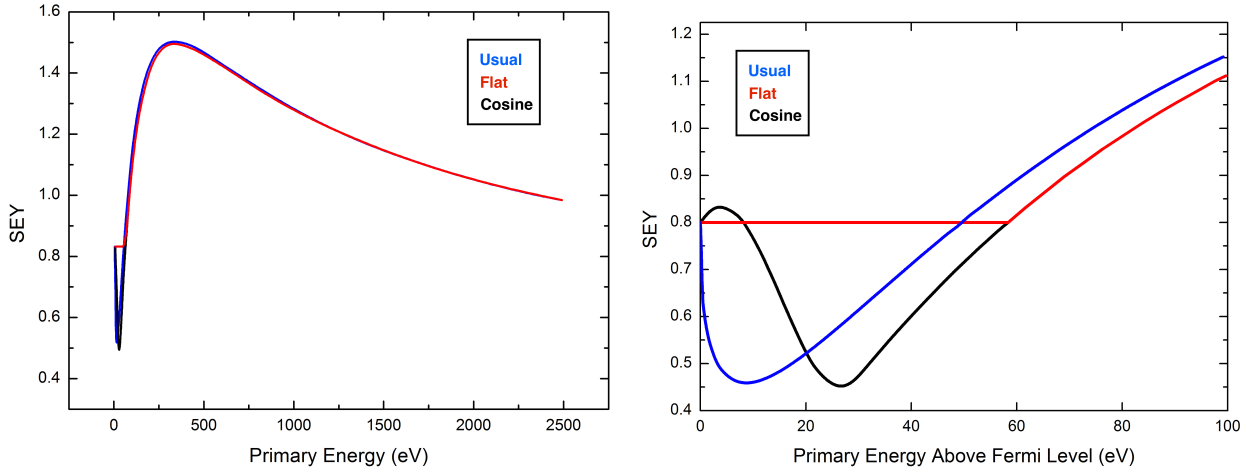

Figure 8.12: SEY curve ($\delta(E)$) for δ_{max}=1.5 and R_0=0.8 for three differently parametrized elastic components $\delta_{elas}(E)$: Usual parametrization (red curve); Flat parametrization (green curve) and cosine parametrization (blue curve). Inset: zoom on the low energy region.

In one case we assume:

$$\delta_{elas}(E) = \begin{cases} R_0 - \delta_{true}(E) & \text{if } \delta_{true}(E) < R_0 \ , \ E < E_{max} \\ 0 & \text{elsewere} \end{cases} \tag{8.6}$$

This distribution, called "Flat" in Fig. 8.12, consists in the simple assumption to have a constant value $\delta(E) = R_0$ for the LE-SEY. Such value was deliberately chosen to be below 1, since, initially, the study what happened to simulations for $\delta(0) = R_0 = 1$, is not a target of study, since it is, as previously discussed, in the so called "blind region" but to see the effect of a significant LE-SEY in the 1 to 20 eV region, where we can confidently measure.

We also study the case in which the elastic component of the SEY is given by:

$$\delta_{elas}(E) = \begin{cases} R_0 \cos^2\left(\frac{\pi}{2}\frac{E}{E_0}\right) & \text{if } E < E_0 \\ 0 & \text{elsewere} \end{cases} \tag{8.7}$$

This distribution, called "Cosine" in Fig. 8.12, allows having a higher LE-SEY than by using the usual model still maintaining a local minimum in the LE region. Since the LHC magnets are superconducting, being operated at 1.9 K, it is important to understand and control the heat load on the cryogenic system. To protect the cold bore (vacuum envelope) from sincrotron radiation and image currents, a beam screen is inserted into the beam line.

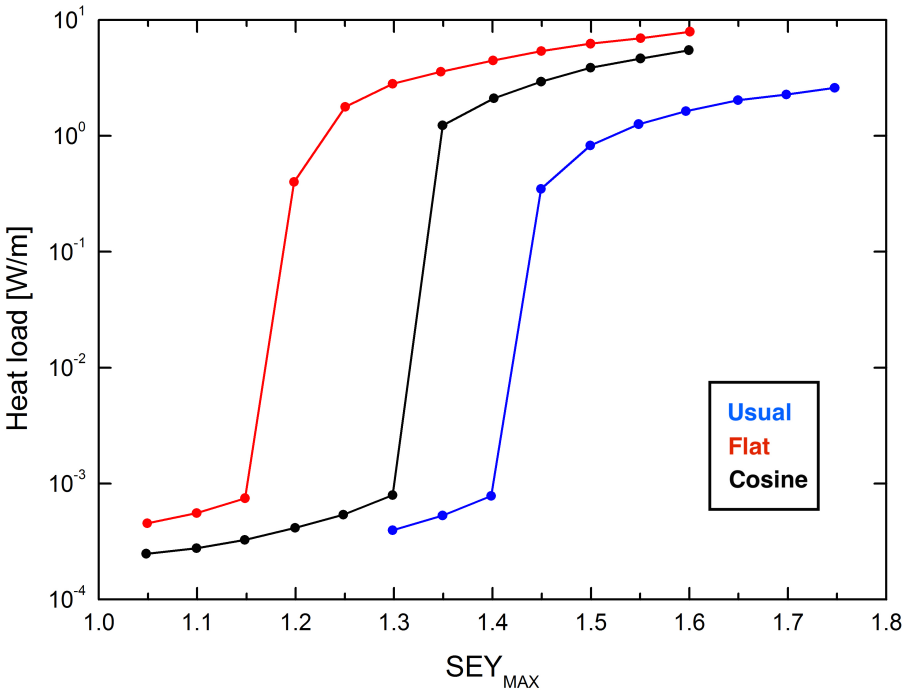

Figure 8.13: Simulated heat load as a function of the δ_{max} parameter for the different LE-SEY behaviors.

The beam screen will be held at a temperature between 5 and 20 K. The available beam screen cooling capacity is exceeded if the EC-induced heat load surpasses 1 to 1.5 W/m [63] in any of the two rings of the LHC, and in this case, the EC will limit the achievable machine performance. In Fig. 8.13, the simulated EC induced heat load as a function of δ_{max} are shown for the three different parametrization of the SEY in the LE region and otherwise identical SEY and simulation parameters.

The simulations confirm a significant impact of the LE-SEY on the e^- cloud buildup behavior. In particular the δ_{max} threshold (heat load $>$ 1 to 1.5 W/m) becomes significantly lower for a constant LE-SEY at 0.8 rather than for the usual parametrization, and heat load above threshold gets significantly enhanced. Note that in all three cases the SEY at zero energy has been set to 0.8 suggesting that, more than the actual SEY at 0 eV, it is the overall behavior of the LE-SEY which can significantly influence ECE predictions in LHC. These results call for a more detailed effort to insert in the simulation codes realistic SEY and LE-SEY parametrization to obtain a better simulation accuracy.

8.7 Summary

This work allowed us to confirm the possibility of measuring LE-SEY with great confidence and without experimental artifacts above less than 1 eV from sample WF. This observation clarifies the apparent discrepancy of literature data which can be simply ascribed to the different samples studied and to their degree of contamination. It has been confirmed that clean metal as Cu, Ag and Au show the same low reflectivity behavior. The measurement of the sample WF however has been proved to be extremely sensitive to small changes of the e^-gun energy offset variations, and due to the lack of reliability of e^-gun energy displayed value, accurate WF determination was not achievable. Further studies are required to address in detail this issue. On the other hand, preliminary calculations show that the LE-SEY detailed knowledge is indeed important to correctly simulate and predict EC effects.

Chapter 9

Studies on Secondary Electron Emission of Carbon

The low SEY properties of sp^2 carbon has often led to the project of using graphitic carbon thin films for the reduction of the SEY and multipacting phenomena in particle accelerators and in space devices. When considering this approach as a possible way to face the Multipactor effect in critical environments, important issues arise related to the level of structural quality necessary to guarantee a low SEY and to the stability of the graphitic carbon layers being exposed for long time to hostile working conditions.

In this study we have modified the surface of Highly Oriented Pyrolytic Graphite (HOPG) by introducing controlled amount of lattice damage by subsequent cycles of Ar^+ ion bombardment at low kinetic energy (150 eV). In the case of graphene, that is single layer of graphite, the nucleation of defects induced by the low energy Ar^+ ion has been recently investigated by STM. It has been shown that when impacting the surface the Ar^+ ion determine the removal of C atoms leaving vacancies in the graphene layer, whose dimension and relative distances grow and decrease, respectively, with increasing irradiation dose [230]. When moving from single layer to bulky graphitic samples, the ion induced damaging will interest not only the surface layer but will extend to deeper layers depending on the ion kinetic energy. Total current spectroscopy (TCS) studies have reported on the effect of the crystalline disorder on the secondary emission properties of HOPG providing some relation between the electronic band structure of graphite and the presence of specific spectroscopic

features in angle resolved and integrated SE curves [223, 231–233]. However no systematic characterization capable of providing a quantitative estimation of the evolution of SEY with structural disorder has been so far carried out.

9.1 The effect of structural disorder on the secondary emission of graphite

A pristine defect density in the lattice of the graphitic films is determined by the unavoidable need of adopting deposition technologies compatible with the coating of macroscopic, odd shaped vacuum vessel or device components. On the other hand, the permanence of the graphitic films in front of intense ECs and ionized particle fluxes might result in a further deterioration of their near surface layers. It is therefore important to establish up to which extent the low SEY properties of graphitic films are preserved while its structural quality is ruined by external factors, or in other words, how the optimal SEY characteristics of graphitic films are related to the perfectness of the sp^2 lattice.

9.1.1 Despription of the experiment

The experiment was performed in the Material Science Laboratory of the INFN-LNF at Frascati (Rome, Italy), in the set-up previously described in Sec. 5.2.1. The HOPG sample was cleaved with adhesive tape before being loaded into the UHV system. Prolonged thermal annealing at temperatures of $\sim$ 1000 K was carried out to desorb contaminants whose absence was then crosschecked by XPS core level analysis. The HOPG samples was then Ar^+ ion bombarded for increasing time ($t_{[sp]}$) up to 180 minutes at 150 eV and Ar pressure of $5 \cdot 10^{-6}$ mbar. After each ion bombardment dose, the HOPG was brought to atmosphere and cleaved again. After each ion bombarding cycle, ultraviolet (UPS) and X-ray photoelectron spectroscopy (XPS) analysis of the surface, as well as SEY measurements were carried out.

For the UPS and XPS spectra, photoelectrons were excited by the non-monochromatic radiation of a HeII (40.8 eV) or an MgKα (1253.6 eV) source, respectively. The SEY and

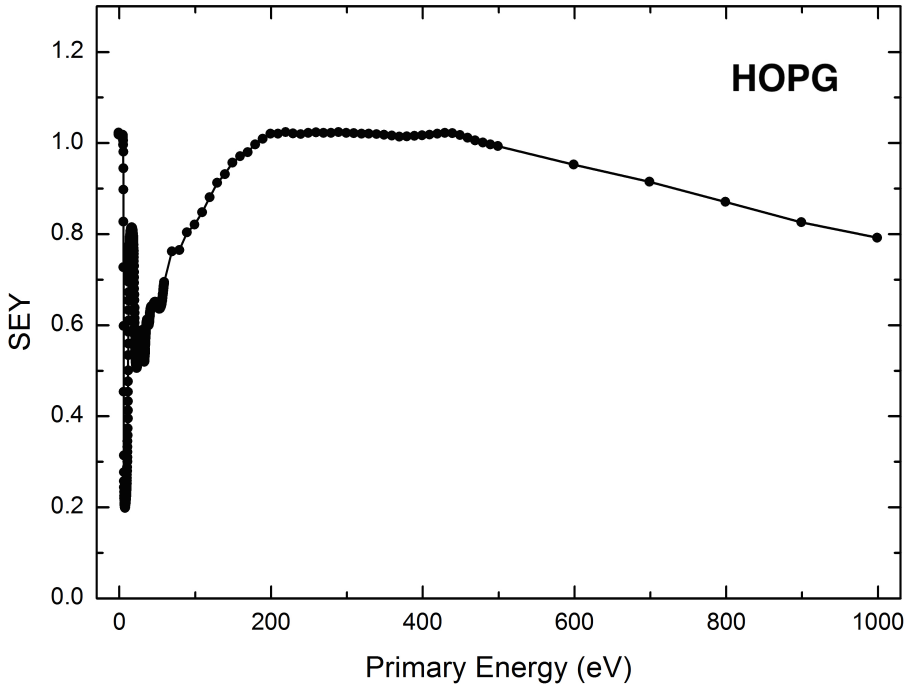

Figure 9.1: SEY results measured on "as cleaved" HOPG.

LE-SEY measurement techniques are described in detail in Sec. 5.4.1.1 and 8.2 respectively. In the design of the set-ups used to perform such experiments, great care has been taken to eliminate spurious effects affecting the determination of LE-SEY. The zero of the primary energy scale was set in correspondence of the onset of SEE from the sample. The Raman spectra were measured ex-situ by using a Horiba XploRA Raman microscope system with a 100x objective at λ=532 nm was used to avoid heat induced sample damage or graphitization.

9.1.2 SEY Results

Fig. 9.1 shows the SEY curve measured on pristine HOPG after cleaving and annealing, which represents the closest to perfect sp^2 lattice achievable with the techniques available in the laboratory. The curve exhibits a SEY_{max} value of 1.0. The determination of the value of $E_{0,m}$ is not straight forward in this case since the energy range within which SEY can be assumed to reach its maximum point appears to vary from 200 to 420 eV, which nevertheless is in agreement with experimental results previously published, [20, 125, 126]. The curves in Fig. 9.2 elucidate how the effect of ion bombardment is to progressively decrease in the SEY values above 300 eV while shifting $E_{0,m}$ to lower values. After the

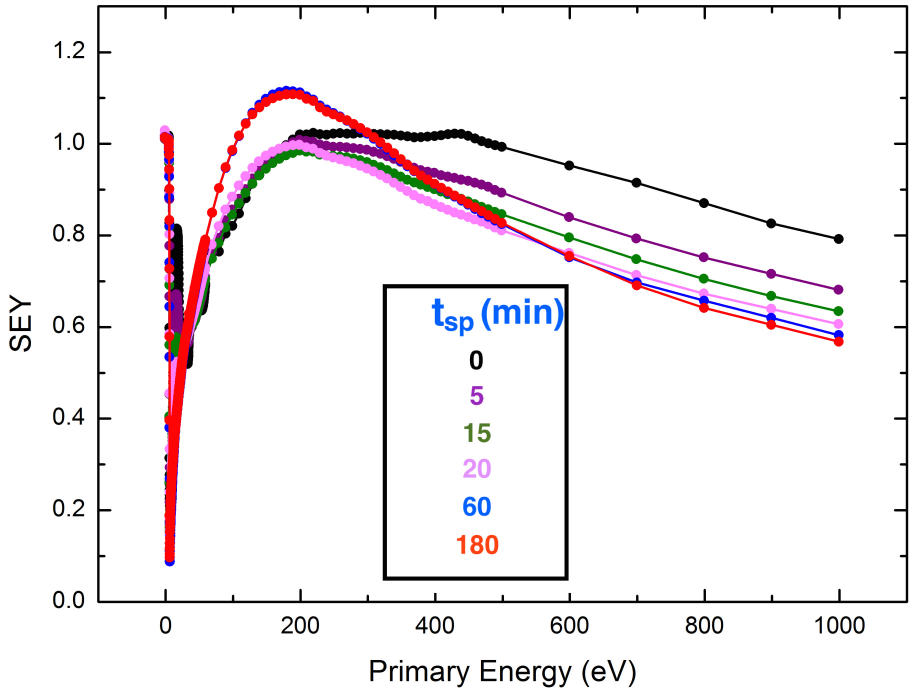

Figure 9.2: Evolution of SEY with ion bombardment.

maximal ion dose the SEY at 1000 eV reduces from the value of 0.80 measured for the pristine HOPG to 0.58. It is worth noting that SEY_{max} slightly decreases for low ion bombardment dose whereas for $t_{sp} > 15min$ rises reaching values up to 1.1. After such value was reached, no further evolution of the SEY curves was observed revealing that after $t_{sp} > 180min$ a saturation point regarding the effects of ion bombardment on SEY of HOPG was achieved.

Several factors might be at the origin of the observed anomaous behavior of SEY. As it has been demonstrated in previous Chapters, the electron emitting properties of certain material strongly depend on the surface morphology of the sample under study. Also, sputtering techniques have been proved to be a very efficient way of achieving high aspect ratio roughness with the capability of drastically modify SE emitting properties of materials under study. Even though the sputtering procedures carried out in this experiment were not performed in the presence of a low sputtering yield masking material, as it was the case of the achieved roughness presented in Ch. 6 and 7, a change in the morphology of the surface due to unmasked sputtering remains as a possible cause of the SEY behavior. Unlike the rough morphology obtained on technical Ag coatings, aspect ratio of the HOPG surfaces under study was low enough to make AFM analysis possible to carry out. In

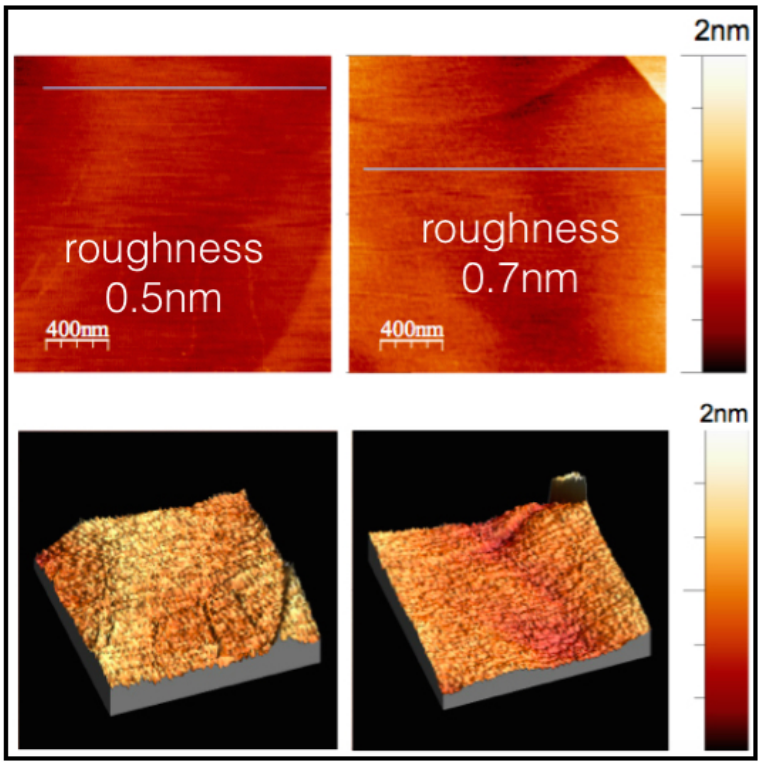

Figure 9.3: **Left:** AFM image obtained from on "as cleaved" HOPG **Right:** AFM image obtained from on fully bombarded HOPG.

order to study the possible corrugation originated at the surface by the Ar^+ impact the morphology of the *as cleaved* and *fully bombarded* sample ($t_{sp} = 180min$) was studied.

AFM Analysis The images shown in Fig. 9.3 exhibit slightly different roughness values of 0.5 nm and 0.7 nm for the as cleaved and fully bombarded HOPG, respectively in a morphology of low aspect ratio protuberances of similar shape and size for both samples.

Although it is widely known that the electron emitting properties of certain materials strongly depend on their surface morphology, and that the roughness may originate both an increase and a decrease in SEY, depending on the shape of the grooved surface (see Sec. 4.3.3) , the negligible morphological differences found by AFM analysis indicate that in the evolution of SEY with ion bombardment observed in Fig.9.2 the role of surface roughening can be neglected. In order to find the origin of the evolution of SEY parameters with ion bombardment time, a more intensive study of the observed SEY behavior will be presented in Sec. 9.2 according to the results obtained after photoemission, and raman spectroscopies performed after each ion bombarding cycle.

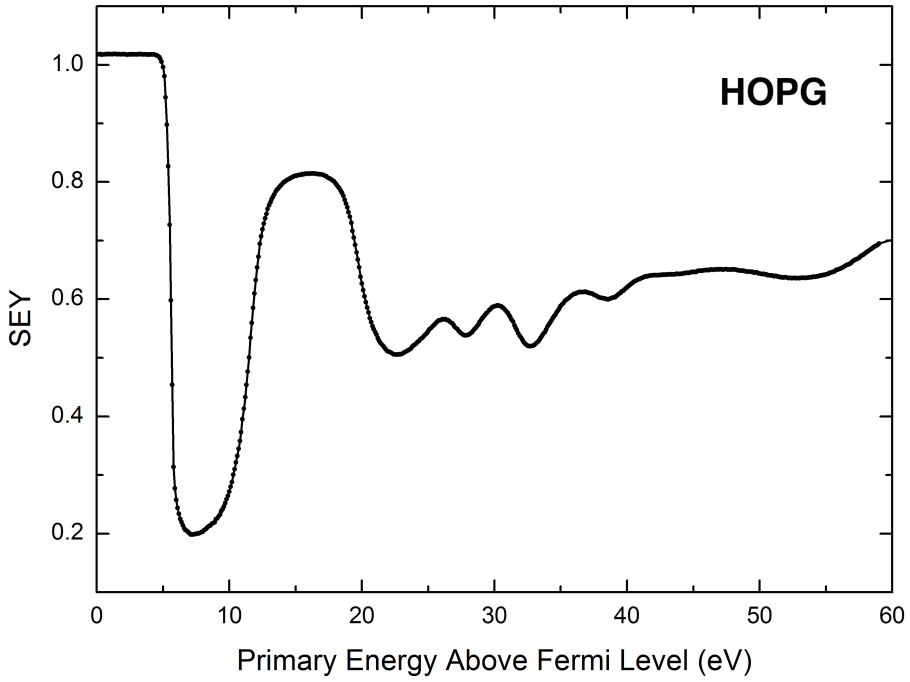

Figure 9.4: LE-SEY results measured on "as cleaved" HOPG.

9.1.3 LE-SEY Results

A more detailed information is derived from the LE-SEY curve measured with high resolution in energy in the low E_0 region. Fig. 9.4 clearly shows that, as previously observed for Ag, Au and Cu clean surfaces in Ch.8, SEY is 1 for E_0 smaller than the sample WF as the electrons are totally reflected, then it rapidly decreases to 0.20 and above 5 eV starts to rise again. Similarly to the results obtained in Ch.8, LE-SEY shows structures which carry the information about the elastic and inelastic electron-solid interactions. However in the case of HOPG unlike for polycrystalline metals, such structure is charachterized by its sharpness, ascribed to the better crystallinity of HOPG in comparison to samples studied in Ch.8.

In the case of HOPG similar structures were observed in experiments carried out in the past by means of total current spectroscopy (TCS) [232]. In TCS the current absorbed by the sample at each primary energy is measured providing information of the elastic electron reflectivity $R(E)$ or equivalently, the elastic transmission $T(E)$. As previously explained in Ch.8, at very low incident energies, typically 0-40 eV, the SEY is dominated by elastically scattered electrons, thus the relationship between TCS and LE-SEY, is straightforward, being both spectroscopies dependent on the elastic electron reflectivity of the sample under

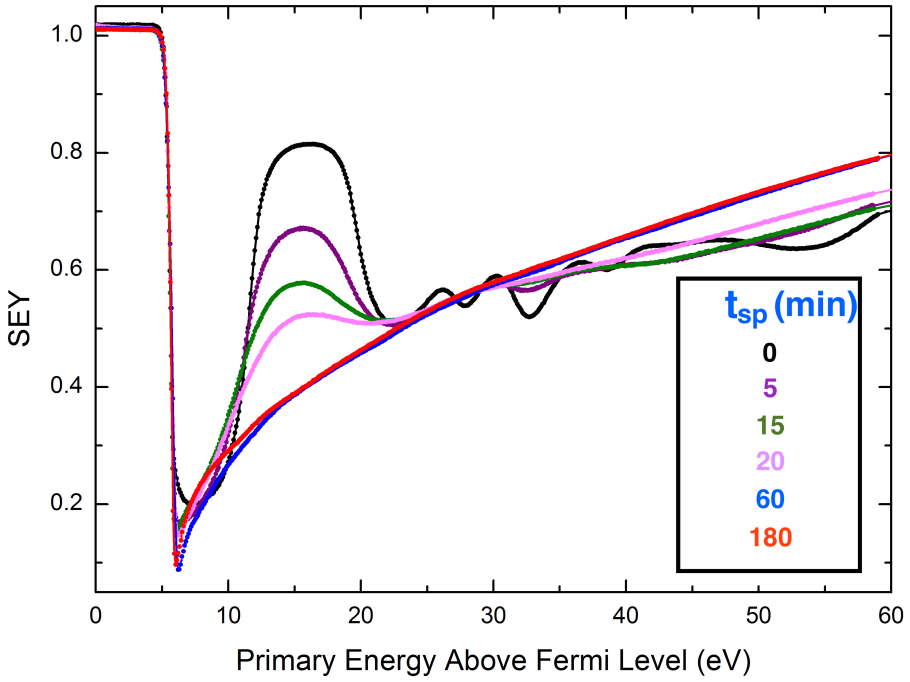

Figure 9.5: Evolution of LE-SEY with ion bombardment.

study. In the case of LE-SEY. Moreover even hough SEY and hence LE-SEY represent the total amount of electrons released from the sample per incident electron, the measurement procedure is constituted by two steps according to Eqn. 3.28. Firstly the impigning primary current I_p is measured, secondly the current absorbed by the sample I_p is measured which constitute indeed a TCS measurement. Nevertheless it is necessary to emphasize the fact that the behavior of TCS and LE-SEY with respect the reflectivity of the sample would be opposite. i.e. an increase in the reflectivity of the sample would be observed as a decrease of intensity in TCS, while intensity of LE-SEY would be increased, and vice versa.

Unlike for the results obtained by means of UPS see Sec9.1.5, in which the information obtained is restricted to the valence (occupied) electronic states, it has been established that TCS and hence LE-SEY spectroscopies give direct information on the unoccupied band structure of solids [231, 232]. It is known that incident electron plane waves strongly couple with electronic states delocalized in the impinging electron direction [234]. In this case the experiment was carried out at normal incidence to the surface of the sample, hence it is expected a strong coupling with the delocalized states parallel to the c axis in $\Gamma - A$ direction in the Brillouin zone [234–236]. In terms of atomic orbitals, the state should be in general oriented surface-perpendicular, as it is the case of the π orbitals[234], thus states of essentially 2D character, localized in the surface-perpendicular direction, are not expected

to take up any current remaining then $T(E)$ invariant.

A rather broad and intense peak centered at $\sim$ 10 eV above the WF is observed for HOPG LE-SEY curve as a consequence of an extremely high reflectivity attributed to the characteristic interlayer state [234, 237] of well ordered graphite, which is connected by a strong $k_\perp$ dispersion with the anti bonding Γ_3^+ band [234]. The decrease in the reflectivity is observed for several well defined energies corresponding to intense absorption of incoming electrons, due to band structure coupling. Apart from band structure, electron absorption due to collective oscillations of the electrons in the solid as plasmons have also been reported [232, 234] . According to previous works, the structure observed at energies of $\hbar w_p \sim 26.5$ eV and $\hbar w_s = \hbar w_p/\sqrt{2} \sim 22.2$ eV have been ascribed to bulk and surface plasmon of graphite respectively.

As ion bombardment begins, the structures in the SEY curve of HOPG smear out. The contribution of the surface plasmon disappears already at $t_{sp} = 5min$, revealing damages in the crystal surface. The increasing amorphization determines an undefined crystal orientation, which makes the $k_\perp$ dispersion no longer to be along the $\Gamma - A$ direction uniquely. The structural defects in the lattices has a detrimental effect on the sharpness of the spectral structures. As clearly shown in Fig. 9.5, the damage induced broadening progressively damps the modulations in the SEY curves until reaching a smooth profile at t_{sp}=60 min, which remains stable after further Ar^+ doses. Since every LE-SEY analysis was performed in different e^- gun working cycles the measured WFs values were not assumed to be trustable, due to possible differences on the working parameteres of the electronics of the power supplies involved in the measurement (see Sec. 8.5.2), thus no analysis regarding the WF of the sample or its possible variations was carried out. Instead, all the curves onsets were located corresponding to a WF = 5 eV according to values found in the literature [179, 238–240].

9.1.4 XPS

The formation of sp^3 C atoms in the damaged surface can be evaluated by comparing the C1s spectra measured on the pristine HOPG and after the heaviest Ar^+ dose shown in Fig.2b. For the pristine sample the peak is located at BE of 284.14 eV, which is the

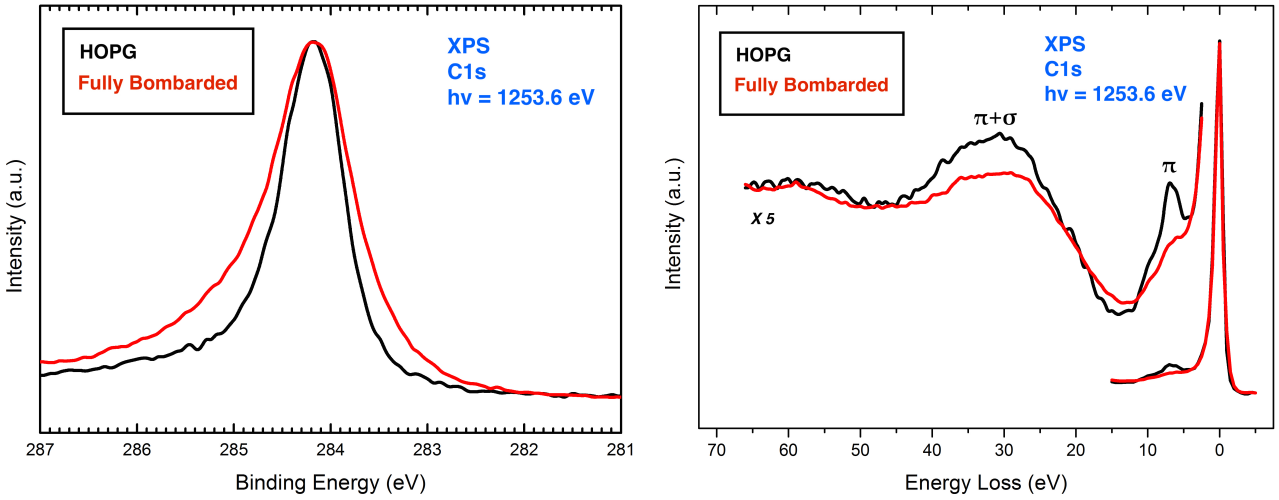

Figure 9.6: **Left:** Valence band spectra measured on the HOPG samples as a function of the bombarding time. **Right:** UPS spectra in the Fermi level region measured on the HOPG samples as a function of the bombarding time.

typical energy position for sp^2 hybridized C atoms, and has a FWHM of 0.8 eV, a value determined by the energy resolution of our experimental setup, whereas after sputtering the BE is 284.10 eV and the FWHM increases to 1 eV. The absence of a C1s component at BE of $\sim$ 285.5 in correspondence of sp^3 hybridized C atoms, demonstrates that, for the Ar^+ energy and doses used in this study, the structural disorder induced by the ion impact does not lead to a measurable rehibridization of the C-C bonds, while the line shape broadening confirms the high defect density in the graphitic lattice.

Fig.2b shows the energy loss spectra of inelastically scattered C1s electrons, exhibiting the π and $\pi+\sigma$ loss features at 6 and 30 eV above the C1s peak maximum, respectively. While the $\pi+\sigma$ plasmons are weakly affected by ion bombardment, the π plasmon contribution smears as ion doses increase, in agreement with crystal amorphization.

9.1.5 UPS

The extent of Ar^+ induced HOPG amorphization was monitored by UPS spectroscopy. The valence band spectrum measured in normal emission at photon energy of 40.8 eV on the pristine HOPG surface is shown in Fig. 9.7. The sharp σ and π band at binding energy (BE) of 3 and 7 eV respectively, attest the high crystalline order of the sample lattice. The strong decrease of the π band intensity already at t_{sp}=5 min indicates the formation of a considerable density of structural defects which ruin the aromatic character of the graphitic

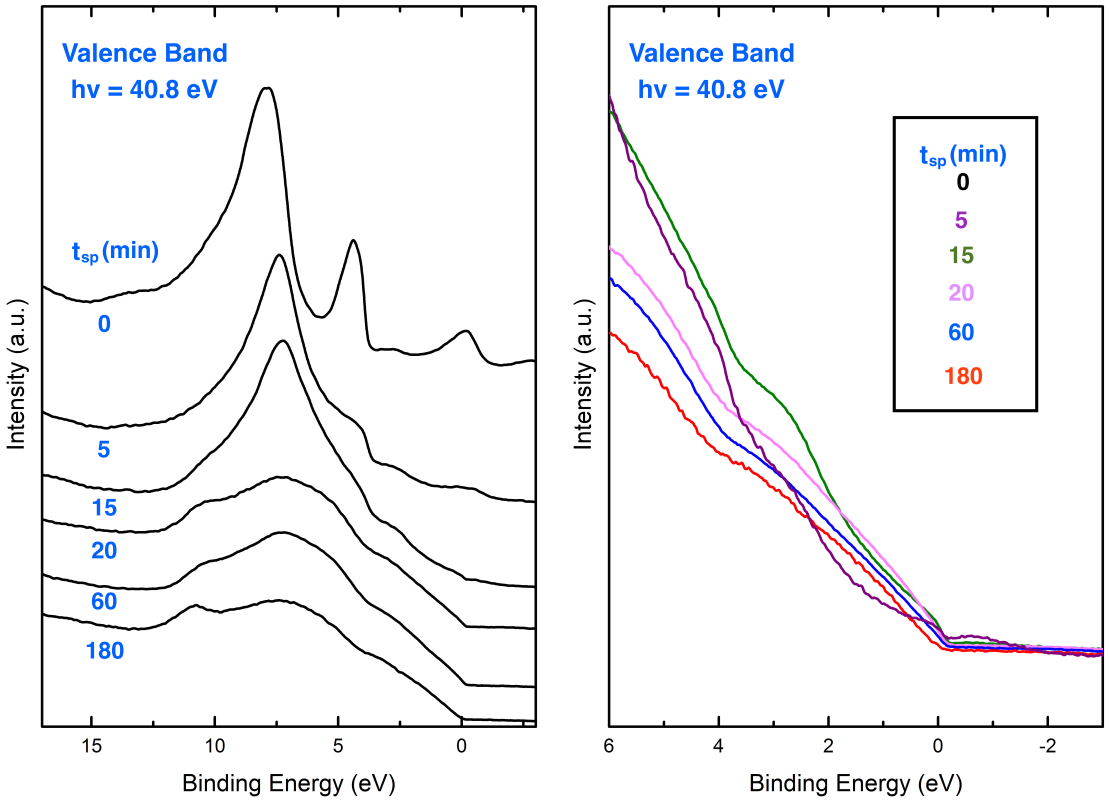

Figure 9.7: **Left:** Valence band spectra measured on the HOPG samples as a function of the bombarding time. **Right:** UPS spectra in the Fermi level region measured on the HOPG samples as a function of the bombarding time.

network. It is worth noting that the π band damping parallels the loss of the spectral structures in the LE-SEY curves in agreement with the comparable surface sensitivity of the electrons emerging from the sample. In the VB spectra measured up to t_{sp} of 15 min the still definite σ band reveal the presence of ordered hexagonal domains whereas the broad unstructured features observed for $t_{sp} \geq 20$ min closely resembling the line shape measured on quasi amorphous carbon surfaces, demonstrates a strong surface disorder. No variation in the band gap was observed, remaining absent for all ion bombarding stages, which proves that despite the evident amorphization achieved, 3-fold geometry is not present in the carbon crystalline network.

9.1.6 Raman

Left panel of Fig. 9.8 shows the Raman spectra measured on HOPG as a function of the ion dose. Each spectrum is normalized to its respective G band and the results for each sample are displaced vertically for clarity. For each Ar^+ dose the Raman spectra were measured at least in 4 different points although only one representative spectra is plotted

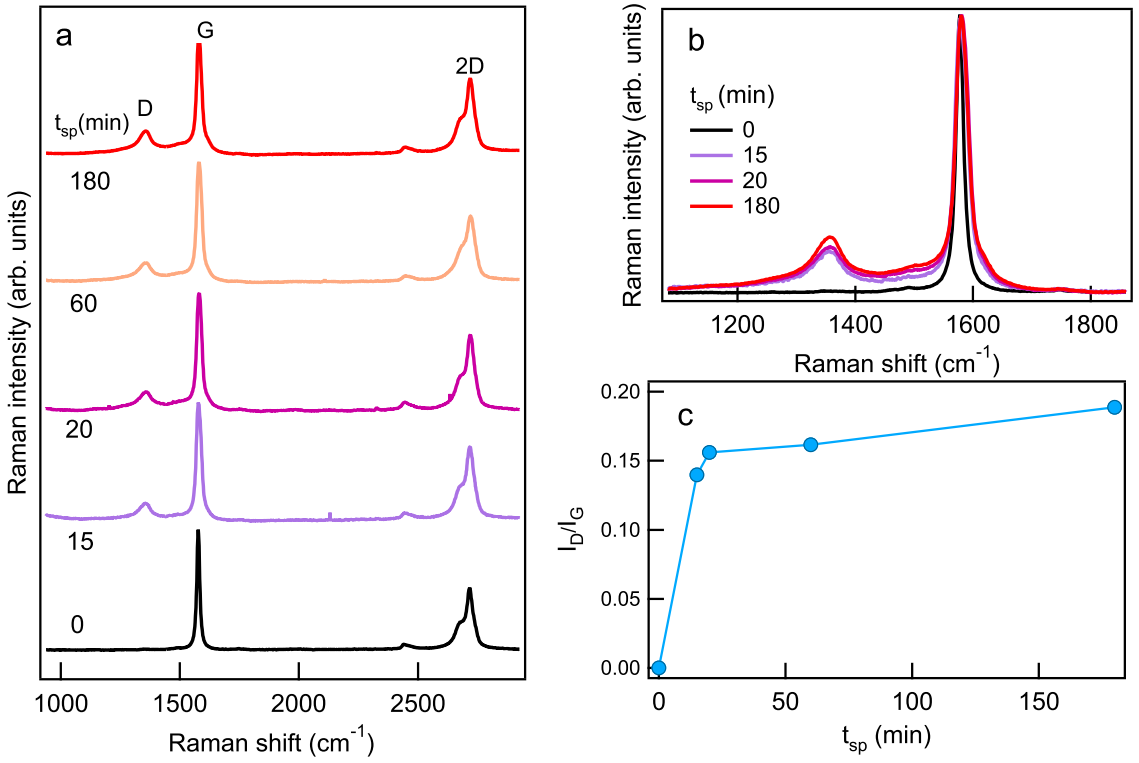

Figure 9.8: **Left:** Raman spectra measured on HOPG as a function of the ion dose. **Upper Right:** Magnification of the normalized Raman spectra in the region of peak D. **Bottom Right:**The ratio R=D/G as a function of t_{sp}

in the figure. For pristine HOPG the spectrum is composed of two bands, G at 1585 cm^{-1} and 2D at 2700 cm^{-1}. After ion bombardment, with the onset of lattice disorder, the peak D, which is prohibited in the perfect hexagonal lattice, appears at 1350 cm^{-1}, as the presence of defects in the aromatic rings makes it allowed. The intensity of D rises with the ion dose, being directly proportional to the number of defects in the sp^2 lattice. The curves in the upper right panel of Fig. 9.8 show that the spectral positions of D and G remain fixed at their initial values, excluding the onset of sp^2 $\rightarrow$ sp^3 rehibridization, in agreement with behavior of the C1s core level. The direct comparison among the different spectra shown in the upper right panel of Fig. 9.8 reveals that the rising lattice disorder causes the increase of the spectral background. This derives from the enhanced inelastic photon-phonon scattering in the presence of a higher density of defects, which contributes to the breakdown on the momentum selection rules. The bottom right panel of Fig. 9.8 shows the ratio R=D/G as a function of t_{sp} . The saturation of R at high Ar$^+$ doses indicates that ion induced damaging is confined in a thin sample layer while the underlying bulk remains unaffected.

9.2 Bi-layered sample SEY model

After AFM analysis, It has been assumed that the evolution of SEY parameters with the ion bombardment dose can not be ascribed only to a change in the surface morphology. On the other hand, photoemission spectroscopy analysis revealed that XPS C1s peak remains centered at the same BE revealing that the evolution of SEY of HOPG with ion doses can not be ascribed to a sp^2 to sp^3 transformation [20, 106, 241, 242].

A strong correlation between the electronic structure close to the Fermi level and the yield of SE's has been proved [126, 242, 243], in such a way that a prohibited energy interval for the scattering electrons due to the presence of a possible band gap may reduce the probability for SE's to lose energy trough electron-electron collisions, resulting on an increase of the SEY values. However despite a clear amorphization of the crystalline structure of the HOPG sample achieved due to ion bombardment, no variation in the band gap was observed, remaining absent for all ion bombarding stages, which confirms XPS results demonstrating that 3-fold geometry is not present in the carbon crystalline network. Nevertheless the observed evolution of the VB features after UPS analysis of the treated samples, confirm the crystal damaging of the samples after ion beam exposure.

It has been reported that crystal defects play an important role on the electrical properties of garphite, resulting on a reduction of the IMFP of electrons moving within it[244–247]. Such effects were experimentally confirmed revealing that the localized states that appear near the defect sites act as scattering centers for electron waves. Thus, one can expect that such defects will result in a drop of conductance, which, must have drastical effects on the SE emitting phenomena within the material under study [26, 53]. The crystal defects originated after ion bombardment, and the consequent increase of electron scattering are assumed to be present exclusively within the range of penetration depth of the bombarding ions, and hence deeper regions of the sample, which remain undamaged would present no anomalous electron scattering. Thus in the proposed bi-layered model the sample is composed by two consecutive domains $\mathfrak{D}_1$ and $\mathfrak{D}_2$ of different and homogeneous electron IMFP λ_1 and λ_2 repectively and disposed along the x direction (depth) as pictorially explained in Fig. 9.9.

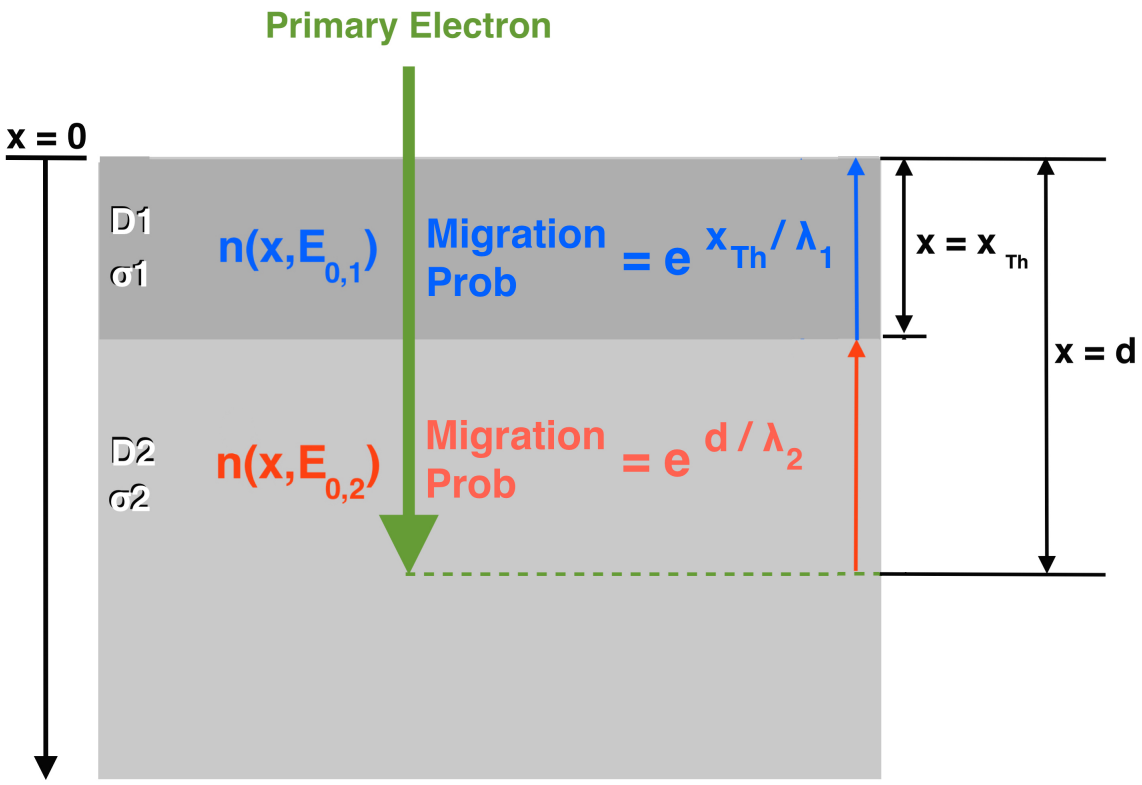

Figure 9.9: Model proposed for the bi-layered sample.

The SEY equation proposed by Dionne [26, 53] was used order to understand the observed evolution of SEY parameters as a function of the Ar^+ ion bombardment. As previously noted, SEY measurements on fully bombarded graphite HOPG reached a saturation point after which, SEY is not further modified and hence the crystalline structure within the outermost layers of the sample is assumed to be evenly damaged.

In order to reproduce the effect of the inhomogeneous electrical conductivity, the integral expression of Dionne's formula presented in Sec. 3.2.1 [26, 53] must be modified in such a way that the physical processes involved in the SE behavior is described by the correspondent physical parameters the domain within which they are generated.

Based on the relationship between the energy of the primary electrons and their range exposedin Sec. 3.2

$$d = \frac{E_0^n}{n \cdot A} \tag{9.1}$$

a primary energy threshold E_{Th} can be defined as the primary energy needed for an electron to trespass the outermost Domain $\mathfrak{D}_1$, at a depth $x = x_{Th}$, and start traveling through the subjacent Domain $\mathfrak{D}_2$. According to this definition Dionne's formula for primary energies $E_0 < E_{Th}$, at which electron range d is smaller than $x = x_{Th}$, can be rewritten as follows

$$SEY(E) = \int_0^d n(x, E_{0,1}) f(x) dx \tag{9.2}$$

where, as previously pointed out in Sec. 3.2.1, $n(x, E_{0,1})$ is the average number of secondary electrrons produced, assumed to be

$$n(x, E_{0,1}) = -\frac{1}{\zeta}\left(\frac{dE}{dx}\right) \tag{9.3}$$

proportional to the average energy loss per unit path length $\frac{dE}{dx}$, and ζ is the average energy loss per generated SE. The function $f(x)$ represents the probability for a SE produced at x to arrive at the surface and escape, overcoming the WF barrier. and is expressed as

$$f(x) = p_e p_m(x) \tag{9.4}$$

where $p_e = B$ and $p_m(x) = exp(-\alpha x)$ are the escape probability and migration probability respectively.

On the other hand, for primary energies $E_0 > E_{Th}$, at which electron range d is greater than $x = x_{Th}$ Dionne's formula becomes

$$SEY(E) = \int_0^{x_{Th}} n(x, E_{0,1}) f_1(x) dx + \int_0^d n(x, E_{0,2}) f_2(x) dx \tag{9.5}$$

In this special case $E_{0,1}$ represents the energy of the primary electrons penetrating into $\mathfrak{D}_1$, and correspondingly $E_{0,2}$ represents the energy of the primary electrons penetrating into $\mathfrak{D}_2$. The function $f_2(x)$ which represents the probability for a SE produced at Domain $\mathfrak{D}_2$ to arrive at the surface and escape, needs in this case to be redifined,

$$f_2(x) = p_e p_m(x) p'_m(x) \tag{9.6}$$

where $p'_m(x)$ is the migration probability of a SE produced at $\mathfrak{D}_1$ travelling through $\mathfrak{D}_2$, leading to

$$f_2(x) = B \cdot e^{-\alpha_1 x_{Th}} \cdot e^{-\alpha_2 x_{E02}} \tag{9.7}$$

At this point, it is worth to express SEY equations as a function of the average IMFP of the SE's which according to what was exposed in Sec. 3.2.1 $\lambda_i^s = 1/\alpha_i$. By doing so, Dionne's equation for $E < E_{Th}$ is expressed as

$$SEY(E_{0,1}) = \left(\frac{B}{\xi}\right)(nA\lambda_1^s)^n \left(\frac{d}{\lambda_1^s}\right)^{\frac{(1-n)}{n}} (1 - e^{d/\lambda_1^s}) \tag{9.8}$$

which suffers no modification with respect the orginal mono-layered model, since electron ranges remain within $\mathfrak{D}_1$. In the second case however the solution of the integral differs from Eqn. 9.8 and is expressed as follows [248]:

$$\begin{aligned} SEY(E_{0,1}) = &\left(\frac{B}{\xi}\right)(nA_1\lambda_1^s)^n \left(\frac{d(E_{0,1})}{\lambda_1^s}\right)^{\frac{(1-n)}{n}} (1 - e^{(x_{Th}/\lambda_1^s)}) + \\ &+ e^{(x_{Th})/\lambda_1^s} \left(\frac{B}{\xi}\right)(nA_2\lambda_2^s)^n \left(\frac{d(E_{0,2})}{\lambda_2^s}\right)^{\frac{(1-n)}{n}} (1 - e^{d(E_{0,2})/\lambda_2^s}) \end{aligned} \tag{9.9}$$

The left summand of the Eqn. 9.9 represents the contribution of $\mathfrak{D}_1$ of thickness x_{Th} to the SEY at energies higher than E_{Th} at which electron ranges penetrate into D2. The exponential factor $e^{-\alpha'(x_{Th})}$ that multiplies the right summand of Eqn. 9.9, finds its physical meaning in the attenuation of the SE's produced at $\mathfrak{D}_2$ while travelling within $\mathfrak{D}_1$. Such exponential factor appears multiplying the expression of the SEY of the subjacent material that composes $\mathfrak{D}_2$.

In this work, the above exposed model was used in order to fit the results obtained for the ion bombarded HOPG.

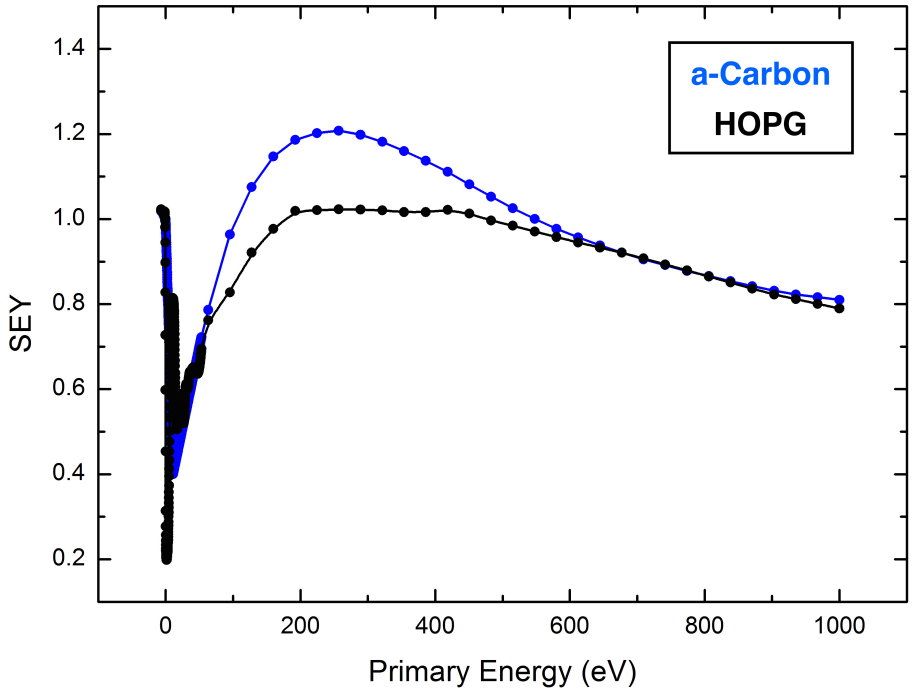

Figure 9.10: SEY results measured on "as cleaved" HOPG (Black line) and a-C according to [106](Blue line).

The SEY of the subjacent undamaged HOPG that composses $\mathfrak{D}_2$ was measured at the first stage of the experiment, and represented with a black line in Fig. 9.10. Since after an ion bombardment period of $t_{sp} = 180min$ the behavior of SEY has revealed a saturation in the crystalline damage of the HOPG sample, $\mathfrak{D}_1$ has been assumed to be homogeneously formed by sp^2 bonded a-C, which SE emitting properties are well known. SEY results measured on a-C carried out at LNF-INFN which synthesis procedure is explained elsewhere[106], are shown in Fig. 9.10 in comparison with the results obtained for "as cleaved" HOPG.

In order to validate the SEY described by Eqn. 9.9 for the proposed bi-layered sample model, the unknown values of A, α and (B/ξ) of both HOPG and a-C must be estimated. To do so, SEY^{HOPG} and SEY^{a-C} which experimental values are shown in Fig. 9.10, were calculated by using Dionne's formula, and values of A, α and (B/ξ) were chosen to give the best fit to the experimental results. As previously reported in Sec. 3.2.1 the known experimental values of $E_{0,m}$ and SEY_{max} are related to the unknown physical parameters as follows [26, 53]:

$$E_{0,m} = 2.3(A\lambda_s)^{0.74} \quad ; \quad SEY_{MAX} = 0.9\left(\frac{B}{\zeta}\right)(A\lambda_s)^{0.74} \tag{9.10}$$

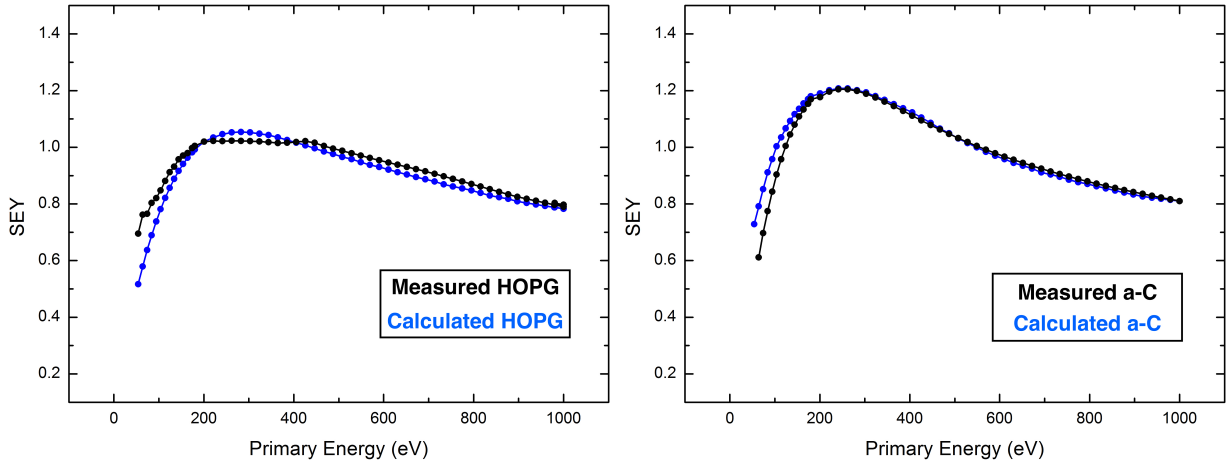

Figure 9.11: **Left:** Comparison between calculated SEY curves by using Dionne's formula (BLue line) and experimental SEY results measured on "as cleaved" HOPG. **Right:** Comparison between calculated SEY curves by using Dionne's formula (Blue line) and experimental SEY results measured on a-C according to [106].

	SEY_{max}	$E_{0,m}$	A	λ^s **(nm)**	(B/ζ) **(keV^{-1})**	χ^2
HOPG	1.07	270	497	1.25	0.010	0.18
a-C	1.21	240	796	0.67	0.012	0.06

Table 9.1: Physical parameters obtained after HOPG and a-C SEY curve fitting obtained by using Dionne's formula.

By making use of Eqns. 9.10 the parameters needed to fit SEY^{HOPG} and SEY^{a-C} were found, and the results of the fittings are shown in Fig. 9.11. The parameters of A α and (B/ξ) obtained according to the measured value of $E_{0,m}$ and SEY_{max} are presented in Table 9.1. As it can be seen in Fig. 9.10 , the energy range within which SEY^{HOPG} can be assumed to reach its maximum point appears to vary from 200 to 420 eV, and hence the determination of $E_{0,m}$ is not straightforward. However an intermediate value of $E_{0,m}$= 280 eV was found to be the most appropriate value to fit the calculated SEY curve to the experimental results.

χ^2 was calculated to test the accuracy of the fits carried out revealing satisfactory results for both SEY^{HOPG} and SEY^{a-C}. Once the values of the parameters A α and (B/ξ) were estimated they can be used to validate the proposed bi-layered model.

At this point, it is possible to estimate the vaues of x_{Th} and E_{Th}. On one hand, Open access SRIM simulation software [249] was used to calculate the range of the bombarding 150 eV Ar^+ ions, which coincides with the depth x_{Th} at which the transition from $\mathfrak{D}_1$ to $\mathfrak{D}_2$ happens, resulting in a value of x_{Th}=1.20 nm $\pm$ 0.15. On the other hand, according to the SEY curve fittings previously carried out, the parameters involved in Eqn. 9.1 are known, and hence the value of E_{Th} is now achievable. Rewriting Eqn. 9.1 as

$$E_{Th} = (x_{Th} \cdot n \cdot A)^{1/n} \tag{9.11}$$

a value of E_{Th}=175 eV was obtained for A=497 keV^{-1}, n = 1.35 [26, 229], and x_{Th}=1.20 nm.

At this point, some conclusions can be reached regarding the physical parameters presented in table. 9.1, and the E_{Th} and x_{Th} thresholds values obtained. According to Eqn. 9.1 and making use of the estimated primary electron absorption coefficient A of both HOPG and a-C, The actual electron range for this bilayered sample can be calculated. Fig. 9.12 shows the electron range obtained for the sample studied in which a sudden increase at $E_{Th} = 174eV$ is observable. When electrons bombard the sample during the SEY measurement procedure with energies below E_{Th}, their ranges lay within the damaged region and loose their energy, generating SE's at a depth closer to the surface. this effect results in an increase of their scape probability, which results in the observed increase of SEY in the right panel of Fig. 9.1. Whereas more energetic electrons travel deeper into the solid, interacting with the undamaged HOPG atoms. On the other hand, the sudden change of the SE's IMFP that takes place at x_{Th} has an important effect on the SE's generated within $\mathfrak{D}_2$. As a result of such inhomogeneous IMFP, the migration to the surface of SE's generated at depths greater than the ion range, must be substantially reduced decreasing their scape probability which results in the observed decrease of the SEY values at $E_0 > E_{Th}$.

Once the value of E_{Th} is known, it is important to emphasize certain points regarding Eqn. 9.9. Firstly it must be noticed that as previously explained the energy $E_{0,2}$ of the electrons reching $\mathfrak{D}_2$, differs from the energy $E_{0,1}$ of the primary electrons due to the loss of energy that primary electrons suffer when traveling thruogh $\mathfrak{D}_1$. This effect results as pictorially explained in Fig. 9.13 in a displacement of the contribution of SEY^{D2} towards higher primary energies, being such contribution equal to zero for $E_{0,1} < E_{Th}$. For simplicity, since at high energies up to 1000 eV the electron range is some orders of magnitude higher than x_{Th}=1.2nm, it has been assumed that $E_{0,2} = 0$ when $E_{0,1} = E_{Th}$, and $E_{0,2} = E_{0,1}$ when $E_{0,1} = 1000eV$.

Secondly, analyzing Eqn. 9.9, and taking into account the formula that describes the SEY of an homogenous monolayered sample in Eqn. 9.8, Eqn. 9.9 can be rewritten as

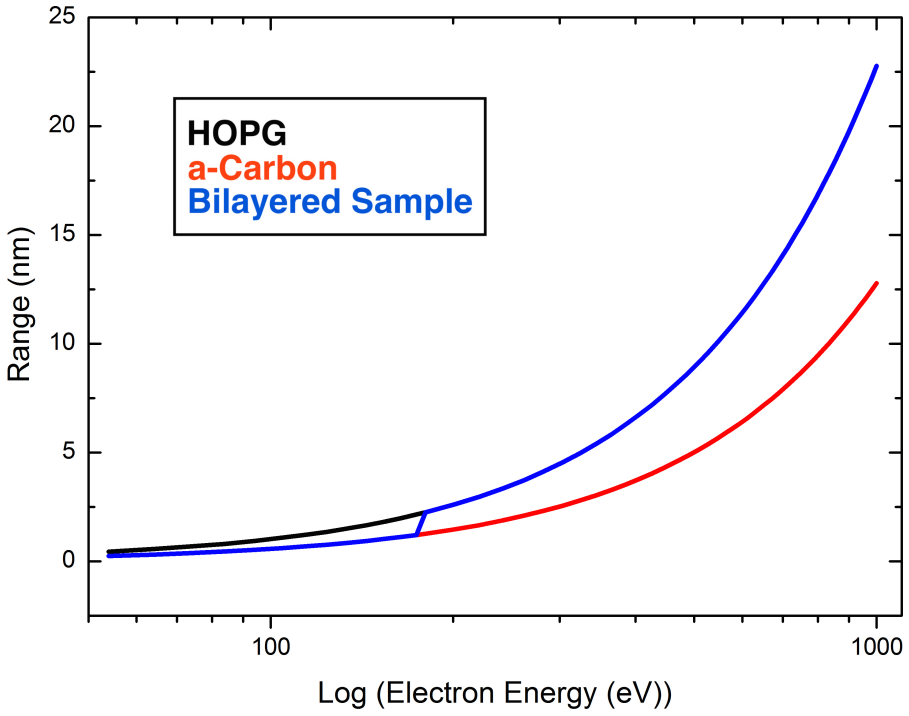

Figure 9.12: Calculated electron ranges of HOPG (Black line), a-C (Red line) and HOPG after an ion bombardment period of $t_{sp} = 180min$ (Blue line).

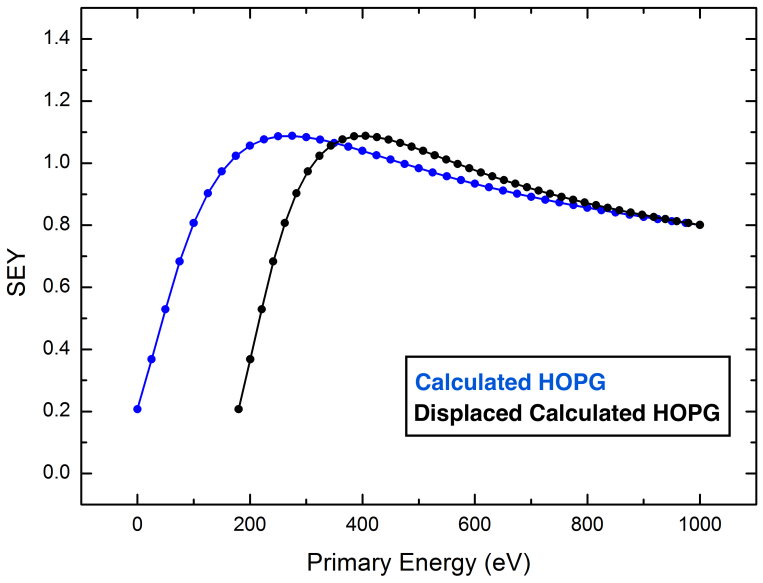

Figure 9.13: Graphical representation of the displacement of the contribution of the subjacent undamaged HOPG to the total SEY due to the energy loss of the electrons after travelling through $\mathfrak{D}_1$ (Black line), in comparison with the SEY curve of HOPG.

$$SEY(E_{0,1}) = SEY^{a-C}(E_{0,1})\frac{(1-e^{-\alpha' 1.2nm})}{(1-e^{-\alpha' d_{E_{0,1}}})}+ \\ +e^{-\alpha(1,2nm)}SEY^{HOPG}(E_{0,2}) \tag{9.12}$$

The bi-layered sample SEY curve was calculated by making use of Eqns. 9.8 and 9.12, obtaining a result that agrees with the observed behavior of the SEY curve measured on the bombarded graphite sample exposed to $t_{sp} = 180min$. A comparison between both calculated and experimentally obtained curves is shown in fig.9.14.

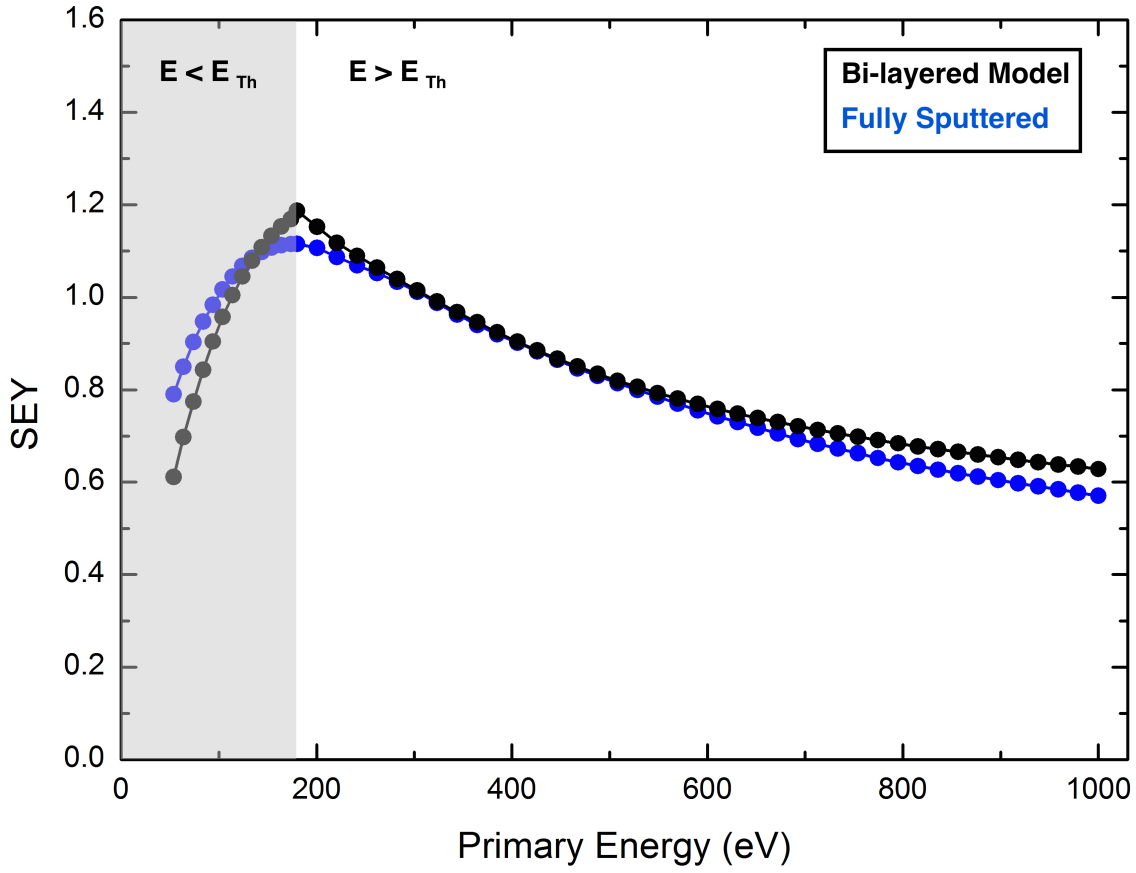

Figure 9.14: Calculated SEY curve resulting from the bi-layered sample model equations (Black line) in comparison with SEY measured on damaged HOPG after an ion bombardment period of $t_{sp} = 180min$ (Blue line).

Satisfactorily, one can observe that $E_{0,m}$ of both curves coincide at $E_{0,1} \sim 174$ eV, in good agreement with the value of E_{Th}, consistent with the fact that at primary energies higher than E_{Th}, electrons travel through the domain $\mathfrak{D}_2$ of lower absorption coeficient A_{D2} suffering substantially less scattering than in $\mathfrak{D}_1$ and penetrating deeper into the sample. However the SEs, with kinetic energies below 50 eV, when traveling towards the surface,

impact in the domain D1 and its higher SE absorption coefficient α_{D1} impedes the migration of electrons to the surface, therefore SEY results to be lower than for undamaged HOPG.

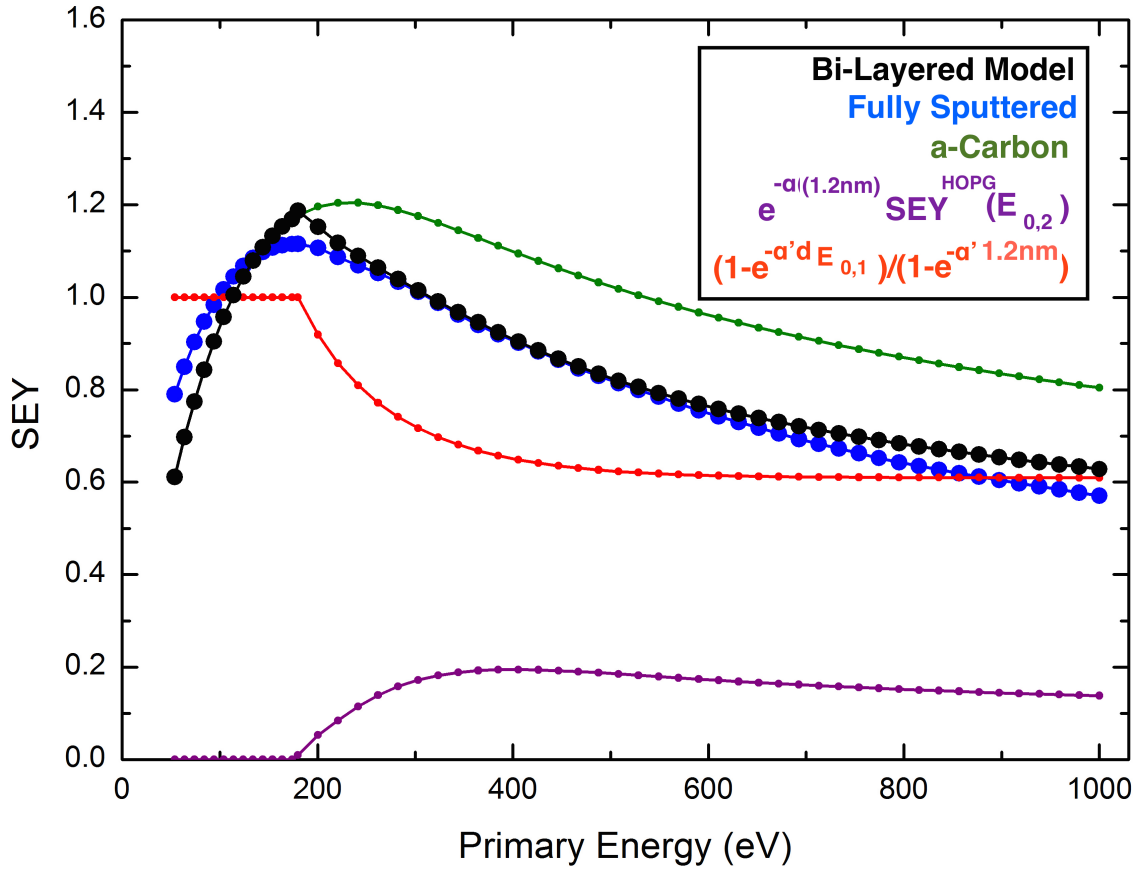

Figure 9.15: Calculated SEY curve resulting from the bi-layered sample model equations (Black line) in comparison with SEY measured on damaged HOPG after an ion bombardment period of $t_{sp} = 180min$ (Blue line).

Fig. 9.15 shows the calculations previously presented in Fig. 9.14, together with all the contributions of the components involved in Eqns. 9.8 and 9.12. Such representation is indeed very instructive to understand the phenomena that takes place during the SEY measurement process of a bi-layered sample. The term $(1 - e^{-1.2nm/\lambda_s^1})/(1 - e^{-d_{E_{0,1}/\lambda_s^2}})$ is represented with a red line in Fig. 9.15 which shows that as the energy increases, after trespassing E_{th}, the contribution of $\mathfrak{D}_1$ i.e. (a-C), decreases and no longer depends on the primary electron energy, when x_{th} becomes negligible comparing with the electron range. Hence it reaches a steady value at E $\sim$ 600 eV. The green line represents the SEY of the a-C, which at $E > E_{th}$ is multiplied by the term $(1 - e^{-1.2nm/\lambda_s^1})/(1 - e^{-d_{E_{0,1}/\lambda_s^2}})$. Note that at $E > E_{th}$ the values of the calculate SEY coincide with SEY^{a-C}, since for that energy, electron ranges remain below x_{th}. The purple line of Fig. 9.15 represents the contribution of the subjacent HOPG after multiplying $SEY^{HOPG}(E_{0,2})$ by the term

$e^{-\alpha(1,2nm)}$, and ilustrates the strong damping effect that the a-C overlaying domain has on the SE's generated at $\mathfrak{D}_2$ i.e. the subjacent HOPG.

9.3 Summary

The amorphization of the crystalline structure of HOPG by 150 eV Ar^+ bombardment on the sample was confirmed by means of UPS, XPS, Raman and LE-SEY spectroscopies. LE-SEY measurements revealed spectral structure correspondent to unoccupied band structure of graphite. Such smeared out as the sputtering process and the consequent crystalline amorphization started. An anomalous evolution of SEY with the sputtering time was observed. Accordingly, a bi-layered sample model with IMFP and primary electron absorption coefficient variant in depth was proposed in order to elucidate the origin of such behavior.

Chapter 10

Conclusions

The two main objectives of this work are: •The development of anti-Multipactor coatings of low SEY and low power insertion losses for technological applications in satellite RF wave guide devices, particularly in K_u-*Band Low Pass Filters*. •The comprehensive study of the SEE processes; their dependance with the morphological, chemical, and cristalographic state of the sample and their role on the EC build up and heat load enhancement.

The experimental research related to the first point was carried out in the framework of the ESA ITI project "Optimization of Surface Roughness of Anti-Multipactor Coatings for Low Insertion Losses and Secondary Emission Suppression for High Power RF Components in Satellite Systems". The reduction of SEY was achieved by applying nano-structuring ion beam processes on the metallic surfaces of the satellite RF devices, whose interaction with SE impedes their escape to vacuum. The strategy to achieve this aim has followed the next scheme:

- Two different techniques based on preferential masked ion etching were used in order to achieve nano structured coatings of low SEY, namely, *Ti Cone Technique* and *Ion Assisted Magnetron Sputtering Technique*
- Both techniques were developed and improved during a previous period of research whose results were presented in Ch. 6. In such period intensive studies were performed in order to obtain the required skills for the use of the plasma based techniques

and the optimization of the appropriate treatment procedures and experimental conditions

- According to the knowledge obtained in Ch. 6, the *K_u-Band Low Pass Filters* were treated. Those filters obtained through the *Ti Cone* and *Ion Assisted Magnetron Sputtering Techniques* were tested in order to measure their Multipactor and IL properties.

The aim of this part of the work was settled according to the actual and very specific demanded necesities of the aerospatial industry, which ensures the straighforward application of the knowledge obtained as resulting from this research. Nevertheless, the rquirements of the project pushed us to spare in the time employed to develop our research, and hence certain limitations arise regarding the techniques available to develop such studies with the desired scientific methodology. For these reasons, only qualitative analysis of the properties studied was performed. In spite of the initial difficulties in finding the process techniques and conditions to produce strong surface roughness on Ag plating with high aspect ratio and small size, the techniques and the procedures are well defined and easy to apply and **the dependance of the morphology with controllable parameters as ion flux, ion energy, substrate temperature and exposure time was studied and understood**, leading to extremely valuable information for the anti-Multipactor research field. Eventhough It was proved that backscattered electrons, which directionality is constrained to a certain solid angle are more sensible to changes in the morphology of the surface than true secondaries, the reduction of SEY was confirmed to be dominated by the effect that rough surfaces have on the true secondary electrons, since the latter represent the vast majority of the emitted electrons. A clear increase in the secondary electrons cut-off of the measured EDC spectra was observed, which was ascribed to an increase of the WF due to surface roughening. Such assumption is in clear contradiction with studies published by other authors, which reveals the necessity of performing further studies regarding this aspects. The *Ti cone technique* was discarded as an anti-Multipactor strategy, for two main reasons, i.e. Even though the enhancement of the power insertion losses were reduced with respect those obtained in previous projects, it still remained well above the maximum accepted. Also the surface formed after the Ti-cone technique procedure resulted to be very inhomogeneous, revealing that for samples of

larger area than witness samples, this technique does not provide an homogeneous source of Ti.

On the other hand, it was concluded that the ion assisted magnetron sputtering technique represents a strategy sensible to ion current changes but of very reproducible results. Three of the four treated filters showed a multipactor threshold larger than the minimum 6000 W demanded by the objectives of the project, and one of them showed no Multipactor within the power range provided by measurement equipments, which reveals satisfactory results for their anti-Multipactor applications. It is noticeable that in good agreement with previous observations second discharges happen at higher RF power that first discharges which means that after a multipactor discharge has taken place, the threshold tends to increase due to the effect that electron irradiation has on the chemical state of the wall surface due electron conditioning or *Scrubbing*.

None of the treated filters revealed an insertion loss enhancement larger than the 20% of the initial value, which represents unprecedent good result of extremely great importance for the aerospatial industry. It was proved that when reducing nano-strucutre size to values sufficiently low comparing to the skin depth of the transmitted wave, the RF power loss due to skin effects are practically unaltered from its initial value.

The experimental work related to a comprehensive study of the SEE processes allowed us to confirm the **possibility of measuring LE-SEY with great confidence and without experimental artifacts above less than 1 eV from sample WF**. It was concluded that the discrepancies found in literature can be simply ascribed to the different samples studied and to their degree of contamination, being their actual composition and metallicity of the outermost layers, which significantly alter the reflectivity at zero landing energies. It was also confirmed that clean metals as Cu, Ag and Au, as well as annealed HOPG show the same low reflectivity behavior, and its analysis subtle differences related to different electronic properties of each material. The measurement of the sample WF by means of LE-SEY techniques however, has been proved to be extremely sensitive to small changes of the e^-gun energy off-set variations, and due to the lack of reliability of e^-gun energy displayed value, accurate WF determination was not achievable so far. Further improvements in the experimental set-up are required to address in detail this

issue, specially in presence of a well defined and thick over layer in order to study the effect of the presence of controlled contaminants on the WF. On the other hand, preliminary calculations show that the LE-SEY detailed knowledge is indeed important to correctly simulate and predict EC effects. The simulations confirm a **significant impact of the LE-SEY on the EC buildup behavior. In particular the heat load SEY_{Max} threshold, defined as the value at which the available beam screen cooling capacity is exceeded, becomes significantly lower for higher LE-SEY values**. It has been observed that more than the actual SEY at 0 eV, it is the overall behavior of the LE-SEY which can significantly influence EC predictions in LHC.

After HOPG amorphization experiments, it has been shown that **the degree of crystallinity is a determinant factor in the SEE properties of graphite**. Supported by the fact that LE-SEY shows structures which carry information about the elastic and inelastic electron-solid interactions, it has been shown that LE-SEY spectroscopies give direct information on the unoccupied band structure of solids due to strong coupling with electronic states delocalized in the impinging electron direction. When the crystallinity of HOPG is ruined due to Ar^+ bombardment, the contribution to the spectra arises from different polar angles which originates the smearing of the spectral structures. Besides, **crystalline amorphization of HOPG has been proved to be capable of modifying also the behavior the SEY due to the variations in the IMFP of secondary electrons** produced by an increase of the scattering of the electrons with the concentration of defects. Based on the results obtained, a bi-layered sample model was proposed to elucidate the origin of the anomalous behavior of SEY. The results obtained were in good agreement with the hypothesis of a damaged overlayer which impedes the migration of low energy SE's produced below it. Such effect was ascribed to a decrease of the IMFP of the SE's due to an increase of the concentration of defects within the crystalline network.

The major contributions of this work are the achievement of anti-Multipactor coatings with unprecedent improveed properties in IL and an improvement of the present knowledge regarding the process involved in SEE phenomena. Also the development of techniques for accurately measuring LE-SEY in an extremely low energy range was achieved, together with the understanding of the repercussion that such data has on the EC research field.

Chapter 11

Conclusiones

Los dos objetivos principales de este trabajo son: •El desarrollo de recubrimientos anti-Multipactor de baja emisión secundaria y bajas pérdidas de inserción para aplicaciones tecnológicas en dispositivos de radio frecuencia de satélites, en particular *Filtros de Paso Bajo de la Banda* K_u. •El estudio de los procesos de emisión secundaria de electrones; su dependencia con el estado morfológico químico y cristalino de las muestras y su papel en la formación de la nube de electrones.

La investigación experimental relacionada con el primer punto, se ha desarrollado en el marco del proyecto ITI de la ESA "Optimization of Surface Roughness of Anti-Multipactor Coatings for Low Insertion Losses and Secondary Emission Suppression for High Power RF Components in Satellite Systems". La reducción de SEY se obtuvo por medio de procesos de nano-estructuración en las superficies metálicas de los dispositivos de radio frecuencia de satélites, cuya interacción con los electrones secundarios impide su emisión al vacío. La estrategia para lograr los objetivos han seguido el siguiente esquema:

- Se han usado dos técnicas diferentes basadas en el *etching* iónico preferencial para obtener recubrimientos nano-estructurados de bajo SEY, a saber; *Técnica del cono de Ti* y *Técnica de Sputtering por Magnetron Asistido por Iones*

- Ambas técnicas fueron desarrolladas y mejoradas durante un periodo de investigación previo cuyos resultados se expusieron en el Capítulo 6. En dicho periodo se realizaron estudios intensivos para obtener las habilidades necesarias para usar las técnicas de

deposición y la optimización los procedimientos y condiciones experimentales apropiados

- Los filtros de guía de onda fueron tratados de acuerdo con los conocimientos adquiridos en el Capítulo 6. Se testearon aquellos filtros obtenidos por medio de las técnicas *Técnica del cono de Ti* y *Técnica de Sputtering por Magnetron Asistido por Iones* para medir sus propiedades de Multipactor y pérdidas de inserción.

El objetivo de esta parte del trabajo realizado se definió de acuerdo con los estrictos requerimientos de la industria aerospacial, lo cual asegura la aplicación directa de los conocimientos obtenidos a raíz de esta investigación. Sin embargo dichos requerimientos hicieron necesaria la escatimación del tiempo empleado en desarrollar la investigación, y por lo tanto ciertas limitaciones surgieron de acuerdo con las técnicas disponibles para desarrollar dichos estudios con la deseada metodología científica. Por estos motivos, deben llevarse a cabo análisis mas avanzados en el futuro. A pesar de las dificultades iniciales de encontrar las técnicas para producir superficies rugosas de alta relación de aspecto y tamaño reducido, las técnicas usadas y sus procedimientos están bien definidas y son fáciles de aplicar. **Además la dependencia de la morfología con parámetros controlables como el flujo de iones, su energía, la temperatura del substrato y el tiempo de exposición han sido analizadas y entendidas**, lo que constituye información extremadamente valiosa para el campo de investigación del Multipactor.

Aunque se ha probado que son los electrones retrodispersados aquellos mas susceptibles a sufrir la reabsorción en las vecindades de la rugosidad, se ha confirmado que la reducción del SEY está dominada por el efecto que la rugosidad tiene en los electrones secundarios verdaderos, ya que estos últimos representan una basta mayoría de los electrones emitidos.

Se ha observado un claro aumento en el límite del pico de los electrones secundarios a bajas energías en las medidas de EDC. Este efecto ha sido adscrito a un aumento en la función de trabajo del material debido a la formación de la rugosidad. Esta afirmación sin embargo está en clara contradicción con los resultados encontrados en la bibliografía y por tanto futuros estudios deben ser realizados de manera mas detallada con respecto a este tema en el futuro. La técnica del cono de Ti fue finalmente descartada como estrategia

anti-multipactor por dos razones principales, estas son: Aunque el aumento de las perdidas de inserción fue reducido con respecto a los valores obtenidos en proyectos anteriores, la reducción no fue suficiente en base a los requerimientos del proyecto. Además la superficie formada por el tras el tratamiento resultó ser altamente inhomogenea.

Por otra parte, se concluyó que la técnica de sputtering por magnetrón asistido por iones representa una estrategia sensible a cambios en el flujo de iones sin embargo los resultados han sido altamente reproducibles. Tres de los cuatro filtros estudiados con esta técnica mostraron límites de Multipactor por encima de los 6000 W exigidos por los objetivos del proyecto, entre los cuales, uno de ellos no mostró descarga Multipactor en el rango de potencia en el cual se testeó, lo que revela los satisfactorios resultados para aplicaciones anti-Multipactor. Es notable el hecho de que de acuerdo con observaciones previas, las segundas descargas multipactor ocurren a potencias mas altas que las primeras en un mismo dispositivo, lo que significa que tras la primera descarga, el límite de multipactor tiende a incrementarse. Tal incremento ha sido adscrito al cambio en el estado químico de la superficie del filtro que tiene lugar tras el condicionamiento electrónico o *Scrubbing*.

Ninguno de los filtros tratados ha revelado un incremento de las perdidas de inserción superior al 20%, lo que representa un resultado favorable sin precedentes de suma importancia para la industria aeroespacial. Se ha demostrado que al reducir el tamaño de las nano-estructuras superficiales a valores comparables con la longitud de penetración de la onda transmitida en el sólido, las pérdidas por inserción permanecen prácticamente inalteradas.

El trabajo experimental realizado en cuanto el estudio de los procesos de emisión secundaria de electrones nos permitió confirmar la **posibilidad de medir LE-SEY con gran confidencia sin artefactos experimentales a energías menores que 1 eV sobre la función de trabajo de la muestra medida**. Se concluyó también que las discrepancias encontradas en la literatura pueden ser adscritas a diferentes grados de contaminación de las muestras, siendo la composición de las capas mas externas de la contaminación las que alteran significativamente la reflectividad de los electrones a energías cercanas a 0 eV.

Se ha confirmado también que superficies metálicas libres de contaminantes como Cu, Ag, Au, así como HOPG, muestran el mismo comportamiento de baja reflectividad a bajas

energías. Sin embargo, la medida de la función de trabajo de los materiales a través de las medidas de LE-SEY, es extremadamente sensible a los pequeños cambios en la medida de la energía primaria de los electrones por parte de la fuente de alimentación del cañón. Debido a la consecuente falta de confidencialidad, valores precisos de las funciones de trabajo no son obtenibles hasta la fecha. Se requieren futuras mejoras en el montaje experimental para abordar este aspecto con detalle.

Por otra parte, cálculos preliminares muestran que el conocimiento de LE-SEY es de gran importancia para simular correctamente y predecir los efectos de la nube de electrones. Las simulaciones confirmaron un **gran impacto de LE-SEY en el comportamiento de la nube de electrones en su formación**. En particular, el valor limite de SEY_{Max} para el cual la carga de calor aceptable es excedida, es notablemente mas bajo para valores de LE-SEY altos. Ha sido también observado que son los valores de LE-SEY en toda la región de baja energía, mas que los valores cercanos a 0 eV, los que juegan un papel importante en las predicciones del comportamiento de la nube de electrones en el LHC.

Tras los experimentos de amorfización de HOPG se ha mostrado que **el grado de cristalinidad es un factor determinante para las propiedades de emisión secundaria de electrones en grafito**. Se ha demostrado que LE-SEY provee información directa de los estados no ocupados de la estructura de bandas de los sólidos debido a un fuerte acoplamiento con los estados electrónicos de-localizados en la dirección de impacto de los electrones primarios. Cuando la estructura cristalina del HOPG se arruina debido al bombardeo iónico, la contribución al espectro LE-SEY proviene de diferentes ángulos polares, lo que origina la pérdida de definición de las estructuras espectrales. Además, **se ha demostrado que la amorfización de la estructura cristalina del HOPG tiene efectos en el recorrido libre medio de los electrones secundarios**, producido por un incremento de la dispersión de los electrones con la concentración de defectos. Basándose en los resultados obtenidos, se ha propuesto un modelo de muestra bi-capa, para elucidar el origen de el comportamiento anómalo del SEY observado. Los resultados obtenidos concuerdan con la premisa de que una capa superficial de carbono amorfizado impide la migración de los electrones secundarios producidos debajo de ella, lo que provoca una reducción del recorrido libre medio de los electrones secundarios debido a a un incremento en la concentración de defectos en la red cristalina.

Las mayores contribuciones de este trabajo son la realización de recubrimientos anti-Multipactor con mejoras sin precedentes relacionadas con las propiedades de pérdidas de inserción y la mejora del entendimiento de los procesos involucrados en los fenómenos de emisión secundaria de electrones. Además, se ha logrado el desarrollo de técnicas de medida precisa de LE-SEY en un rango de energía extremadamente bajo, junto con el entendimiento de la repercusión que dichos datos tienen en el campo de investigación de la nube de electrones.

Appendix A

The Sample Preparation Set-up at UAM

This appendix constitute a complementation of Sec. 5.2.3. A a detailed graphical explanation of the sample preparation set-up at UAM is presented. The set-up is presented in Fig. A.1 in which the main parts are marked with circled letters. Those letters will be cited in Appendix B to explain the surface treatment procedures followed. Those main parts are:

- **Ⓐ:** *Commonwealth* Kauffman ion gun (see Sec. 5.3.1.1)
- **Ⓑ:** MDC (USA) RF magnetron sputtering source (see Sec. 5.3.1.3)
- **Ⓒ:** High precision leak valve
- **Ⓓ:** 8" Conflat port sealed with Viton gasket
- **Ⓔ:** UHV gate large conductance valve to pumping
- **Ⓕ:** UHV right-angle low conductance valve

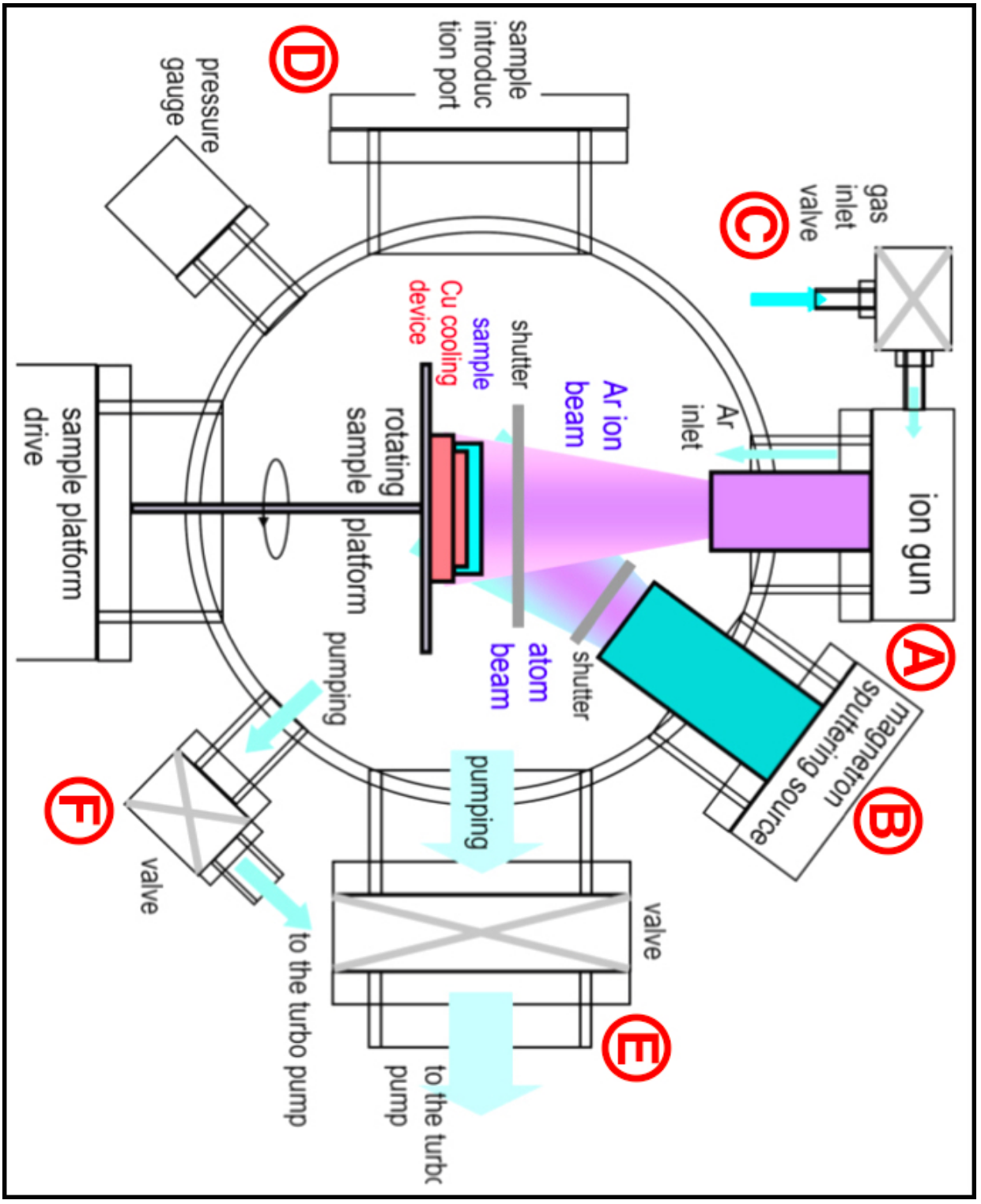

Figure A.1: Schematic description of the synthesis set-up at UAM.

Appendix B

Surfaces Treatment Procedure

In this appendix the detailed procedure, step by step, followed during the surface treatments are presented

Witness Surface Procedure The treatment procedure was carried out in the sample preparation set-up at UAM, (see Sec. 5.2.3). In the following, all despcriptions will be supported and referenced to Fig. A.1. A horizontal rotating sample platform is located in the center of the spherical chamber. A cooling device or anvil, formed by a copper cylinder of 75 mm diameter and 19 mm height is located at the center of the chamber. It moderates samples temperature while strong ion bombardment, maintaining it well below 100°C (see Sec. 6.3.3). The witness samples are installed ensuring a proper thermal contact by using screws to attach them to the copper anvil. The ion source Ⓐ, is located at normal incidence, aligned with the rotation axis of the cylindrical anvil on the sample platform. The magnetron sputtering head Ⓑ is located forming an angle of 35° with the normal to the sample. The flange and tube of the spherical chamber where the ion gun is installed are cooled by a fan. High purity Ar gas is let inside the system through the ion gun and regulated by a UHV leak valve (VGS) Ⓒ. The beam intensity profile depends on the parameters of the ion gun as explained in Sec. 5.3.1.2. Samples are introduced and taken out using an 8' Conflat port Ⓓ sealed with Viton gasket with the system vented with nitrogen. Several viewing ports allow to see and to light the sample in the platform from different angles. Every coating was applied on two samples at the same time in order

to observe possible dependencies of the morphology obtained on unexpected parameters. Before starting the sample preparation procedure, the system is vented with nitrogen, in order to open it and introduce the samples. Once the sample is located at the center of the chamber, the introduction port is closed and the system pumped with large conductance turbo pump valve Ⓔ and UHV right-angle valve Ⓕ open. The system is pumped for at least 24 h until pressure is below $2x10^{-7}$ mb, usually below $1x10^{-8}$ mb. At this point, in order to avoid equipment damages, pumping is limited by setting the turbo pump to low speed. Large conductance valve of turbo pump Ⓔ is then closed while UHV right-angle valve Ⓕ is maintained half open. Ar gas is let in using gas inlet valve until pressure rises to the desired value and the treatment procedure starts. When the procedure is finished, sample platform shutter is set on again and the sample is then maintained in vacuum for 24 hours in order to let ensure a complete cooling down of the sample.

Ku-Band Low Pass Filters Treatment Procedure The treatment procedure was carried out in the sample preparation set-up at UAM, (see Sec. 5.2.3). A horizontal rotating sample platform is located in the center of the spherical chamber. A cooling device or anvil, formed by a copper cylinder of 75 mm diameter and 19 mm height is located at the center of the chamber. It moderates samples temperature while strong ion bombardment, maintaining it well below 100°C (see Sec. 6.3.3). The filter shells are installed ensuring a proper thermal contact by using an extra cooling device that accurately fits the rear part of the Filter shell and ensures appropriate thermal contact with the copper anvil. The ion source Ⓐ is located at normal incidence, aligned with the rotation axis of the cylindrical anvil on the sample platform. The magnetron sputtering head Ⓑ is located forming an angle of 35° with the normal to the sample. The flange and tube of the spherical chamber where the ion gun is installed are cooled by a fan. High purity Ar gas is let inside the system through the ion gun and regulated by a UHV leak valve (VGS) Ⓒ. The beam intensity profile depends on the parameters of the ion gun as explained in Sec. 5.3.1.2. Filter shells are introduced and taken out using an 8' Conflat port Ⓓ sealed with Viton gasket with the system vented with nitrogen. Several viewing ports allow to see and to light the sample in the platform from different angles. Before starting the sample preparation procedure, the system is vented with nitrogen, in order to open it and introduce the samples. Once the sample is located at the center of the chamber, the introduction port is closed and the

system pumped with large conductance turbo pump valve and UHV right-angle valve Ⓔ open. The system is pumped for at least 24 h until pressure is below $2x10^{-7}$ mb, usually below $1x10^{-8}$ mb. At this point, in order to avoid equipment damages, pumping is limited by setting the turbo pump to low speed. Large conductance valve Ⓔ of turbo pump is then closed while UHV right-angle valve Ⓕ is maintained half open. Ar gas is let in using gas inlet valve until pressure rises to the desired value and the treatment procedure starts. When the procedure is finished, sample platform shutter is set on again and the sample is then maintained in vacuum for 24 hours in order to let ensure a complete cooling down of the sample. The roughness treatment is applied on each shell independently. When the first shell has been treated, it is kept in the chamber under vacuum conditions and protected from Ti and Ar^+ fluxes during the treatment procedure of the second shell, and the second shell is treated following the same procedure as for the first shell. Both shells were treated under the same conditions. When both shells have been treated, the second stage of the treatment is done. To perform the second stage both shells are located together at the center of the horizontal rotating sample platform, and the Au overlayer is applied.

Bibliography

[1] Philo Taylor Farnsworth. Television by electron image scanning. *Journal of the Franklin Institute*, 218(4):411–444, October 1934.

[2] J. Rodney M. Vaughan. Multipactor. *Electron Devices, IEEE Transactions on*, 35(7):1172–1180, 1988.

[3] ECSS Secretariat. *space ingenieering multipaction design and test.* ESA, 2003.

[4] Richard Woo. *Final report on RF voltage breakdown in coaxial transmission lines.* Jet Propulsion Laboratory, California Institute of Technology, 1970.

[5] Sergio Anza, Carlos Vicente, Jordi Gil, Michael Mattes, Dieter Wolk, Ulrich Wochner, Vicente E. Boria, Benito Gimeno, and David Raboso. Prediction of multipactor breakdown for multicarrier applications: the quasi-stationary method. *Microwave Theory and Techniques, IEEE Transactions on*, 60(7):2093–2105, 2012.

[6] R. A. Kishek, Y. Y. Lau, L. K. Ang, A. Valfells, and R. M. Gilgenbach. Multipactor discharge on metals and dielectrics: Historical review and recent theories. *Physics of Plasmas (1994-present)*, 5(5):2120–2126, 1998.

[7] Ana Ruiz, Elisa Román, Pilar Lozano, Mariano García, Luis Galán, Isabel Montero, and David Raboso. UHV reactive evaporation growth of titanium nitride thin films, looking for multipactor effect suppression in space applications. *Vacuum*, 81(11):1493–1497, 2007.

[8] Joel Rasch, Dan Anderson, Mietek Lisak, V. E. Semenov, and J. Puech. Microwave corona breakdown in a gas-filled rectangular resonator cavity. *Journal of Physics D: Applied Physics*, 42(5):055210, 2009.

[9] F. Höhn, W. Jacob, R. Beckmann, and R. Wilhelm. The transition of a multipactor to a low-pressure gas discharge. *Physics of Plasmas (1994-present)*, 4(4):940–944, 1997.

[10] Leung Tsang, Henning Braunisch, Ruihua Ding, and Xiaoxiong Gu. Random rough surface effects on wave propagation in interconnects. *Advanced Packaging, IEEE Transactions on*, 33(4):839–856, 2010.

[11] Christopher L. Holloway and Edward F. Kuester. Power loss associated with conducting and superconducting rough interfaces. *Microwave Theory and Techniques, IEEE Transactions on*, 48(10):1601–1610, 2000.

[12] Roberto Cimino and Theo Demma. Electron cloud in accelerators. *International Journal of Modern Physics A*, 29(17), 2014.

[13] G. I. Budker, G. I. Dimov, and V. G. Dudnikov. Experiments on producing intensive proton beams by means of the method of charge-exchange injection. *Soviet Atomic Energy*, 22(5):441–448, May 1967.

[14] G. I. Budker, G. I. Dimov, and V. G. Dudnikov. Proceedings of the International Symposium on Electron and Positron Storage Rings, Saclay, 1966. 1966.

[15] B Jenninger V Baglin. *Pressure and heat load in a LHC type cryogenic avucum system subjected to electron CLOUD*, 31st advanced icfa beam dynamics workshop on electron-cloud effects, napa, ca, usa, 19 - 23 apr 2004, pp.123-137 edition.

[16] T. Demma, S. Petracca, F. Ruggiero, G. Rumolo, and F. Zimmermann. Maps for electron cloud density in Large Hadron Collider dipoles. *Physical Review Special Topics - Accelerators and Beams*, 10(11), November 2007.

[17] Humberto Maury Cuna, Jesús Guillermo Contreras, and Frank Zimmermann. Simulations of electron-cloud heat load for the cold arcs of the CERN Large Hadron Collider and its high-luminosity upgrade scenarios. *Physical Review Special Topics - Accelerators and Beams*, 15(5), May 2012.

[18] G. Rumolo G. Rumolo and F. Zimmermann. Cern report. *CERN*, 2002.

[19] Proceedings, international workshop on multibunch instabilities in future electron and positron accelerators (MBI97). 1997.

[20] R. Cimino, M. Commisso, D. R. Grosso, T. Demma, V. Baglin, R. Flammini, and R. Larciprete. Nature of the decrease of the secondary-electron yield by electron bombardment and its energy dependence. *Physical review letters*, 109(6):064801, 2012.

[21] H. Bruining and J. H. De Boer. Secondary electron emission: Part i. secondary electron emission of metals. *Physica*, 5(1):17–30, 1938.

[22] L. Austin and H. Starke. Ueber die Reflexion der Kathodenstrahlen und eine damit verbundene neue Erscheinung secundärer Emission. *Annalen der Physik*, 314(10):271–292, 1902.

[23] H. Bruining. *Physics and Applications of Secondary Electron Emission: Pergamon Science Series: Electronics and Waves-a Series of Monographs*. Pergamon, January 1962.

[24] E. M. Baroody. A theory of secondary electron emission from metals. *Physical Review*, 78(6):780–787, June 1950.

[25] Nathan D. Zameroski. *Effects of Surface Conditioning, Morphology, and Temperature on Secondary Electron Emission*. University of New Mexico, 2004.

[26] Gerald F. Dionne. Effects of secondary electron scattering on secondary emission yield curves. *Journal of Applied Physics*, 44(12):5361–5364, December 1973.

[27] Wolfgang S. M. Werner, Francesc Salvat Pujol, Werner Smekal, Rahila Khalid, Friedrich Aumayr, Herbert Störi, Alessandro Ruocco, and Giovanni Stefani. Contribution of surface plasmon decay to secondary electron emission from an al surface. *Applied Physics Letters*, 99(18):184102, October 2011.

[28] Z. J. Ding, H. M. Li, R. Shimizu, and K. Gotod. On the energy distribution of secondary electrons emitted from metals. *Journal of Surface Analysis*, 15(2):186–194, 2008.

[29] Shinichiro Michizono, Yoshio Saito, Yasushi Yamano, Shinichi Kobayashi, and others. Secondary electron emission of sapphire and anti-multipactor coatings at high temperature. *Applied surface science*, 235(1):227–230, 2004.

[30] Michael Kussmaul, Michael J. Mirtich, and Arthur Curren. Ion beam treatment of potential space materials at the NASA lewis research center. *Surface and Coatings Technology*, 51(1):299–306, 1992.

[31] Juan De Lara, Francisco Pérez, Manuel Alfonseca, Luis Galán, Isabel Montero, Elisa Román, and David Raboso Garcia-Baquero. Multipactor prediction for on-board spacecraft RF equipment with the MEST software tool. *Plasma Science, IEEE Transactions on*, 34(2):476–484, 2006.

[32] G. G. Fuentes, R. J. Rodriguez, M. García, L. Galán, I. Montero, and J. L. de Segovia. Spectroscopic investigations of cr, CrN and TiCr anti-multipactor coatings grown by cathodic-arc reactive evaporation. *Applied surface science*, 253(18):7627–7631, 2007.

[33] Guoxin Cheng and Lie Liu. Monte carlo modeling of secondary electron emission and its incorporation in particle simulations of electron–surface interaction. *Computer Physics Communications*, 182(6):1295–1303, 2011.

[34] Sébastien Clerc, John R. Dennison, Ryan Hoffmann, and Jonathan Abbott. On the computation of secondary electron emission models. *Plasma Science, IEEE Transactions on*, 34(5):2219–2225, 2006.

[35] M. A. Furman and M. T. F. Pivi. Simulation of secondary electron emission based on a phenomenological probabilistic model. *Lawrence Berkeley National Laboratory*, 2003.

[36] Kenneth G. Mckay. Secondary electron emission. In L. Marton, editor, *Advances in Electronics and Electron Physics*, volume 1, pages 65–130. Academic Press, 1948.

[37] A. Shih, J. Yater, C. Hor, and R. Abrams. Secondary electron emission studies. *Applied surface science*, 111:251–258, 1997.

[38] C. G. H. Walker, M. M. El-Gomati, A. M. D. Assa'd, and M. Zadražil. The secondary electron emission yield for 24 solid elements excited by primary electrons in the range 250–5000 eV: a theory/experiment comparison. *Scanning*, 30(5):365–380, 2008.

[39] N. Hilleret, C. Scheuerlein, and M. Taborelli. The secondary-electron yield of air-exposed metal surfaces. *Applied Physics A*, 76(7):1085–1091, 2003.

[40] R. Cimino, I. R. Collins, M. A. Furman, M. Pivi, F. Ruggiero, G. Rumolo, and F. Zimmermann. Can Low-Energy Electrons Affect High-Energy Physics Accelerators? *Physical Review Letters*, 93(1), June 2004.

[41] J. Cazaux. Electron back-scattering coefficient below 5 keV: Analytical expressions and surface-barrier effects. *Journal of Applied Physics*, 112(8):084905, 2012.

[42] M. M. El Gomati, C. G. H. Walker, A. M. D. Assa'd, and M. Zadražil. Theory experiment comparison of the electron backscattering factor from solids at low electron energy (250–5,000 eV). *Scanning*, 30(1):2–15, 2008.

[43] Wolfgang S. M. Werner, Igor S. Tilinin, and Markus Hayek. Angular distribution of electrons reflected elastically from noncrystalline solid surfaces. *Physical Review B*, 50(7):4819–4833, August 1994.

[44] V. Baglin, G. Vorlaufer, Noël Hilleret, I. Collins, and Bernard Henrist. A Summary of Main Experimental Results Concerning the Secondary Electron Emission of Copper, August 2001.

[45] Lamberts Photometrie : [Photometria, sive De mensura et gradibus luminus, colorum et umbrae] (1760) : Lambert, Johann Heinrich, 1728-1777 : Free Download & Streaming.

[46] J. L. H. Jonker. The angular distribution of the secondary electrons of nickel. *Philips Res. Repts*, 6(372).

[47] H. Seiler. Secondary electron emission in the scanning electron microscope. *Journal of Applied Physics*, 54(11):R1–R18, 1983.

[48] Prashanth Kumar, C. Watts, T. Svimonishvili, Mark Gilmore, and Edl Schamiloglu. Characterization of the Dose Effect in Secondary Electron Emission. In *Plasma Science, 2007. ICOPS 2007. IEEE 34th International Conference on*, pages 530–530. IEEE, 2007.

[49] M. Belhaj N Bundaleski. Influence of the Incident Angle on Energy Dependence of a Secondary Electron Emission Yield. 2013.

[50] H. Salow. *Z. Tech. Phys*, 21(8), 1940.

[51] Bipin Kumar Agarwal. Variation of secondary emission with primary electron energy. *Proceedings of the Physical Society*, 71(5):851, May 1958.

[52] Robert G. Lye and A. J. Dekker. Theory of secondary emission. *Physical Review*, 107(4):977, 1957.

[53] Gerald F. Dionne. Origin of secondary electron yield curve parameters. *Journal of applied Physics*, 46(8):3347–3351, 1978.

[54] J. R. Young. Penetration of electrons in aluminum oxide films. *Physical Review*, 103(2):292, 1956.

[55] A. J. Dekker. Secondary electron emission. *Solid State Physics*, 6:251–311, 1958.

[56] Miguel A. Furman and Glen R. Lambertson. The electron-cloud instability in the arcs of the PEP-II positron ring. *Lawrence Berkeley National Laboratory*, 1998.

[57] Cimino.

[58] M. J. Mandell, P. R. Stannard, and I. Katz. NASCAP programmer's reference manual. *Final Report Maxwell Labs., Inc., La Jolla, CA. S-Cubed Div.*, 1, 1993.

[59] P. Mader, C. Feat, M. Humbert, J.-C. Lafond, P. Lepeltier, J. Puech, and J. Sinigaglia. TAS-F multipactor results in EVEREST project. In *2014 8th European Conference on Antennas and Propagation (EuCAP)*, pages 1651–1654, April 2014.

[60] Christian Scheuerlein. *The influence of an air exposure on the secondary electron yield of copper*. diplom. de, 2002.

[61] Asena Kuzucan, Holger Neupert, Mauro Taborelli, and Herbert Störi. Secondary electron yield on cryogenic surfaces as a function of physisorbed gases. *Journal of Vacuum Science & Technology A*, 30(5):051401, 2012.

[62] Stephen Myers. The large hadron collider 2008–2013. *International Journal of Modern Physics A*, 28(25):1330035, October 2013.

[63] U. Wagner. *Proc. Chamonix XIII*, 2004.

[64] Richard Woo and Akira Ishimaru. A similarity principle for multipacting discharges. *Journal of Applied Physics*, 38(13):5240–5244, December 1967.

[65] J. Petit A. Woode. Diagnostic investigations into the mulatipactor effect and susceptibiity zone measurements and parameters affecting a discharge. *ESTEC Working Paper*, 1989.

[66] J. Lara F. Perez. Cest and mes: Tools for the simulation of radio frequency electric discharges in waveguides. *Simulation Modelling Practice and Theory*, 2008.

[67] M. A. Gusarova, V. I. Kaminsky, L. V. Kravchuk, S. V. Kutsaev, M. V. Lalayan, N. P. Sobenin, and S. G. Tarasov. Multipacting simulation in accelerating RF structures. *Nuclear Instruments and Methods in Physics Research Section A: Accelerators, Spectrometers, Detectors and Associated Equipment*, 599(1):100–105, 2009.

[68] David M. Pozar. *Microwave Engineering*. John Wiley & Sons, Hoboken, NJ, edición: 0004 edition, 2012.

[69] Kai Chang. *RF and microwave wireless systems*, volume 161. John Wiley & Sons, 2004.

[70] L. D. Landau and E. M. Lifshitz. *The Classical Theory of Fields, Fourth Edition: Volume 2*. Butterworth-Heinemann, Oxford u.a., 4 edition edition, January 1980.

[71] Ernest A. Dorko, Richard S. Hughes, and Clelland R. Downs. Solid state reaction kinetics. differential scanning calorimetric determination of the solid state decomposition kinetics and activation parameters of n-aryl-n'-tosyloxydi-imide n-oxides. *Analytical Chemistry*, 42(2):253–256, 1970.

[72] Fawwaz T. Ulaby. Fundamentals of Applied Electromagnetics Prentice Hall. *Upper Saddle River, NJ*, page 218, 1997.

[73] Sophocles J. Orfanidis. *Electromagnetic Waves and Antennas. ECE Department Rutgers University. 94 Brett Road, Piscataway, NJ 08854-8058. orfanidi@ ece. rutgers. edu.*

[74] Ngai Wong Quan Chen. Efficient numerical modeling of random rough surface effects for interconnect internal impedance extraction. pages 152–157, 2008.

[75] Quan Chen, Hoi Wai Choi, and Ngai Wong. Robust simulation methodology for surface-roughness loss in interconnect and package modelings. *Computer-Aided Design of Integrated Circuits and Systems, IEEE Transactions on*, 28(11):1654–1665, 2009.

[76] Samuel P. Morgan Jr. Effect of surface roughness on eddy current losses at microwave frequencies. *Journal of Applied Physics*, 20(4):352–362, April 1949.

[77] Dejan S. Filipovic Milan V. Lukic. Modeling of 3-d surfave roughness effects with application to u-coaxial lines. *IEEE Transactions on Microwave Theory and Techniques*, 55(3), 2007.

[78] Akira Matsushima and Katsuya Nakata. Power loss and local surface impedance associated with conducting rough interfaces. *Electronics and Communications in Japan (Part II: Electronics)*, 89(1):1–10, 2006.

[79] A. Valfells, L. K. Ang, Y. Y. Lau, and R. M. Gilgenbach. Effects of an external magnetic field, and of oblique radio-frequency electric fields on multipactor discharge on a dielectric. *Physics of Plasmas (1994-present)*, 7(2):750–757, 2000.

[80] V. Semenov, E. Rakova, N. Zharova, D. Anderson, M. Lisak, and J. Puech. Simulations of the multipactor effect in hollow waveguides with wedge-shaped cross section. *IEEE Transactions on Plasma Science*, 36(2):488–493, April 2008.

[81] ECA Akoma Henry, D. A. Ogundele, O. Agboola, and Y. A. Adediran. Matlab® analysis of the DC magnetic fields multipactor suppression model for rectangular waveguides. In *Advanced Computer Theory and Engineering (ICACTE), 2010 3rd International Conference on*, volume 4, pages V4–97. IEEE, 2010.

[82] C. M. Lyneis, H. A. Schwettman, and J. P. Turneaure. Elimination on electron multipacting in superconducting structures for electron accelerators. *Applied Physics Letters*, 31(8):541–543, October 1977.

[83] Ivan Arregui, Fernando Teberio, Israel Arnedo, Aintzane Lujambio, Magdalena Chudzik, David Benito, Txema Lopetegi, Rolf Jost, F.-J. Gortz, Jordi Gil, and others.

High-power low-pass harmonic filters with higher-order and non-mode suppression: Design method and multipactor characterization. *Microwave Theory and Techniques, IEEE Transactions on*, 61(12):4376–4386, 2013.

[84] Ivan Arregui, Fernando Teberio, Israel Arnedo, Aintzane Lujambio, Magdalena Chudzik, David Benito, Txema Lopetegi, Rolf Jost, F.-J. Gortz, Jordi Gil, and others. Multipactor characterization with a ring resonator of low-pass harmonic filters designed for high-power operation. *Microwave Theory and Techniques, IEEE Transactions on*, 61(12):4376–4386, 2013.

[85] Eric Chojnacki. Simulations of a multipactor-inhibited waveguide geometry. *Physical Review Special Topics - Accelerators and Beams*, 3(3):032001, March 2000.

[86] M. Mostajeran and M. Lamehi Rachti. Importance of number of gap crossings on secondary emission in the simulation of two-sided multipactor. *Journal of Instrumentation*, 5(08):P08003, August 2010.

[87] J. Hueso, C. Vicente, B. Gimeno, V.E. Boria, S. Marini, and M. Taroncher. Multipactor effect analysis and design rules for wedge-shaped hollow waveguides. *IEEE Transactions on Electron Devices*, 57(12):3508–3517, December 2010.

[88] Chao Chang, Guozhi Liu, Chuanxiang Tang, Changhua Chen, and Jinyong Fang. Review of recent theories and experiments for improving high-power microwave window breakdown thresholdsa). *Physics of Plasmas (1994-present)*, 18(5):055702, May 2011.

[89] J. Halbritter. On conditioning: Reduction of secondary and rf field emission by electron, photon, or helium impact. *Journal of Applied Physics*, 53(9):6475–6478, September 1982.

[90] L.Galán et al. Coatings to prevent multipactor effect in rf high power components for space. Technical report, Final Report, ESA-ESTEC Contract P.O. 162594 (1996), ESA (1998).

[91] L. Galan, C. Moranti, F. Rueda, and J. M. Sanz. Study of secondary emission properties of materials used for high power RF components in space. *NASA STI/Recon Technical Report N*, 88:30012, March 1988.

[92] Valentin Nistor, Luis A. González, Lydya Aguilera, Isabel Montero, Luis Galán, Ulrich Wochner, and David Raboso. Multipactor suppression by micro-structured gold/silver coatings for space applications. *Applied Surface Science*, 2014.

[93] Esa 4025 final report, mulcopim'11.

[94] Ludwig Reimer. *Scanning Electron Microscopy: Physics of Image Formation and Microanalysis*. Springer Science & Business Media, September 1998.

[95] J. B. Johnson and K. G. McKay. Secondary electron emission of crystalline MgO. *Physical Review*, 91(3):582–587, August 1953.

[96] A. R. Nyaiesh, E. L. Garwin, F. K. King, and R. E. Kirby. Properties of thin antimultipactor TiN and cr2o3 coatings for klystron windows. *Journal of Vacuum Science & Technology A*, 4(5):2356–2363, September 1986.

[97] E. L. Garwin, E. W. Hoyt, R. E. Kirby, and T. Momose. Secondary electron yield and auger electron spectroscopy measurements on oxides, carbide, and nitride of niobium. *Journal of Applied Physics*, 59(9):3245–3250, May 1986.

[98] E. L. Garwin, F. K. King, R. E. Kirby, and O. Aita. Surface properties of metal nitride and metal carbide films deposited on nb for radio frequency superconductivity. *Journal of Applied Physics*, 61(3):1145–1154, February 1987.

[99] P. Prieto and R. E. Kirby. X-ray photoelectron spectroscopy study of the difference between reactively evaporated and direct sputter-deposited TiN films and their oxidation properties. *Journal of Vacuum Science & Technology A*, 13(6):2819–2826, 1995.

[100] S. I. Castaneda, N. Dıaz, D. Raboso, I. Montero, L. Galán, and F. Rueda. Effects of air exposure on ion beam assisted TiN: O coatings to prevent multipactor. *Journal of Vacuum Science & Technology A*, 21(6):2007–2012, 2003.

[101] D. Wolk, P. Lozano, M. García, I. Montero, L. Galán, C. Prieto, F. Galán-Estella, E. García-Camarero, and D. Raboso. Coatings on mg alloys for reduction of multipactor effects in RF components. *Proceedings of MULCOPIM*, 2005.

[102] K. Ohmi and Frank Zimmermann. Head-tail instability caused by electron clouds in positron storage rings. *Physical review letters*, 85(18):3821, 2000.

[103] J. J. Song. Multipacting study of the RF window at the advanced photon source. In *Particle Accelerator Conference, 1999. Proceedings of the 1999*, volume 2, pages 789–791. IEEE, 1999.

[104] K. Oide. Observation and cure of the electron cloud effect at the KEKB low energy ring. *Chamonix XI, CERN SL-2001-003 (DI)*, 2001.

[105] M. Nishiwaki and S. Kato. Graphitization of inner surface of copper beam duct of KEKB positron ring. *Vacuum*, 84:743–746, 2010.

[106] R. Larciprete, D. R. Grosso, M. Commisso, R. Flammini, and R. Cimino. Secondary electron yield of cu technical surfaces: Dependence on electron irradiation. *Physical Review Special Topics-Accelerators and Beams*, 16(1):011002, 2013.

[107] C. Yin Vallgren, G. Arduini, J. Bauche, S. Calatroni, P. Chiggiato, K. Cornelis, P. Costa Pinto, B. Henrist, E. Métral, H. Neupert, G. Rumolo, E. Shaposhnikova, and M. Taborelli. Amorphous carbon coatings for the mitigation of electron cloud in the CERN super proton synchrotron. *Physical Review Special Topics - Accelerators and Beams*, 14(7), July 2011.

[108] L. Calliari, M. Filippi, and N. Laidani. Electron beam irradiation of hydrogenated amorphous carbon films. *Surface and Interface Analysis*, 36(8):1126–1129, 2004.

[109] Denis Syomin and Bruce E. Koel. Selectivity of bond-breaking in electron-induced dissociation of hydrocarbon films on au surfaces. *Surface Science*, 492(1–2):L693–L699, October 2001.

[110] Olivier Guise, Hubertus Marbach, Jeremy Levy, Joachim Ahner, and John T. Yates Jr. Electron-beam-induced deposition of carbon films on si(1 0 0) using chemisorbed ethylene as a precursor molecule. *Surface Science*, 571(1–3):128–138, November 2004.

[111] R. Cimino and I. R. Collins. Vacuum chamber surface electronic properties influencing electron cloud phenomena. *Applied surface science*, 235(1):231–235, 2004.

[112] R. Cimino, M. Commisso, T. Demma, A. Grilli, M. Pietropaoli, L. Ping, V. Sciarra, V. Baglin, P. Barone, and A. Bonnanno. Electron energy dependence of scrubbing efficiency to mitigate ecloud formation in accelerarors. *Proceedings of EPAC08, Genoa, Italy*, 2008.

[113] S. W. Lee, Y. J. Baik, C. J. Kang, and D. Jeon. Suppression of secondary electrons from diamond by whisker formation. *Applied Surface Science*, 215(1–4):265–268, June 2003.

[114] A. N. Curren. *IEEE Int. Electron Devices Meeting, Washington, DC, USA. NASA Technical Paper 2967*, 1993.

[115] V. Baglin, J. Bojko, C. Scheuerlein, Oswald Gröbner, M. Taborelli, Bernard Henrist, and Noël Hilleret. The secondary electron yield of technical materials and its variation with surface treatments, September 2000.

[116] G. Stupakov and M. Pivi. Suppression of the effective secondary emission yield for a grooved metal surface. *Preprint SLAC-TN-04-045, SLAC*, 2004.

[117] J. Kawata, K. Ohya, and K. Nishimura. Simulation of secondary electron emission from rough surfaces. *Journal of Nuclear Materials*, 220–222:997–1000, April 1995.

[118] M. Pivi, F. K. King, R. E. Kirby, T. O. Raubenheimer, G. Stupakov, and F. Le Pimpec. Sharp reduction of the secondary electron emission yield from grooved surfaces. *Journal of Applied Physics*, 104(10):104904, November 2008.

[119] A. Roth. *Vacuum Technology.* Elsevier, December 2012.

[120] L. N. Rozanov. *Vacuum Technique.* CRC Press, April 2002.

[121] John F. O'Hanlon. *A User's Guide to Vacuum Technology.* John Wiley & Sons, March 2005.

[122] David C. Jiles. *Introduction to Magnetism and Magnetic Materials, Second Edition.* CRC Press, June 1998.

[123] David R. Lide. *CRC Handbook of Chemistry and Physics, 84th Edition.* CRC Press, June 2003.

[124] Milton Ohring. *Materials Science of Thin Films, Second Edition.* Academic Press, San Diego, CA, 2 edition edition, October 2001.

[125] N. R. Whetten. Secondary electron emission of pyrolytic graphite cleaved in a high vacuum. *J. Appl. Phys.*, 34:771–773, 1963.

[126] J. M. Ripalda, I. Montero, L. Vázquez, D. Raboso, and L. Galán. Secondary electron emission and photoemission studies on surface films of carbon nitride. *J. Appl. Phys.*, 99:043513, 2006.

[127] K. Vanheusden, W. L. Warren, C. H. Seager, D. R. Tallant, J. A. Voigt, and B. E. Gnade. Mechanisms behind green photoluminescence in ZnO phosphor powders. *Journal of Applied Physics*, 79(10):7983–7990, 1996.

[128] Y. Park, V. Choong, Y. Gao, B. R. Hsieh, and C. W. Tang. Work function of indium tin oxide transparent conductor measured by photoelectron spectroscopy. *Applied Physics Letters*, 68(19):2699–2701, May 1996.

[129] L Chkoda, C Heske, M Sokolowski, E Umbach, F Steuber, J Staudigel, M Stößel, and J Simmerer. Work function of ITO substrates and band-offsets at the TPD/ITO interface determined by photoelectron spectroscopy. *Synthetic Metals*, 111–112:315–319, June 2000.

[130] R Schlaf, H Murata, and Z. H Kafafi. Work function measurements on indium tin oxide films. *Journal of Electron Spectroscopy and Related Phenomena*, 120(1–3):149–154, October 2001.

[131] M. G. Helander, Z. B. Wang, J. Qiu, M. T. Greiner, D. P. Puzzo, Z. W. Liu, and Z. H. Lu. Chlorinated Indium Tin Oxide Electrodes with High Work Function for Organic Device Compatibility. *Science*, 332(6032):944–947, May 2011.

[132] N. Koch, A. Kahn, J. Ghijsen, J.-J. Pireaux, J. Schwartz, R. L. Johnson, and A. Elschner. Conjugated organic molecules on metal versus polymer electrodes: Demonstration of a key energy level alignment mechanism. *Applied Physics Letters*, 82(1):70–72, 2003.

[133] Jinsong Huang, Zheng Xu, and Yang Yang. Low-Work-Function Surface Formed by Solution-Processed and Thermally Deposited Nanoscale Layers of Cesium Carbonate. *Advanced Functional Materials*, 17(12):1966–1973, 2007.

[134] Fernando Ojeda Álvarez. *Mecanismos de crecimiento y estructura de películas delgadas de SiO2 obtenidas mediante deposición química en fase de vapor*. PhD thesis, Universidad Autónoma de Madrid, 1999.

[135] D. Briggs and M. P. Seah. *Practical Surface Analysis, Auger and X-ray Photoelectron Spectroscopy*. Wiley, November 1990.

[136] Dave A. Shirley. High-resolution X-ray photoemission spectrum of the valence bands of gold. *Physical Review B*, 5(12):4709, 1972.

[137] S. Tougaard and B. Jørgensen. Inelastic background intensities in XPS spectra. *Surface Science*, 143(2):482–494, 1984.

[138] C. D. Wagner, L. E. Davis, M. V. Zeller, J. A. Taylor, R. H. Raymond, and L. H. Gale. Empirical atomic sensitivity factors for quantitative analysis by electron spectroscopy for chemical analysis. *Surface and Interface Analysis*, 3(5):211–225, 1981.

[139] David Briggs and Martin P. Seah. Practical surface analysis by auger and x ray photoelectron spectroscopy. *D. Briggs, & M. P. Seah,(Editors), John Wiley & Sons, Chichester 1983, xiv+ 533*, 1983.

[140] Wiley: Practical Raman Spectroscopy: An Introduction - Peter Vandenabeele.

[141] Wiley: Raman Spectroscopy in Graphene Related Systems - Ado Jorio, Mildred S. Dresselhaus, Riichiro Saito, et al.

[142] Derek J. Gardiner. Introduction to Raman Scattering. In Dr Derek J. Gardiner and Dr Pierre R. Graves, editors, *Practical Raman Spectroscopy*, pages 1–12. Springer Berlin Heidelberg, 1989.

[143] Enrique Rodríguez Cañas. Estudio del frente de crecimiento en láminas delgadas de Au. 2010.

[144] Mordechay Schlesinger and Milan Paunovic. *Modern Electroplating*. John Wiley & Sons, February 2011.

[145] Iouri Bojko, Noël Hilleret, and Christian Scheuerlein. Influence of air exposures and thermal treatments on the secondary electron yield of copper. *Journal of Vacuum Science & Technology A*, 18(3):972–979, 2000.

[146] Javier Muñoz-García, Luis Vázquez, Mario Castro, Raúl Gago, Andrés Redondo-Cubero, Ana Moreno-Barrado, and Rodolfo Cuerno. Self-organized nanopatterning of silicon surfaces by ion beam sputtering. *Materials Science and Engineering: R: Reports*, 86:1–44, 2014.

[147] K. Zhang, O. Bobes, and H. Hofsäss. Designing self-organized nanopatterns on Si by ion irradiation and metal co-deposition. *Nanotechnology*, 25(8):085301–085301, 2014.

[148] K. Zhang, H. Hofsäss, F. Rotter, M. Uhrmacher, C. Ronning, and J. Krauser. Morphology of Si surfaces sputter-eroded by low-energy Xe-ions at glancing incident angle. *Surface and Coatings Technology*, 203(17):2395–2398, 2009.

[149] Adrian Keller and Stefan Facsko. Ion-induced nanoscale ripple patterns on Si surfaces: theory and experiment. *Materials*, 3(10):4811–4841, 2010.

[150] M. Castro, R. Gago, L. Vázquez, J. Muñoz-García, and R. Cuerno. Stress-induced solid flow drives surface nanopatterning of silicon by ion-beam irradiation. *Physical Review B*, 86(21):214107, 2012.

[151] Tanmoy Basu, Jyoti Ranjan Mohanty, and T. Som. Unusual pattern formation on Si (100) due to low energy ion bombardment. *Applied Surface Science*, 258(24):9944–9948, 2012.

[152] T. Škereň, K. Temst, W. Vandervorst, and A. Vantomme. Ion-induced roughening and ripple formation on polycrystalline metallic films. *New Journal of Physics*, 15(9):093047, September 2013.

[153] Barbara Šetina Batič and Monika Jenko. Orientation-dependent ion beam sputtering at normal incidence conditions in FeSiAl alloy. *Journal of Vacuum Science & Technology A*, 28(4):741–744, July 2010.

[154] J. Y. Wang, S. Hofmann, A. Zalar, and E. J. Mittemeijer. Quantitative evaluation of sputtering induced surface roughness in depth profiling of polycrystalline multilayers

using Auger electron spectroscopy. *Thin Solid Films*, 444(1–2):120–124, November 2003.

[155] Gozde Ozaydin, Ahmet S. Özcan, Yiyi Wang, Karl F. Ludwig, Hua Zhou, Randall L. Headrick, and D. Peter Siddons. Real-time x-ray studies of Mo-seeded Si nanodot formation during ion bombardment. *Applied Physics Letters*, 87(16):163104, 2005.

[156] Christian Teichert, Christian Hofer, and Gregor Hlawacek. Self-organization of Nanostructures in Inorganic and Organic Semiconductor Systems. *Advanced Engineering Materials*, 8(11):1057–1065, 2006.

[157] Gozde Ozaydin, Ahmet S. Özcan, Yiyi Wang, Karl F. Ludwig, Hua Zhou, and Randall L. Headrick. Real-time X-ray studies of the growth of Mo-seeded Si nanodots by low-energy ion bombardment. *Nuclear Instruments and Methods in Physics Research Section B: Beam Interactions with Materials and Atoms*, 264(1):47–54, 2007.

[158] Noriaki Matsunami, Y. Yamamura, Y. Itikawa, N. Itoh, Y. Kazumata, S. Miyagawa, K. Morita, R. Shimizu, and H. Tawara. Energy dependence of the yields of ion induced sputtering of monatomic solids. *Unknown*, 1, 1983.

[159] Arthur N. Curren and Kenneth A. Jensen. Secondary electron emission characteristics of ion textured copper and high purity isotropic graphite surfaces. 1984.

[160] Sven Macko, Frank Frost, Martin Engler, Dietmar Hirsch, Thomas Höche, Jörg Grenzer, and Thomas Michely. Phenomenology of iron-assisted ion beam pattern formation on Si (001). *New Journal of Physics*, 13(7):073017, 2011.

[161] B. Khanbabaee, A. Biermanns, S. Facsko, J. Grenzer, and U. Pietsch. Depth profiling of Fe-implanted Si (100) by means of X-ray reflectivity and extremely asymmetric X-ray diffraction. *Journal of Applied Crystallography*, 46(2):505–511, 2013.

[162] Michael D. Abràmoff, Paulo J. Magalhães, and Sunanda J. Ram. Image processing with ImageJ. *Biophotonics international*, 11(7):36–43, 2004.

[163] Thermocouple Sensor, Thermocouple wire & Cables|Vacker UAE.

[164] John A. Thornton. The microstructure of sputter deposited coatings. *Journal of Vacuum Science & Technology A*, 4(6):3059–3065, November 1986.

[165] L. Hultman, W.-D. Münz, J. Musil, S. Kadlec, I. Petrov, and J. E. Greene. Low energy (100 eV) ion irradiation during growth of TiN deposited by reactive magnetron sputtering: Effects of ion flux on film microstructure. *Journal of Vacuum Science & Technology A*, 9(3):434–438, May 1991.

[166] F. Adibi, I. Petrov, J. E. Greene, L. Hultman, and J.-E. Sundgren. Effects of high flux low energy (20–100 eV) ion irradiation during deposition on the microstructure and preferred orientation of Ti0.5al0.5n alloys grown by ultra high vacuum reactive magnetron sputtering. *Journal of Applied Physics*, 73(12):8580–8589, June 1993.

[167] A. Lousa and S. Gimeno. Ion assisted deposition of thin films by substrate tuned radio frequency magnetron sputtering. *Journal of Vacuum Science & Technology A*, 15(1):62–65, January 1997.

[168] G. Carter. The effects of surface ripples on sputtering erosion rates and secondary ion emission yields. *Journal of applied physics*, 85(1):455–459, 1999.

[169] Tanmoy Basu, Debi Prasad Datta, and Tapobrata Som. Transition from ripples to faceted structures under low-energy argon ion bombardment of silicon: understanding the role of shadowing and sputtering. *Nanoscale research letters*, 8(1):1–8, 2013.

[170] R. Mark Bradley and James M. E. Harper. Theory of ripple topography induced by ion bombardment. *Journal of Vacuum Science & Technology A*, 6(4):2390–2395, July 1988.

[171] Maxim A. Makeev, Rodolfo Cuerno, and Albert-László Barabási. Morphology of ion-sputtered surfaces. *Nuclear Instruments and Methods in Physics Research Section B: Beam Interactions with Materials and Atoms*, 197(3–4):185–227, December 2002.

[172] Kun Zhang, Marc Brötzmann, and Hans Hofsäss. Surfactant-driven self-organized surface patterns by ion beam erosion. *New Journal of Physics*, 13(1):013033, January 2011.

[173] H. Hofsäss, K. Zhang, A. Pape, O. Bobes, and M. Brötzmann. The role of phase separation for self-organized surface pattern formation by ion beam erosion and metal atom co-deposition. *Applied Physics A*, 111(2):653–664, October 2012.

[174] A. Redondo-Cubero, R. Gago, F. J. Palomares, A. Mücklich, M. Vinnichenko, and L. Vázquez. Nanopatterning dynamics on Si(100) during oblique 40-keV Ar^{+} erosion with metal codeposition: Morphological and compositional correlation. *Physical Review B*, 86(8):085436, August 2012.

[175] K. Zhang, M. Brötzmann, and H. Hofsäss. Sharp transition from ripple patterns to a flat surface for ion beam erosion of Si with simultaneous co-deposition of iron. *AIP Advances*, 2(3):032123, September 2012.

[176] M. Chelvayohan and C. H. B. Mee. Work function measurements on (110), (100) and (111) surfaces of silver. *Journal of Physics C: Solid State Physics*, 15(10):2305, April 1982.

[177] Hans Lomholt Skriver and N. M. Rosengaard. Surface energy and work function of elemental metals. *Physical Review B*, 46(11):7157, 1992.

[178] K. Jakobi. 3.1.2.4 work function data. In G. Chiarotti, editor, *Electronic and Vibrational Properties*, number 24b in Landolt-Börnstein - Group III Condensed Matter, pages 56–68. Springer Berlin Heidelberg, 1994.

[179] Bert de Boer, Afshin Hadipour, M. Magdalena Mandoc, Teunis van Woudenbergh, and Paul WM Blom. Tuning of Metal Work Functions with Self-Assembled Monolayers. *Advanced Materials*, 17(5):621–625, 2005.

[180] R. P. Netterfield, P. J. Martin, C. G. Pacey, W. G. Sainty, D. R. McKenzie, and G. Auchterlonie. Ion assisted deposition of mixed tio2 sio2 films. *Journal of Applied Physics*, 66(4):1805–1809, August 1989.

[181] William E. Slink and Peter B. DeGroot. Vanadium titanium oxide catalysts for oxidation of butene to acetic acid. *Journal of Catalysis*, 68(2):423–432, April 1981.

[182] K. Hiehata, A. Sasahara, and H. Onishi. Local work function analysis of Pt/TiO2 photocatalyst by a Kelvin probe force microscope. *Nanotechnology*, 18(8):084007, 2007.

[183] Akihito Imanishi, Etsushi Tsuji, and Yoshihiro Nakato. Dependence of the Work Function of TiO2 (Rutile) on Crystal Faces, Studied by a Scanning Auger Microprobe. *The Journal of Physical Chemistry C*, 111(5):2128–2132, February 2007.

[184] A Cultrera, L Boarino, G Amato, and C Lamberti. Band-gap states in unfilled mesoporous nc-TiO $_2$: measurement protocol for electrical characterization. *Journal of Physics D: Applied Physics*, 47(1):015102, January 2014.

[185] Osamu Tonomura, Tomoko Sekiguchi, Naomi Inada, Tomoyuki Hamada, Hiroshi Miki, and Kazuyoshi Torii. Band Engineering of Ru/Rutile-TiO2/Ru Capacitors by Doping Cobalt to Suppress Leakage Current.

[186] Ye Wan, Yanbo Li, Qing Wang, Ke Zhang, and Yuhou Wu. The relationship of surface roughness and work function of pure silver by numerical modeling. *Int. J. Electrochem. Sci*, 7:5204–5216, 2012.

[187] W. Li and D. Y. Li. On the correlation between surface roughness and work function in copper. *The Journal of Chemical Physics*, 122(6):064708, February 2005.

[188] W. Li and D. Y. Li. Influence of surface morphology on corrosion and electronic behavior. *Acta Materialia*, 54(2):445–452, January 2006.

[189] Mingshan Xue, Juan Xie, Wen Li, Fajun Wang, Junfei Ou, Chenggang Yang, Changquan Li, Zhenchen Zhong, and Zhonghao Jiang. Changes in surface morphology and work function caused by corrosion in aluminum alloys. *Journal of Physics and Chemistry of Solids*, 73(6):781–787, June 2012.

[190] Jacques Cazaux. Calculated effects of work function changes on the dispersion of secondary electron emission data: Application for Al and Si and related elements. *Journal of Applied Physics*, 110(2):024906, 2011.

[191] H. J. Hopman and J. Verhoeven. Secondary electron emission data of cesiated oxygen free high conductivity copper. *Applied surface science*, 150(1):1–7, 1999.

[192] H. J. Hopman, H. Zeijlemaker, and J. Verhoeven. Secondary electron emission data of cesiated oxygen free high conductivity copper (II). *Applied surface science*, 171(3):197–206, 2001.

[193] M. S. Chung and T. E. Everhart. Simple calculation of energy distribution of low-energy secondary electrons emitted from metals under electron bombardment. *Journal of Applied Physics*, 45(2):707–709, 1974.

[194] Jacques Cazaux. Calculated influence of work function on SE escape probability and secondary electron emission yield. *Applied Surface Science*, 257(3):1002–1009, 2010.

[195] Eugene D. Sharp. A high power wide band waffle iron filter. *Microwave Theory and Techniques, IEEE Transactions on*, 11(2):111–116, 1963.

[196] Leo Young and Bernard M. Schiffman. New and improved types of waffle-iron filters. In *Proceedings of the Institution of Electrical Engineers*, volume 110, pages 1191–1198. IET, 1963.

[197] Levy Ralph. *Aperiodic tapered corrugated waveguide filter*. Google Patents, August 1971. US Patent 3,597,710.

[198] F. E. Beamish. *The Analytical Chemistry of the Noble Metals*. Elsevier, October 2013.

[199] T. Bligaard, Jens Kehlet Nørskov, Søren Dahl, J. Matthiesen, Claus H. Christensen, and J. Sehested. The Brønsted–Evans–Polanyi relation and the volcano curve in heterogeneous catalysis. *Journal of Catalysis*, 224(1):206–217, 2004.

[200] Jooho Kim, Enrique Samano, and Bruce E. Koel. Oxygen adsorption and oxidation reactions on Au (211) surfaces: Exposures using O 2 at high pressures and ozone (O 3) in UHV. *Surface science*, 600(19):4622–4632, 2006.

[201] Raymond A Serway. *Principles of physics*. Saunders College Pub., Fort Worth, 1998.

[202] S. Tanuma, C. J. Powell, and D. R. Penn. Calculations of electron inelastic mean free paths. *Surface and Interface Analysis*, 37(1):1–14, 2005.

[203] D. Y. Petrovykh, J. M. Sullivan, and L. J. Whitman. Quantification of discrete oxide and sulfur layers on sulfur-passivated InAs by XPS. *Surface and interface analysis*, 37(11):989–997, 2005.

[204] P. Prieto, L. Galan, J. M. Sanz, and F. Rueda. An xps study of the kinetics of dissolution of zro2 in alphazr. *Surface and Interface Analysis*, 16(1-12):535–539, 1990.

[205] Charles Kittel, Paul McEuen, and Paul McEuen. *Introduction to solid state physics*, volume 8. Wiley New York, 1976.

[206] *European Cooperation for Space Standardization (ECSS), Space engineering-multipactor design and test, ECSS-E-20-01A*, rev 1 edition, March 2013.

[207] V.E. Semenov, E.I. Rakova, D. Anderson, M. Lisak, and J. Puech. Importance of Reflection of Low-Energy Electrons on Multipactor Susceptibility Diagrams for Narrow Gaps. *IEEE Transactions on Plasma Science*, 37(9):1774–1781, September 2009.

[208] V. Baglin. Tech. rep. lhc- project-report-433, cern. Technical report, 2000.

[209] V. Baglin. *LHC Project Report 472, CERN*, 2001.

[210] J. Wang, Pu Wang, M. Belhaj, and J.-C.M. Velez. Modeling facility effects on secondary electron emission experiment. *IEEE Transactions on Plasma Science*, 40(10):2773–2780, October 2012.

[211] M. Belhaj. *Proceedings of ECLOUD'12*, page 137, 2013.

[212] Roberto Cimino. Surface related properties as an essential ingredient to e-cloud simulations. *Nuclear Instruments and Methods in Physics Research Section A: Accelerators, Spectrometers, Detectors and Associated Equipment*, 561(2):272–275, 2006.

[213] R. Cimino. *Proc. of the 31st ICFA Advanced Beam Dynamics Workshop on Electron-Cloud Effects ECLOUD 04*, 2004.

[214] I. H. Khan, J. P. Hobson, and R. A. Armstrong. Reflection and diffraction of slow electrons from single crystals of tungsten. *Physical Review*, 129(4):1513–1523, February 1963.

[215] I. M. Bronshtein and B. S. Fraiman. *Secondary electron emission.* Nauka, Moscow, 1969.

[216] Z. Yakubova and N. A. Gorbatyi. Reflection of slow electrons from the (110) face of a tungsten crystal. *Soviet Physics Journal*, 13(11):1477–1482, 1970.

[217] G. A. Hass. *Journal of Vacuum Science and Technology*, 13(479), 1976.

[218] I. M. Bronshtein. *Sov. J. Tech.-Phys*, 3(2271), 1958.

[219] H. Heil. *Physical Review*, 164(881), 1961.

[220] A. N. Andranov. *Proceedings of ECLOUD'12, CERN-2013-002*, page 161, 2012.

[221] Jacques Cazaux. Reflectivity of very low energy electrons ($<$ 10 eV) from solid surfaces: Physical and instrumental aspects. *Journal of Applied Physics*, 111(6):064903, 2012.

[222] J. Roupie, O. Jbara, T. Tondu, M. Belhaj, and J. Puech. The study of electron emission from aluminum in the very low primary energy range using monte carlo simulations. *Journal of Physics D: Applied Physics*, 46(12):125306, March 2013.

[223] A. Dittmar Wituski, M. Naparty, and J. Skonieczny. Angle dependent total current spectroscopy of graphite surfaces of various anisotropy. *Journal of Physics C: Solid State Physics*, 18(12):2563, April 1985.

[224] Günter Wilkening and Ludger Koenders. *Nanoscale Calibration Standards and Methods: Dimensional and Related Measurements in the Micro and Nanometer Range*. John Wiley & Sons, May 2006.

[225] G. Iadarola. *Proceedings of IPAC2013, Shanghai, China*, page 1131, 2013.

[226] G. Iadarola and G. Rumolo. *Proceedings of Proceedings on ECLOUD'12 (2013)*. CERN-2013-002, p. 189., -002, p. 189. edition, 2013.

[227] Giovanni Iadarola. Electron cloud studies for CERN particle accelerators and simulation code development, May 2014.

[228] V. Baglin, I. Collins, B. Henrist, N. Hilleret, and G. Vorlaufer. *LHC Project Report 472*. CERN, 2001.

[229] M. A. Furman and M. T. F. Pivi. Probabilistic model for the simulation of secondary electron emission. *Physical Review Special Topics-Accelerators and Beams*, 5(12):124404, 2002.

[230] Liljeroth. Structural manipulation of the graphene/metal interface with ar+ irradiation. *Phys. Rev. B*, 88:155419, 2013.

[231] R. F. Willis, B. Fitton, and G. S. Painter. Secondary electron enlission spectroscopy and the observation of high energy excited states in graphite: Theory and experiment. *Phys. Rev. B*, 9:1926–1937, 1974.

[232] P. J. Mlert and M. H. Mohamed. An experimental study of the energy dependence of the total yield due to the incidence of low energy electrons onto graphite surfaces. *J. Phys. C: Solid State Phys.*, 15:6457–6462, 1982.

[233] A. Hoffman, P.J.K. Paterson, and S. Prawer. Effect of low energy argon ion irradiation on the secondary electron emission spectrum og highly oriented pyrolytic graphite. *Nucl. Instrum. Meth. Phys. Res.*, 51:226–231, 1990.

[234] V. N. Strocov, P. Blaha, H. I. Starnberg, M. Rohlfing, R. Claessen, J.-M. Debever, and J.-M. Themlin. Three-dimensional unoccupied band structure of graphite: Very-low-energy electron diffraction and band calculations. *Physical Review B*, 61(7):4994, 2000.

[235] N. A. W. Holzwarth, Steven G. Louie, and Sohrab Rabii. X ray form factors and the electronic structure of graphite. *Physical Review B*, 26(10):5382–5390, November 1982.

[236] R. C. Tatar and S. Rabii. Electronic properties of graphite: A unified theoretical study. *Physical Review B*, 25(6):4126–4141, March 1982.

[237] M. Posternak, A. Baldereschi, A. J. Freeman, E. Wimmer, and M. Weinert. Prediction of Electronic Interlayer States in Graphite and Reinterpretation of Alkali Bands in Graphite Intercalation Compounds. *Physical Review Letters*, 50(10):761–764, March 1983.

[238] Wilford N. Hansen and Galen J. Hansen. Standard reference surfaces for work function measurements in air. *Surface science*, 481(1):172–184, 2001.

[239] M. M. Beerbom, B. Lägel, A. J. Cascio, B. V. Doran, and R. Schlaf. Direct comparison of photoemission spectroscopy and in situ Kelvin probe work function measurements on indium tin oxide films. *Journal of electron spectroscopy and related phenomena*, 152(1):12–17, 2006.

[240] Rudy Schlaf. Tutorial on Work Function. *Dept. of Electrical.*

[241] Detailed investigation of the low energy secondary electron yield (sey) of technical cu and its relevance for the lhc. *PR ST submitted*, 4.

[242] Rosanna Larciprete, Davide Remo Grosso, Antonio Di Trolio, and Roberto Cimino. Evolution of the secondary electron emission during the graphitization of thin C films. *Applied Surface Science*, 328:356–360, 2015.

[243] N. E. Nickles. *The Role of Bandgap in the Secondary Electron Emission of Small Bandgap Semiconductors: Studies of Graphitic Carbon.* All Graduate Theses and Dissertations. Paper 1696. *http* : *//digitalcommons.usu.edu/etd/*1696, 2002.

[244] Tetsuo Tanabe. Radiation damage of graphite - degradation of material parameters and defect structures. *Physica Scripta*, 1996(T64):7, January 1996.

[245] Narjes Gorjizadeh, Amir A. Farajian, and Yoshiyuki Kawazoe. The effects of defects on the conductance of graphene nanoribbons. *Nanotechnology*, 20(1):015201, January 2009.

[246] Dmitrii L. Maslov, Vladimir I. Yudson, Andres M. Somoza, and Miguel Ortuño. Delocalization by disorder in layered systems. *Physical review letters*, 102(21):216601, 2009.

[247] Banhart. Structural defects in graphene. *ACS nano*, 5(1):26–41, 2010.

[248] SeGi Yu, Whikun Yi, Taewon Jeong, Jeonghee Lee, Jungna Heo, Chang Soo Lee, D. Jeon, and J. M. Kim. Secondary electron emission for layered structures. *Journal of Vacuum Science & Technology A*, 20(3):950–952, 2002.

[249] James F. Ziegler, Jochen P. Biersack, and Matthias D. Ziegler. *SRIM, the stopping and range of ions in matter.* Lulu. com, 2008.